Abiogenically Relevant Self-Assembly Processes Within Silica Hydrogels

KAMAL GASIM SHAALAN ALBDEERY

Submitted in accordance with the requirements for the degree of
Doctor of Philosophy

The University of Leeds
School of Chemistry

September 2019

Reference for jointly authored publication

1. Gorrell, I.B., Henderson, T.W., Albdeery, K., Savage, P.M., Kee, T.P., Chemical Transformations in Proto-Cytoplasmic Media. Phosphorus Coupling in the Silica Hydrogel Phase. Life 2017, 7(4), 45.

This paper contains material from Chapter 2 of this thesis. Specifically in includes some results from scanning electron microscopy, BET surface area measurements and dynamic light scattering studies on silica hydrogels that had been prepare for analysis via critical point drying. All the phosphorus chemistry in this paper was performed by IBG, TWH & PMS. TPK wrote the manuscript.

2. Amphiphilic Self-Assembly in the Silica Hydrogel Phase. Implications for Abiogenesis (based on material in chapter 3). K. Albdeery, S. Alanazi and T. P. Kee.
   Manuscript in preparation, to be submitted to *Life*

3. Molecular Diffusional Behaviour of Condensed Phosphates in the Silica Hydrogel Phase (based on material in chapter 5) K. Albdeery, George Hodgin and T. P. Kee.
   Manuscript in preparation, to be submitted to *Life.*

Dedicated to…

My dear mother Mrs Fatima Alsafi (may Allah bless her soul), your voice left me with tears since the early stage of my PhD journey but your soul will be with me forever. You were my first mentor and your words still touching my heart when remembers and may Allah give me strength and faith to hold what you learn me. I will always remember how you gently held my hand and help me to write my first letter ever. Thank you, mom, for everything and wish to gather in heaven.

Acknowledgements

I would like to express my sincere gratitude to my supervisor Dr Terence P. Kee for his time, patient, helping, encouragement, guiding and advice during my research time. I could not achieve this work without his unlimited support. Thanks are due to the Government of Iraq, Ministry of Higher Education and Scientific Research for their financial support of this work. The Iraqi cultural attaché in London for their support during my research time. I would like to thank my co-supervisor Dr Paul Thornton for his valuable advices, helping, support and efforts during my research time more especially when he spends hours to revise my previous reports.

I would like to thank the love of my life, Mrs Anaam Alrakhat my wife and the mother of my three angels Ridha, Jaffar and Ayah, for her continuous support and unconditional love during my dark times.

I would like to thank my dad, my brothers and my sisters for their unconditional love, support, and encouragement. My dear family, day after day, I realize how much you both sacrificed to give us a better life. I love you all from the bottom of my heart.

I would like to thank Prof. Dejian Zhou and Prof. Patrick McGowan for them valuable corrections and feedback on my transfer report. In addition I would thank Mr Martin Fuller for helping me in critical point drying, Mr Stuart Micklethwaite for helping to perform scanning electron microscopy, Mr David Fogarty for help and support on the UV and Fluorescence spectroscopy instruments (and for reminding me to wear my lab coat and safety specs), Dr Algy Kazlauciunas for training on dynamic light scattering and performing the thermal analysis, Dr Angela Bejarano-Villafuerte and Dr Alex Kulak for helping in the SEM images, BET and EDX and Dr Mark Howred, Dr Mathias Nilsson, Dr Laura Castanar acedo and Gabriel Rossetto for their combined technical expertise in performing DOSY experiments. Finally, I would like to thank Mrs A. Luty and all staff members at the University of Leeds.

Abstract

In this thesis are presented studies which are aimed at elucidating the effects, if any, that the hydrogel phase has in influence chemical processes of relevance to abiogenesis over the aqueous phase. The significance of this is set in the light of the hydrogel hypothesis which suggests that the most primitive organisms would have emerged within a hydrogel environment rather than purely an aqueous one.

Chapter 1 provides an introduction to the fundamental principles of interest to this work, discusses hydrogels, their synthesis, properties, applications and especially their potential role in abiogenesis. Also discussed are the concepts of amphiphilic self-assembly and molecular diffusions which are two molecular behaviours that have been looked at in most detail here. This chapter then concludes with some discussion of the analytical techniques used within the project.

Chapter 2 describes the preparation of silica hydrogels (the main hydrogel used in this work) along with methods for isolating the silica matrix and surface analyses using electron microscopy and associated techniques (BET, EDX). This section also includes the results of dynamic light scattering and thermogravimetric studies on silica hydrogels.

Chapter 3 outlines how amphiphilic self-assembly of a probe molecule, sodium dodecylsulphate (SDS), behaviour differs between the aqueous and silica hydrogel phases. This is achieved through measurements of critical micelle concentrations in both phases using UV-VIS spectrophotometry and colorimetric reporter dyes (merocyanine 540 and pinacyanol chloride). The key outcome being that CMC's are definitively reduced in the salt-containing silica hydrogel over the pure aqueous phase.

Chapter 4 describes investigations into a decolourisation phenomenon observed with the merocyanine 540 dye which says it complete colour bleach at high silicate concentrations of the hydrogel. Whilst the investigations did not produce a definitive answer to this issue it did highlight a protective role for amphiphiles in the decolourisation and also led, indirectly, to observations allowing us to probe gelation times using simple light scattering.

Chapter 5 discusses the use of diffusion order spectroscopy (DOSY) as a technique for measuring and comparing molecular diffusion coefficients in both aqueous and silica hydrogel phases. Molecules of prebiotic significance such as the adenosine phosphates and condensed phosphates, AMP, ADP, ATP as well as the sugar d-ribose. Results suggest that direct measurements of

diffusion coefficients in the silica hydrogel phase is effective and offers a potentially useful tool for probing more complex diffusional behaviours.

Chapter 6 contains the experimental details from Chapters 2-5 and Chapter 7 offers a summary, conclusions and future work perspective.

Abbreviations

˚C	degrees Celsius
µL	microliter
µm	micrometre
3D	three dimensions
Abs	absorption
ADP	adenosine diphosphate
AMP	adenosine monophosphate
ATP	adenosine triphosphate
BET	Brunauer-Emmett-Teller (surface area analysis)
CAC	critical aggregation concentration
CHC	critical hydrogen-bonding concentration
CMC	critical micelle concentration
CMC	critical micelle concentration
CP/MAS	cross polarization and magic-angle spinning
CPD	critical point drying
CVC	critical vesicle concentration
D_2O	deuterium water
DLS	dynamic light scattering; Z-average, size average
DOSY	diffusion-ordered spectroscopy
DSC	differential scanning calorimetry
DTG	differential thermogravimetry
eV	electron volts
EXD	energy dispersive X-ray

FID	Fourier Transformation of the imported
GNAT	general NMR analysis toolbox
Gw	Gaussian
HR	high resolution
Hrs	hours
Hz	hertz
I	intensity
ICTAC	The International Confederation for Thermal Analysis and Calorimetry
K	Kelvin
LEMAS	Leeds Electron Microscopy and Spectroscopy Centre
lw	Lorentzian
M	molar (moles per litre)
MC540	merocyanine 540
MC^{s*}	excited singlet merocyanine 540
MHz	megahertz
Min	minute
mM	millimoles per litre
mS	milliSiemens
NIR	near infrared
nm	nanometre
NMR	nuclear magnetic resonance
PAH	polycyclic aromatic hydrocarbon
PC	pinacaynol chloride
PFG	pulsed field gradient
ppm	part per million

RF	radio frequency
SAXS	small angle X-ray scattering
SDS	sodium dodcecylsulphate
SEM	scanning electron microscopy
SGHs	silica hydrogels
SMO	singlet molecular oxygen
SOP	standard operating protocol
ST.Dev	standard deviation
STE	stimulated echo
TA	thermal analysis
TEM	transition electron microscopy
TGA	thermogravimetric analysis
UV-Vis	UV-Visible
WAXS	wide angle X-ray scattering

Table of Contents

List of Figures

List of Tables

List of Schemes

Chapter 1 Introduction and Background

The aim of this chapter is to explain the structural concept of silica hydrogel along with its importance in abiogenesis studies as a reaction environment in which most likely to be present in Hadean period. The next part of this chapter mainly focus on techniques and instrumentations which used during my study and the theory principles behind it.

1.1 Hydrogels

A hydrogel is a three-dimensional network composed of a (macro)molecule that is dispersed in water, forming a structure that contains large amounts of water. This ability is due to cross-linkage of the hydrophilic chains of the gelator[1]. The following definition of a hydrogel by P. W. Atkins has widely acknowledged: “*it is a semi-rigid mass of a lyophilic sol in which all the dispersion medium has been absorbed by the sol particles*”[2].

The term ‘hydrogel’ should fulfil the following criteria and phenomenological characteristics to be considered as a gel system: (a) it consists of at least two different components one of which is an aqueous phase, and (b) the formation of matrices which are solid, soft or solid-like components [3].

1.1.1 Applications of silica hydrogels(SHGs)

In the work described in this report, commercially available sodium silicate solutions (water glass) have been to prepare silica hydrogels. The repeat unit of the hydrogel chain is shown in Figure 1-1

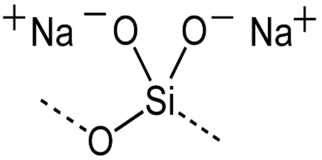

Figure 1-1 Structure for commercially available aqueous sodium silicate solution

The polymer chains of silica hydrogels (SHG’s) usually exist in a random orientation coiled around each other [1]. Several recent applications of silica hydrogels have appeared, of which the following are highlights:

1- The hydrogels can be used as the basis for drug delivery systems [4-6]
2- Silica hydrogel hybrid beads have been developed as an array chip used in the medical field as cancerous tumour markers [7].
3- Used in producing a hydrophilic and gel-like biological interface coating material by using a method called Low-Pressure Plasma without any reaction of a functional group in the aqueous phase [8].
4- Biodegradable systems for wound healing [9].
5- Sugar-based hydrogels have been developed as food additives [10].
6- Scaffolds in tissue engineering [11]
7- According to Wang '*hydrogel composites may be used as a growth factor and cell carriers for cardiovascular tissue engineering'* [12].
8- Hydrogels have been developed as biosensors in a neural control system [13].
9- Hydrogels have been proposed as a plausible environment for the first, primitive proto-cells within the field of cellularity emergence. [14].
10- Hydrogels have been used as control systems to regulate fluid flow within microfluidic channels [15]
11- Hydrogels are routinely used in the field of cell engineering and regenerative medicine as culture models due to their viscoelastic nature[16].
12- Recent biomedical applications for hydrogels have seen them used as enzyme-responsive systems inside cells [17].
13- Hybrid organic-inorganic films, prepared by the sol-gel method, have been used as a coating material to reduce corrosion in aluminium pipes[18].

1.1.2 Importance of Hydrogels in Abiogenesis

The origin of life problem continues to challenge scientists, philosophers and the general public alike. From the scientific perspective, scientists are trying to understand how the first, primitive cellular life forms could have emerged on the early, Hadean earth. This involves consideration of which physical and chemical conditions would have been required, which environments are suitable for the growth and division of the first such cellular organisms and whether mineral surfaces or deep oceanic vents, among others are implicated [14, 19-25]. To answer these questions, an implicit presumption is made that a biological cell, is essentially an aqueous suspension of solutes. Thus, it is usually considered that pre-cellular environments would also most likely conform to an aqueous suspension either by itself or in close proximity to a mineral surface with the potential to act as a catalyst/partitioning material [26]. Consequently, all essentially prebiotic chemical studies have been conducted within environments that resemble: (i) fresh water aqueous, (ii) salt water aqueous, (iii) wetting-drying cycles, (iv) the aqueous-mineral interface. it has been proposed that another environment may be as important if not more important that these others, and that is a hydrogel. Why? If we are trying to understand the emergence of the most primitive life on earth, then this life is most probably viewed as a unicellular organism. Unicellular organisms exist today of course and It has been shown that their basic environment is one of cytoplasm, and this is best described as being a hydrogel rather than an aqueous suspension [26].

Despite this connection, to date there have been remarkably few experimental studies published, to the best of our knowledge, that explore abiogenesis experiments within hydrogel environments[27]. The idea was recognised and promoted as a theoretical hypothesis in the mid-2000's. Trevors and Pollack in 2005 proposed that '*a primitive hydrogel was a more suitable environment for the assembly of pre-cells, and ultimately cells capable of growth and division'*. Gels, for example, retain their integrity even in the absence of a membrane as they have a definitive separation mechanism from its immediate aqueous environment that is due to differences in natural density or viscosity. The hydrogel environment has the ability to retain a large amount of water, gas bubbles and oily hydrocarbons due to the cross-linked molecular structure [14]. The first, most primitive geological gel environment may have been composed of an oily water mixture interfaced with each other [28]. Such a prebiotic gel may then have transitioned into something akin to a biofilm, by capturing essential nutrients (from the surrounded environment) until a sufficient level of required concentration of reactant molecules was achieved to enable the first integrated chemical machines from which life ultimately emerged [14]. Williamson *et al* reported inclusions of crystallised silica colloid, based on textural and chemical characterisation within a Topaz granite and the colloidal origin of inclusions of Varlamoffite in the Topaz [29]. Silica colloid crystal was probably trapped in a form of hydrogel during greisenisation process[1] [30]. These observations are considered amongst the first evidence of formation of silica colloids in high temperature thermal fluid systems [29].

1.1.3 Formation and Structural Analysis of Silica Hydrogels (SHG's)

A variety of techniques can be used to provide information concerning the structures of SHGs, for a better understanding of the mechanisms of formation and how the silica hydrogels have the ability to retain large amounts of water. The use of X-ray scattering and dielectric spectroscopy techniques to illustrate water confined within the 3D structure of optically transparent SHGs is especially powerful [31].

Sol-gel preparation methods have been used to prepare SHG and measurements have been conducted on samples after having experienced various ageing times, the results were then compared with previous results obtained using near infrared (NIR) absorption spectroscopy. The results of X-ray scattering techniques provide an estimation of the size and structure of the pores present within the matrix and the irregular distribution of water molecules around the SHGs. For example, the average pore size of 0.5 M SHG was found to be 162 nm. This contribution [32] presents structural (Wide Angle X-ray Scattering, WAXS), and Small Angle X-ray Scattering, SAXS) and dynamic (dielectric relaxation spectroscopy) studies on water molecules trapped in the cross-linked structure of SHGs and compare the result data with prior data from NIR spectroscopy.

The dielectric spectroscopy technique which operates at higher temperatures of *ca.* 130-280 K provides information on water dynamics within the 3D structure. The results show that the structure of SHGs can best be described as disordered and depends on the age of the gel samples. It also shows that the distribution of water molecules inside the pores of the matrix is irregular, the disorder of water molecules increasing with an increase in ageing time of the

---

[1] a post magmatic process associated with the origin of high silica granites

sample used. Suggestions have been made that the constraints forced by the gel matrix on trapped water molecules increase with increasing sample age[31].

Another technique, proposed by Ferri, used elastic light scattering to study different formations of a hydrogel, including aerogels and colloidal SHG. These types of gels show mass fractal behaviour (a mass fractal is a structure containing branching and crosslinking to form a 3D network[33]) at length scale under a crossover length and the fractal dimension depends on silica volume and gelation conditions [32].

The surface structures of SHGs have been studied by using the reaction of aluminium chloride ($AlCl_3$) and silicon chloride ($SiCl_4$) with a hydroxyl group on the surface of the gel [34]. Results showed that even on highly dried surfaces, a higher degree of hydroxyl group residuals is paired with each other.

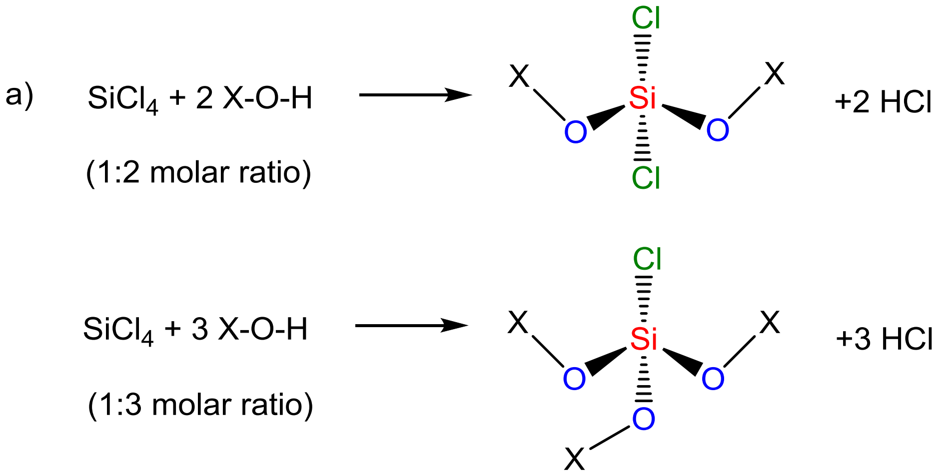

Scheme 1-1: Possible reactions of $SiCl_4$ with surface hydroxyl groups with to yield apparent stoichiometry of 1:2 or 1:3 (X=Na)

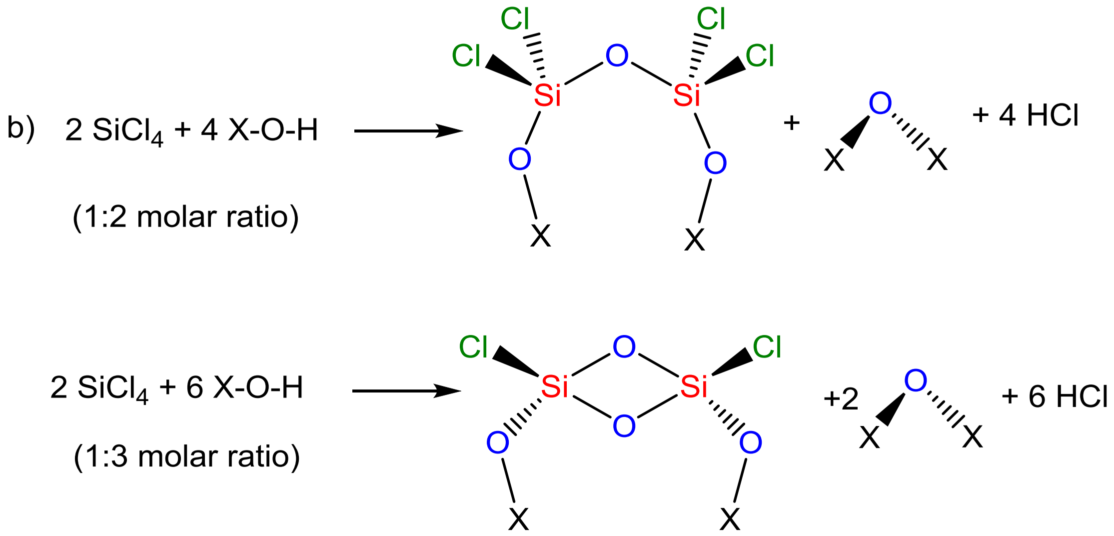

Scheme 1-2: Possible reactions of $SiCl_4$ with surface hydroxyl groups each $SiCl_4$ molecule was allowed to react with only one hydroxyl group but one H_2O molecule was also formed by condensation.

Greater than 95% of hydroxyl groups were found to have undergone chemical transformation at a temperature of 400 °C after drying while higher than 85% of the hydroxyl groups were found to have reacted at 600 °C after drying. The result also showed that if a pair of hydroxyl groups exists, the surface has the ability to reassemble around 111 faces of cristobalite, while when the surfaces are fully hydrated, the surface has the capacity to assemble around 100 cristabolite faces. The cristabolite faces contain two hydroxyl groups attached to one surface silicon atom [34].

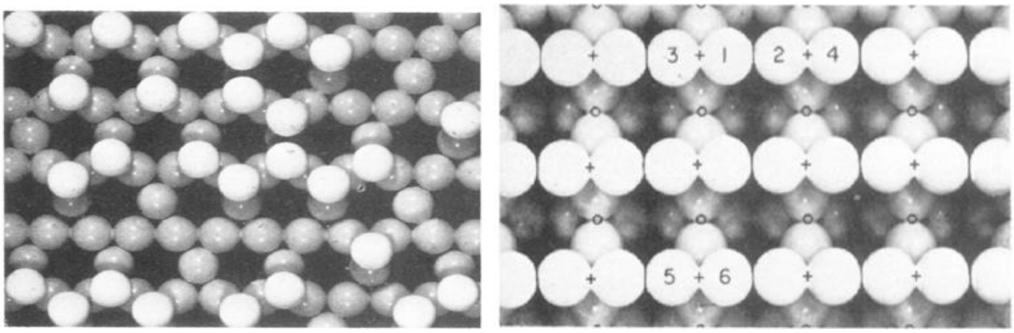

Figure 1-2: Left: Surface hydroxyl group (white) are attached randomly rather than in regular alternation, to surface silicon atoms (not shown), held in interstices between oxide ion (grey). Right: Two hydroxyl groups (white) are held by silicon atoms in interstices beneath the (+ sign). Other silicon atoms are held in interstices beneath the small circles[34]

Sukhayy *et al* studied the silica gel - sodium sulfate composite system by examining their sorbent properties by using wide-angle X-ray scattering and IR-spectroscopy. Results showed that the sorption properties tend to be a non-linear combination of the medium and salt properties which is evidence of expected structure formation, increasing in the crystal hydration and water evaporation rate in a SiO_2 medium[35].

1.1.4 Critical Point Drying (CPD) Technique

Critical Point Drying (CPD) is employed in the biological and medical sciences to dehydrate fragile biological tissue prior to examination of samples by scanning electron microscopy (SEM) or other microscopy techniques (Figure 1-3). It allows preservation of the surface morphology that may be damaged if exposed to evaporative air drying [36]. A similar destructive fate can occur using freeze-drying methods also. Such damage is caused by the surface tension of liquid present in the specimens (mainly water), which upon evaporation from the cell boundary causes increased cell tensile strength and ultimate collapse of the cell structure [37]. A comparison of the surface properties of liquids other than water (e.g acetone) shows that replacing water with a liquid that has lower surface tension can help preserve the internal gel matrix structure. The critical point drying technique involves a substitution of water with another liquid having a lower surface tension to maintain the basic structure of examined specimen in the absence of an aqueous fluid phase. When the surface tension of a liquid became insignificant or reduced to zero, the liquid surface becomes unstable and finally disappears. At this pressure-temperature intersection, liquid and vapour phases co-exist as a new phase, the critical phase (Figure 1-3). When the critical point is reached, it is possible to shift from liquid to gas phase without any sudden change in the gel matrix, and the specimen will transition from wet to dry environment, avoiding contact with the surface and avoiding much of the damage caused by the surface tension [38, 39].

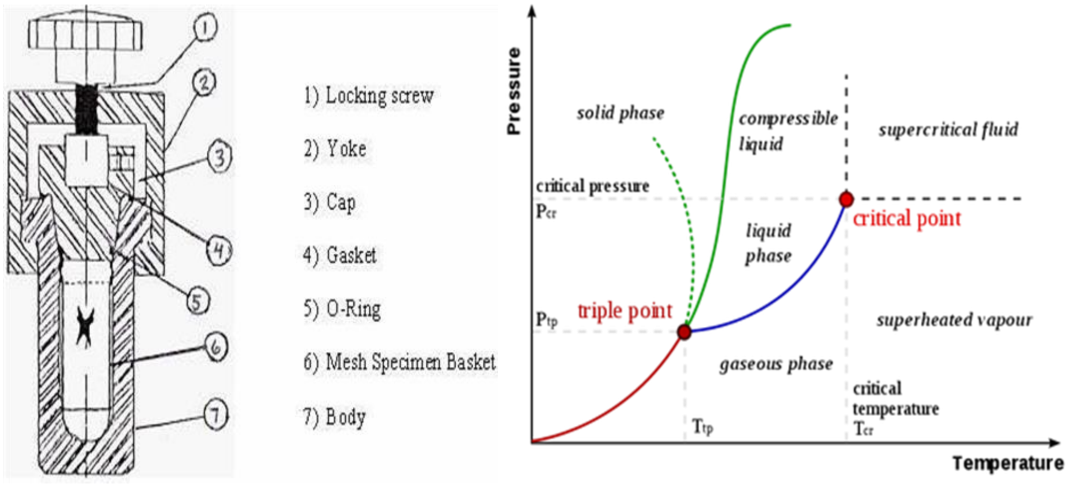

Figure 1-3: Left: Block diagram of critical point of drying CPD instrument. Right: Phase diagram of Critical Point Drying technique [36].

1.1.5 Scanning Electron Microscopy (SEM)

SEM is a form of microscopy that uses high-energy electron beams, focused on the sample to generate different signals from the surface of a solid specimen, allowing the generation of high magnification images, and less than 0.1 µm of the sample morphology. When coupled to an energy dispersive X-ray instrument (EDX), chemical composition information can also be gained as a result of element-specific X-ray emission [40]. The images generated by SEM reveal information about the crystalline structure, surface texture, chemical composition and orientation of materials which forms the sample [41]. A beam of high voltage electrons (~ 5-100 KeV) formed from an electron source which is usually heated tungsten wire is accelerated within a vacuum tube and attracted towards the sample with positive electrical potential as shown in Figure 1-4. The electron beam is then focused on the sample using a set of magnetic lenses. Scanning electron microscopy techniques have the ability to analyse macromolecular compounds, mixtures within their 3D structures or within a biological or cellular environment. Figure 1-4 shows the effect of high voltage electrons incident from the source towards the sample which leads to producing low-energy (< 50 eV) secondary electrons, required sample depth, light emission, back scattered electrons, characteristic X-ray emission, high voltage primary electron path and transmitted electrons [42].

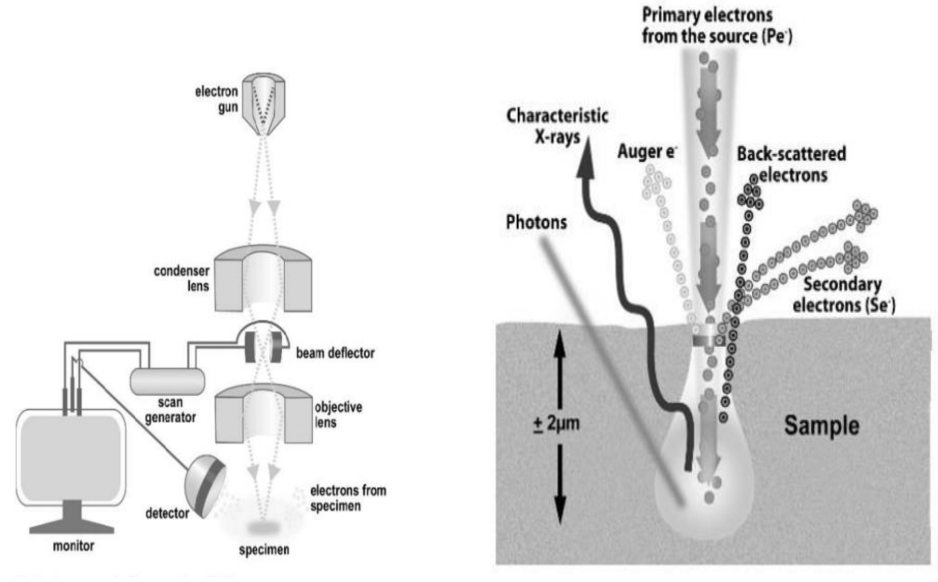

Figure 1-4: Left: Block diagram of scanning electron microscope and indicating parts of the instrument. Right: Effect of bombarding electrons on a solid sample[41]

1.2 *Amphiphile self-Assembly*

1.1.1 Micelle Formation

Surfactant molecules are amphiphilic molecules which are made up of hydrophilic, polar head groups (ionic or non-ionic) and hydrophobic, apolar tail groups [43].

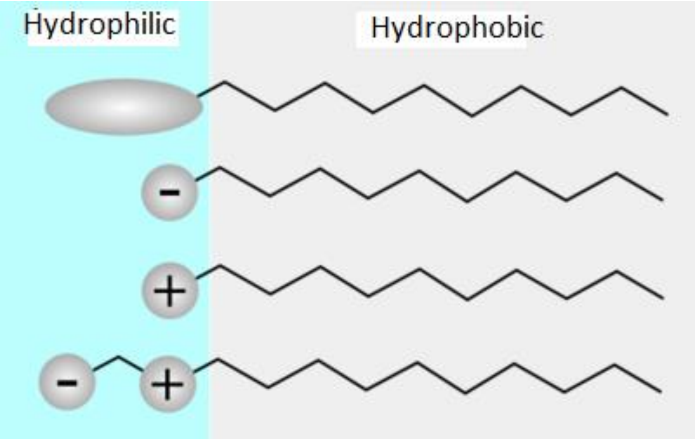

Figure 1-5: Classification of surfactant according to the polarity of the head group: non-ionic, anionic, cationic, amphoteric surfactants

Surfactants are surface-active compounds which reduce the surface tension of water when used in a small concentration and have a wide range of applications in pharmaceuticals, motor oils, detergents, soap industry and as a membrane for mimicking investigations on cellular systems [44].

The importance of amphiphilic surfactants is due to their ability to self-assemble in solution and form a regular dynamic, nanoscale or larger structures. The nanoscale structure determines many features of amphiphiles, related to their specific applications in biomedicine, materials and pharmaceuticals. The self-assembly behaviour of surfactants has been studied widely as a result of this broad-based applicability. The overall shape of these aggregates has a direct effect on the properties of surfactant systems, for example, viscosity, viscoelastic properties and solubility [45].

To choose molecules that have preferred structural properties such as micelles which are globular, spherical or rod-like, or vesicles which are composed of a spherical bilayer, it is essential to understand how amphiphile structure controls the formation shape and size of resulting aggregates [45].

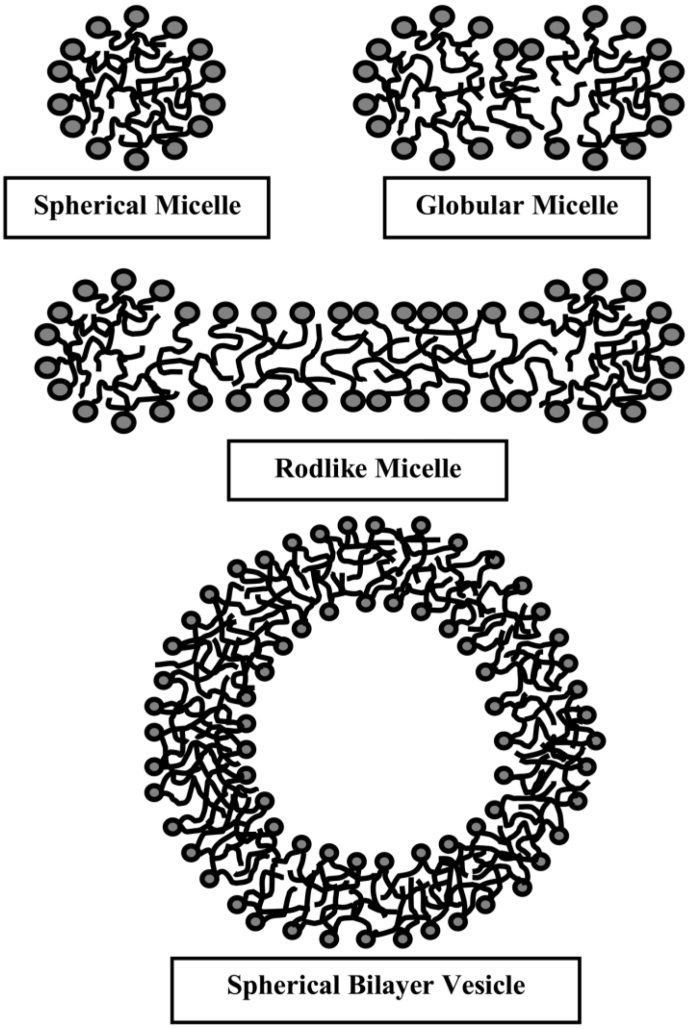

Figure 1-6: Structures formation of surfactant in solution representing various aggregates of micelle and vesicle structur shape

As pointed out by Tanford [46], the driving force behind the self-assembly behaviour of surfactants, may be represented mathematically by the balance of free energies on aggregation , which is equal to '*the difference in the standard state free energy between singly dispersed surfactant molecules present in solution and surfactant molecules present in an isolated aggregate of any shape in solution*'. By using the free energy expression below, the driving force of surfactant aggregation in an aqueous phase and the limited growing process can be viewed as being one of balancing several forces [46].

$$\left(\frac{\Delta\mu_g^o}{kT}\right) = \left(\frac{\Delta\mu_g^o}{kT}\right)_{Transfer} + \left(\frac{\Delta\mu_g^o}{kT}\right)_{Interface} + \left(\frac{\Delta\mu_g^o}{kT}\right)_{Head} \qquad \textbf{Equation 1-1}$$

The term $(\Delta\mu^o{}_g/kT)_{Transfer}$ in the above equation represents a negatively charged free energy transfer of the hydrophobic amphiphile tail from a specific point in solution to the hydrocarbon-like phase in the centre of the aggregate. The following term, $(\Delta\mu^o{}_g/kT)_{Interface}$ is a positively charged limit due to the fact that not the entire surface area of the tail is physically in the aggregate centre, there is still contact between the tail and the aqueous environment. The third term, $(\Delta\mu^{o}_{g}/kT)_{Head}$ is a positive limit representing the repulsive interaction between the head groups that gather at the surface of the aggregated structure directed towards the solvent phase [46]. One factor that affects significantly the self-assembly behaviour molecules in aqueous systems and aggregation behaviour is the ratio of the size between hydrocarbon head group and tail. This ratio dictates the energies of the interaction of both head and tail groups and thus, the morphology of the self-assembled structure observed in practice[47].

A self-assembled micelle structure (Figure 1-7) has been defined by Hine and Martin as '*An aggregate of molecules in a colloid. Small clusters of molecules in which the nonpolar hydrocarbon groups are in the centre and the hydrophilic polar groups are on the outside*' [48].

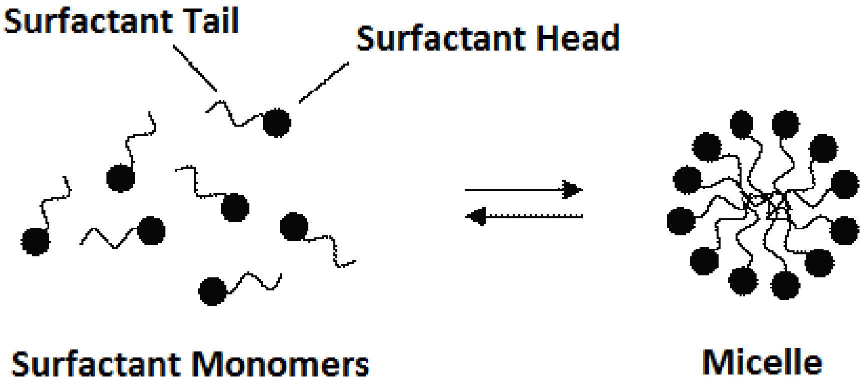

Figure 1-7: The reversible monomer-micelle thermodynamic equilibrium. Indicating the surfactant heads groups (hydrophilic) and the surfactant tails groups (hydrophobic).

Arguably, the most important property of the surfactant is an ability to engage in self-assembly which allows energy-balanced phase separation between hydrophobic and hydrophilic regions[43]. This then permits the more effective dispersion of moderately soluble molecules in water by incorporating them into the hydrophobic interior of the structure [43]. In aqueous solution micelle formation will only take place above a certain minimum concentration called the critical micelle concentration (CMC). Critical micelle concentration is defined as the minimum concentration of molecules at which the vesicle, micelle, hydrogen bonding and aggregates start forming in a solution at a given temperature and pH [49]. The critical micelle concentration is one example of critical assembly concentration number which also includes; critical vesicle concentration (CVC), critical micelle concentration (CMC), critical hydrogen-bonding concentration (CHC) and critical aggregation concentration (CAC). The critical concentration of an analyte which is distributed in a solvent is a significant factor and known as CMC is a key concept for surfactants, while CHC and CAC are a vital concept for biological peptide and portions [49].

1.2.1 Vesicle Formation

Vesicles are hollow aggregates [50], built from bilayers of amphiphilic molecules, distributed into and filled within a solvent.

These aggregates can be described as (below, above and at) equilibrium meta-stable structures and they exhibit a rich variety of different morphologies [50]. Due to their physical and chemical properties, vesicles are used in a wide range of industrial [51-53], and biological [54-59] applications.

Vesicle structures are bounded and soft aggregates which contains a flexible bilayer of amphiphile molecules to form a spherical unilamellar, multilamellar or oligovesicular overall shape, while the size may vary from few nanometres to micro meters [50].

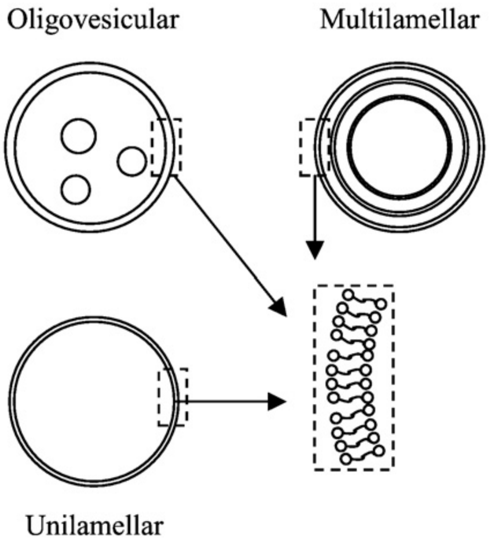

Figure 1-8: Different vesicle bilayer morphologies, the small circles represent the hydrophobic head group and squiggly lines are the hydrophilic tail group [50].

The study of the self–assembly behaviour of mono-hydrocarbon chain amphiphiles has thus focused on phosphate ester (amphiphile) and derivatives because of their aggregation feature and containing mainly on hydrophobic moiety between head and tail group [60].

The investigation of the formation of bilayer by phosphate ester was found to be sensitive to factors that directly affected the shape and vesicle formation rate, these factors are:

1- The pH of the medium [61]
2- The ionic strength of phosphate ester in solution [62]
3- The temperature of the solution were the bilayer formation take place [63]
4- The number of methyl groups in the hydrocarbon chain [60]

1.1.2 Measurements of critical micelle concentrations

Different techniques have been used to measure the CMC of a surfactant such as the surface tension of the surfactant-water mixture, solution conductivity changes and spectroscopic methods, fluorimetry and UV-vis spectroscopy, among others. Below is a brief summary of how these different methods work and a discussion of which methods have been selected for use in this project.

1.1.2.1 Surface Tension & Conductivity methods

Surface tension methods for estimating the CMC for a surfactant are based on the fact that the surface tension of a system decreases with increase in the concentration of surfactant in solution [64]. At concentrations below the CMC, the surfactant molecules exist as separated monomers in solution and aggregate at the surface where aqueous and atmospheric phases interface. The surfactant molecules are in dynamic equilibrium between these states. At equilibrium, at a given set concentration, pressure and temperature parameters, the number of monomeric amphiphilic molecules and monomers adsorbed at the surface is constant [65].

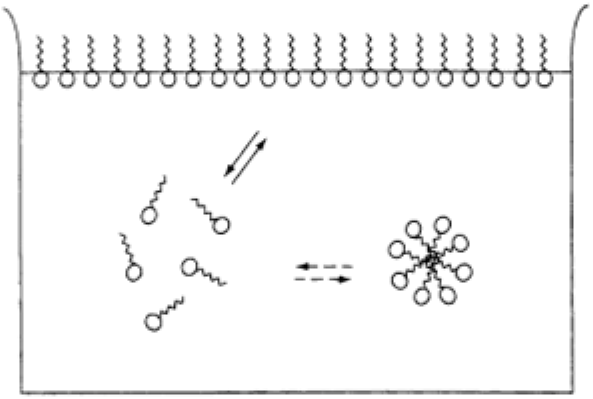

Figure 1-9 Schematic representation of the three states in which surfactant molecules reside in water, i.e. monomers adsorbed at the air/water interface, monomers in the bulk solution and micelles.

Micellisation is essentially a process driven by the entropy change of surfactant molecules interacting with a solvent environment [46]. The process of solvating a surfactant in an aqueous phase leads to a disturbance of the structure of the water molecules within that phase and ultimately decreases the free energy of the solution. The surfactant molecules have a tendency to congregate at the surface where, at the air/water interface, the hydrophobic head group of the surfactant is arranged in a conformation where it can be directed away from the water surface which consequently reduces the free energy of the solution to a minimum. The surfactant molecules distribution caused by water molecules structure can be minimized by the accumulation of surface active molecules into micelles in which the head groups are collectively arranged towards the aqueous phase and the hydrophobic tails phase separate within the micelle and away from the aqueous phase.

However, the surfactant molecules may also have some of their molecular freedom constrained by being restricted within a micellar structure. Besides this effect, in the case of an ionic charged surfactant, these amphiphilic molecules experience electrostatic repulsion effects from the charged head-groups. These forces lead the free energy of the system to increase and hence micelle formation becomes less favourable energetically. Hence, the micellisation process depends on the equilibrium of forces between Van der-Waals and hydrophobic forces and those opposing the formation such as electrostatic repulsion and kinetic energy [66].

The conductivity method for estimating the CMC of a surfactant, which is used only for ionic surfactants, depends on the nature and concentration of mobile ions in ion exchange solution or polymers. The addition of electrolytes to the solution is generally observed to result in a decrease of the CMC value, while this parameter tends to increase with decreasing the charge density of the mobile ions in an ion exchange polymer [67]. The change in the conductivity of a surfactant solution at the CMC point is due to the difference between the degree of ionization of the surfactant below and above the CMC point. Below the CMC point where the aqueous solution of surfactant is free from micelle formation, then the specific conductivity of the solution is due to charges of the surfactants itself.

Above the CMC, the conductivity of the ionic surfactants solution increases. This is explained by, the micelle formation is capturing the charged monomers within the solution [67]. Figure 1-10 shows the formation of the spherical micelle of the negatively charged surfactant SDS in an aqueous solution.

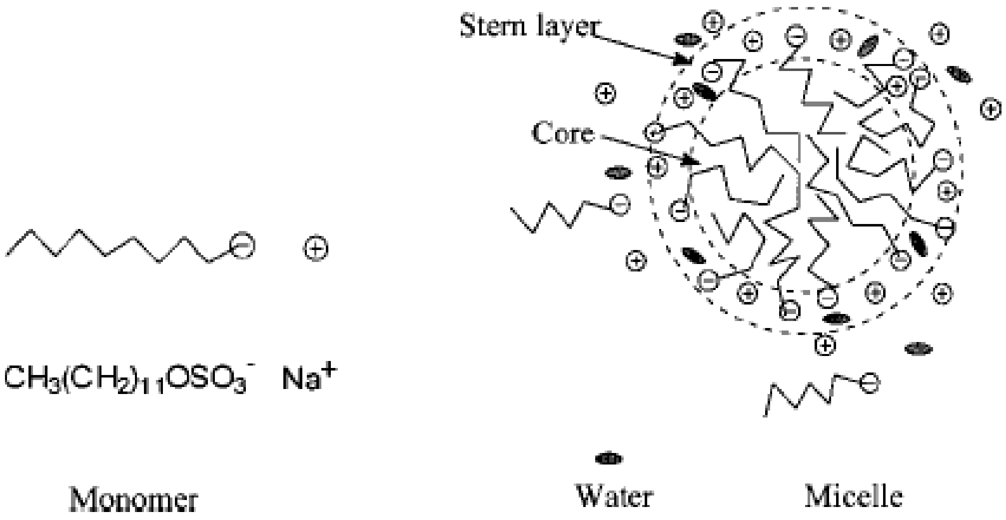

Figure 1-10: The spherical micelle formation of the anionic surfactant SDS in aqueous solution [67]

Colloidal electrolytes show a rather unexpected discontinuity in some physical properties over the short concentration range characterized by the CMC value. Above this point, it is well recognized that the amphipathic ions aggregate while, below the CMC it has been assumed that despite less concentration of electrolytes in the system, ion aggregation still occurs [68].

1.1.2.2 Fluorimetery and UV-Vis spectroscopy methods

Spectroscopic methods are also important tools in the determination of CMC concentrations. The use of spectroscopic methods to determine CMC values of amphiphiles depends on the use of probe molecules which easily partition into micelles and with a specific spectroscopic characteristic change within that micelle structure [69]. The fluorimetric method is based on the dependence of the solvent vibrational band intensities in pyrene solution monomer fluorescence.

Pyrene (Figure 1-11) is a polycyclic aromatic hydrocarbon PAH containing of four benzene rings, resulting in a flat aromatic system and has the chemical formula $C_{16}H_{10}$, and considered to be one of the few condensed aromatic hydrocarbons that show clear vibrational bands in their monomer fluorescence spectra in solution (Figure 1-11). The intensities of the different vibrational bands of pyrene display a strong dependence on the solvent environment due to chemical and physical interactions [70].

The fluorescence method exploits the use of a hydrophobic fluorescent dye which has different fluorescent properties depending upon the physical properties of the system in which it is soluble [71].

The fluorescence probe method shows the importance of solvent dipole moment and dielectric constant on the sensitivity of the method and eventually the value of CMC point [70]. To achieve higher fluorescence quantum yields and clearer spectra, the probe molecules need to be consist of an amphiphilic group with a specific excited state and large electric dipole moments [69].

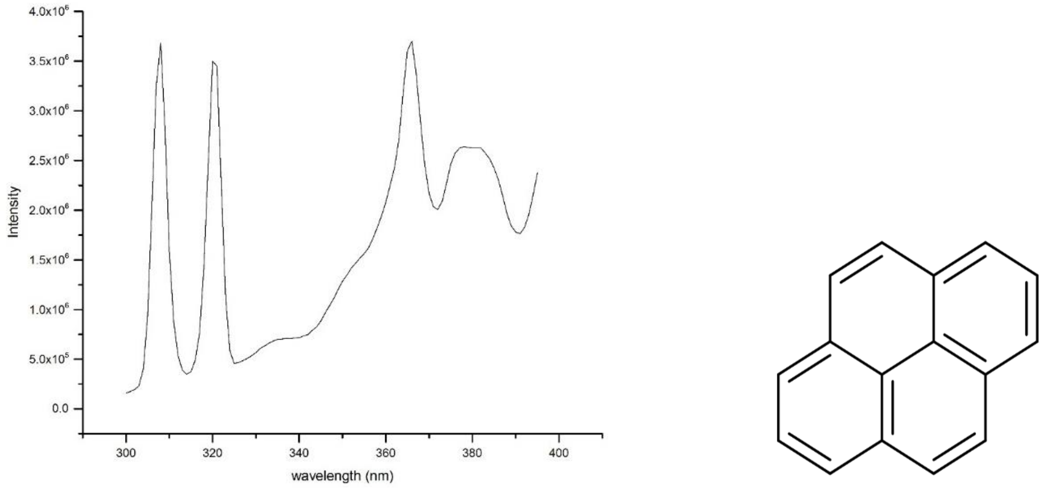

Figure 1-11: Left: Peaks from Flourolog instrument of 1.0 mM of surfactant SDS and pyrene in aqueous phase. Right: Structure of PAH pyrene indicating the flat aromatic ring system.

The spectroscopic features of pyrene change dramatically from a polar to a non-polar environment; making its use in fluorimetric method of CMC determination valuable. This method consist of plotting the peak's intensity against the concentration and the intersection between the lines indicates the CMC estimated value, this method explained in details in Chapter 3.

However, one of the practical issues with pyrene is its rather low water-solubility (0.135 mg/L) which can limit florescent applications in this solvent thus leading to the tendency to form spectrum-clouding microcrystals [69, 72].

However, such issues can frequently be managed by moving from fluorescence techniques to other spectrophotometric methods involving absorption measurements in the UV or visible range of the electromagnetic spectrum. For example, merocyanine 540 and other merocyanine derivatives are among those widely used in spectrophotometric investigations of CMC measurements[73].

Most CMC measurements rely on identifying the marked changes in the specific properties of solutions containing the amphiphile, as their concentration of the latter is increased around the critical micelle concentration or the marked changes in electronic spectra of the probe indicator molecules due to change in excitation-relaxation states [73].

Merocyanine 540 dyes are considered as the most thoroughly characterized of the different dye compounds used as indicators of solvent polarity and in CMC measurements. The change in solvent polarity leads to very large shifts in their electronic spectra. The latter shift the absorption maxima in UV-Visible absorption towards higher wavelength as the polarity of the solvent decreases [73-76].

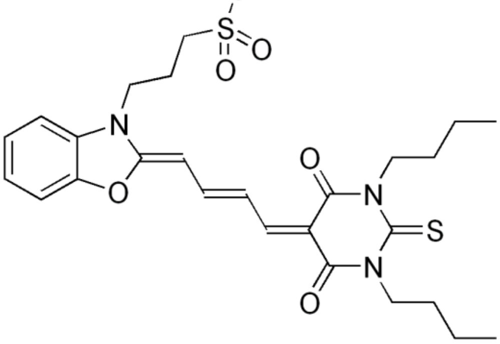

Figure 1-12: Structure of Merocyanine 540

Studies using this technique with Merocyanine 540 as an indication probe show ascending wavelength shifting maxima in its absorption spectrum in solutions containing different detergents over various concentration ranges increasing from below to above the critical micelle concentration. The hydrophobic dye probe based on merocyanine 540 is preferentially solubilized by micelle formation so that the hydrocarbon tail of the molecule breaches the core of hydrophobic micelle while the hydrophilic head group is located in the same microenvironment as the head group of a surfactant forming the micelle[73, 77]. To estimate CMC with the help of merocyanine 540 dye, a method introduced by A. Wicken *et al*[73] involving plot the absorption peaks at two different wavelengths against the concentration of the amphiphile may be used. This method is described in detail in Chapter 3.

1.3 Dynamic Light Scattering (DLS)

In solution, macromolecules are buffeted or being struck by solvent molecules, resulting in a system based on the random motion of macromolecules in the solution. This motion is called Brownian motion (see Figure 1-13), each macromolecule is constantly moving independently of another unless they undergo a collision; their movements are therefore stochastic [78].

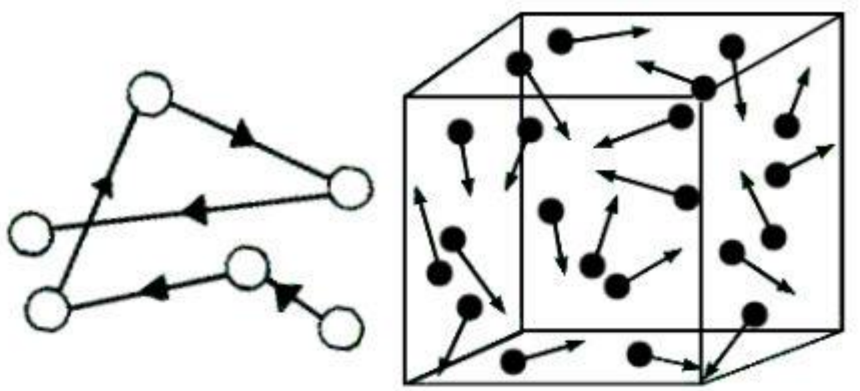

Figure 1-13: Schematic representation of the Brownian motion, random motion of molecules in solutions[78].

When a monochromatic light source undergoes scattering from a system of small, moving particles, this movement can be calculated. Therefore, the geometrical structure, size range and state of motion of macromolecules can also be calculated therefrom. This technique, which is commonly used to measure the diffusivity of macromolecules undergoing Brownian motion, is called photon correlation spectroscopy or dynamic light scattering (DLS)[79].

DLS is one of the most common techniques used to determine the size of particles dispersed in solution. A high energy monochromatic light beam is directed towards a solution within which the molecules are assumed (see Figure 1-14) to behave as though they were spherically symmetrical particles and in random (Brownian) motion. Such random motion causes a Doppler Shift[80] in the light when that light interacts with spherical particles leading to a change in the wavelength of the incident light. This change is related to the size of the molecules and it is possible to calculate the size distribution of the particles along with facets of their motion in solution from an analysis of the scattered light [81]. Figure 1-15 shows the differences in the behaviour of bombarding small molecules which will have higher energy absorbed and lead to an increase the Brownian motion as compared with larger molecules.

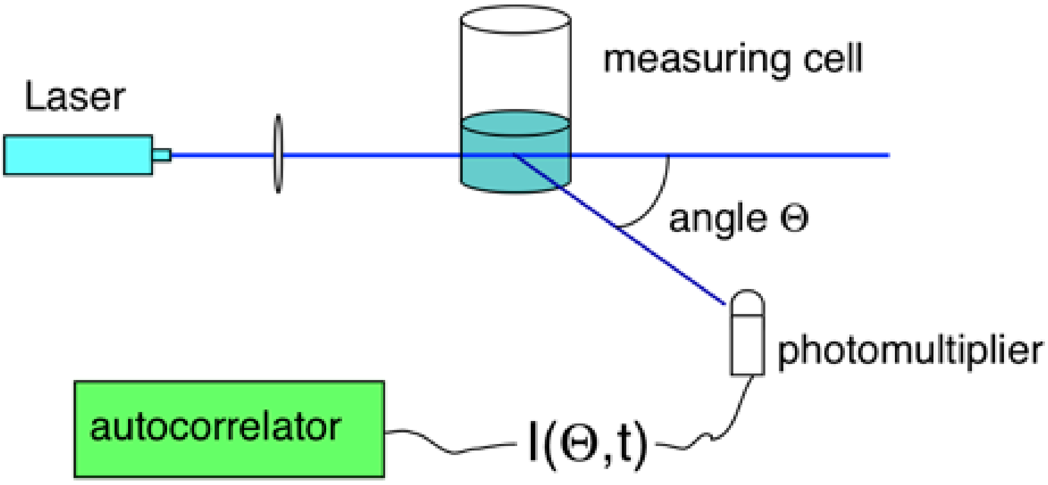

Figure 1-14: Block diagram indicating the parts of dynamic light scattering instrument[78]

Dynamic light scattering techniques have been deployed to address numerous applications in the investigation of dynamic and structural problems in chemistry, biology, and physics. Some of the key advantages and applications of the technique include:

1- The duration of the experiment is short (up to 2 minutes in range).
2- Extensive experience is not required for routine measurements because it is almost all automated

3- This technique has moderated (or relatively low) development costs because most particle sizing commercial systems operate only single angle (90°) and used only a single wavelength (675 nm) monochromatic red light.
4- In principle, the DLS technique is capable of differentiating the state of protein assembly; eg: whether a protein is present in monomer dimeric form [81, 82].

5- DLS is considered as an advanced and high - performance tool for examining the dynamical behaviour of fluids around the critical concentration.
6- Dynamic light scattering can be used in studying laminar or turbulent flows of fluid systems [79].

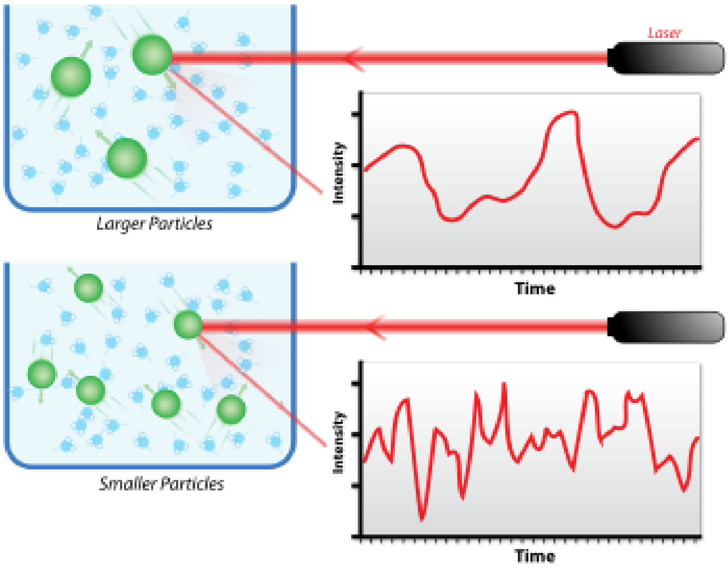

Figure 1-15: DLS result graph of two samples: Larger particles on the top and smaller particles on the bottom[83]

Studies of fluid flow behaviour are easier to perform compared to gelation point determinations which shows a sudden instrument error which is explained in the results chapter. Different techniques are used to study gelation points such as ball-drop and tube-tilting methods[84, 85]. Those methods are based on the difference in flow velocity between two layers (sol and gel layers) of different viscosity. However, for more viscous samples, measurements become less precise and determination of gelation threshold becomes inaccurate. Therefore, Winter *et al*, suggested a new method to determine the gelation threshold using the oscillatory shear method as follows:

The storage, $G'(\omega)$, and loss moduli, $G''(\omega)$, becomes equal to ω^u ,at the gelation point where:

$$\mathbf{G'(\omega) = G''(\omega) \approx \omega^u} \qquad \textbf{Equation 1-2}$$

Where ω is angular frequency and u is viscoelastic exponent [86]. The validity of the above equation was studied and confirmed[87].

The technique of light scattering is considered as a standard method for the description and estimation of shape and size of polymer molecules in solutions. The measurements of the scattering vector or momentum transfer can be calculated by

$$q = |\mathbf{q}| = \left(\frac{4\pi\, n_0}{\lambda}\right) \sin\left(\frac{\theta}{2}\right) \qquad \textbf{Equation 1-3}$$

where λ = wavelength of light in vacuumed tube, n_0 = the refractive index of the solvent, θ = scattering angle. By calculating the scattering intensity as a function of q, the size and shape of sample molecules can subsequently be calculated [88,89].

1.4 Thermal Analysis

The International Confederation for Thermal Analysis and Calorimetry (ICTAC) have defined the concept of thermal analysis (TA) as follows: *'(TA) refers to a group of techniques in which a property of a sample is monitored against time or temperature while the temperature of the sample, in a specified atmosphere, is programmed*'[90] but this definition has been changed subsequently as a result of certain issues which have been raised and such issues are: i) they distinguish between the meaning of analysis and monitoring in terms of thermal experiments; the change in the property and not the property itself which been changed in most of the experiments; the temperature of the surrounding of the sample which been programmed and not the sample itself.

Therefore, the most recent definition suggested and proposed by Hemminger and Sarge [91] as: *'(TA) means the analysis of a change in a property of a sample, which is related to an imposed temperature alteration'* [92].

1.4.1 Thermogravimetry Analysis (TGA)

Calculations of mass differences in the sample as a function of a change in the temperature of the sample which is made using a thermo-balance are capable of revealing information about composition; specifically what proportions of material comprise volatile materials[1]. A thermo-balance (or thermogravimetric analyser) is a mixture of an electronic microbalance with a heat source, a temperature controller and computer for control, which allows the sample to be heated, weighed and/or cooled simultaneously under controlled conditions.

The balance environment needs to be under a controlled system so that it can regulate the pressure according to the experiment's requirement either below, equal to or above the atmospheric pressure and an inert gas atmosphere. Figure 1-16 shows the parts of the TGA instrument and the weighing technique used.

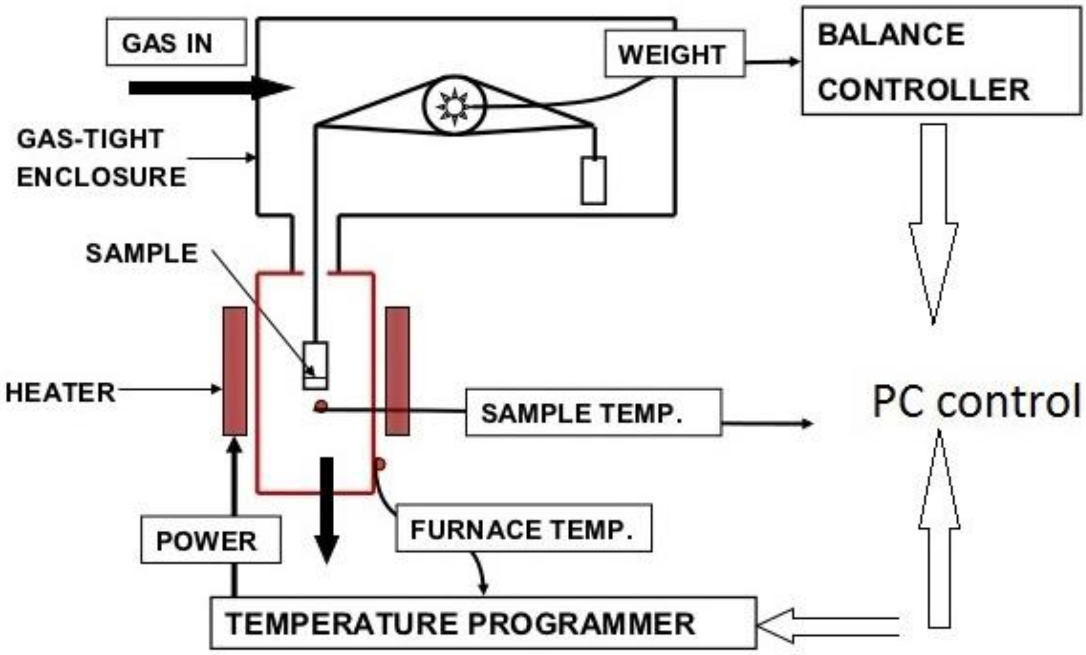

Figure 1-16: Schematic representation of the thermogravimetric instrument used to analysis the SHG samples[93].

---

[1] The mass is the amount of the matter in a sample, whereas weight is the effect of the gravitational force on a mass.

There are different types of balances which can be used in TG analysis depending on the sensitivity required such as the typical electro-balance with a maximum load of 1 g and may be as sensitivity as 1µg[92, 94] and quartz crystal microbalance[95-97] with a sensitivity of up to 0.001 µg[98]. TGA plot shows the flow chart of weight lost percentage against increase the samples temperature and the weight of residue remaining.

1.4.2 Differential Scanning Calorimetry (DSC)

Differential scanning calorimetry (DSC) is a technique used to determine the energetic transitions within the sample and shed light upon the mechanisms of those transformations. Differential scanning calorimetry measures the molar heat capacity of a sample with respect to temperature[99].

A complete thermodynamic characterization of a transition of a sample can be calculated by a sequence of heat gradients with different yields. There are three main features of the information that DSC experiment may provide:

(i) The heat capacity of molecules of the sample.

(ii) The overall thermodynamic parameters (enthalpy change [ΔH], entropy change [ΔS], and heat capacity change [ΔC_p] and;

(iii) The number of intermediate states, the partition function and their thermodynamic parameters[99].

1.5 Diffusion-ordered spectroscopy (DOSY)

Standard nuclear magnetic resonance (NMR) experiments utilise NMR active nuclei and place them in the presence of an external magnetic field, which causes alignment of the nuclear magnetic moment with the external field. When the external magnetic field is constant and homogeneous, the populations of the energy levels of the nuclei at thermal equilibrium have specific values. When an oscillating magnetic radio frequency (RF) field is applied in the transverse plane to the external magnetic field, this causes a change in the population of the energy levels of the nuclei exposed to the transverse field, and the generation of a new magnetic moment along the plane of the RF field, whose amplitude is proportional to the number of nuclear spins present in the sample, which is dependent on the type of nuclei present[100]. As soon as the RF field is removed, the system (nuclear spins) realigns with the external magnetic field and the rate at which this realignment occurs is characterised by the longitudinal (T1) and transverse (T2) relaxation times. The relaxation times represent a loss of coherence in the plane which the RF field was applied. The decaying signal (realignment) of nuclear spins is used in the production of conventional one dimensional NMR spectra, by applying a Fourier-transform operation to the acquired free induction decay time signal, a frequency domain spectrum is acquired[100].

One dimension that is constant for all nuclei in a molecule is the diffusion constant[100], and its connection to the molecular structure is based on the ideas developed by the Stokes-Einstein relation in the way that the diffusion constant depends inversely on the frictional resistance of the molecule[100] (19).

The implementation of diffusion ordered NMR spectroscopy (DOSY) is possible as pulse magnetic field gradient NMR experiments can provide information about translational motion[100, 101]. The principle of obtaining the DOSY spectrum is similar to that of conventional two dimensional NMR, in that a variable is selected which modulates the signal which is detected, and then this variable is incremented to produce a spectrum related to the translation (diffusion) of the investigated molecule. The variable selected in the case of DOSY experiments is the areas of magnetic field gradient pulses[100].

In order to give a more detailed description of a typical DOSY experiment, it is important to first understand all of the parameters which must be controlled in order to attain the diffusion coefficient of a molecule in an NMR sample. Using pulsed field gradients, molecules in a sample can be spatially labelled based on their position in the tube. The Stimulated echo (STE) sequence allows for the calculation of the diffusion coefficient of a molecule in an NMR sample. The STE sequence begins with a 90º radiofrequency pulse. After a delay of time τ, the first gradient pulse δ is applied, the purpose of which is to encode the positions of the molecules. After the first gradient pulse, the molecules in the sample are allowed to diffuse for time Δ before a second gradient pulse δ is applied and the diffusion coefficient can be calculated.

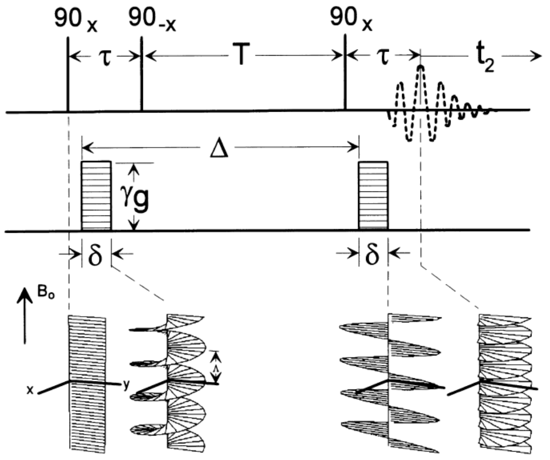

Figure 1-17: The Stimulated Echo Sequence (STE). Top: shows the sequence of pulses and the time differences τ and T between the first and second, and second and third pulses respectively. Middle: demonstrating the refocusing of the magnetisation after the particles are allowed to diffuse for time Δ. Bottom: depiction of the magnetisation helix as a result of the gradient pulse[100].

DOSY spectroscopy is able to separate the NMR signals from the different components within an NMR sample, based on the hydrodynamic radius of the species resulting from its diffusion coefficient. The typical DOSY experiment consists of recording a series of spectra, with incremented pulsed field gradient (PFG) amplitude in a stimulated echo (STE) experiment. The one dimensional NMR spectrum is then transformed into a two dimensional spectrum by performing an exponential fit on the decaying NMR signal amplitude as a function of increasing PFG amplitude and extracting the diffusion constant from the equation used to produce the fit. In an ideal PFG-STE experiment, the decay of the signal amplitude with respect to increasing PFG amplitude is described by the Stejskal-Tanner equation[102].

$$S = S_{\circ} e^{-D\gamma^2\delta^2 g^2 \Delta'}$$ **Equation 1-4**

Where *S* = signal amplitude, S_0 = echo amplitude in absence of diffusion, *D* = diffusion coefficient, δ= gradient pulse width, γ= magnetogyric ratio and Δ' is the diffusion time corrected for the effects of finite gradient pulse width[102].

After applying all the data processing controls, the diffusion coefficient will be generated as spots on a graph related to the NMR peaks, the mothed of checking for the quality of the plot and the accuracy of the diffusion coefficient is the residuals plot. Further details explained in chapter 5 of this project.

1.6 Aims and Objectives

The overarching aim of this project is to study how molecular interactions, of potential relevance to abiogenesis (origins of life studies), could be influenced by geologically plausible hydrogel environments. Specifically, the geologically plausible environment we selected to study was that of the silica hydrogel. Silica being chosen as a result of its gelation behaviour in silification, a key process in rock formation[103]. This involved an examination of:

1- The self-assembly of amphiphiles, both bench-marking systems such as sodium dodecylsulphate (SDS) and study the self-assembly of putatively prebiotic amphiphiles such as long chain phosphates, in silica hydrogel media.

2- Exploring the use of diffusion order spectroscopy as a method of probing molecular diffusivity in the hydrogel medium

This project was built from a number of specific work packages (WP's) :

(i) An analytical analysis of the surface matrix properties and gelation behaviour of silica hydrogels.

(ii) A comparative study of the self-assembly behaviour (micellation) of the representative amphiphiles, SDS (sodium dodecylsulfate) in both the aqueous and silica hydrogel phase.

(iii) An analysis of the behaviour (decolourisation) of amphiphilic dyes used in the measurement of critical micelle concentrations (CMC) *via* spectrophotometric methods.

(iv) An examination of the molecular diffusivity of both small molecules and amphiphiles of relevance to abiogenesis, in the silica hydrogel phase, using diffusion order spectroscopy methods (DOSY)

Chapter 2 Surface Analysis of Silica Matrices from Hydrogels (SHGs)

Presented here are results on the development of a standard operating protocol for the preparation of silica hydrogels which has been used throughout this thesis. This is then followed by a study of the surface morphologies of SHG matrices suitably prepared by Critical Point Drying (CPD) and examined by Scanning Electron Microscopy (SEM), surface area porosity measurements (BET) and Energy Dispersive X-ray spectroscopy (EDX). Subsequently, studies on the process of gelation using Dynamic Light Scattering (DLS) techniques and finally thermal analysis studies on SHG's are reported and discussed.

2.1 Standard Operating Protocol (SOP) for Silica Hydrogels

In order to achieve the project objectives, it was first necessary to be able to prepare SHGs reproducibly using a standard operating protocol. The method that was ultimately decided to exploit in subsequent studies was developed from an earlier, less effective procedure as outlined below:

Method 1: An aliquot (1500 µL) of a concentrated aqueous solution of sodium silicate (≤ 27% SiO_2 and ≤ 10% NaOH) was diluted to 6500 µL in ultra-pure deionised water in a 10 mL volume test tube. Subsequently, concentrated (36.5 – 38 %) hydrochloric acid (250 µL) was added to the silicate solution, and the vessel (normally a test tube) was inverted slowly three times to ensure a homogeneous mixture formed was left undisturbed at ambient temperature to gel. By using this method it was possible to prepare silica hydrogels of 0.5 M overall SiO_2 concentration (see section 2.2 for a discussion of the concentration labels that are used in this thesis) which stabilised and gelled within ca 10 min and which passed a fluctuation test (inverting the tube of hydrogel content without any change of the gel structure see (Figure 2-2). However, it was found that the use of strong mineral acid, HCl as the pH modulating agent of the silicate solution was not able to prepare optically clear hydrogels containing higher concentrations of SiO_2 (above 1 M). Higher concentrations of silicate resulted in both silica precipitation and what appeared to be phase separation within the gel and separated for different layers and appears as precipitate at the bottom of the preparation tube. Figure 2-1 shows inhomogeneous hydrogel formation.

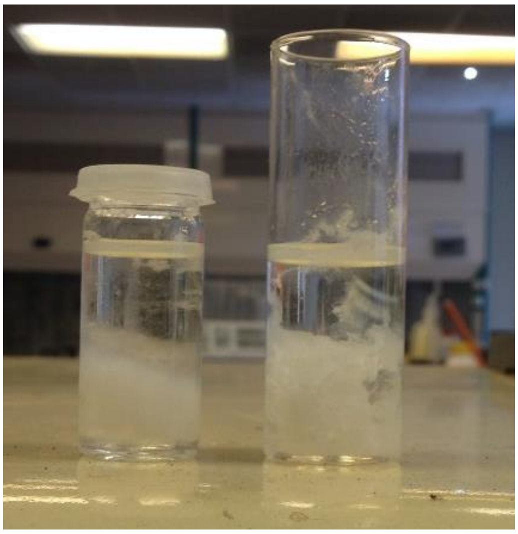

Figure 2-1: Failed sample prepared for higher concentration (1.0M) of SHG indicate the separation of the samples for two different layers

Method 2: A second preparation method was subsequently explored based on one reported by Barge et al[104]. The method involves using glacial acetic acid instead of mineral HCl and is summarised in Table 2-1, where Solution A is added to solution B in a test tube before the combined mixture is inverted slowly several times (3 – 4) in order to ensure effective mixture without being shaken or disturbed too much; the latter leading to significant air bubble formation within the resulting gel. The sample was left un-disturbed for up to 24 hrs, after which time gelation was complete[104]. It was found that this method, which we name as the Barge Method, affords what appears to be homogeneous, optically clear gels in a reproducible fashion with minimal precipitation, certainly when using silicate concentrations of 0.5 – 1.5 M, , as shown in Figure 2-2. The chemical reaction involves two stages, hydrolysis and condensation. Hydrolysis (Scheme 2-1a) involves the protonation of sodium silicate mediated by the glacial acetic acid to form a silanol. The subsequent condensation stage (Scheme 2-1b) consists of a reaction between two silanol groups to form a siloxane bridge, extruding water at the same time.

Table 2-1: composition solutions used in the preparation process of 0.5M SGH using Barge method [104]

Solution A	Solution B
Sodium silicate solution (1.25 mL) which contains (≥ 27% of silicate) and (≥10 sodium hydroxide) mixed with deionised water (6.75 mL)	Glacial acetic acid (360 µL) in deionised water (7.6 mL).

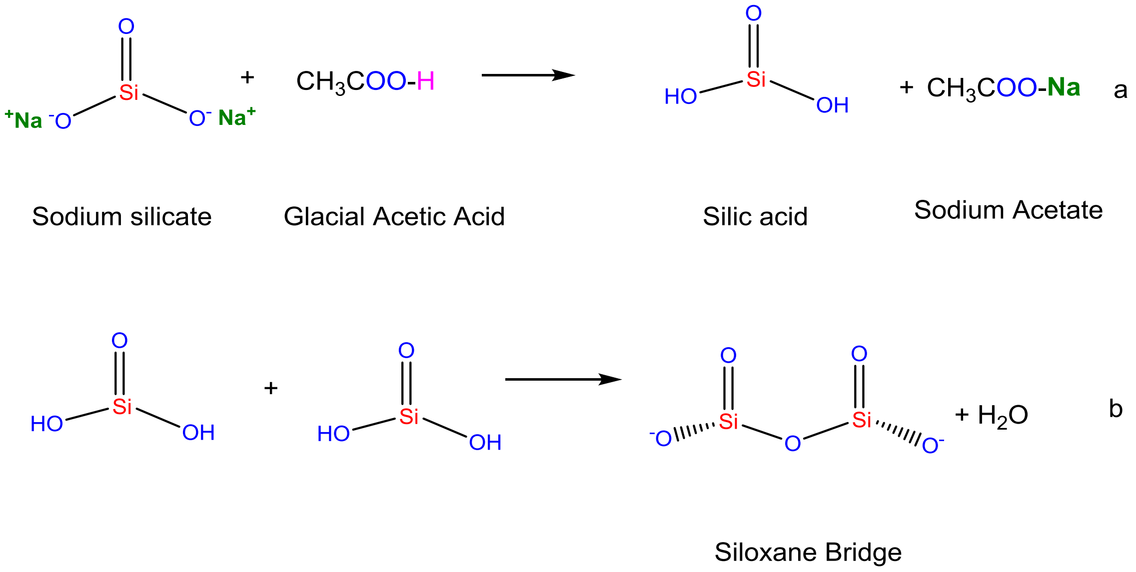

Scheme 2-1: The two primary reaction stages (a) protonation and (b) condensation in the formation of SHGs from aqueous sodium silicate solution.

The effect of using strong acid (HCl) on the formation of SHG changes the protonation step. Strong acids has lower pH than weak acid and as the pH decreases, the H^+ increases and forward reaction forced to the right which leads to form inhomogeneous SHG formation and the precipitates will form from non-reactant silicate or smaller chain of SHG.

2.2 Silica hydrogel nomenclature and calculations

We have selected to categories our standard gel formulations as 0.5 M with respect to SiO_2 on the basis of the following calculations which were used to prepare silica hydrogel in tubes (see Figure 2-2).

It is an arbitrary nomenclature system but one we used for our purposes.

The silicate solution that we use is graded at ≤ 27% SiO_2. Thus, this translates to ≤ 27 g in 100 g of solution and the density of sodium silicate solution =1.39 g/ml (written on the container).

% of silicate = 27 g in 100 ml

= 270 g in 1 litre (total volume of the container)

To calculate the weight of silicate used, we used the equation:

Weight of silicate = density x percentage

270 g x 1.39 = 375.3 g

After calculating the total weight of silicate presented, then molarity of the silicate can be calculated from the equation:

Molarity of silicate = weight/ molecular weight

= 375.3 / 60.1 = 6.24 M Conc. of silicate in sodium silicate solution.

In 'Barge Method' the concentration used: 1.25 ml of sodium silicate solution diluted to a total volume of 16 ml, by applying the dilution equation to calculate the concentration of silicate used as follow:

$M_1 \times V_1 = M_2 \times V_2$

$6.24 \times 1.25 = M_2 \times 16$

M_2 = 0.48 M the standard SHG concentration and we have rounded this figure to the first significant decimal point in the nomenclature to 0.5 M. All other concentrations that have been used in this thesis are calculated based on the above calculations.

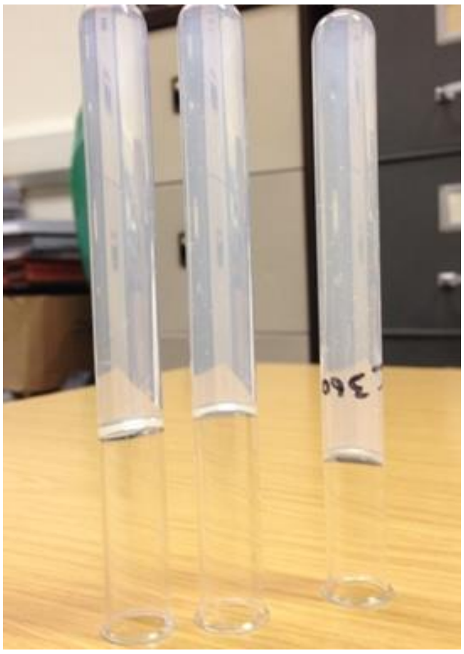

Figure 2-2: Silica hydrogel samples prepared in the lab using the Barge Method. All three identical samples are derived from of 0.5 M silicate.

Comparison between the non-homogenises SHGs samples from Figure 2-1 and the silicate precipitate seen with the one in Figure 2-2, can easily be made. The latter appears optically clear, homogeneous sample and reproduced without visual sings of clouts or precipitates in the bulk of SHG even with higher concentration (1.5 M) of silicate.

Visual clarity is a mandatory features for some of the tests conducted on SHG samples such as DLS.

2.3 Sample preparation for Critical Point Drying (CPD)

It was necessary to first develop a method of sample introduction within the CPD instrument which would allow the fluid to flow both in and out of the sample. To conduct CPD upon the sample, the sample volume required was also rather constrained, needing to occupy a volume smaller than *ca.* 1 mL. This had a significant impact on the methods developed. Three separate samples of SHG, prepared according to the Barge method[104] with initial silicate concentrations of 0.5, 1.0 and 1.5 M were established. Whilst still remaining liquid, each sample was poured carefully into a plastic cuvette tube within which each of the caps had earlier been perforated by a narrow-gauge exit needle to allow water egress and acetone ingress during the CPD process. Each sample was inverted (as shown in Figure 2-3 below) and left to gel over a period of 24 hrs.

Figure 2-3: Identical samples of 0.5M SHG after 24 hrs in plastic tubes perforated earlier from the cap prepared in research lab for the CPD

2.3.1 CPD process

Each set of samples (the instrument can handle three samples concurrently) required *ca* 3 hrs to complete the drying cycle which includes the insertion of acetone to replace water from the silica matrix followed by pumping liquid carbon dioxide through the system and heating to 37.4 ºC to allow acetone and water vapour to be removed. Finally carbon dioxide was allowed to evaporate from the system (instrument shown in Figure 2-4). The size of silica gel shrank and the result is a dried, white stone-like and solid sample with small cracks on the surface. The structural integrity of the silica matrix within the gel form is largely retained (Figure 2-4).

Figure 2-4: Critical point drying instrument within School of Biology, UoL (left). Dried SHG sample of 0.5 M concentration in a petri dish and the weight is 0.0156 g marked with black arrow (right).

2.4 Scanning Electron Microscopy (SEM) Results

2.4.1 0.5 M SHG images

The first set of images (Figure 2-5 & Figure 2-6) focus on pores present on the hydrogel mineral matrix surface which give some indication of the size and shape of pores. The pore size and shape of silica gel has a direct effect on the energy of adsorption and desorption activation energy of molecules interacting with the surface[105]. Figure 2-5, shows a low magnification image (100 µm scale bar) of the fractured silica matrix. The two ringed regions within Figure 2-5 have been examined under slightly greater magnification (1 µm scale bar), the results are illustrated in Figure 2-6. As can be seen from this image, within the undulating terrain of the silica, there are specific larger pores of *ca* 500 nm diameter (ringed).

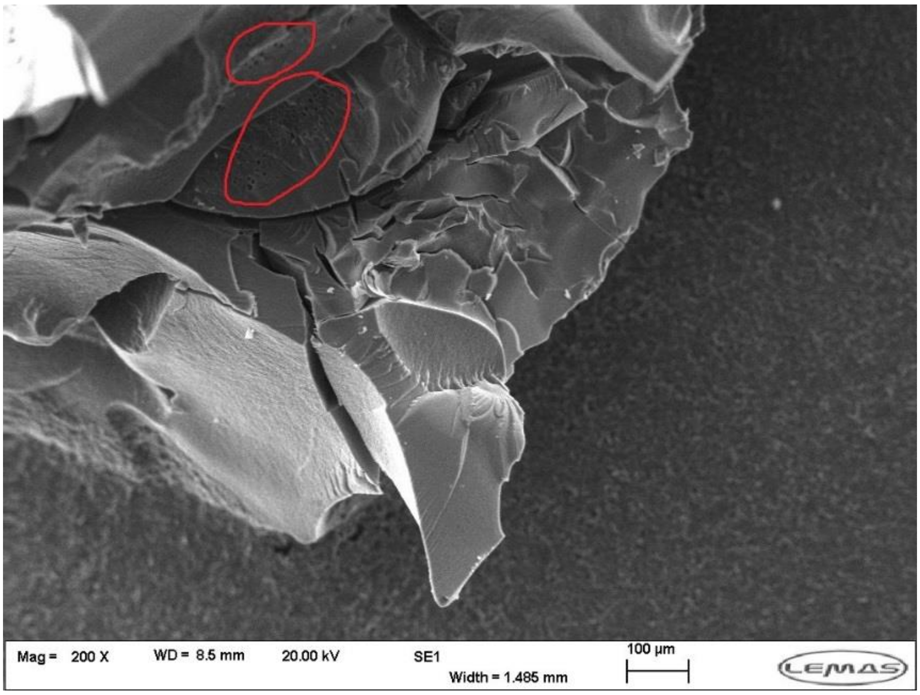

Figure 2-5: Pores present on the surface of CPD-prepared silica hydrogel sample (0.5 M silicate).

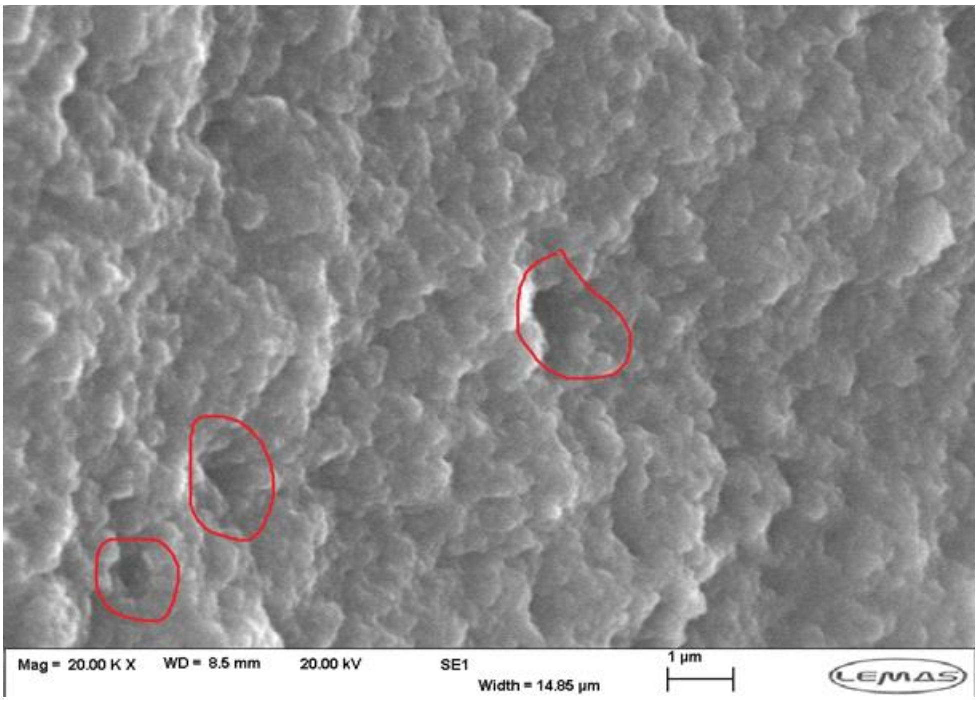

Figure 2-6: Increased magnification of the ringed regions in Figure 3.5 The size of pores present on the surface of silica hydrogel is about 0.5 µm in width.

A second set of images (Figure 2-7 & Figure 2-8) from a different region of the same sample, provide evidence of the cross-linking network formation within the molecular structure of the silica hydrogel. Gel structures possess the ability to absorb large quantities of water without dissolving or collapsing in that medium[31]. Figure 2-8 reveals a silica region which appears rather feathery at this level of magnification. However, under higher magnification, the formation more closely resembles “thorns” overlapping randomly with each other. Each of the thorns (primary thorns) shown in Figure 2-7 is *ca* 5 – 8 µm in length and these shapes appear to have rather unsymmetrical (random) distribution. Under higher magnification (Figure 2-8) the secondary branching growing on the stem of the primary thorn structure and are of the order 0.2 – 0.8 µm in length can be seen. The effect is reminiscent of dendritic growth (cross linkage)[106].

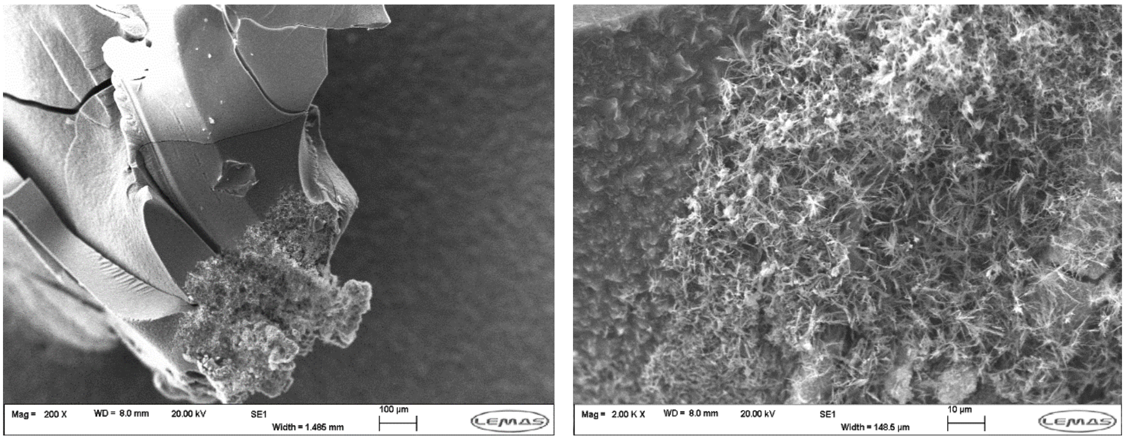

Figure 2-7: Dendritic silica growth on silica (0.5 M silicate) hydrogel matrix of the image on the left and the one to the right is a magnified field of the same view[107].

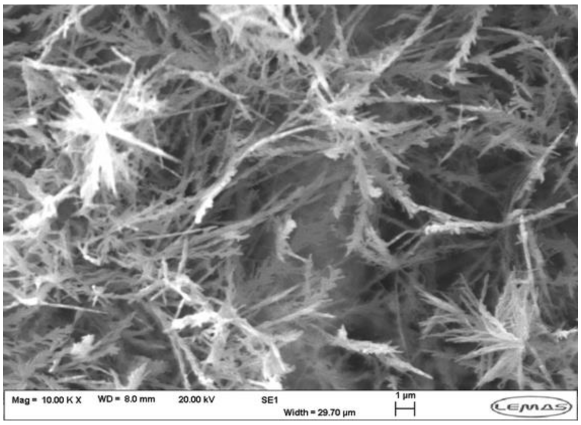

Figure 2-8 Higher magnification image of Figure 2-7 emphasising the dendritic nature of the morphology.

2.4.2 1.0 M SHG images

The above images (Figure 2-5, Figure 2-6, Figure 2-7 and Figure 2-8) were of 0.5 M SHG conducted in Leeds electron microscopy and spectroscopy centre (LEMAS). Below are shown results conducted in collaboration with Dr Angela Bejarano-Villafuerte and Dr Alex Kulak from the Meldrum group at SoC, these performed a surface porosity measurements using the BET method, along with Energy Dispersive X-ray (EDX) and SEM images. The first sample analysed was a 1.0 M SHG prepared and dried through CPD. The resultant images are shown in Figure 2-9:

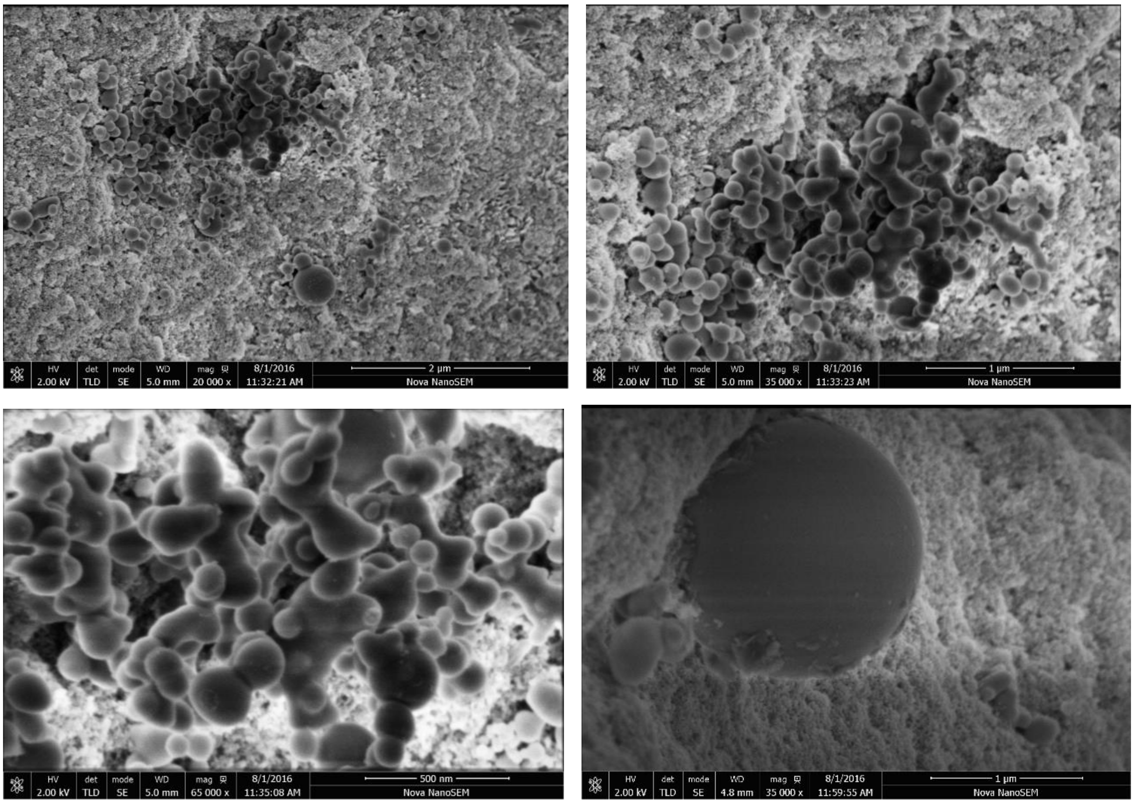

Figure 2-9: Pore blocking by spherical silica particles at two levels of magnification (top), different size of the spherical-shaped of silica.

The first set of images (Figure 2-9) indicates the presence of multiple spherical-shaped silica structures. Figure 2-9 (top) shows a cluster of spherical-shaped silicate structure blocking the pores present on the surface of the sample, those spherical-shaped structures have different diameter *ca* 0.2 – 1.0 µm and are not distributed homogeneously over the surface. Figure 2-9 (bottom) shows higher magnification images of the hydrogel matrix featured in. The BET determined surface area of the sample was found to be 161 m^2/g, with a correlation coefficient equal to 0.99980. This surface area value was lower than expected[108], and is likely to be due to the matrix pores being blocked by the spherical-shaped silicate structure. In addition to the spherical silica morphologies, dendritic growth was also observed as shown in Figure 2-10.

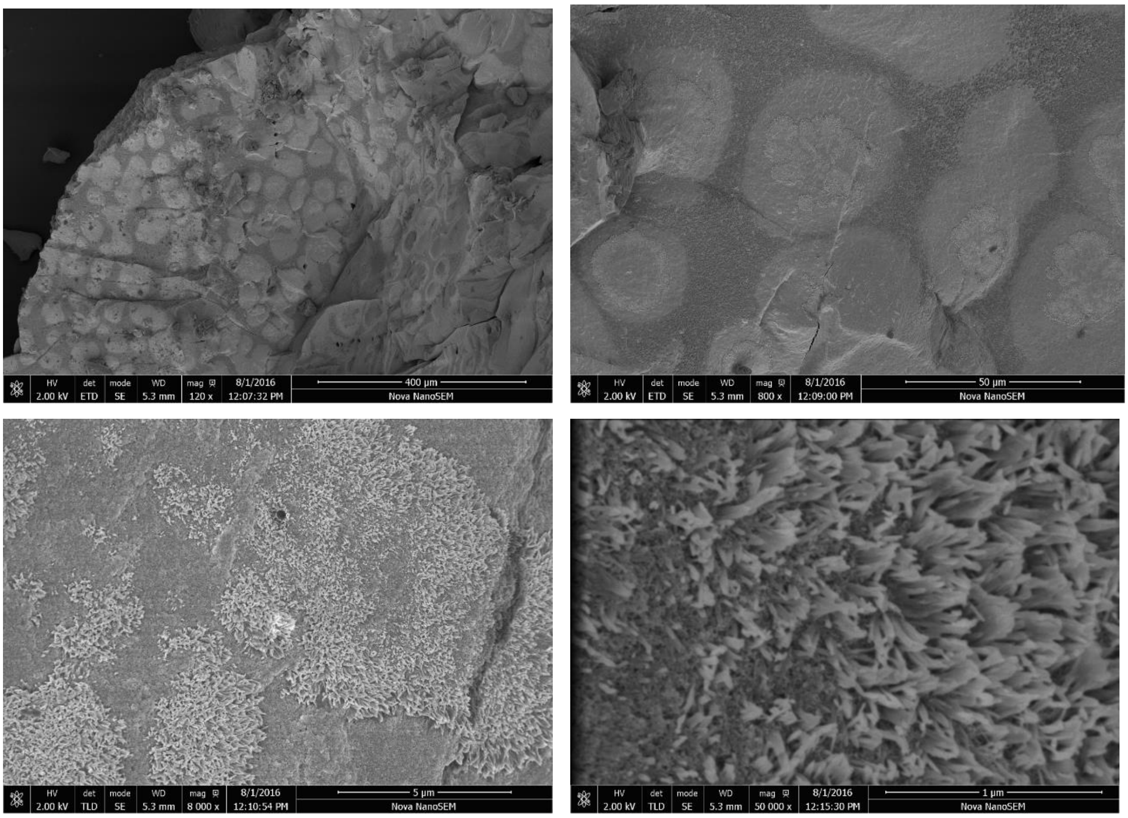

Figure 2-10: Dendritic growth on the surface of a dried 1.0 M SHG sample.

EDX results (Figure 2-12) indicate a difference in level of oxygen, sodium and silicone in the sample and is likely to be due to the high gelation rate of 1.0 M SHG. As outlined above, it became clear that the CPD-produced silica matrices were contaminated with significant amounts of sodium salts (likely to be silicate, acetates and oxides-hydroxides). To overcome the issue of blocked pores and difference in levels of the element’s concentration around different spots within the same sample, which obscured the overall open structure of the silica hydrogel matrix. These salts were removed by dialysis of the CPD-prepared pellets over a period of 4 days in distilled deionised water (see Figure 2-11). The consequence of this was that the salts were removed to reveal a significantly more open and porous silica matrix.

Figure 2-11: Dialysis tube contain SHG sample dissolved in water, tighten from ends and dipped in conical flask containing distilled water

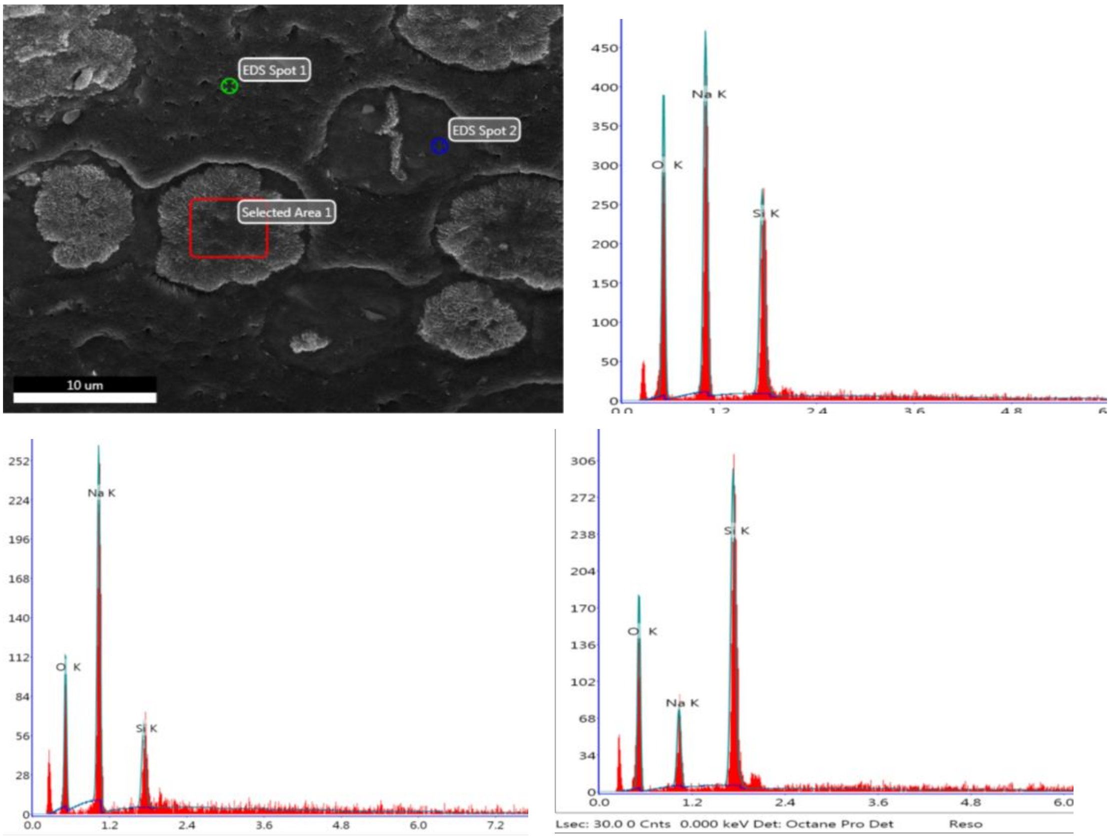

Figure 2-12: EXD results of 1.0M SHG. EDX image(top left); elemental result of Selected Area1 (top right); elemental result of EDS Spot1 (bottom left) and elemental result of EDS Spot2 (bottom right).

After dialysis, the sample was freeze dried and further SEM images were obtained, along with EDX analysis. The images revealed a more open structure, with clear and wide pores present on the surface (Figure 2-13), and significantly equal levels of oxygen and silicon elements were found on the gel matrix, without any traces of sodium. Duplicate BET analyses on post-dialysed samples returned a significantly higher surface area of 410 m^2/g.

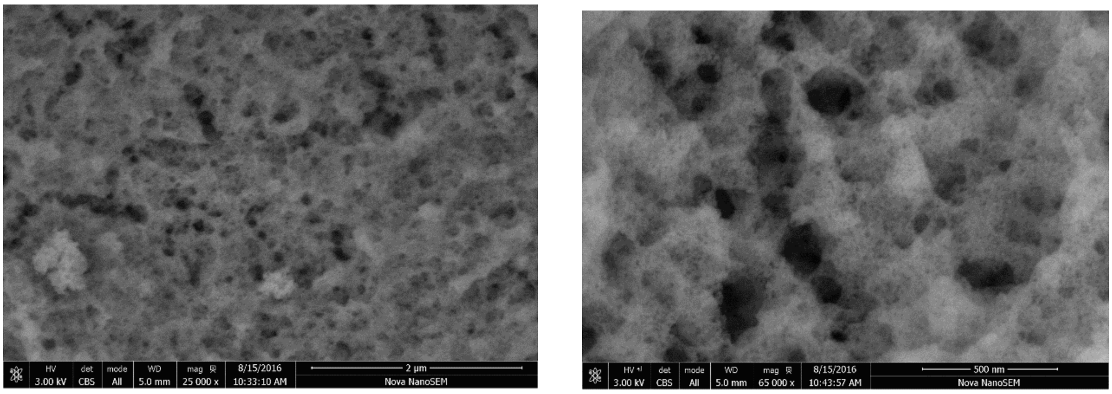

Figure 2-13: The open – structure of the pores present on the surface of 1.0 M of SHG post – dialysis.

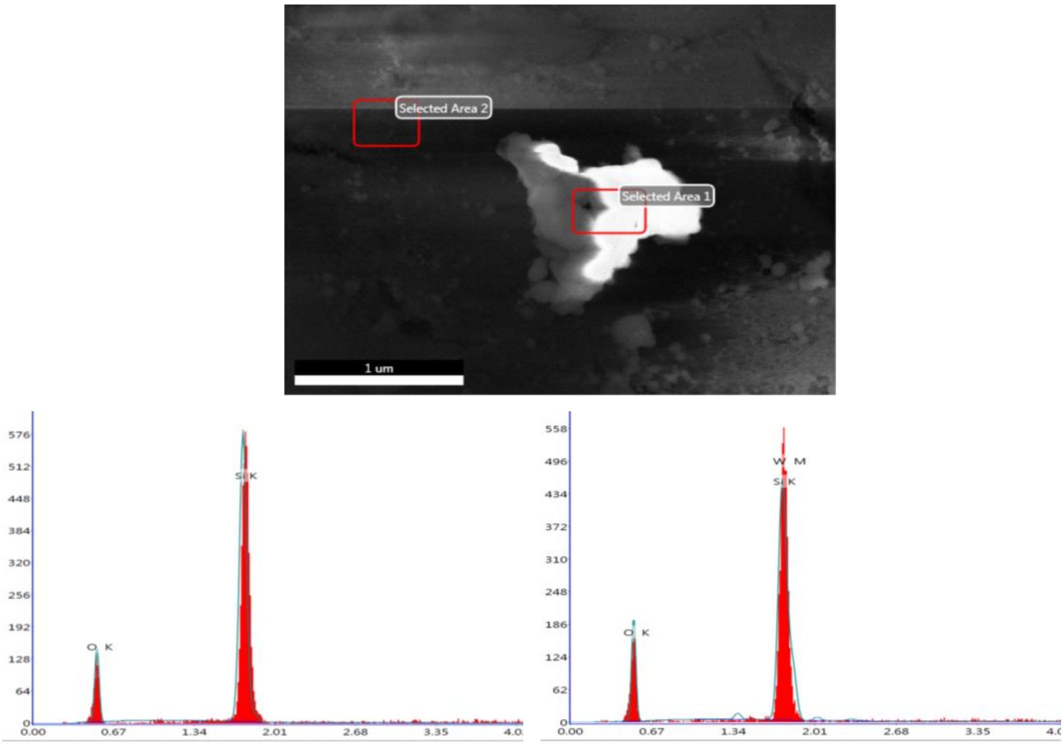

Figure 2-14: EDX results after conducting dialysis and freeze dry show similar distribution of oxygen and silicon elements without sodium.

2.4.3 Sample preparation for SEM-EDX analysis of SHG-pyrophosphate mixtures.

This part of the study has been conducted with the help of Mr George Hodgin as part of his MCHEM research project. This small side-project leads off from the surface studies reported above with the view to pursue an investigation into how charged molecules of potential interest to abiogenesis interact with the surface of the silica matrix of SHG's. In the first instance, a study of how a condensed phosphorus chemical, pyrophosphate (Figure 2-15), might interact with the silica surface was conducted. Pyrophosphate has been considered for some time to have a potential role to play in phosphorylation reactions in prebiotic systems[109] and to explore retention of pyrophosphate under different conditions.

The binding nature of phosphorous containing compounds (namely sodium pyrophosphate, Figure 2-15) to the silica hydrogel polymer matrix was determined through SEM-EDX analysis.

Silica hydrogel samples were prepared with differing sodium silicate concentrations, and for the purpose of this investigation, solution A (which used in Barge method) was saturated with sodium pyrophosphate (170 mg/mL in water).

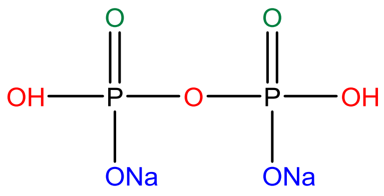

Figure 2-15: Structure of Sodium pyrophosphate dibasic with a chemical Formula: $H_2Na_2O_7P_2$

Table 2-2: Solution A used in Barge Method

SHG's sample	[SSS] / M	Vol. Glacial acetic acid / µL	V of water / µL	Mass of pyrophosphate /g
1	0.5	226	4765	0.4515
2	0.6	226	4765	0.4550
3	0.7	226	4765	0.4560

4	0.8	226	4765	0.4512
5	0.9	226	4765	0.4534
6	1.0	226	4765	0.4515

Table 2-3: Solution B used in Barge Method

SHG Sample	[SSS] / M	V of Water / µL	Vol. SSS / µL
1	0.5	4232	784
2	0.6	3919	1097
3	0.7	3605	1411
4	0.8	3292	1724
5	0.9	2978	2038
6	1.0	2665	2351

After mixing the samples as described in Barge method, the samples were left for 24 hrs so that gelation could occur. Lyophilisation was performed after gel formation was successful in all samples to remove all water from the samples, leaving a white uniform powder after 2 days of freeze drying under reduced pressure. After freeze drying, dialysis was performed on each sample to remove dissolvable salts. In each case, the sample was placed into dialysis tubing (washing into the tubing from the container with distilled water) and the sealed tubing was placed into a water bath which was replenished daily. The dialysis was carried out for 4 days and after this time the remaining solid in the dialysis tubing was subjected to freeze drying. The resulting white uniform powder was then analysed via SEM-EDX. After initial investigations discovered the presence of phosphorus on the surface of the remaining silica, acid dialysis was carried out next on the same samples.

The EDX results of the dialysed SHG samples containing pyrophosphate show that there is a small amount of phosphorus retained within the silica polymer matrix. Figure 2-16 presents EDX data taken for one of the six SHG samples.

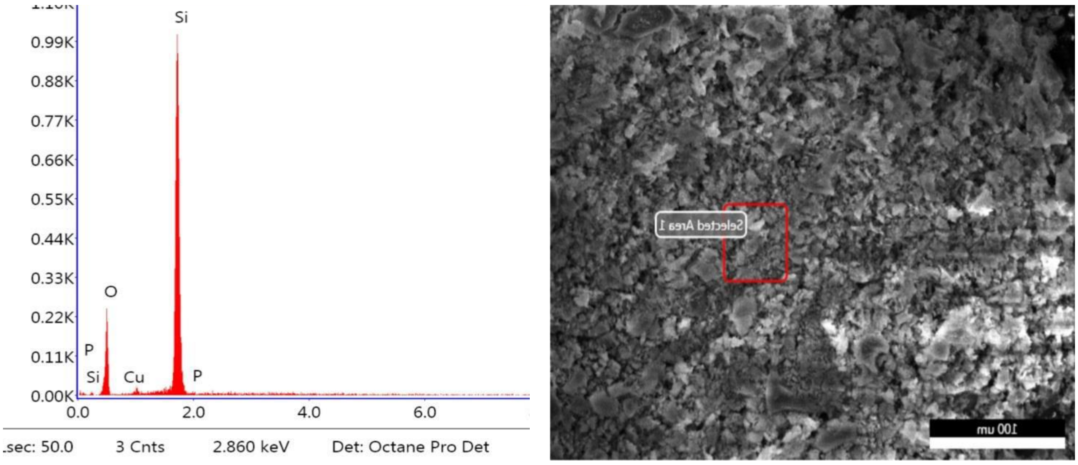

Figure 2-16: SHG sample showing the presence of phosphorus on the surface of the silica sample after the first dialysis, indicating the presence of bound phosphorus to the silica.

The presence of the phosphorus peak indicates that post-dialysis, some phosphorus is present on the surface of the dialysed samples (Figure 2-17). This raises questions about the nature of the binding of the phosphorus containing species to the silica dialysed product. To begin further investigations into this, the EDX map for samples 4 (0.8 M SHG) and 5 (0.9 MSHG) were analysed. The results showed that there was 4% (Figure 2-18) and 6% (Figure 2-17) respective contribution by phosphorus to the total sample mass. The map for phosphorus alone which excludes the silicon and oxygen contributions appears to reveal localised phosphorous neighbourhoods which appear to follow those same locations of silicon and oxygen enrichment. Thus, it appears as though much of the phosphorus may be associated closely with the silica matrix.

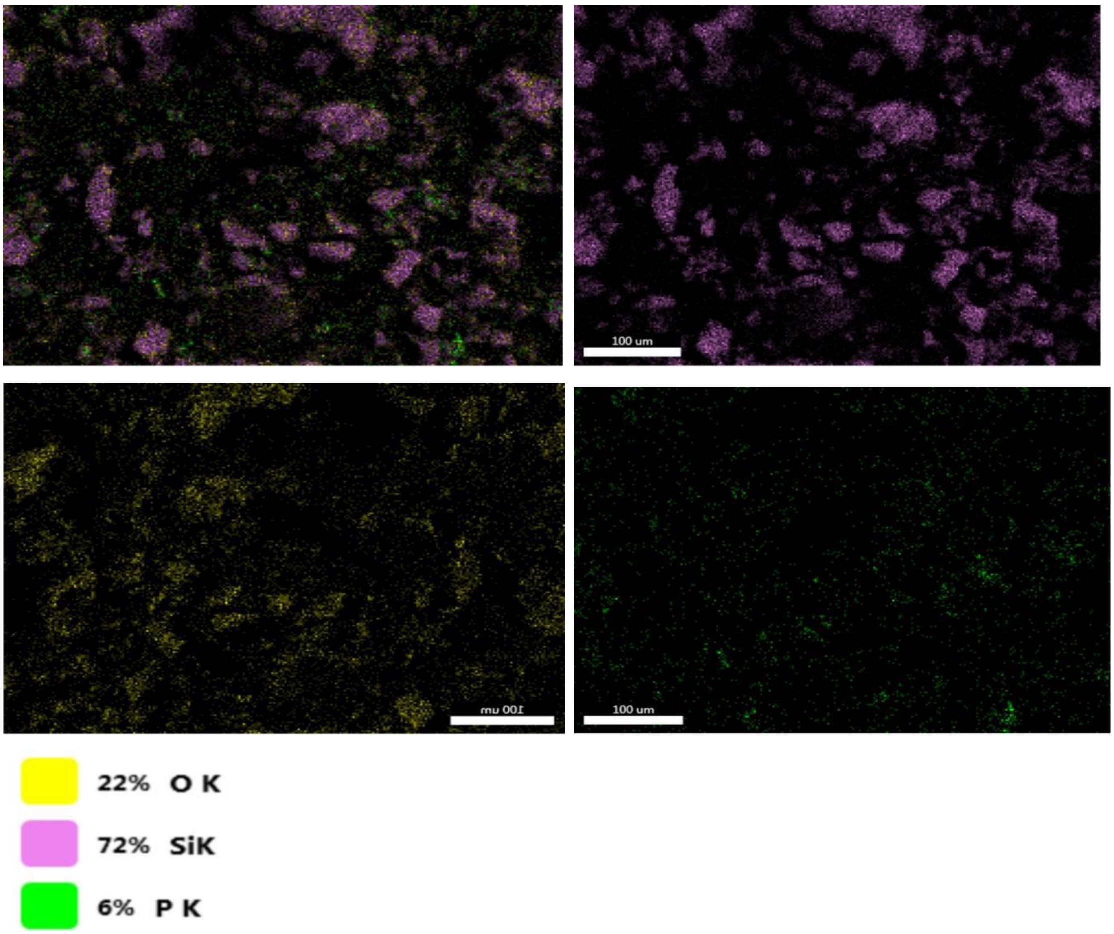

Figure 2-17: EDX map indicating the presence of 6% phosphorus on the surface of the freeze dried dialysis product (sample 5, 0.9 M SHG). Top left image shows all elemental components of the sample. Oxygen elemental traces are in yellow, silicon are in pink and phosphorus are in green.

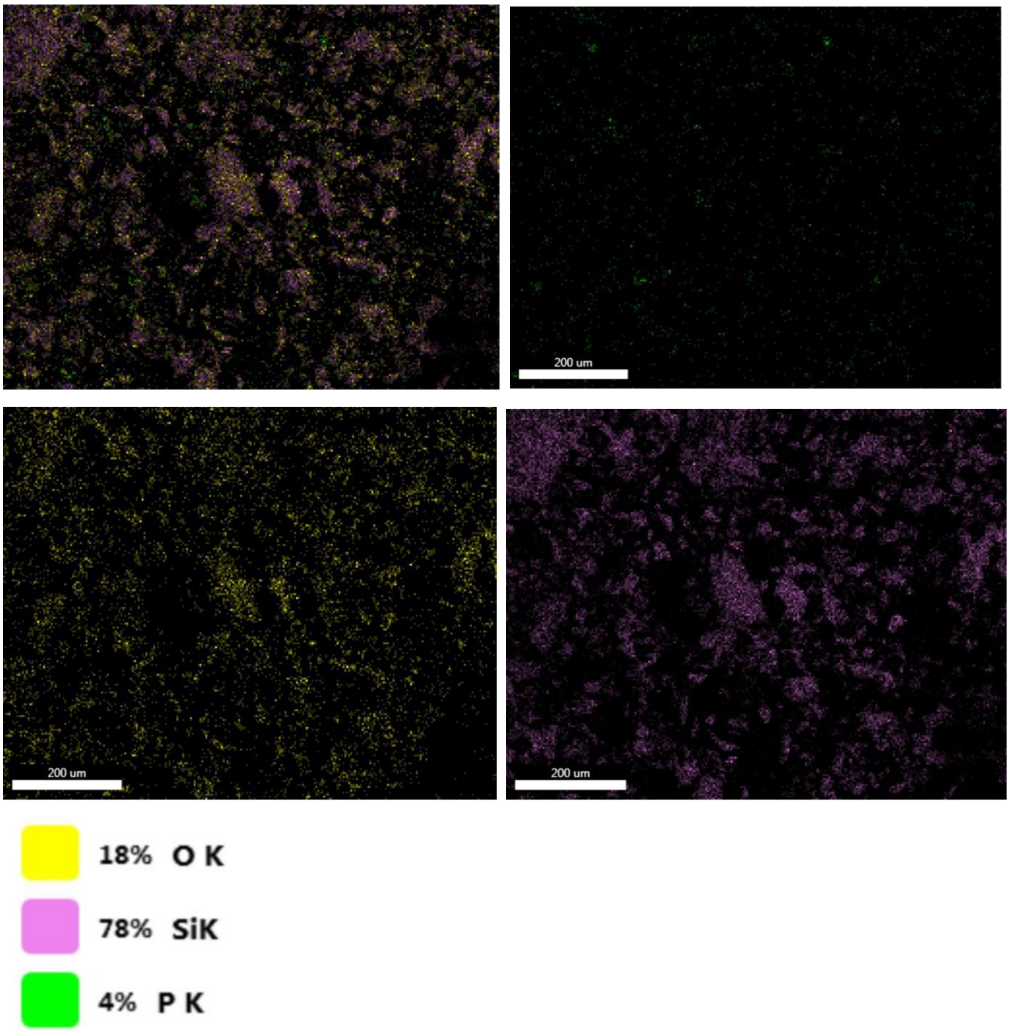

Figure 2-18: EDX map indicating the presence of 4% phosphorus on the surface of the freeze dried dialysis product (sample 4 0.8 M SHG). Top left image shows all elemental components of the sample. Oxygen elemental traces are in yellow, silicon are in pink and phosphorus are in green.

In order to determine if the silica–phosphorus binding could be interrupted by acid, an acid dialysis was performed. The procedure was identical to that described for water dialysis, but in this case, the water bath was adjusted to pH 2 by addition of 37% in water conc. HCl solution.

The EDX results after the acid dialysis showed that all phosphorus traces had disappeared (or below a detection limit) from the EDX map, indicating that the addition of acid had the effect of removing phosphorus from the surface of the silica. The results of this investigation do not imply specifically that pyrophosphate interacts with the silica through either physical or chemical mechanisms, physical binding between the freeze-dried silica sample and the phosphorus containing material may be the more logical explanation.

The EDX techniques has its own reading and accuracy limitation and these limitations are: the sensitivity is limited to 0.1 % of the element's concentration; detector beam length is 1 µM which is not suitable for small details; and the EDX probe needs to be calibrated with a standard solutions of the element under investigation to get optimum results.

This result is important for the argument that life originated in a gel environment as the ability to store essential elements, such as phosphorus, is a key to providing the building blocks for life. Figure 2-19 shows the SEM-EDX analysis for the post-acid dialysis product.

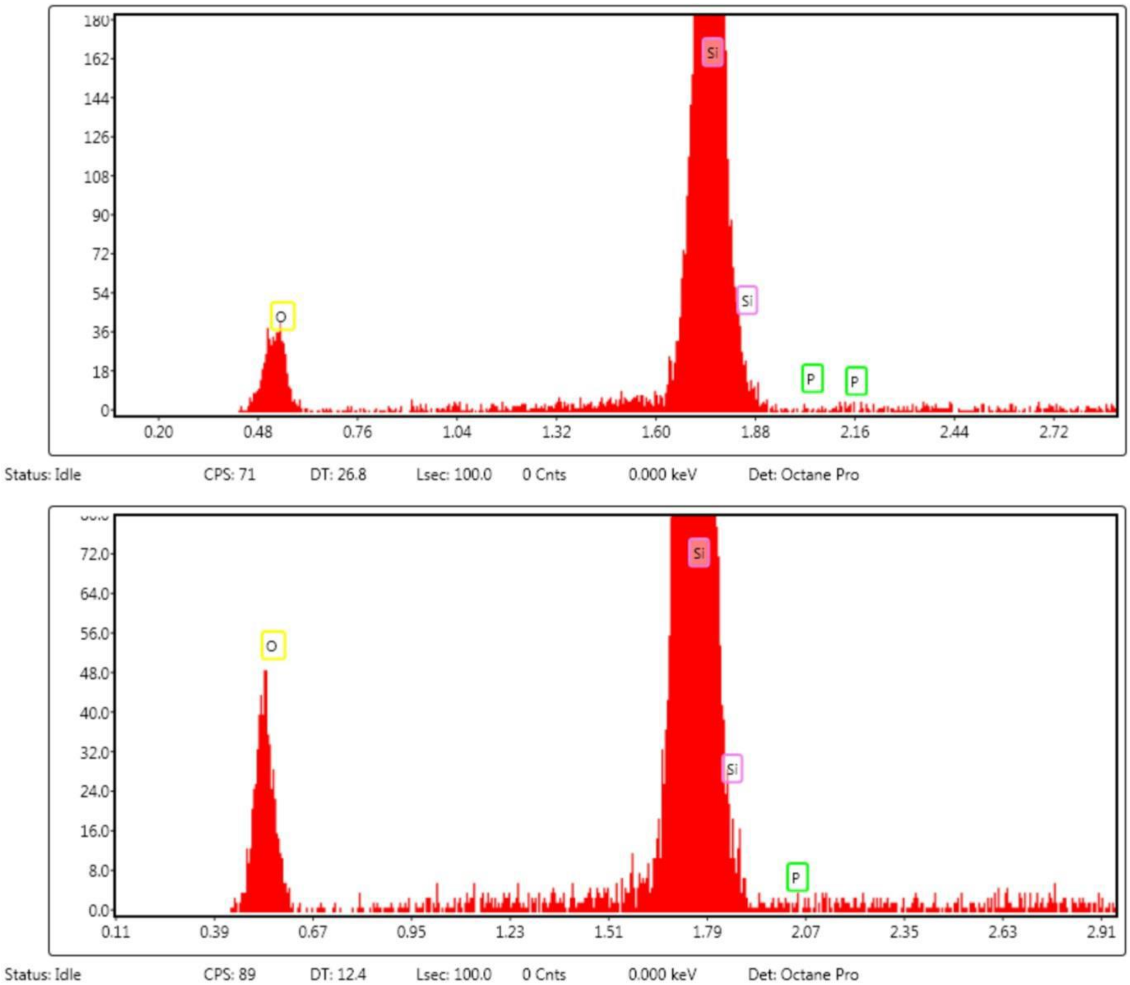

Status: Idle CPS: 71 DT: 26.8 Lsec: 100.0 0 Cnts 0.000 keV Det: Octane Pro

Status: Idle CPS: 89 DT: 12.4 Lsec: 100.0 0 Cnts 0.000 keV Det: Octane Pro

Figure 2-19: Demonstrating the absence of phosphorus on the surface of the silica sample after acid dialysis. Top image shows the initial selected area of study and the bottom image shows that when the area under study is increased, phosphorus is still absent.

2.5 Dynamic Light Scattering (DLS) study of silica gelation

Following analysis of the surface morphology of the CPD-prepared silica matrix of hydrogels, it was decided to explore the process of gelation in slightly more detail *via* particle size analysis using DLS. The mutual influences of (i) the self-assembly of amphiphiles and how they are influenced by hydrogel environments and (ii) how the presence of self-assembled structures (micelles or most importantly vesicles) influences the silica gelation process and matrix morphology that results, were explored. As a prelude to these studies, the process of gelation of the silica systems was examined. Subsequently, will be able to modifying with prebiotic amphiphiles, and examine whether and in what way the gelation behaviour is influenced by the presence of SDS as a probe amphiphile (one with little prebiotic provenance).

2.5.1 Experiment 1. Silica hydrogel sample prepared in an open system

A SHG sample was prepared using the Barge Method described in section 2.1. This gel was based on a 0.5 M sodium silicate solution and was prepared in an open 1 cm disposable cuvette prior to introduction to the instrument. As the study was a time-evolution investigation, the instrument was programmed to collect readings every 10 minutes for a total of 6 hours. The results (displayed in Figure 2-20 and for tabulated data see Table 2-4) show a steady particle size increase in solution up to a maximum of 336 nm after 100 mins. Thereafter, there is a general drop-off to less than 100 nm after 190 mins. Upon monitoring the sample for a longer period, it was noticed that the sample appeared to be drying out and cracked. This was accompanied by a sharp discontinuity in the average particle size around the 440 min mark. It may be suggested that this is a reflection of the drying process and so all subsequent experiments were performed within closed systems which resulted in the elimination of these problems (Figure 2-21 and Figure 2-23). The increase in size average corresponds to light scattering that is a result of the onset of hydrogel formation. Following hydrogel formation, the light scattering is reduced until solvent evaporation occurs at *ca.* 440 minutes. This secondary increase in light scattering is absent when the hydrogels were assessed in a closed system due to the prevention of solvent evaporation.

Table 2-4: Data results of Figure 2-20

Time /min	Z-average/ nm	Time/min	Z-average/ nm	Time/min	Z-average/ nm
0	338.7	170	209	340	31.65
10	16.94	180	228.6	350	29.95
20	21.45	190	106	360	27.42
30	28.15	200	81.64	370	25.97
40	37.67	210	81.99	380	24.67
50	49.44	220	69.56	390	25.25
60	66.79	230	64.44	400	25.64
70	86.93	240	61.31	410	29.88
80	118.2	250	58.1	420	29.87
90	159.2	260	54.42	430	29.18
100	336.2	270	40.06	440	221.7
110	278.8	280	43.3	450	557
120	308	290	36.15	460	286.1
130	315	300	34.37	470	184.3
140	202	310	36.47	480	40.84
150	184.5	320	32.36	490	216.8
160	197.2	330	31.75		

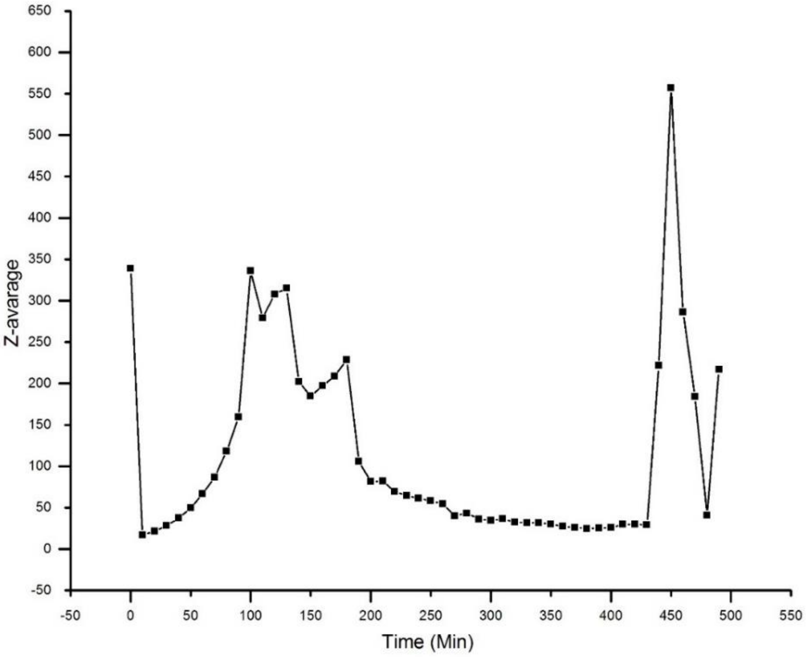

Figure 2-20: DLS result of first experiment indicating gelation process of pre-diluted 0.5 M SHG sample and evaporation effect in an open system.

Figure 2-20 and Figure 2-21 both reveal the gelation of 0.5 M SHG within open and closed systems respectively, the analytical runs were conducted using the same instrumental settings and experimental conditions. We note that the maximum Z-average values (340 nm and 520 nm, respectively), and the time required to reach those peak values (100 min and 48 min, respectively) are different. The most likely reason for such a difference in readings is that for preparing the sample used in Figure 2-20, the evaporation of water molecules from the sample surface was faster in the open system and increased due to continues incidence of the light beam on the sample. Figure 2-21, the sodium silicate solution was pre-diluted for 5 days before using it for preparation, while for the sample used to produce Figure 2-23, silicate solution were prepared just before it was used. The data shown in Figure 2-22 for polydispersity index (PdI) against time collected from the same experiment run in Figure 2-21. The PdI results (Figure 2-22) showed inhomogeneous (polydisperse) distribution of particles population and while it’s difficult to ascertain the size distribution due to technical issues[110], and the size average method more common to use.

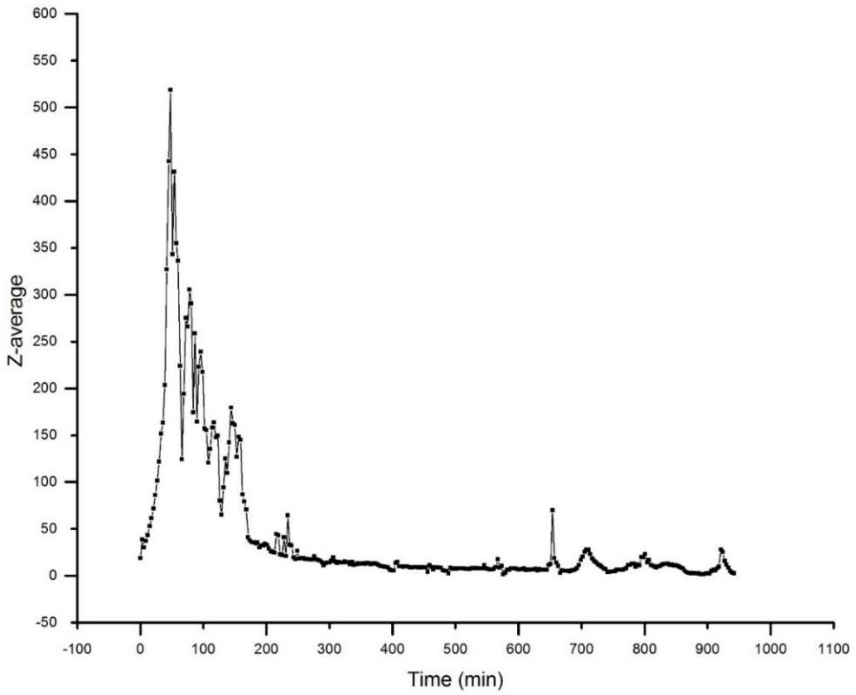

Figure 2-21: DLS result indicating gelation process of pre-diluted 0.5 M SHG sample and evaporation effect in a closed system.

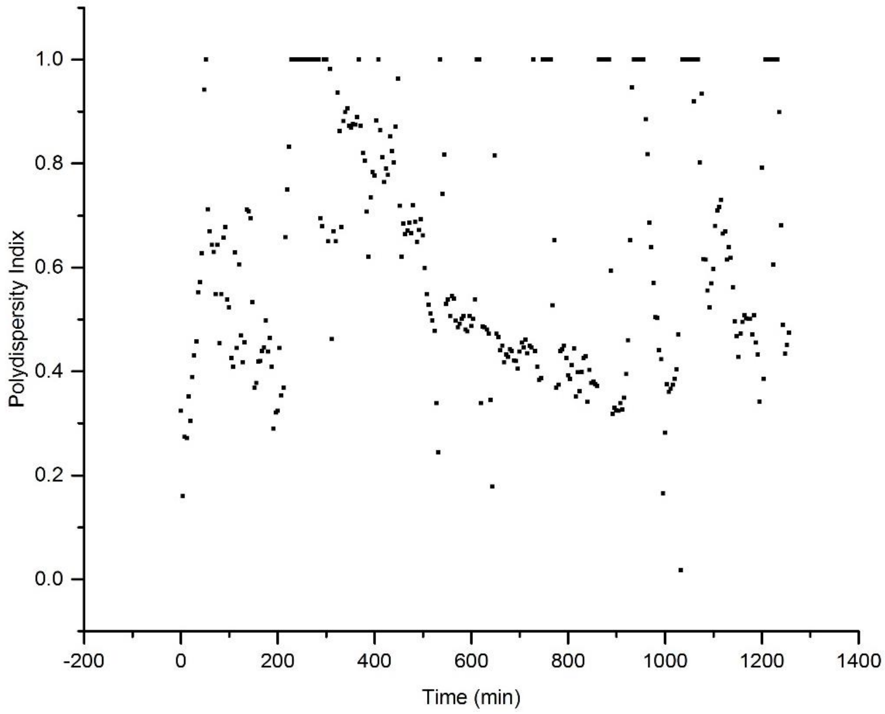

Figure 2-22: Polydispersity index against time of the DLS data of 0.5 M of SHG sample within closed environment. The same experiment in Figure 2-21.

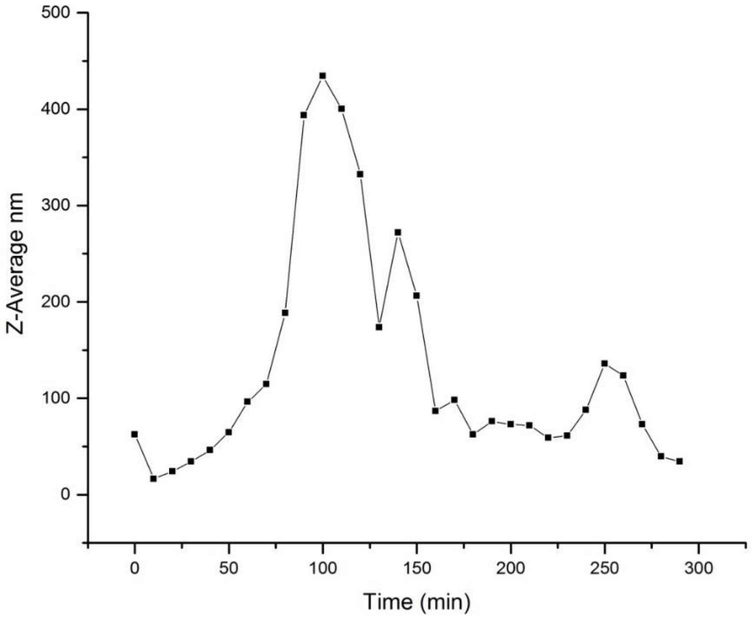

Figure 2-23: The DLS results for freshly prepared 0.5 M of Silica hydrogel in a closed system indicating the Z-average against gelation time.

2.5.2 Experiment 2. Silica hydrogel in the presence of surfactant (SDS)

A silica hydrogel sample was prepared using 0.5 M silicate solution and along with the acid phase (Barge Method), SDS was included at a concentration of 10 mM which is above the CMC point measured in SHG phase (*vide infra*). The particle size distribution was again monitored using DLS in a closed system. The overall shape of the trace is similar to that of Figure 2-21 and Figure 2-23, here the Z-average value increases in the early phase of gelation, reaching a peak Z-average of 750 nm after 144 minutes (Figure 2-24). A subsequent drop off in Z-average, after this point is also observed.

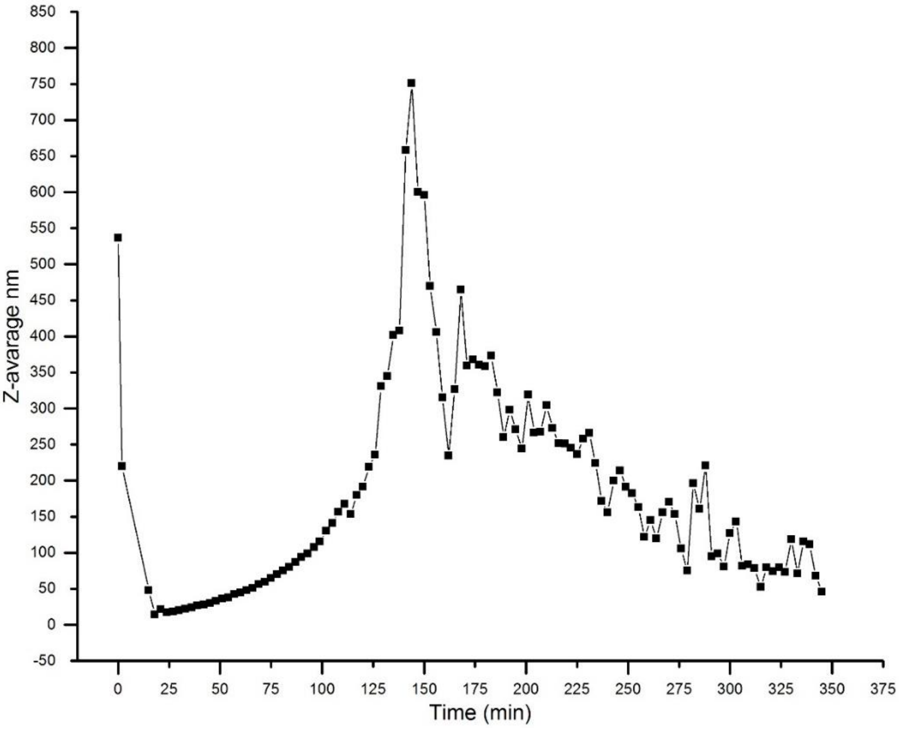

Figure 2-24: First run of the DLS experiment within 0.5 M SHG contain of 10 mM of SDS in the closed system indicating the Z-average against time of gelation

This result suggest that the amphiphile is stabilising, to some degree, the particles of silica in solution resulting in both larger average particle sizes and longer gelation times. To probe this system further a similar experiment to that of Figure 2-24 with SDS at a lower concentration of 1 mM (below the CMC of SDS in water at ambient temperature) was performed. The results are shown in

Figure 2-25 and reveal, consistent with the above hypothesis, lower maximum particle sizes at the 520 nm mark.

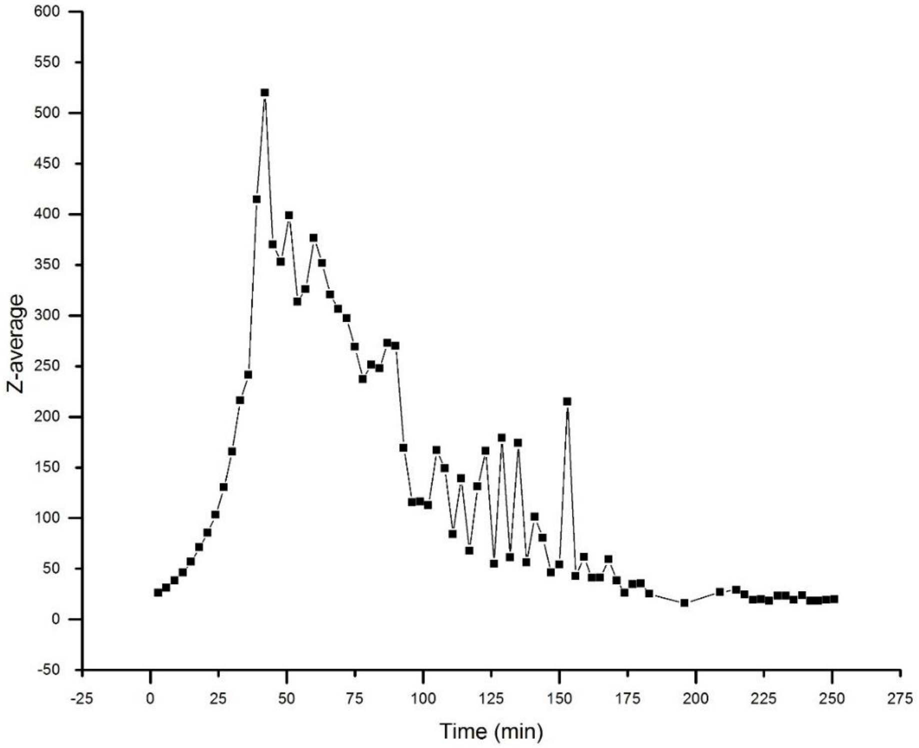

Figure 2-25: DLS results of 1 mM of SDS in 0.5 M of silica gel in a close system indicating the Z-average against time of gelation

The DLS techniques has operations limit of detection (LOD) and these limitations are:

If large particles even in small quantities are present within the sample, still accounted; if the solution is more dense than aqueous, there is a sedimentation possibility and lead to error in data like what happened with the SHG samples; the instrument resolution leads to the instrument will not be able to distinguish between particles located close to each other; if the sample is highly concentrated leads to cause multiple scattering of the light caused by the light which scattered by a particle will scattered by another particle before it could be detected[111].

2.6 UV-Visible Spectrophotometry on Silica Hydrogels. Baseline Shifting and Light Scattering

We noticed during our studies on MC 540 decolourisation (described in details in chapter 4) in SHG's that the baseline displayed significant deviations from those expected and observed in the aqueous phase. These deviations are not due to instrument correction errors as they are not seen at all in any of the aqueous systems that have analysed and also, they display a time-dependency. Moreover, these baseline devastations are present irrespective of the presence of an absorbing molecule such as merocyanine. In other words, they appear to be a feature of the silica hydrogel formulation itself. An example of this is displayed in Figure 2-26 where one can see the baseline drifting effect when the SHG formulation at 0.9 M is examined between 400 – 650 nm, in the absence of any additives. The samples themselves are optically clear but there is a clear "absorbance" displayed in the spectra. However, an increase in effective absorbance is perhaps best translated as a decrease in effective transmittance. Thus, light can fail to be transmitted through a sample as a result of molecular absorbance as in the presence of MC 540 or it could result from light scattering due to particles present in the system, an observation that has been made.

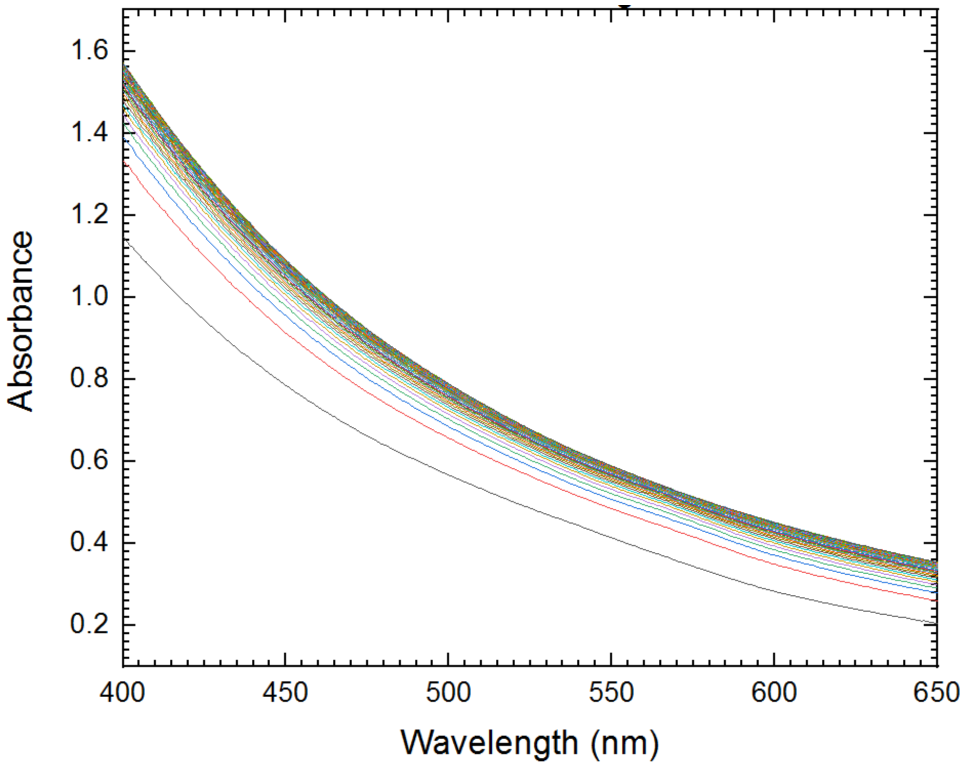

Figure 2-26: Baseline shifting within 0.9 M SHG in the absence of any absorbing molecules, illustrating the scattering effect

Particles within SHGs intercede with UV absorbance investigations[112]. Given that particulates in systems are known to induce scattering effects[112], it was of interest to confirm that aqueous solutions of silicate do not display the same baseline behaviour as those presented by the gel formulations themselves. By ‘particulates’ this refers to air bubbles, colloidal-wisps, precipitates and silicate particles in a gel phase and we suspect that it is silicate particles (the physical SHG) that are likely to have had the greatest impact on UV light scattering on the basis of the time-dependence.

Consider again Figure 2-26, over time, the baseline shifted in the kinetic scans (as shown in Figure 2-26). This happened for each kinetics scan. Hence, scattering had the potential to distort raw data.

Absorbance (A) and transmittance (T) are related by a derivative of Beer-Lambert law:

$$\boldsymbol{A = 2 - \log_{10}}(\%\boldsymbol{T}) \qquad \textbf{Equation 2-1}$$

SHGs with high silicate concentration have high absorbance. This correlates with low light transmittance (Figure 2-27). The higher concentration of SHG, the greater the number of polymer chains in the polymer network, so the more compact the system is. Thus, the greater the number (or effective pores size) of silicate particles. In addition, there are smaller pores for photons to travel through. Therefore, the SHG blocks incident light rays to a greater extent and hence limits transmittance (and *vice versa*).

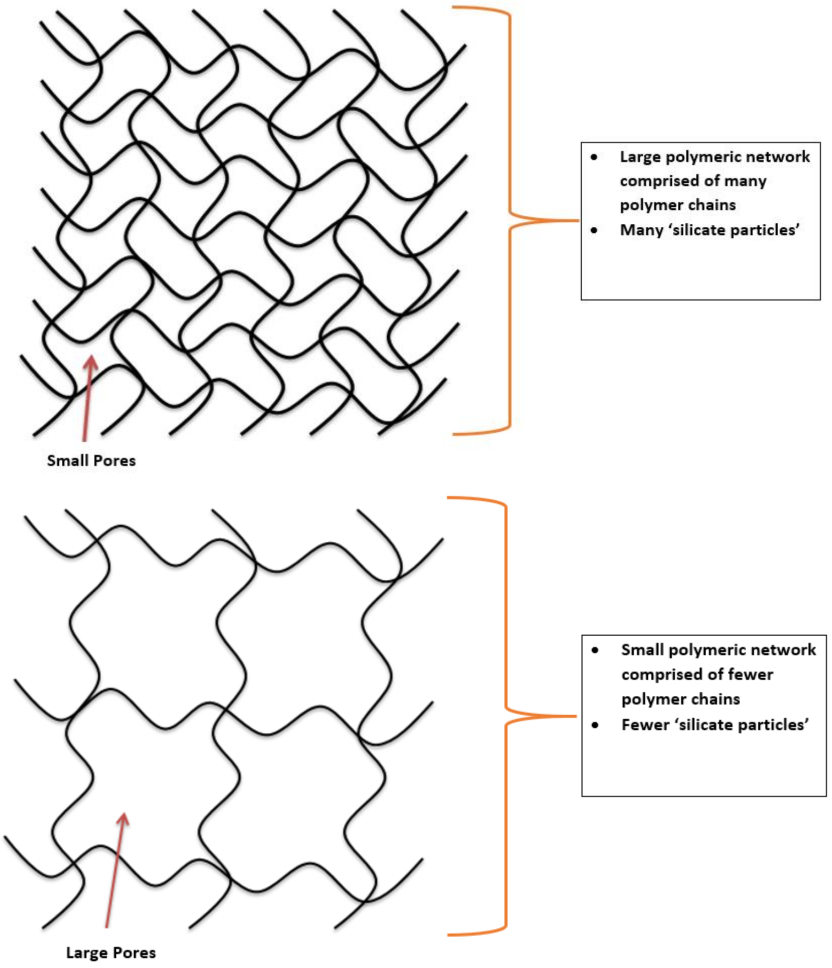

Figure 2-27: Effect of pores on the transmittance of SHG, a higher concentration of SHG leads to small pores and hence low transmittance

We envisage therefore that the baseline migration is following the light scattering behaviour of a changing, gelling system and that once the baseline has converged to a steady state, this corresponds to a scenario in which the gel formation, at least in terms of light scattering, has reached an equilibrium point. In Figure 2-28, Figure 2-29 and Figure 2-30 reveals this convergent behaviour in the baseline behaviour of silica hydrogel formulations of 0.7, 0.9 and 1.0 M SHG. One can clearly see in each of these samples that the light scattering effect is consistently stronger at the lower wavelength range and increases (in terms of transmittance lowering) as the silicate concentration increases.

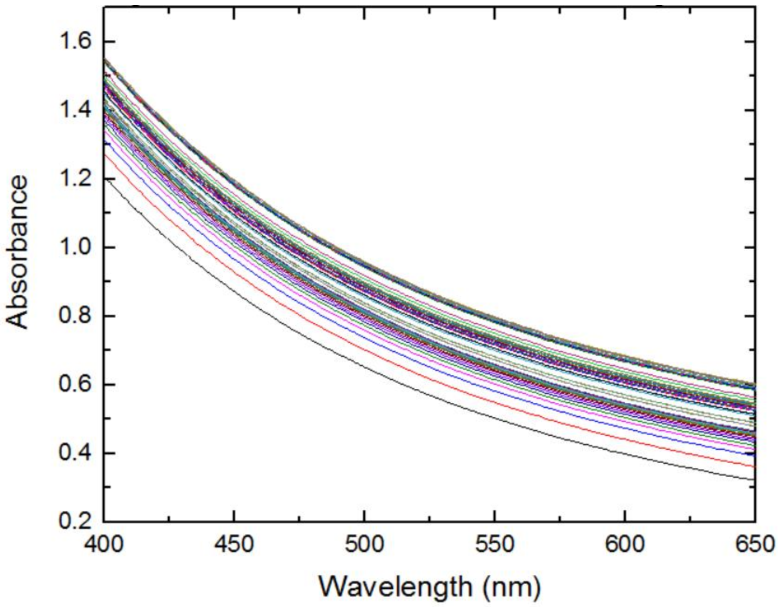

Figure 2-28: Baseline shift of 0.7 M SHG of 12 hrs time with a gradual decrease in increment size with time leading to baseline convergence

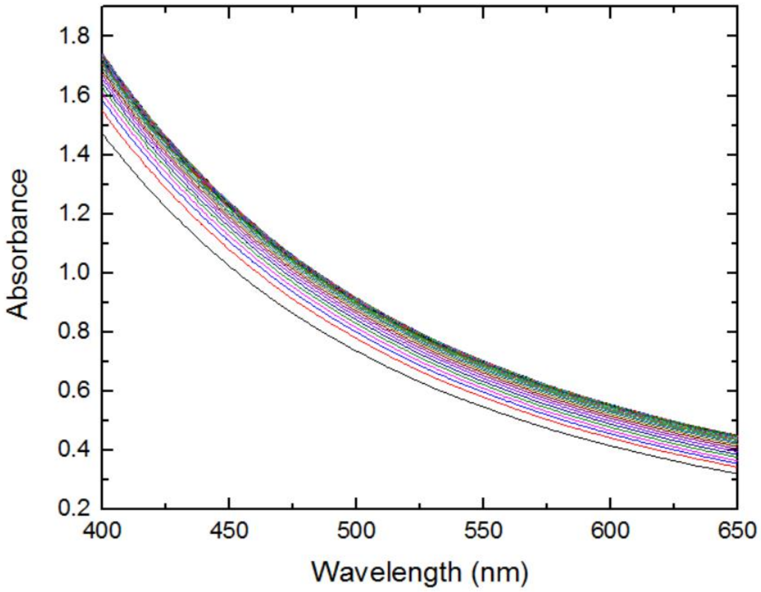

Figure 2-29: Baseline shift of 0.9 M SHG of 12 hrs time with a gradual decrease in increment size with time leading to baseline convergence

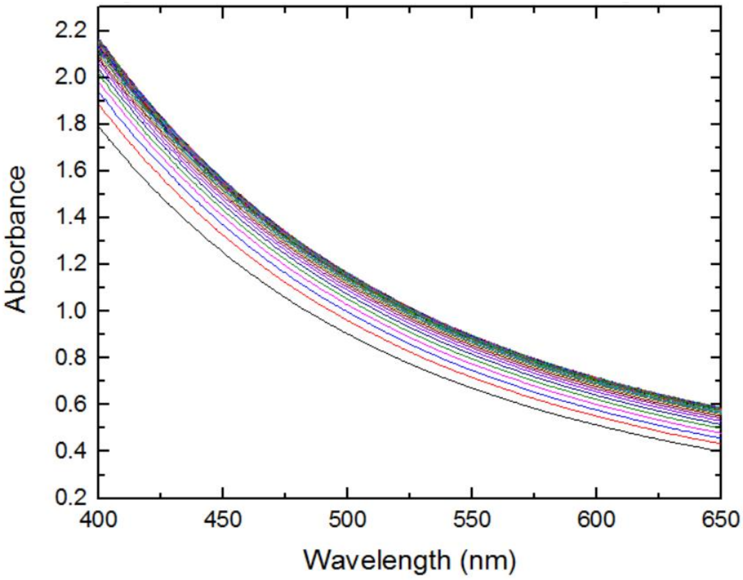

Figure 2-30: Baseline shift of 1.0 M SHG of 12 hrs time with a gradual decrease in increment size with time leading to baseline convergence

While Figure 2-28, Figure 2-29 and Figure 2-30 are useful, it is difficult to extract increment-size convergence information (gelation timescale) in this format. Therefore, by plotting absorbance as a function of time at fixed wavelength 410 nm, 510 nm and 610 nm (low, intermediate and high wavelengths) from the data above illuminated the baseline shift phenomenon more clearly and Figure 2-31, Figure 2-32 and Figure 2-33 shown these data.

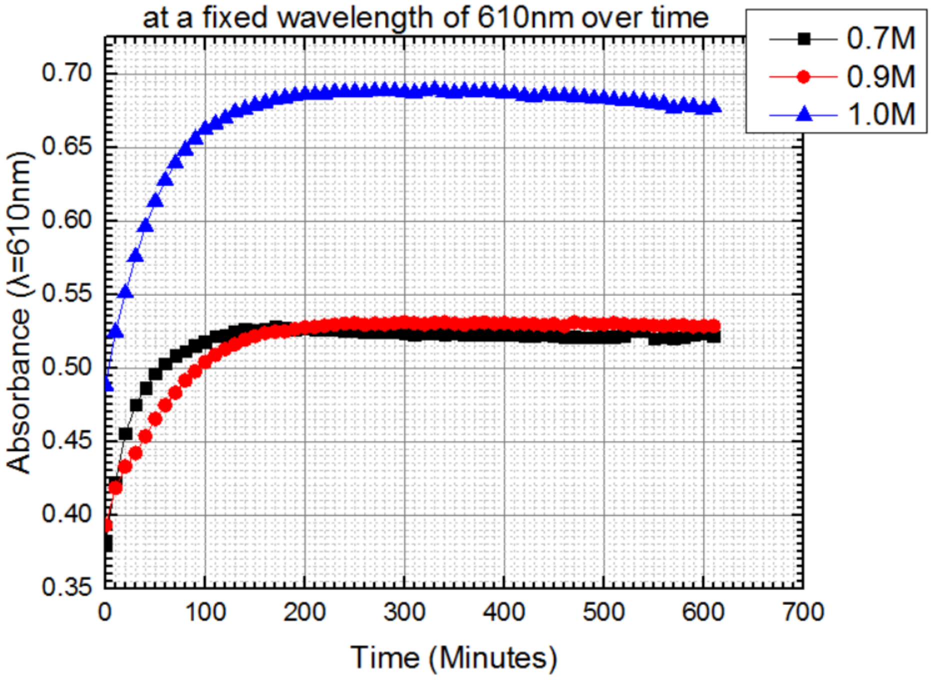

Figure 2-31: The variation of light scattering with respect to SHG concertation at a fixed wavelength of 610 nm over time

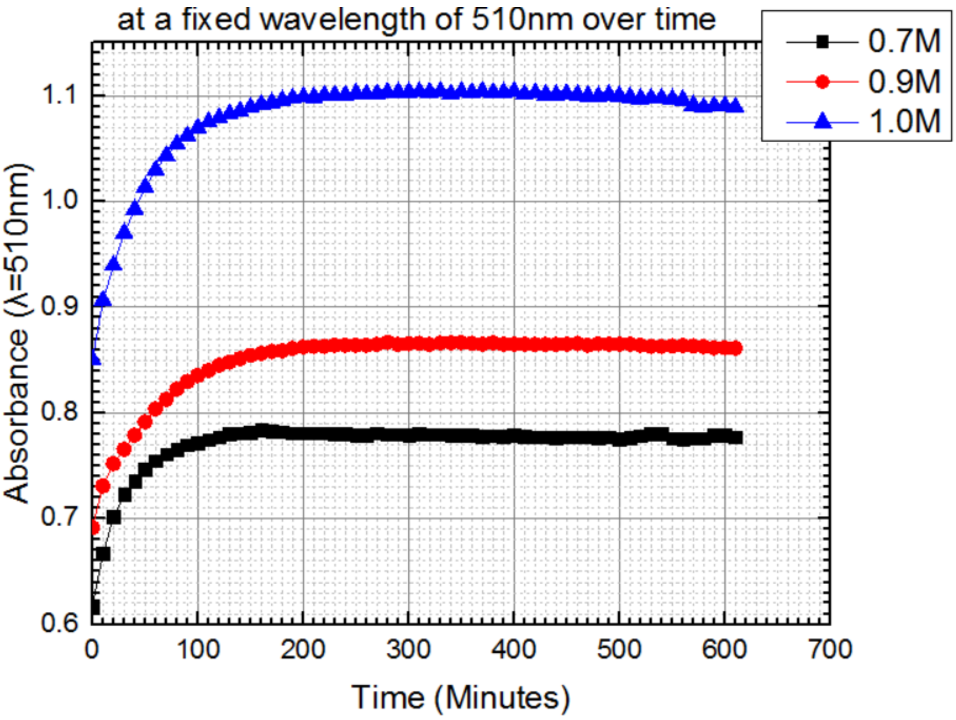

Figure 2-32: The variation of light scattering with respect to SHG concertation at a fixed wavelength of 510 nm over time

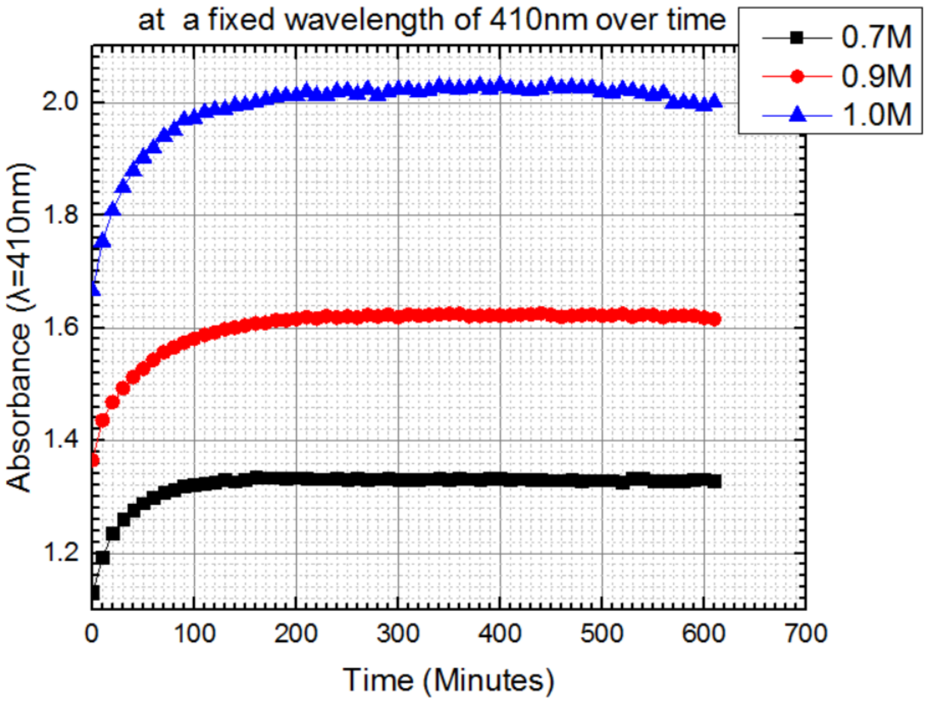

Figure 2-33: The variation of light scattering with respect to SHG concertation at fixed wavelength of 410 nm over time

Figure 2-31, Figure 2-32 and Figure 2-33 show increased absorbance with time until the data plateau and a stable baseline is reached. We envisage that this may allow us a mechanism to measure gelation times based on equilibration or steady state light scattering. Calcabrini, M. and Onna, D. studied the gelation time of a silica gel sample by calculation the increasing in scatting intensity with a pre-designed 3D-printed spectrophotometer[113].

A plot of the derivative of absorbance with respect to time versus time (first differential plot) was constructed for each SHG at each pre-selected wavelength, Figure 2-34 shows plots of three SHG concentrations which are 0.7, 0.9 and 1.0 M at 610 nm. The first differential plot shows the point at which the graph plateaus more clearly than Figure 2-31. The first data point at which dA/dt is equal to zero corresponds to the plateau points in Figure 2-31. Thus, this is the point at which the scattering effect that we are observing appears to reach an equilibrium point for each SHG.

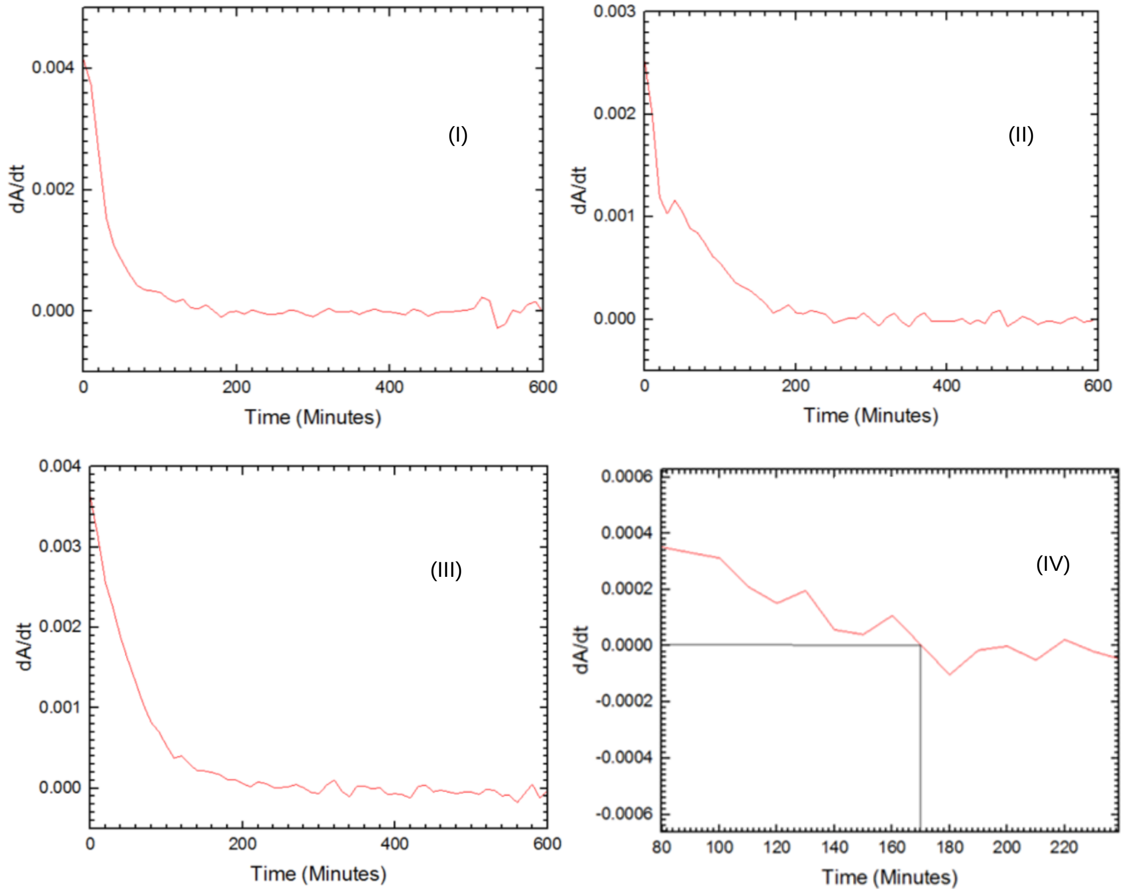

Figure 2-34: First differential graph of (I) 0.7 M, (II) 0.9 M, (III) 1.0 M and (IV) 0.7 M (expanded) SHG at 610 nm.

The plateau times are very similar for the same SHG irrespective of which wavelength of light is probed (Table 2-5). This consistency shows evidence to support that the initial plateau point corresponds to gelation completion, as gelation is a single and unified process that happens throughout the structure at the same time. As SHG concentration increased the plateau time increased. Thus, the longer the gelation time. This was unexpected as, by eye, 0.7 M SHG took longer to gel than 1.0 M SHGs. However, on a molecular level, gelation was still underway at the higher SHG silicate concentration as the observation suggests. This is plausible as there are a greater number of polymeric chains which need to network together to form crosslinked structure as shown in Chapter 2. The process entails a 'disorder-order' transition, so is entropically unfavourable[112]. The ordering, *via* networking, would be more thermodynamically and energetically unfavourable for the 1.0 M SHG as there is movement from a high entropy state to a low entropy state. This unfavourability results in longer gelation ('disorder-order' transition) times. Hence, 1.0 M SHG have longer gelation times than 0.7 M SHG. The DLS results (section 2.5) indicates an approximate gelation time for 0.5 M SHG at 144 minutes which seems to agree with the overall trends shown in Table 2-5.

Table 2-5: Gelation completion time according to the plateau time

	[SHG] / M		
Wavelength (nm)	**0.7**	**0.9**	**1.0**
610	170 min	245 min	260 min
510	165 min	240 min	258 min
410	167 min	240 min	255 min

2.7 Thermal analysis of silica hydrogels

The analysis of the thermal behaviour of SHGs were examined by various techniques that produce complementary information. In the first instance, analysis of several SHG's (nominally 0.5 M – 1.0 M) using the thermogravimetric analysis (TGA) reveals the loss of volatile components and mass decrease through heating. Use of TGA analysis also reveals information about the on-set of mass loss and the total volatile mass lost throughout the heating procedure.

In the cases of the 0.5 M – 1.0 M SHG's (Figure 2-35 a-f) we can see that mass loss begins at ca 25 ˚C in each case and that the weight loss in each SHG sample amounts to 94.6, 93.6, 92.2, 91.6, 90.5, 89.3% respectively. This means that for the 0.5 M SHG for example, the solid silica matrix accounts for 5.4% of the total mass, illustrating clearly how such a small mass matrix is capable of entraining more than 17 times its own mass in water. In each case, volatile loss has ceased between 150-175 ˚C

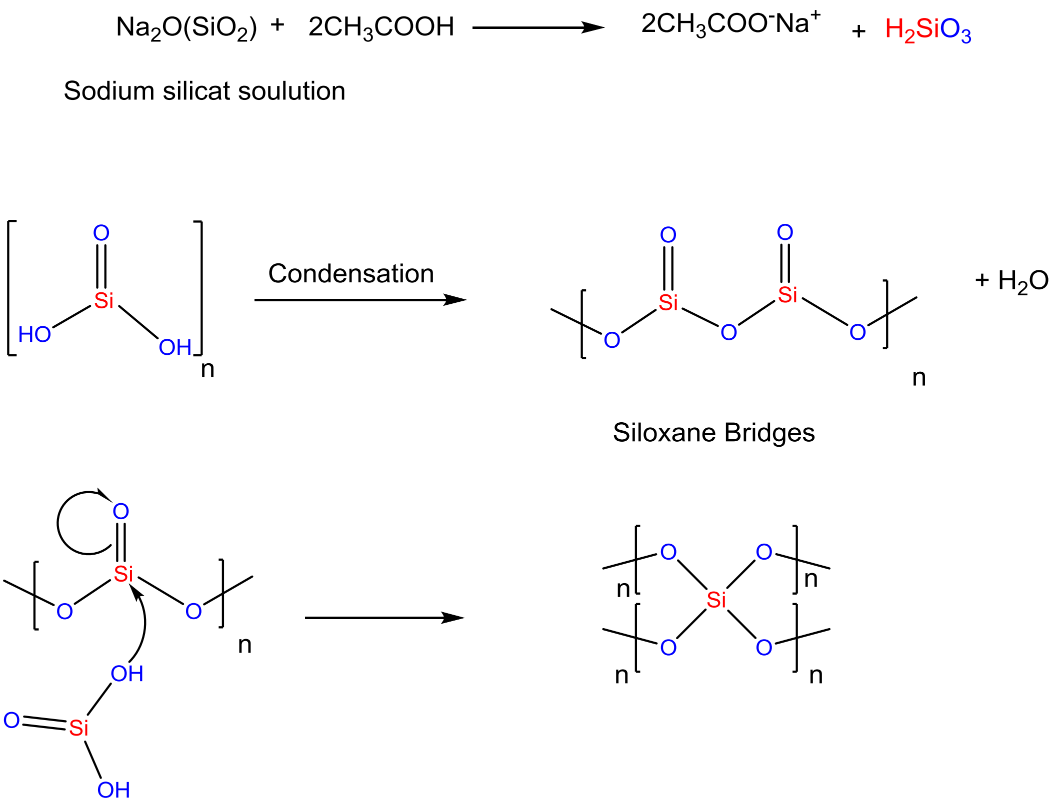

Scheme 2-2: Formation reaction and mechanism of forming three dimensional structure of the silica hydrogel.

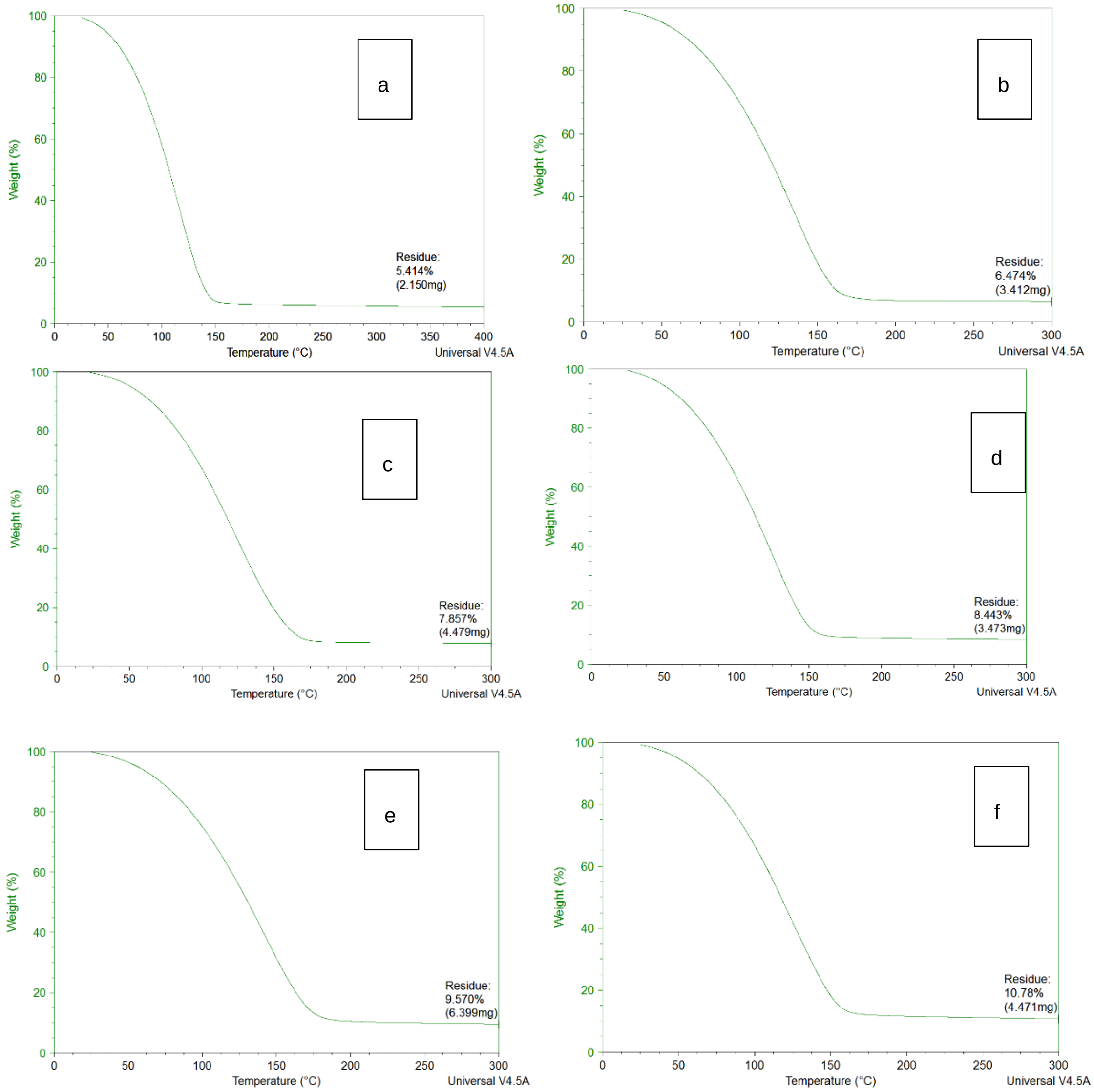

Figure 2-35: Thermal gravimetric analysis of 0.5 M (a); 0.6 M (b); 0.7 M (c); 0.8 M (d); 0.9 M(e) and 1.0 M (f) silica hydrogel sample

2.7.1 TGA derivative curves

Whilst the overall mass loss can be seen clearly in the images Figure 2-35, the second derivative of the TGA trace affords slightly different information. This derivative plot is called differential thermogravimetry (DTG) and affords information on the different stages of mass lose, rather in the same way as differential scanning calorimetry (DSC). Examination of the DTG trace in Figure 2-36, shows that there are three weight-loss events; at 126.08 ˚C, 137.03^{o}C and then at 144.42 ˚C. First expectation that these events are representative of different stages of water loss but, section 2.7.2 showed practically it’s not the case. For each of these three processes, the percentage weight loss per degree temperature is ca 0.02, 0.05 and 0.06 demonstrating that as temperature increases but not sufficient to do the weight loss. It is not entirely obvious what the individual processes involved might be but it may be envisaged that the lowest temperature step may equate to removal of the least tightly bound water, the free water.

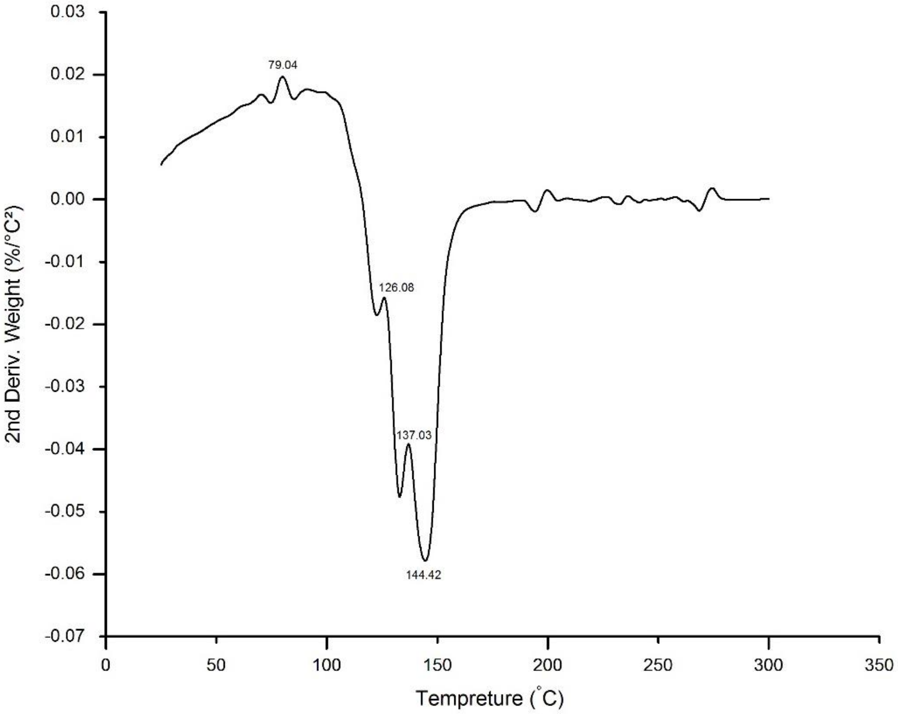

Figure 2-36: Second derivatives of the TGA curve of SHG with 0.5 M

The weight percentage/C^2 of the second derivative plotted against temperature increases instead of weight percentage in the Figure 2-35.

The plot of the second derivative of 0.6 M SHG shows one thermal event at 150.95 ˚C and the inflection point at 160.20 ˚C as appears in Figure 2-37. At a slightly higher concentration of SHG, the number of thermal events increased to five below the inflection point which indicates water molecules are not easy to evaporate from the matrix material. Thermal events happened at ˚C 102.85, 112.52, 129.18,151.09 and 162.17 with an inflection point at 168.49 as shown in Figure 2-38 The inflection point refers to the end of major events and the sample removed all volatile molecules from the bulk.

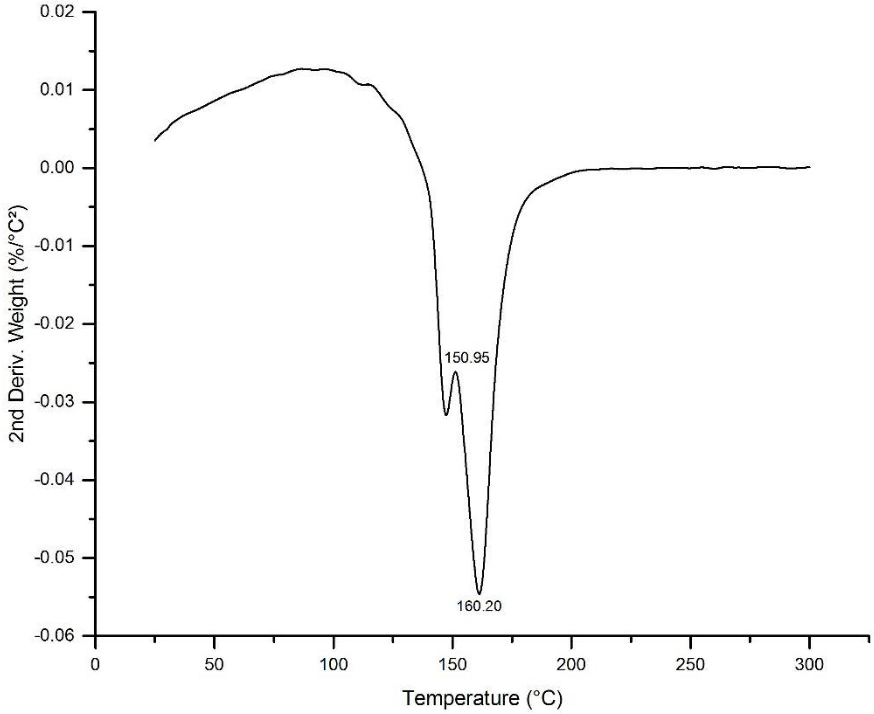

Figure 2-37: Second derivatives of the TGA curve of SHG with 0.6 M with a single peak thermal shoulder.

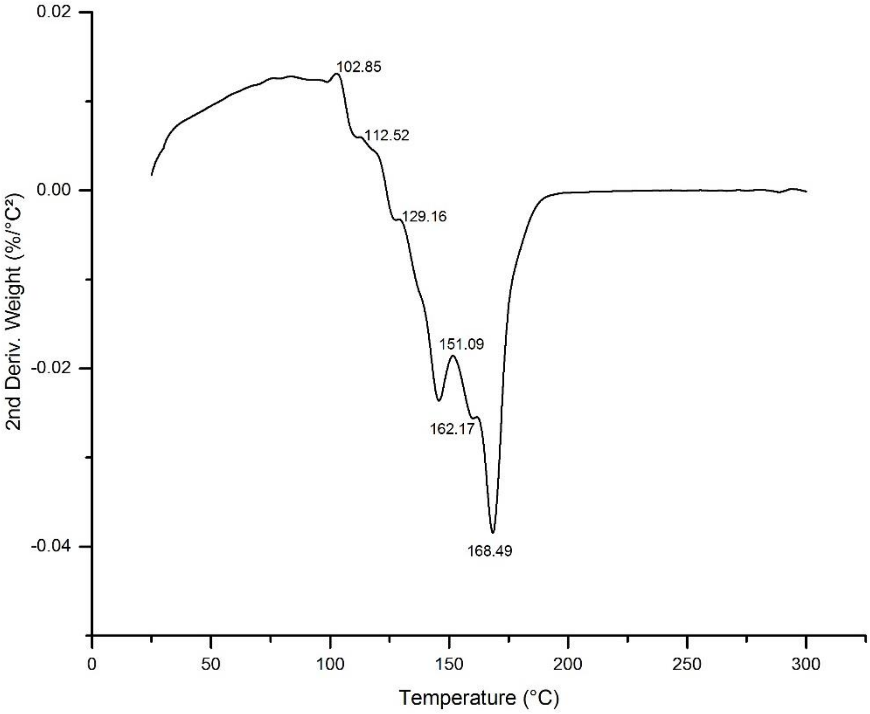

Figure 2-38: Second derivatives of the TGA curve of SHG with 0.7 M with a five peaks thermal shoulder.

At 0.8 M shown in Figure 2-39 of SHG a wide hump-like peak appears in the plot when heating from 25 ≈100 ˚C and then the thermal shoulders appears at ˚C 123.38, 135.86, 148.53 and finally the inflection point at 153.38 ˚C.

With 0.9 M of SHG, a similar observation of a broad, hump-like peak is can be seen from 35 ˚C to about 139 ˚C (Figure 2-40) where the first thermal shoulder event happens while the next shoulder appears at 155 ˚C prior to the inflection point at 172 ˚C.

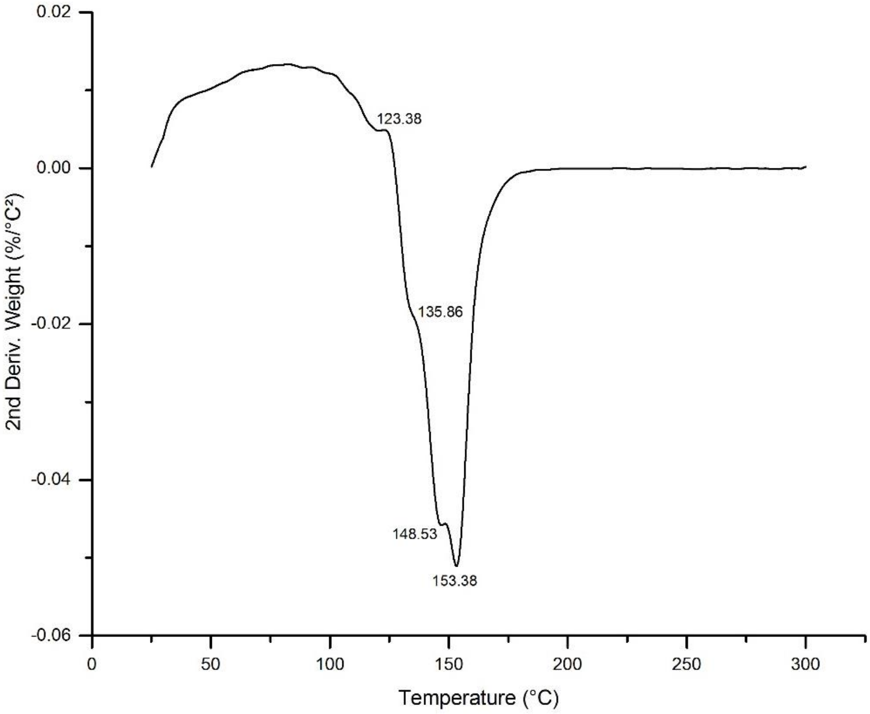

Figure 2-39: Second derivatives of the TGA curve of SHG with 0.8 M with a three major peaks thermal shoulder.

The highest concentration of the SHG sample which is 1.0 M has the a similar hump starts from beginning of heating to 109 ˚C then a sharp dropdown with two thermal shoulders at around 130 ˚C and 138 ˚C and the inflection point at 154.46 ˚C as it appears in Figure 2-41.

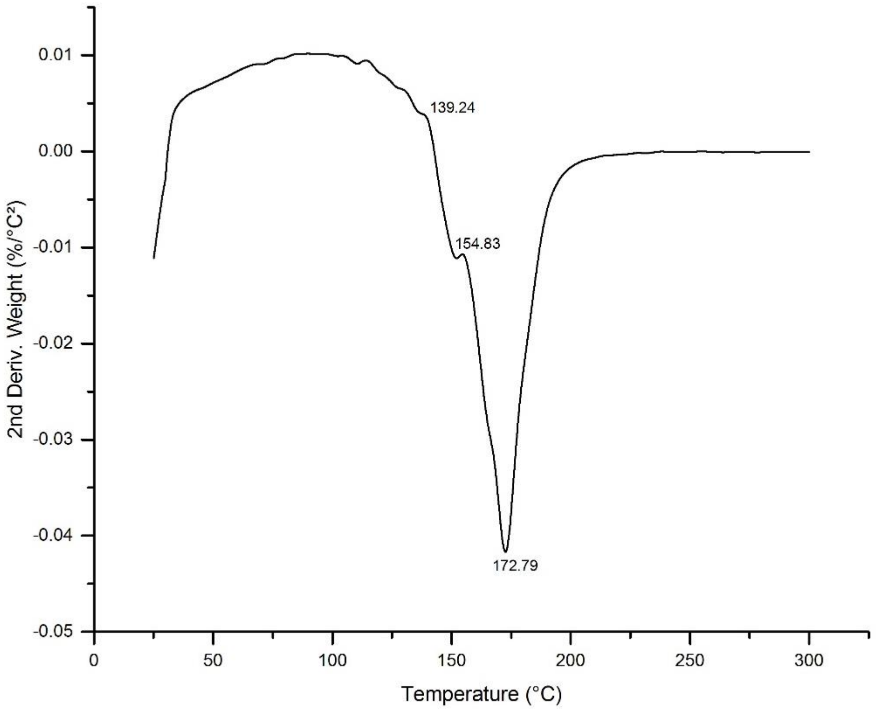

Figure 2-40: Second derivatives of the TGA curve of SHG with 0.9 M with a three major peaks thermal shoulder.

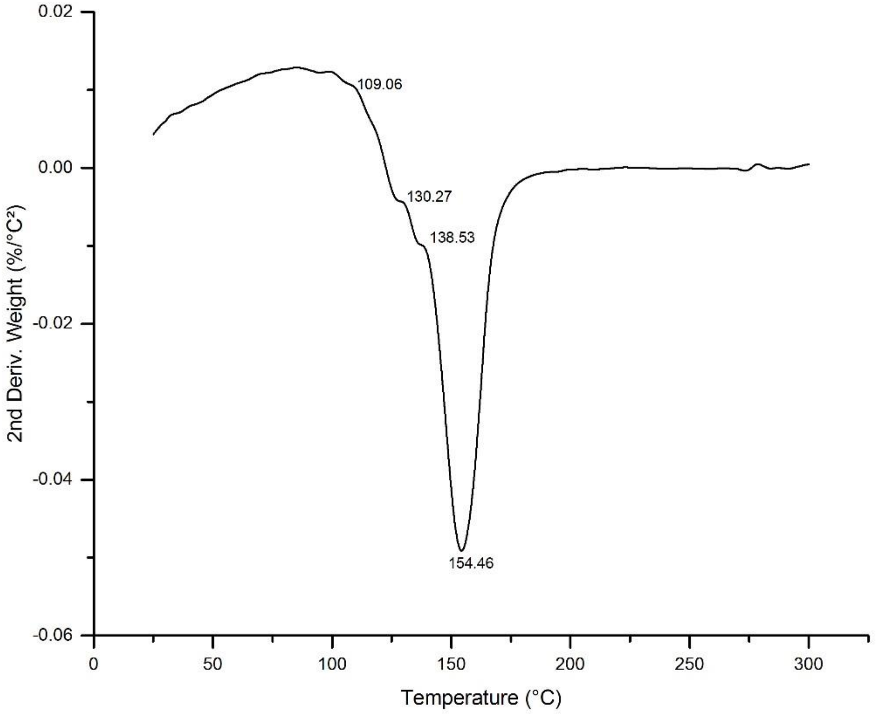

Figure 2-41: Second derivatives of the TGA curve of SHG with 1.0 M with a three major peaks thermal shoulder.

2.7.2 Fixed Temperature TGA Experiments

The plot in Figure 2-36, which is related to the thermal events of the Second derivative of TGA curve, shows that three such events appears in 0.5 M SHG gel sample at 126.06, 137.03 and the inflection point at 144.42 ˚C. These thermal events seems to give an indication about water lost stages from the sample and decided to examine these stages.

The 0.5 M SHG sample have been introduced to fixed temperature TGA analysis at 126, 137 and 144 ˚C and see whether any change in the water (weight) lost and results are explained below:

Three samples with identical concentration at 0.5 M of SHG delivered to the TGA analysis and run the experiment but with a constant temperature for the whole duration of the experiment. At 126 ˚C run, the majority of water loss happened below 20 minutes and the weight lost curve appears to show a constant decreasing over heating as shown in Figure 2-42 with a residue of 5.9 % of the total sample’s weight.

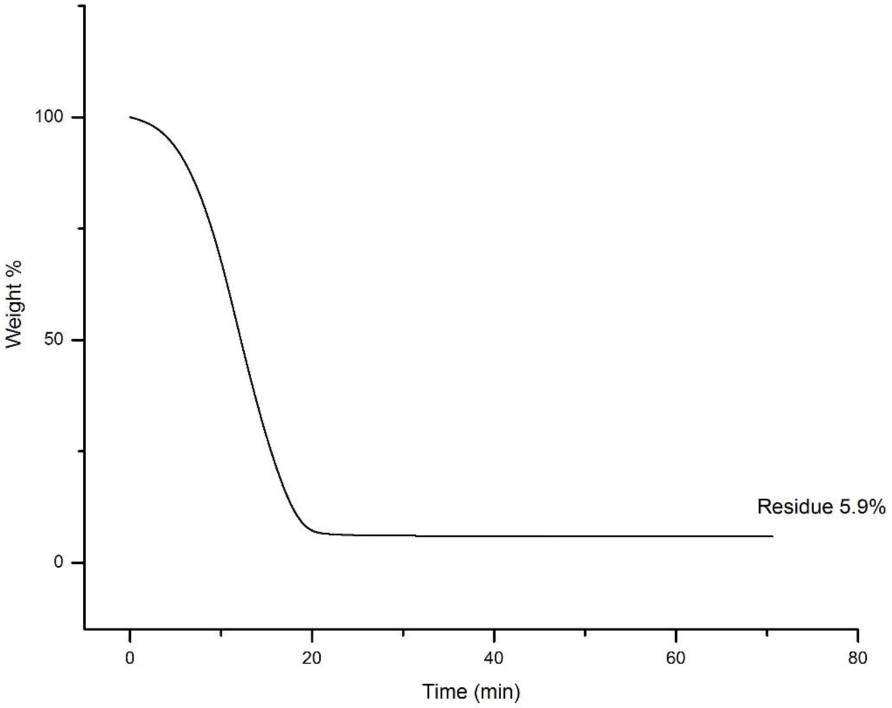

Figure 2-42: Plot of first run of TGA within 0.5 M SHG at 126 ˚C indicating percentage of weight lost per minute

At 137 ˚C run, the overall shape of the plot is similar to the one of 126 ˚C run in which the majority of the weight lose happened below 20 min and the residue percentage is equals to 5.8 % as shown in Figure 2-43.

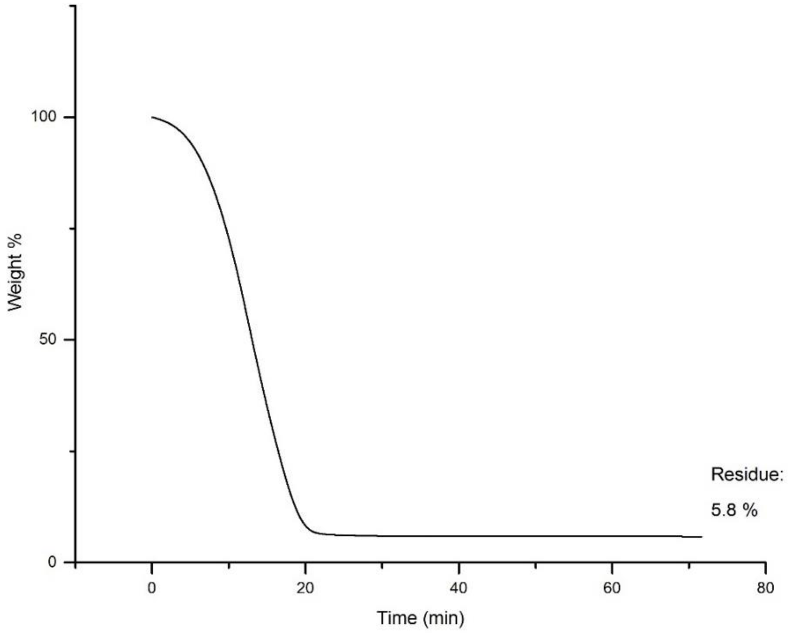

Figure 2-43: Plot of first run of TGA within 0.5 M SHG at 137 ˚C indicating percentage of weight lost per minute

At the final experiment of 144 ˚C run, again the same overall shape and time required to losing most of the water with a residue percentage 6.4 % as shown in Figure 2-44.

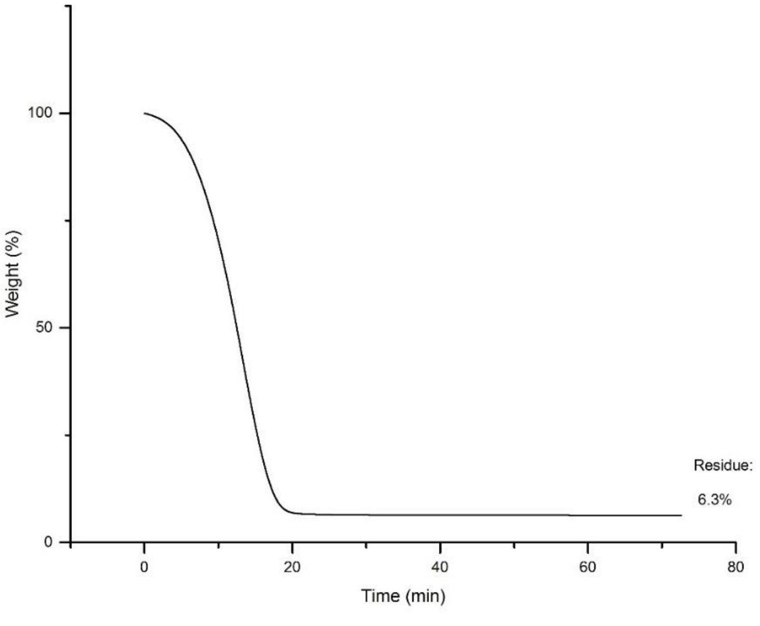

Figure 2-44: Plot of first run of TGA within 0.5 M SHG at 144 ˚C indicating percentage of weight lost per minute

It’s difficult to distinguish between these three temperature events as they appear to have very similar envelopes. This is not unsurprising as the temperature differences are small between each curve ($\Delta T = 11$ and 7 ^oC respectively). The respective gradients for the weight loss curves are shown in Figure 2-45 where it can be seen there is some variation of percentage weight loss across time window. In order to say something more conclusive on whether such changes are linked to fundamental differences of thermodynamics of may be reflective of statistical differences within samples, one would need to perform multiple repetitions at each temperature to ascertain standard deviations. In the absence of such experiments here, we can only tentatively conclude that the overall profiles of water removal at these three temperatures appears broadly similar.

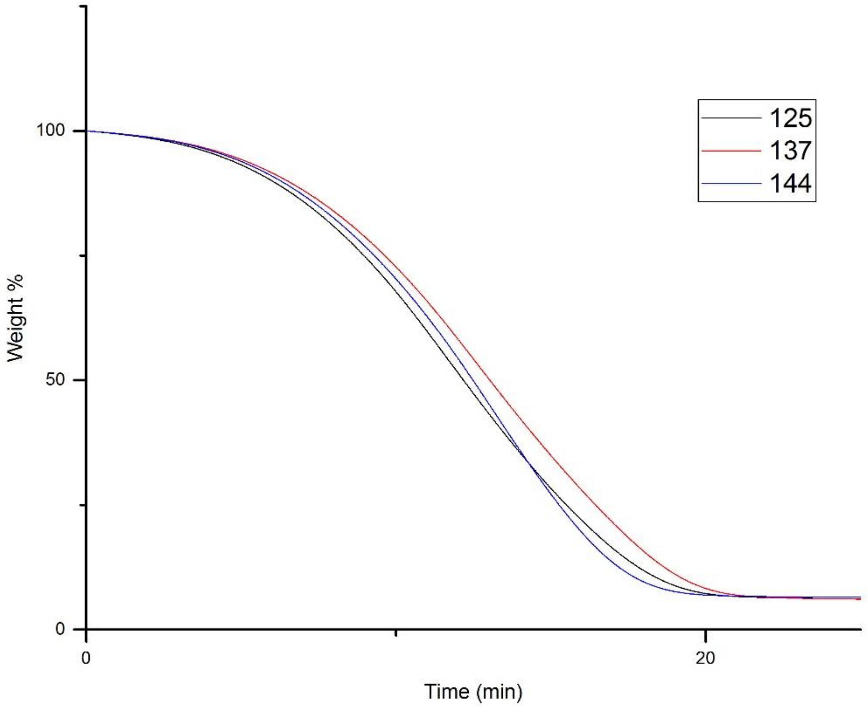

Figure 2-45: Overlay plot of the three chosen temperature degrees. Time range selected from 0 – 25 min to easy distinguish between lines.

2.8 Conclusion

Overall, the content and main conclusions from this chapter may be summarised as follows:

1. A standard operating protocol (SOP) for preparing silica gels has been identified as effective and reproducible
2. Surface analysis of hydrogel matrix silica (SEM, EDX, BET) obtained following critical point drying and dialysis reveals a porous and open morphology with surface area of *ca.* 400
3. Dynamic light scattering experiments suggest that the presence of an amphiphile such as sodium dodecylsulfate (SDS) influences the particle size distribution in the sol phase. Particle size increasing in the presence of SDS
4. Thermal analyses demonstrate the large weight percentage of water in the standard gel formulations we use here (*ca*. 95% water content in the 0.5 M SHG)

Chapter 3 Measurements of Critical Micelle Concentrations in the Silica Hydrogel Phase

3.1 Aims of the work Described in this Chapter

The main objective of this section of the work was to examine whether a representative amphiphile, sodium dodecylsulfate (SDS) might undergo different self-assembly processes in the SHG phase compared to the aqueous phase. Therefore, this chapter reports measurements of the critical micelle concentration (CMC) of SDS within a range of SHG environments and comparison to the aqueous phase

Grzybowski defined the term of self-assembly as follows: '*Self-assembly is the autonomous organization of components into patterns or structures without human intervention,'* behaviour which has been used widely both in natural and in modern technology[114]. The reasons behind the importance of the concept of self-assembly are many[115, 116] but the one which is most related to the work described in this thesis is the how self-assembly processes may or may not be influenced by moving from an aqueous phase to a hydrogel phase.

To place that in context, biological cell membranes consist of self-assembly structures which are essential for developing the biological activities of living cells and functional organs[117] and these in turn emerge from a cellular cytosol material which is hydrogel in nature.

What is explored in this chapter is how the process of amphiphile self-assembly changes when being transferred from the aqueous phase to the hydrogel phase. In doing this, a selection has made to work with SDS as a representative amphiphile. We do not intend at any time to argue that SDS had any prebiotic provenance. In addition, selected to work with SHGs because of their prebiotic provenance (refer back to Chapter 1).

The amphiphile SDS is a negatively charged surfactant and consists of a 12-carbon tail attached to a sulphate head group with a chemical formula $CH_3(CH_2)_{11}SO_4Na$. it is used in many cleaning and hygiene products[75]

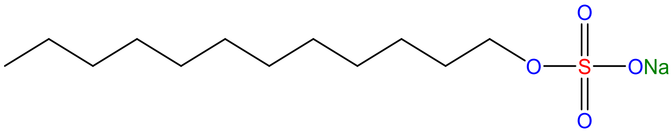

Figure 3-1: Chemical structure of sodium dodecylsulfate (SDS) indicating the 12-carbon tail and sulphate head group

However, before conducting specific experiments within SHG's, it was necessary to address two key issues: (i) do the various different measurement techniques of CMC give convergent answers in aqueous media or, if not, why not? and (ii) which of the various analytical methods for CMC determination would be best translated to the SHG environment?

Therefore, benchmark experiments were performed to determine critical micelle concentrations of SDS in the aqueous phase using the following analytical techniques:

1- Surface tension measurements
2- Solution conductivity
3- Spectrophotometry
4- Fluorimetry

3.2 Measurements of SDS CMC in Aqueous Environments

3.2.1 Surface Tensiometry

The first benchmark experiment was performed using the capillary rise method [64] to calculate the surface tension of aqueous solutions containing different concentrations of the surfactant SDS. The surface tension values for different capillary can be calculated according to the relation with capillary rise and radius of capillary as follows:

Surface tension (γ) = ρ x r x g x h/2 **Equation 3-1**

Where ρ is the density of water at 20 °C, r; is radius of capillary, h is the capillary rise and g is the acceleration due to gravity (9.80665 m s^{-2}).

The surface tension, γ, of the surfactant solution decreases with an increase in concentration of surfactant molecules in the solution. For concentrations below the CMC, surfactant molecules are distributed between the bulk of the solution and the surface, both concentration (in bulk and surface) increases until the CMC is reached. At the CMC , the bulk concentration of the individual surfactant molecules is constant. Above the CMC, the saturation level of bulk concentration of surfactant is reached [64].

In Table 3-1 results of this experiment where it can clearly be seen that the surface tension of the surfactant solution decreasing with increasing surfactant concentration. The dependence of surface tension on the log e value of surfactant concentration is called the surface tension isotherm and is used to estimate the CMC graphically [64].

Table 3-1: Results for the surface tension method for calculating the CMC of the surfactant SDS

[SDS] mM	Height in capillary/m	surface tension/ $N.m^{-1}$	-Ln [SDS] mM
1.25	0.022	0.0646	6.68
2.5	0.015	0.044	5.99
5	0.012	0.0352	5.29
7.5	0.011	0.0323	4.89
10	0.01	0.0293	4.60
15	0.008	0.0234	4.19

Figure 3-2 shows a plotted graph of the result of surface tension isotherm which is used to estimate the CMC of SDS. From the graph and the data collected, it is possible to estimate the CMC from the inflection point to be 6.1 mM. This experiment was performed only once hence there are no error bars on the graph. This is because it is not likely that we could use this method for our gel systems because SHGs are very viscus to raise up in capillary tube.

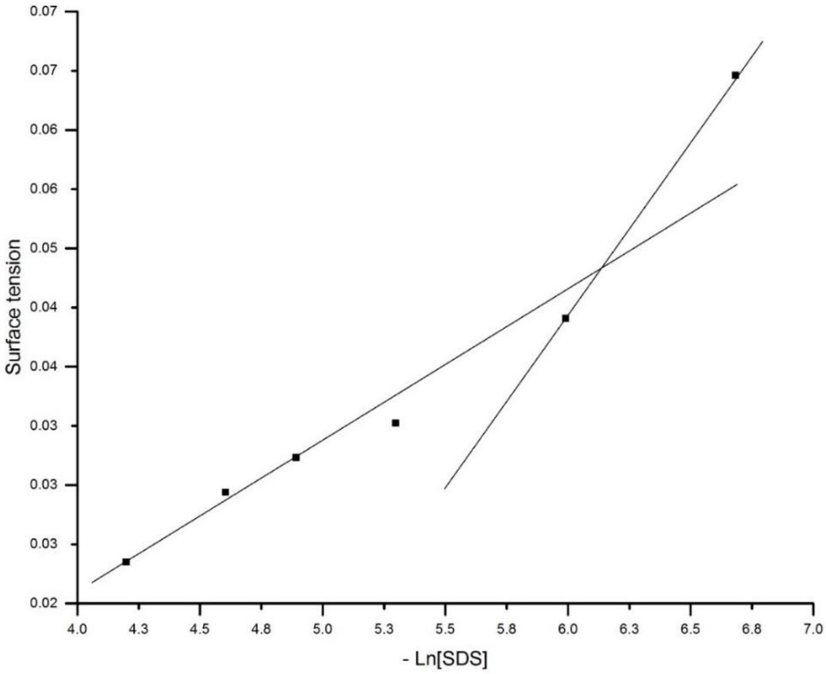

Figure 3-2: Plotted graph between the surface tension against (-Ln[SDS]) in mM and the inflection point used to estimate the CMC point of the surfactant.

3.2.2 Solution Conductivity

The second benchmark experiment involved using the method of solution conductivity to calculate the CMC value of SDS. The experimental procedure is described in the Experimental chapter and the experiment was performed in triplicate (see Table 3-2 for readings). Figure 3-3 shows a plotted graph for average conductivity of all three runs, in which different concentrations of SDS are plotted against the average conductivity values measured. From the graphs, a discontinuity in the value of conductivity of micellar solution is observed due to micelle formation although the exact estimation for the point is always subject to an element of subjectivism. The combined average results of each individual reading issued to calculate the CMC value for the surfactant SDS, is equal to 7.8 mM.

Table 3-2: The results for the conductivity method for calculating the CMC of surfactant SDS. Experiments were performed in triplicate

[SDS] mM	Run 1st mS	Run 2nd mS	Run 3rd mS	Average
0.000	0.020	0.300	0.100	0.140
0.498	48.500	38.200	35.700	40.800
0.990	92.700	74.700	72.600	80.000
1.478	137.100	108.900	106.800	117.600
1.961	148.100	144.400	143.300	145.267
2.439	217.000	177.400	176.000	190.133
2.913	257.000	210.000	209.000	225.333
3.382	292.000	240.000	239.000	257.000
3.846	326.000	270.000	269.000	288.333
4.306	356.000	299.000	298.000	317.667
4.762	383.000	324.000	324.000	343.667
5.213	411.000	348.000	348.000	369.000
5.660	436.000	370.000	370.000	392.000
6.103	460.000	390.000	390.000	413.333
6.542	483.000	411.000	411.000	435.000
6.977	503.000	431.000	430.000	454.667
7.407	525.000	451.000	450.000	475.333
7.834	544.000	467.000	469.000	493.333
8.257	563.000	485.000	487.000	511.667
8.676	583.000	502.000	503.000	529.333
9.091	601.000	518.000	518.000	545.667
9.502	618.000	534.000	534.000	562.000
9.910	635.000	550.000	550.000	578.333
10.314	652.000	563.000	565.000	593.333
10.714	669.000	578.000	579.000	608.667
11.111	685.000	592.000	594.000	623.667
11.504	700.000	606.000	608.000	638.000
11.894	715.000	619.000	620.000	651.333
12.281	730.000	632.000	634.000	665.333
12.664	745.000	646.000	647.000	679.333
13.043	760.000	656.000	660.000	692.000
13.420	773.000	669.000	672.000	704.667

13.793	786.000	681.000	684.000	717.000
14.163	799.000	693.000	696.000	729.333
14.530	812.000	705.000	708.000	741.667
14.894	823.000	716.000	720.000	753.000
15.254	835.000	728.000	732.000	765.000
15.612	846.000	739.000	743.000	776.000
15.966	857.000	751.000	754.000	787.333
16.318	868.000	762.000	764.000	798.000
16.667	879.000	763.000	775.000	805.667
17.012	889.000	773.000	785.000	815.667
17.355	899.000	783.000	797.000	826.333
17.695	909.000	794.000	807.000	836.667
18.033	919.000	804.000	817.000	846.667
18.367	930.000	814.000	828.000	857.333
18.699	939.000	824.000	839.000	867.333
19.028	949.000	835.000	849.000	877.667
19.355	959.000	845.000	858.000	887.333
19.679	969.000	855.000	869.000	897.667
20.000	979.000	865.000	879.000	907.667

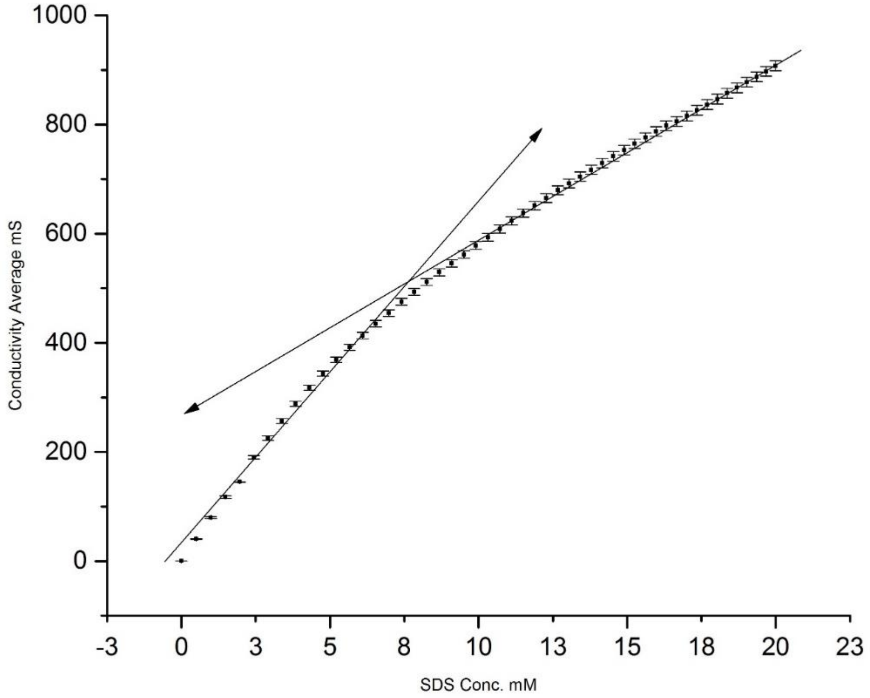

Figure 3-3: Result of average runs of the conductivity experiment to calculate the CMC point of the surfactant SDS.

3.2.3 Fluorescence Spectroscopy

The fluorescence spectrum of pyrene in the aqueous phase exhibits four predominant peaks (Figure 3-5). Pyrene is a polycyclic aromatic hydrocarbon (PAH) containing four benzene rings, resulting in a flat aromatic system and has the chemical formula $C_{16}H_{10}$. The irradiation peaks appear at 302, 366, 377 and broad peak at 420 nm.

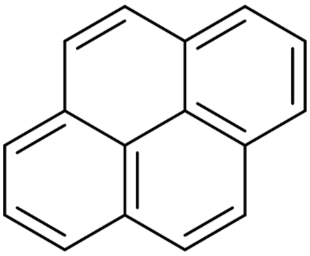

Figure 3-4: Structure of PAH pyrene indicating the flat aromatic ring system.

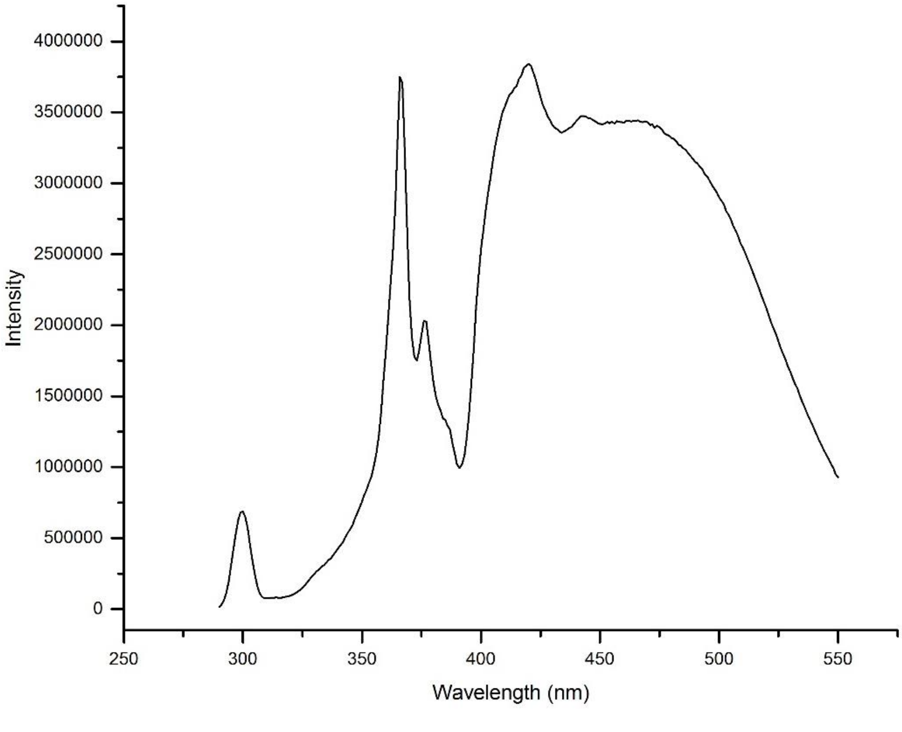

Figure 3-5: Peaks from Flourolog instrument of 12 mM of surfactant SDS and pyrene in aqueous phase

It has been shown by Kalyanasundaram and Thomas that the ratio of the first and third peak intensities are sensitive parameters to estimate the CMC point of surfactants [118]. Another fluorescence method used to calculate CMC points has been described by Wong *et al*, which is based on an assumption that any shifting of the fluorescence maximum wavelength arises from dye molecules experiencing changes in their environment. These changes are envisaged to be the result of micelle formation[119]. This method (i.e Wong method) involves measurement of only the first maximum fluorescence peak at 305 nm which is used to estimate the CMC within aqueous media as follow:

A series of 15 different concentrations of the surfactant SDS were prepared in disposable cuvettes, each one containing an ethanolic solution of pyrene. The final concentration of pyrene in each cuvette was 1x10^{-5} M. Table 3-3 collects the intensity (I) of three fluorescence peaks of pyrene as a function of the concentration of SDS. The fourth peak of pyrene is a broader peak and the exact intensity is not accurate (see Figure 3-5). This experiment is a one-off run.

Table 3-3: The florescence intensities of a series of different concentrations of surfactant SDS solutions at three predominant peaks in an aqueous phase

[SDS] mM	I_{305}	I_{365}	I_{377}
1	3637160	3699160	2626900
2	3608820	3624240	3464300
3	3744720	3693400	3773710
4	3737590	3753840	3755670
5	3672370	3781620	3752140
6	2027740	3723130	3564650
7	581840	3781860	2710650
8	595730	3781170	3001760
9	624970	3796990	3625840
10	225970	3800170	3433720
11	801620	3760530	2290870
12	687760	3749440	2023270
13	676790	3790140	3211710
14	662360	3752440	2203720
15	789960	3802710	1311050

A graph can be plotted between the intensity of the first fluorescence maximum centre against the surfactant concentration (Figure 3-6; the Wong method). The initial peak intensities at lower amphiphile concentration (below CMC point) seem to be rather stable with comparable peak intensities; however these values decrease sharply around the CMC point and finally the system is stabilised again by similar peak intensities above the CMC point. From the graph below, an estimation of the CMC point of the surfactant SDS in aqueous phase from the inflection points where the rate of decrease accelerates which is 6.9 (± 0.4) mM. The ESD value calculated from the data shown in the graph based on the best fit of the data selected points. The red shadow is generated automatically by the OrigenPro software.

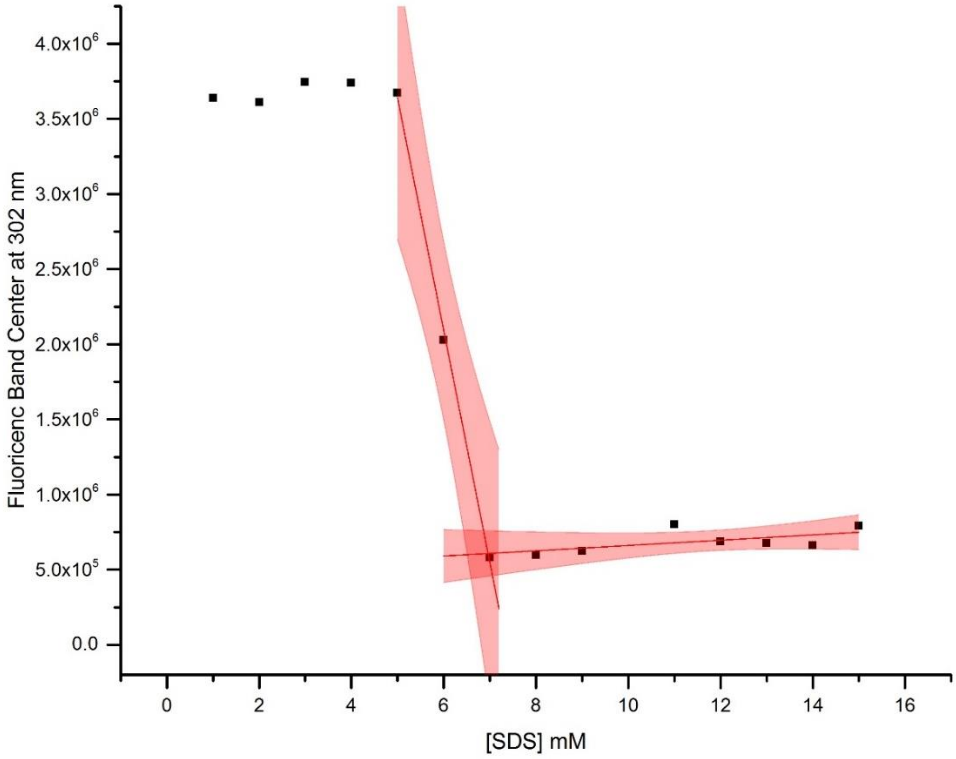

Figure 3-6: Plotted graph of the SDS concentration in millimoles per litre against the intensities of the first fluorescence band centre values in the aqueous phase by pyrene

This experiment was a prospective choice to be used to estimate the CMC within SHG environments due it’s compatibility in principle with different media, i.e. the SHG prepared directly in a disposable cuvette and the cuvette could be loaded to the instrument without any further addition or mobility of SHG. However, initial results of the use of this fluorescent method in the SHG phase suggested that there was some behaviour in that phase which did not really allow us to obtain good quality usable data (Figure 3-7). Therefore, we decided against further investigation of fluorescence as a method for use in the SHG phase.

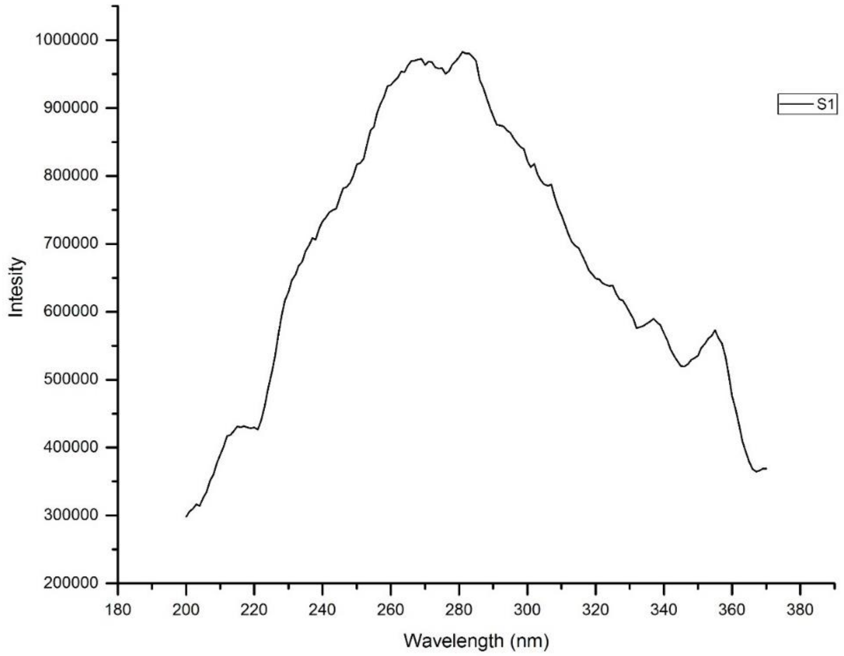

Figure 3-7: Peaks from Flourolog instrument of 0.9 mM of surfactant SDS and pyrene in SHG phase

3.2.4 Visible Spectrophotometry

To estimate the CMC of surfactant SDS in the aqueous phase using spectrophotometry, two different methods were used which involve using two different dyes, merocyanine 540 (MC 540) and pinacyanol chloride (PC). In using the first of these dye probes, the ratio of absorbance at two key maxima, 558 and 524 nm are plotted against the concentration of SDS whilst the use of pinacaynol chloride dye system involves plotting absorbance at 608 nm against SDS concentration. concentration of SDS and absorption at 605 nm plotted against concentration of SDS pinacyanol chloride.

3.2.4.1 Merocyanine 540 method

A procedure was used based on a study described by A. Wicken *et al.*[73] as follows. A series of different concentrations of SDS were prepared in a test tubes and mixed with an ethanolic solution of a red dye MC 540, resulting the dye concentration in each tube being 1x10^{-5} M.

Figure 3-8 showed a steady increase of the absorbance of merocyanine 540 dye with increasing in the concertation within aqueous solution, two maxima wavelengths used and both would fit perfectly with a linear fit (see Table 7-1 and Table 7-2 for the fitting equations).

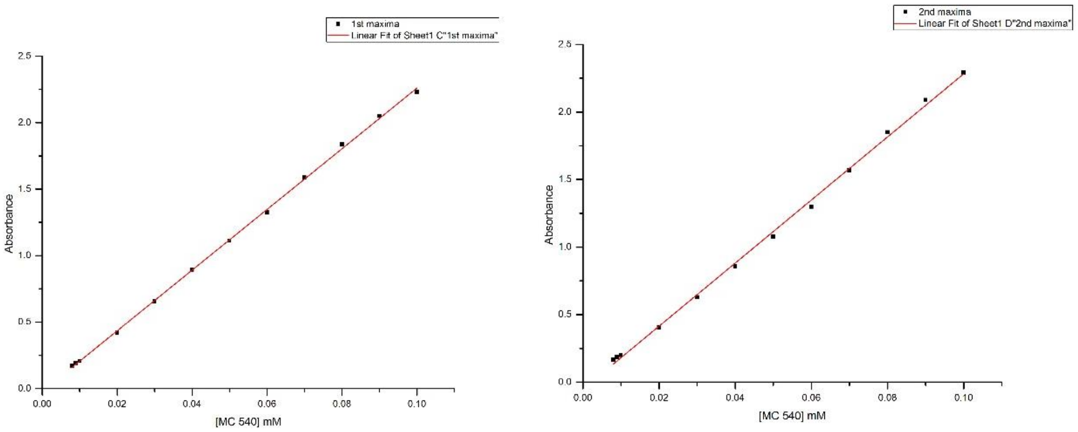

Figure 3-8: Absorption-Concentration plot for the dye MC 540 indicating a linear increasing of the absorption with increasing the dye's concentration of two different wavelengths

Analysis of the visible spectrum *via* UV-Vis absorption spectrophotometry, revealed a double peak pattern with maxima at 524 nm and 558 nm with the former diminishing in size and the latter growing in size as the concentration of SDS increased (see Figure 3-9).

The final concentration of surfactant, the absorbance of each maxima and the ratio of both maxima are shown in Table 3-4. For each concentration of surfactant, the maximum absorbance of MC 540 dimer (II) was noted and the maximum absorbance of the monomeric form (I) noted also and a graph plotted between the surfactant SDS concentration in millimoles per litre (mM) against the ratio of these absorbance values. Figure 3-10 reveals the absorption spectra of each SDS concentration in the range 1-17 mM.

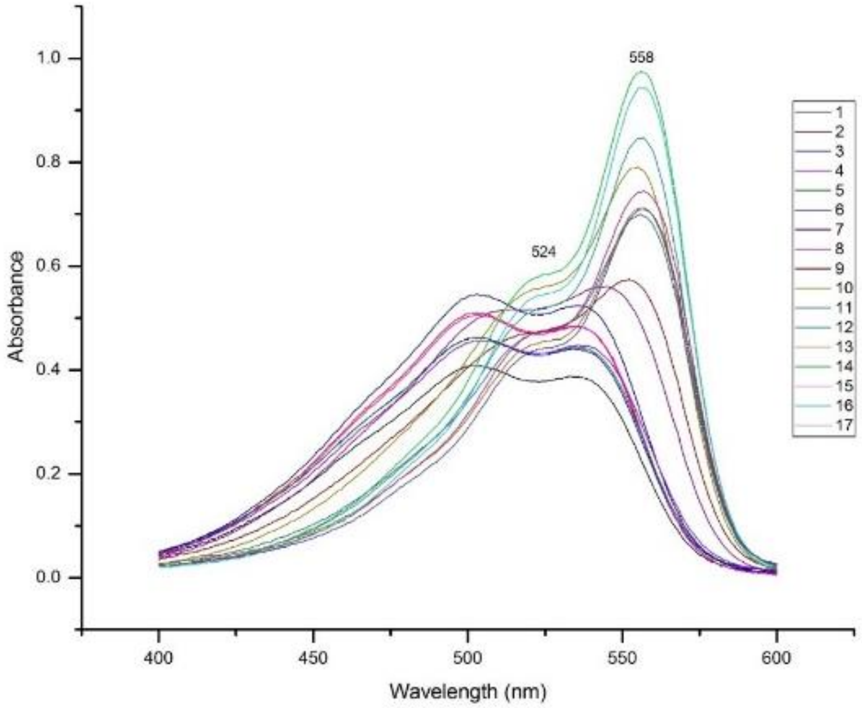

Figure 3-9: The absorption of each concentration of the surfactant SDS from 1 – 17 mM in aqueous phase using the MC540 spectrophotometric method .

Table 3-4 The absorption values of a series of different concentrations of surfactant SDS solutions at two λ_{max} in the aqueous phase. Three repetitive have been used and the average between them used in the plot.

	First run			Second run			Third run				
[SDS] mM	**Abs 524**	**Abs. 558**	**524/558**	**Abs 524**	**Abs. 558**	**524/558**	**Abs 524**	**Abs. 558**	**524/558**	**Average**	**ST. Dev**
1.0	0.387	0.408	0.948	0.445	0.468	0.950	0.391	0.411	0.952	0.950	0.002
2.0	0.485	0.510	0.951	0.417	0.437	0.954	0.496	0.520	0.954	0.953	0.002
3.0	0.439	0.462	0.951	0.489	0.512	0.955	0.430	0.451	0.953	0.953	0.002
4.0	0.483	0.506	0.955	0.412	0.431	0.955	0.477	0.498	0.958	0.956	0.002
5.0	0.444	0.462	0.962	0.498	0.518	0.963	0.444	0.462	0.961	0.962	0.001
6.0	0.524	0.546	0.960	0.455	0.472	0.964	0.501	0.518	0.966	0.963	0.003
7.0	0.448	0.457	0.980	0.513	0.523	0.981	0.437	0.445	0.980	0.981	0.001
8.0	0.561	0.518	1.083	0.476	0.444	1.072	0.554	0.512	1.081	1.079	0.006
9.0	0.574	0.475	1.208	0.649	0.520	1.248	0.518	0.406	1.275	1.243	0.034
10.0	0.790	0.560	1.412	0.633	0.468	1.354	0.559	0.379	1.478	1.415	0.062
11.0	0.700	0.473	1.480	0.823	0.516	1.594	0.658	0.436	1.509	1.528	0.059
12.0	0.846	0.519	1.632	0.687	0.448	1.534	0.807	0.490	1.646	1.604	0.061
13.0	0.712	0.454	1.567	0.872	0.514	1.696	0.687	0.440	1.561	1.608	0.076
14.0	0.974	0.583	1.671	0.696	0.439	1.585	0.856	0.501	1.707	1.654	0.062
15.0	0.742	0.473	1.568	0.950	0.551	1.726	0.674	0.417	1.615	1.637	0.081
16.0	0.944	0.544	1.736	0.749	0.471	1.593	0.895	0.508	1.761	1.696	0.091
17.0	0.709	0.440	1.610	0.957	0.544	1.759	0.735	0.457	1.609	1.659	0.086

The absorbance ratio of monomer to dimer absorbance values increase with increasing the surfactant concentration due to the solvatochromic[120] and the CMC point is estimated to be at the inflection point shown in Figure 3-10.

The rate of increasing of peak ratio accelerated around the inflection point and the CMC value of the surfactant SDS is estimated from the graph at 10.8 ±0.6 mM.

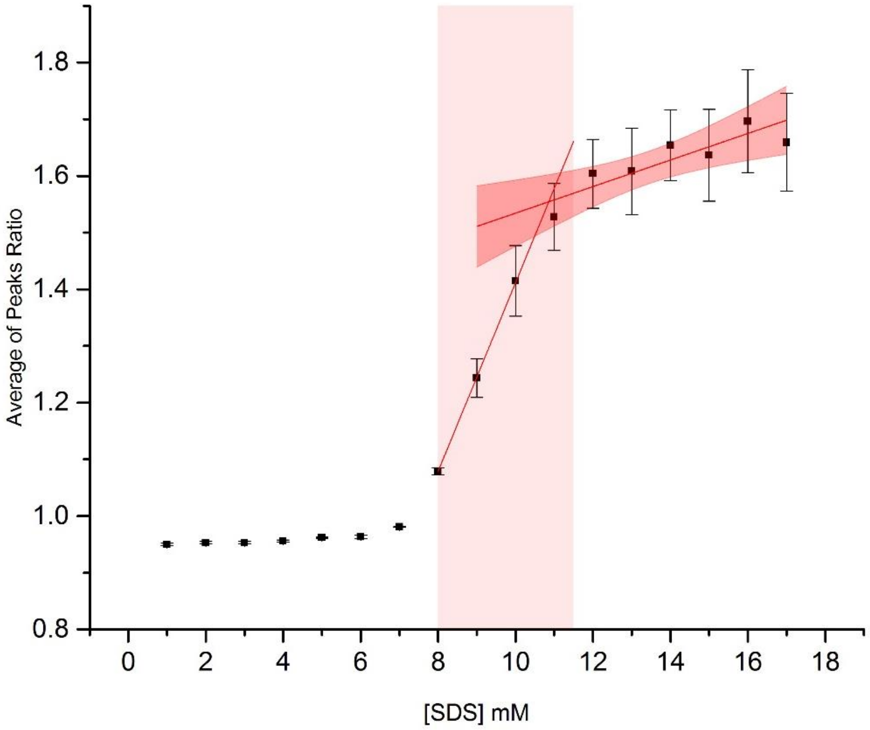

Figure 3-10: Plotted graph between the SDS concentration (mM) and the ratio between the absorbance of monomeric to dimeric values in aqueous phase by using MC 540 as UV-Vis dye detector

3.2.4.2 Pinacyanol chloride method

Pinacyanol chloride (1,1′-diethyl-2,2′-carbocyanine chloride, 2,2′-trimethinequinocyanine chloride, Quinaldine blue), abbreviated as PC is a cationic dye which is part of conjugated cyanine dyes. It has the formula $C_{25}H_{25}ClN_2$. and Figure 3-11 shows it's structure.

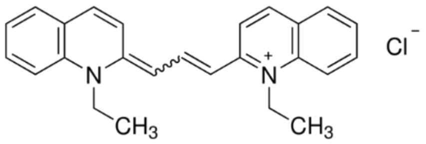

Figure 3-11: The chemical structure of pinacyanol chloride

The amphipathic nature of PC confers solubility in a wide range of solvents, including water, ethanol and chloroform. Due to a high polarization of the chromophoric chain, PC has the ability to self-aggregate and this is a common phenomenon in the aqueous solution of cyanine dyes[121]. Water has a high dielectric constant which facilitates the formation of aggregates by decreasing the electrostatic repulsion between the cationic dye molecules[121].

Cyanine dyes of the type which PC belongs to, have deep colours and are frequently used as reporter dyes in a range of spectroscopic methods[121].

To estimate the CMC value of the surfactant SDS, a method has been suggested by T. Namani and P. Walde[122] in which a series of different concentrations of SDS were prepared in test tubes and mixed with an ethanolic solution of a blue dye PC, resulting the dye concentration in each tube being 1×10^{-5} M. Figure 3-12 shows the absorption in the visible region of PC in the presence of SDS at a range of concentrations of series of SDS concentrations. Experiments were performed in triplicate.

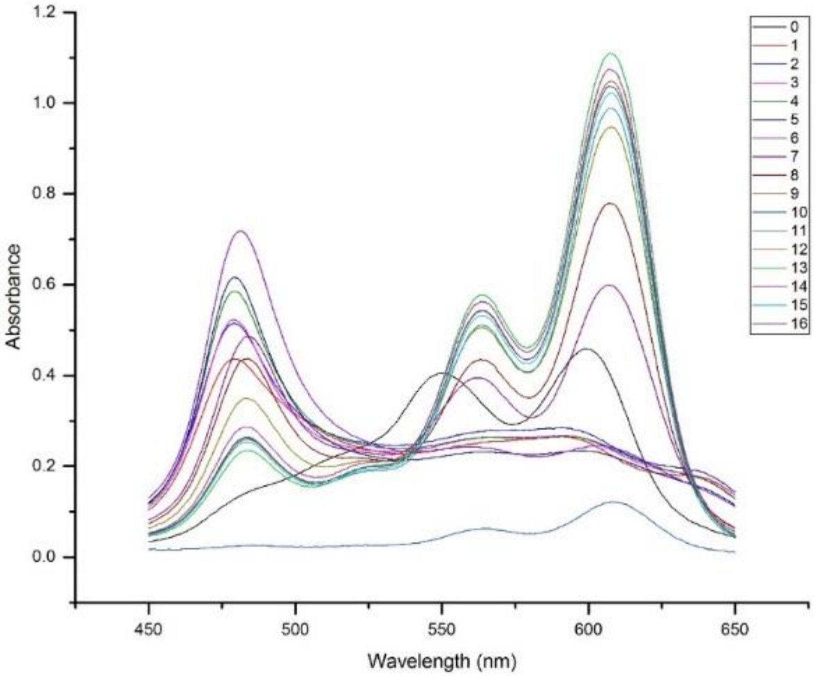

Figure 3-12: The absorption of each concentration of the surfactant SDS from 1 – 16 mM in aqueous phase using the PC spectrophotometric method.

This method consists of plotting the concentration of SDS in mM against the absorption maximum at 608 nm. The final concentration of surfactant, the absorbance of 608 nm maxima, the average of the three repeat runs and the error (standard deviation of sample) are shown in Table 3-5. For each concentration of surfactant, the maximum absorbance of PC was noted and a graph plotted between the surfactant SDS concentration in millimoles per litre (mM) against the absorbance values. Figure 3-13 reveals the absorption spectra of each SDS concentration in the range 1-16 mM. The rate of increasing of peaks absorbance accelerated around the inflection point and the CMC value of the surfactant SDS is estimated from the graph at 7.8 ± 0.4 mM and the value which have been reported in previous study equals to 8.0 mM[121].

Table 3-5: The absorption values of a series of different concentrations of surfactant SDS solutions at 605 nm in the aqueous phase. Three repetitive have been used and the average between them used in the plot.

[SDS]mM	1st run	2nd run	3rd run	Average	St. Dev.
0	0.430	0.002	-	0.216	0.303
1	0.236	0.220	0.250	0.235	0.015
2	0.256	0.232	0.260	0.250	0.015
3	0.244	0.218	0.265	0.242	0.023
4	0.247	0.239	0.255	0.247	0.008
5	0.228	0.214	0.263	0.235	0.025
6	0.244	0.239	0.178	0.221	0.037
7	0.594	0.584	0.587	0.588	0.005
8	0.771	0.954	0.850	0.858	0.092
9	0.934	0.916	1.052	0.967	0.074
10	1.105	0.962	1.105	1.058	0.083
11	0.974	1.006	0.953	0.977	0.026
12	1.033	0.993	1.078	1.035	0.043
13	1.096	1.079	1.052	1.076	0.022
14	1.060	1.126	1.121	1.102	0.036
15	1.005	1.144	1.150	1.100	0.082
16	1.022	1.054	1.175	1.084	0.081

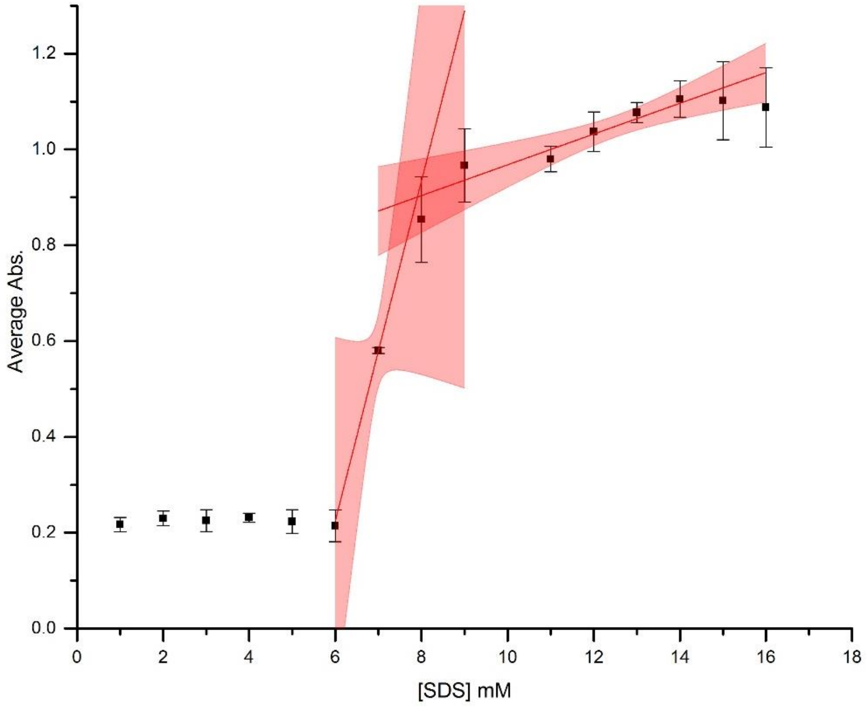

Figure 3-13: Plotted graph between the SDS concentration (mM) and the absorbance at 506 nm in aqueous phase by using PC as UV-Vis dye detector

In summary, the measurement of CMC values for SDS has been examined in the aqueous phase using several different methods. The results obtained indicate that CMC measurements are dependent to some extent on the measurement method used as shown in Table 3-6 which shows these differences. Of the techniques used in aqueous solution, we have selected to use visible spectrophotometry in the SHG phase.

Table 3-6: Summery of CMC values of SDS depending on the method and probe used.

Method	**Probe**	**CMC (mM)**
UV-vis	Merocyanine 540	7.3 ±0.1
UV-vis	Pinacyanol Chloride	7.8 ± 0.4
Florescence	Pyrene	6.0
Conductivity	NaOH	7.9
Tensiometry	--	6.1

3.3 Measurements of Critical Micelle Concentrations (CMC) of SDS in Silica Hydrogel (SHG) Environments

From the possible analytical tools for CMC measurement in an aqueous environment, we have selected spectrophotometry as the most likely to be compatible and applicable with a SHG media. The conductivity method involves continuous addition of sodium hydroxide which is not applicable when exploring the gel phase as it results in the gel environment being changed. The similar issue arises with tensiometry as explained in 3.2.1 where the flow of a gel phase being so different to that of an aqueous solution would likely influence the results of such experiments. Fluorescence spectroscopy using pyrene returns only poor data so we have not pursued this any further. Thus we embarked on a series of UV-Vis spectroscopic experiments to measure the CMC of sodium dodecylsulfate in the silica hydrogel phase .

3.3.1 Merocyanine 540 as reporter dye

In order to measure the CMC of the surfactant SDS in a silica hydrogel phase created from a sodium silicate solution, the same procedure was employed as that used in the aqueous phase. Once again, the novelty of these experiments is that the CMC of an amphiphile within a silica hydrogel, related to an early earth geological environment, has not previously been examined. However, the hydrogel phase has such potential significance within the context of life emergence that we have engaged with that here[7].

3.3.1.1 Measurement of SDS CMC within a 0.5 M SHG

A series of concentrations of the surfactant SDS was prepared directly in disposable cuvettes with the final concentration of SDS shown in Table 3-7. To each cuvette was also added a mixture of 0.5 M of sodium silicate solution, acid solution (i.e: Barge method of production of SHG) and an ethanolic solution of red dye MC540 to afford a final concentration of merocyanine of

1×10^{-5} M. The systems were allowed to gel for 24 hrs prior to analyses so that we could ensure we were operating under the SHG environment.

The samples show a similar overall peak shape to that in an aqueous environment with a slight change in the dimer peak maximum from 558 (±2) nm to 560 (±2) nm (Figure 3-14)

Table 3-7: The absorption values of a series of different concentrations of surfactant SDS solutions at two λ_{max} (524, 560 nm) in 0.5M silica hydrogel phase.

	First run			second run			Third run				
[SDS] mM	524 nm	560 nm	560/524	524 nm	560 nm	560/524	524 nm	560 nm	560/524	Average	St. Div.s
0.5	0.271	0.231	0.850	0.244	0.218	0.894	0.278	0.273	0.981	0.908	0.067
0.75	0.292	0.420	1.440	0.297	0.383	1.292	0.362	0.586	1.620	1.451	0.164
1	0.353	0.705	1.997	0.365	0.747	2.048	0.372	0.772	2.077	2.041	0.040
1.5	0.382	0.923	2.417	0.389	0.942	2.420	0.447	0.961	2.147	2.328	0.156
2	0.301	0.887	2.949	0.383	0.992	2.590	0.402	0.953	2.371	2.637	0.292
3	0.398	1.055	2.650	0.391	1.048	2.682	0.412	1.002	2.433	2.589	0.135
5	0.378	1.056	2.795	0.399	1.095	2.747	0.423	1.018	2.408	2.650	0.211
7	0.407	1.107	2.720	0.387	1.094	2.825	0.403	1.025	2.544	2.696	0.142
8	0.409	1.114	2.726	0.391	1.110	2.839	0.401	1.008	2.515	2.693	0.164
9	0.444	1.161	2.614	0.401	1.111	2.769	0.387	0.987	2.551	2.645	0.112
10	0.409	1.115	2.729	0.321	1.064	3.313	0.400	1.019	2.545	2.862	0.401
12	0.388	1.088	2.804	0.393	1.118	2.847	0.393	1.007	2.561	2.738	0.154
15	0.403	1.124	2.789	0.384	1.101	2.871	0.385	0.993	2.579	2.746	0.151
18	0.408	1.133	2.775	0.382	1.105	2.890	0.840	1.317	1.568	2.411	0.732
21	0.394	1.123	2.849	0.419	1.155	2.757	0.399	1.021	2.559	2.722	0.148

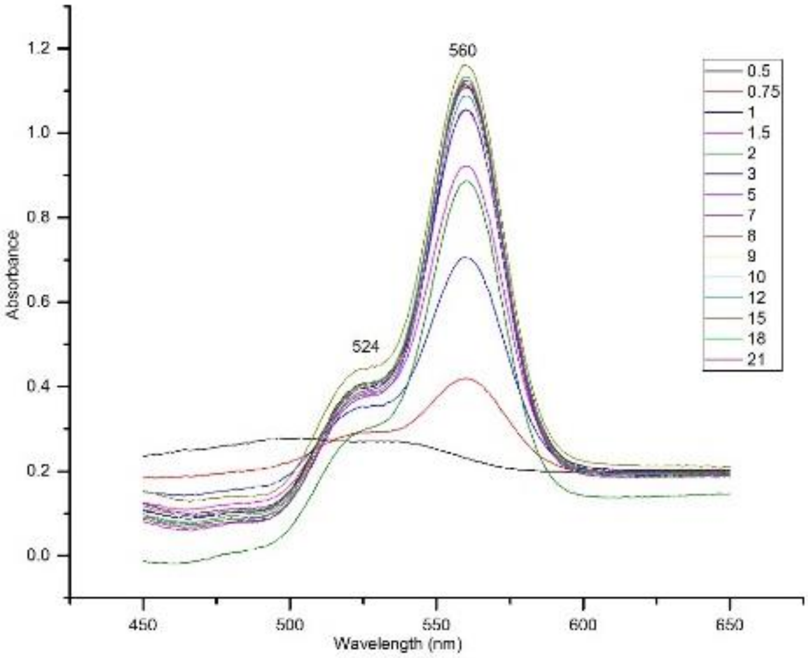

Figure 3-14: The absorption of each concentration of the surfactant SDS from 0.5 – 21 mM within 0.5M SHG phase using the MC540 spectrophotometric method for the first measurements. The reaming two are listed in the appendix as (Figure 7-5 and Figure 7-6)

The absorbance ratio of monomer to dimer values decrease with increasing surfactant concentration due to the solvatochromic shift and the CMC point is estimated to be at the inflection point shown in Figure 3-15. The rate of increase accelerated at the inflection point and the CMC value of the surfactant SDS is estimated to be 1.3 ± 0.7 mM

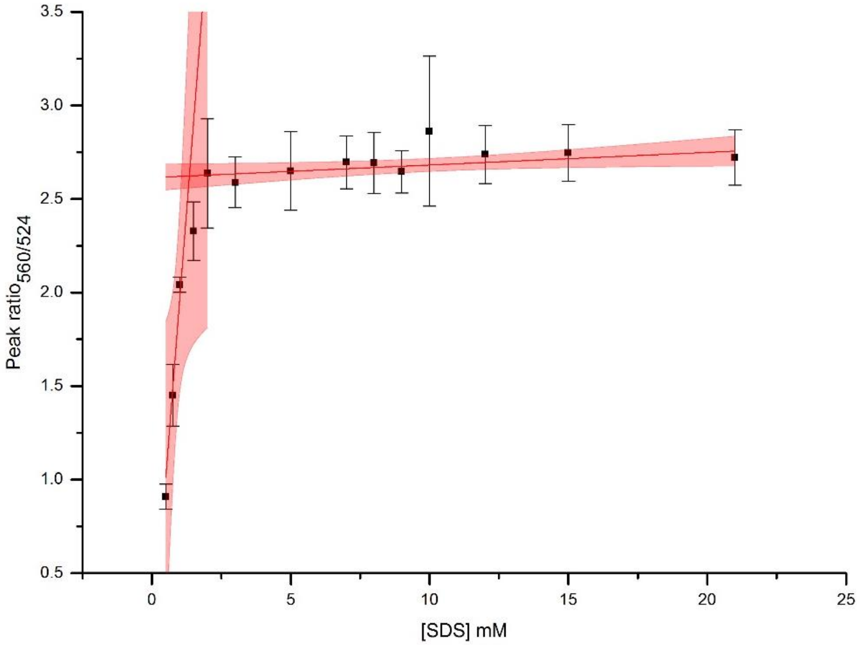

Figure 3-15: Graph of SDS concentration (mM) and absorbance ratio between monomeric and dimeric merocyanine 540 in 0.5 M silica hydrogel phase. The inflection point indicates the CMC point of the surfactant in SHG.

Regarding the graph represented in Figure 3-15, there are a few points which need to be clarified and discussed. In the aqueous phase, there are three regions in the CMC curve: (i) below the CMC, (ii) between the on-set and (iii) equilibrium point and everything after that point. It is important to emphasise that the data we are reporting is absorbance data on the reporter dye which tells us about its self-assembly state. Essentially, PC exists principally as a monomer when it becomes incorporated into a micelle structure and so the 608 nm band associated with that form becomes dominant. This in turn is sensitive to the degree of micellation.

Below the CMC region represents that environment whereby the surfactant molecules are at low concentration, associated mainly at the air-water boundary (see Figure 1-9) in the solution and do not engage in self-assembly. As the surfactant concentration increases the molecules start to aggregate and micelle formation begins; this is effectively the onset point of micelle formation. The last region represents the phase where micelle formation is essentially complete and what we are observing here is a plateau or equilibrium point for the concentration of monomeric form of pinacyanol chloride

These three regions are clearly visible in the aqueous environment graph as shown in Figure 3-10 (or lower and upper inflection points), but within the SHG's media, we visualize two of them only, the onset point is not clearly defined. Now this could of course be due to the fact that onset is taking place at such low concentrations, lower than we have examined here. This means that what we have done in our investigations is to explore the change in the equilibrium transition point (iii) and compare that between aqueous and SHG phases.

It is probable that this change in transition behaviour is linked to the salt content of the SHG's as in related experiments performed in aqueous salt solution by another member of the Kee group, as similar observation is made that the onset transition point apparently vanishes at higher salt concentrations (see section 3.4.2)

3.3.1.2 CMC of SDS in 0.6 M SHG

When a higher concentration of silicate solution is used to prepare the SHG (0.6 M silicate), the corresponding measurements lead to an even more reduced CMC value. Table 3-8 show the data used to plot Figure 3-16). The overall shape of the MC540 peaks within 0.6 M SHG have a similar peak maxima. Figure 3-17, shows the raw absorption data which have been used in Table 3-8 to estimate the CMC point at 1.1 ± 0.2 mM.

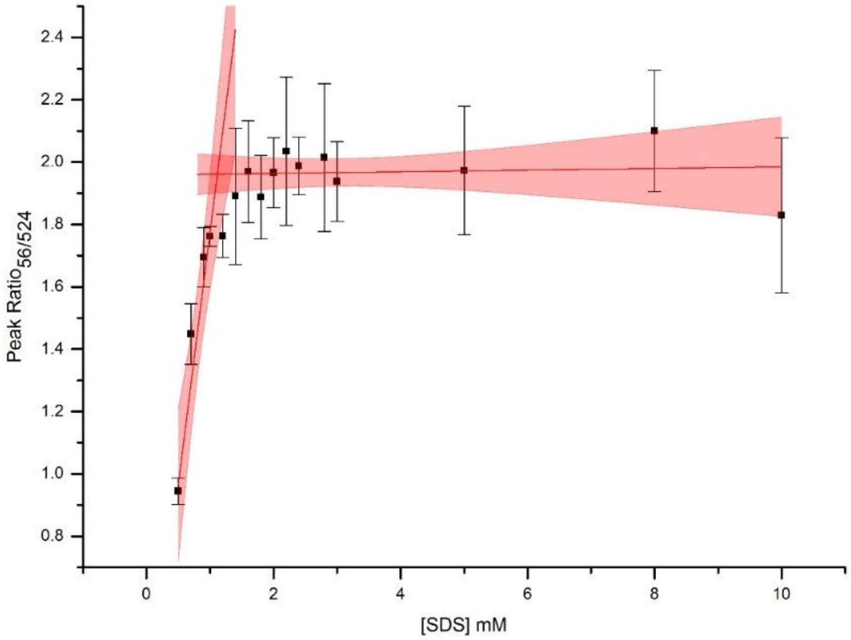

Figure 3-16: Graph of SDS concentration (mM) and absorbance ratio between monomeric and dimeric merocyanine 540 in 0.6 M silica hydrogel phase. The inflection point indicates the CMC point of the surfactant in SHG.

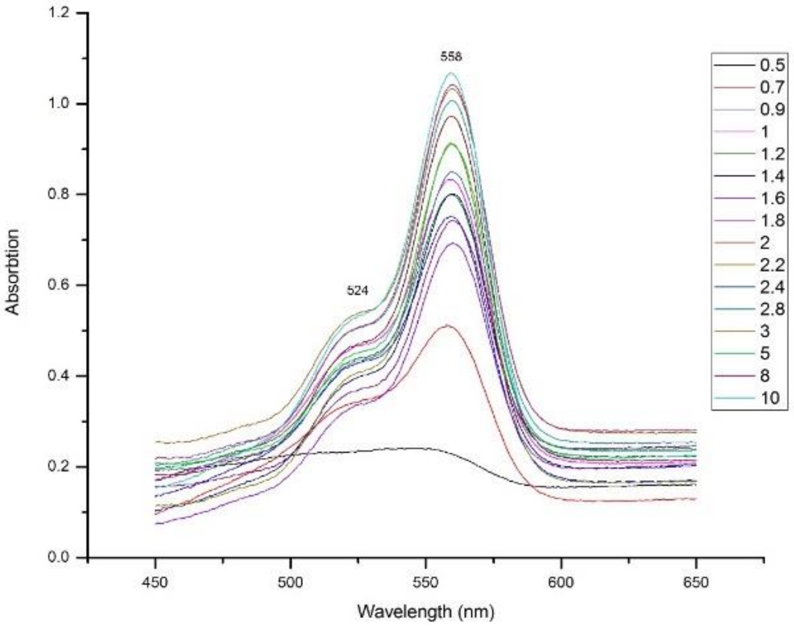

Figure 3-17: The absorption of each concentration of the surfactant SDS from 0.5 – 10 mM within 0.6M SHG phase using the MC540 spectrophotometric method.

Table 3-8: The absorption values of a series of different concentrations of surfactant SDS solutions at two λ_{max} (524, 560 nm) in 0.6 M silica hydrogel phase.

	First run			second run			Third run				
[SDS] mM	**524 nm**	**560 nm**	**560/524**	**524 nm**	**560 nm**	**560/524**	**524 nm**	**560 nm**	**560/524**	**Average**	**St. Div**
0.5	0.233	0.236	0.990	0.216	0.230	0.937	0.351	0.387	0.905	0.944	0.043
0.7	0.513	0.343	1.496	0.517	0.342	1.513	0.724	0.542	1.336	1.448	0.098
0.9	0.751	0.429	1.752	0.724	0.414	1.749	0.789	0.498	1.585	1.695	0.096
1.0	0.833	0.468	1.781	0.881	0.495	1.780	0.810	0.470	1.725	1.762	0.032
1.2	0.799	0.440	1.818	0.873	0.489	1.785	0.958	0.568	1.686	1.763	0.069
1.4	0.801	0.398	2.013	0.875	0.433	2.020	1.017	0.621	1.639	1.891	0.218
1.6	0.694	0.336	2.062	0.733	0.355	2.066	0.935	0.525	1.780	1.969	0.164
1.8	0.743	0.368	2.018	1.007	0.531	1.896	1.127	0.644	1.750	1.888	0.134
2.0	0.972	0.471	2.063	0.961	0.522	1.843	1.076	0.540	1.993	1.966	0.112
2.2	0.914	0.409	2.235	0.906	0.432	2.098	1.090	0.615	1.772	2.035	0.238
2.4	0.850	0.434	1.958	0.856	0.409	2.092	0.895	0.468	1.913	1.988	0.093
2.8	1.006	0.505	1.992	0.746	0.330	2.262	1.097	0.613	1.790	2.015	0.237
3.0	1.033	0.539	1.918	0.863	0.416	2.075	0.948	0.520	1.821	1.938	0.128
5.0	0.910	0.451	2.017	0.963	0.551	1.748	0.985	0.457	2.153	1.973	0.206
8.0	1.042	0.508	2.052	0.816	0.353	2.314	1.095	0.566	1.933	2.100	0.194
10.0	1.067	0.532	2.005	-	-	-	1.089	0.658	1.654	1.829	0.249

3.3.1.3 CMC of SDS in 0.7 M SHG

Moving to a higher initial silicate concentration of 0.7 M produced a more erratic data set (Table 3-9 and Figure 3-18). It was observed that this system appeared to gel very quickly (within a six hours at ambient temperature for a 0.5 M silicate solution to less than ten minutes for (0.6 and 0.7) M to less than 30 seconds 1.0 M silicate respectively (*vide infra*); however see Chapters 2 & 4 for a more detailed discussion of gelation times. Moreover, an unexpected observation was made at these higher concentration silicate systems. It was noticed that the cuvettes which contains SDS, SHG and merocyanine began to decolourise once the system had gelled, so that with the 1.0 M silicate system, all colour of the merocyanine was lost within a few hours of sample preparation. This intriguing observation has been the subject of a more detailed investigation (sees Chapter 5 of this report).

Again the overall shape of (Figure 3-18) of the peaks look similar to absorption within the aqueous and lower concentrations of SHG with two clearly observable maxima at 560 and 524 nm (the latter of which changes to become more of a shoulder on the side of the 560 nm band) and the ratio between these two value are plotted against concentration of SDS to estimate the CMC value as 1.1 ± 0.4 mM (Figure 3-19).

Table 3-9: The absorption values of a series of different concentrations of surfactant SDS solutions at two λ_{max} (524, 560 nm) in 0.7 M silica hydrogel phase

	First run			Second run			Third run				
[SDS] mM	560 nm	524 nm	560/524	560 nm	524 nm	560/524	560 nm	524 nm	560/524	Average	St. Div.s
0.5	0.29572	0.17041	1.73537	0.27340	0.18988	1.43988	0.27434	0.15064	1.82115	1.66547	0.20001
0.7	0.81344	0.39921	2.03760	0.68859	0.29728	2.31626	0.70398	0.31023	2.26921	2.20769	0.14916
0.9	0.89448	0.35749	2.50209	0.94982	0.43046	2.20649	0.90235	0.38666	2.33367	2.34742	0.14827
1.2	0.97066	0.39892	2.43317	0.84954	0.27874	3.04771	1.00004	0.39223	2.54960	2.67683	0.32642
1.4	1.25983	0.74072	1.70080	0.75258	0.13438	5.60026	1.11414	0.46959	2.37259	3.22455	2.08466
1.6	0.86772	0.22761	3.81235	0.92371	0.29690	3.11112	1.16675	0.48442	2.40851	3.11066	0.70191
1.8	1.02321	0.37858	2.70271	1.09575	0.41026	2.67081	1.28848	0.59640	2.16042	2.51131	0.30430
2	0.91128	0.35907	2.53788	0.52850	0.11866	4.45358	1.06086	0.39150	2.70973	3.23373	1.05990
2.4	1.01555	0.29772	3.41100	1.11475	0.39808	2.80027	1.04806	0.38713	2.70724	2.97284	0.38230
2.8	1.06420	0.32963	3.22844	1.13405	0.45576	2.48825	1.01109	0.32010	3.15859	2.95842	0.40868
3	1.09696	0.37766	2.90460	1.16687	0.47126	2.47604	1.08438	0.36287	2.98833	2.78966	0.27480
5	1.15678	0.34964	3.30845	1.15295	0.42997	2.68145	1.08698	0.34278	3.17104	3.05365	0.32957
7	1.32231	0.54159	2.44150	1.02272	0.37392	2.73507	1.21245	0.49901	2.42970	2.53542	0.17299
10	1.05636	0.33527	3.15078	1.13443	0.37778	3.00286	1.13050	0.39336	2.87392	3.00919	0.13853

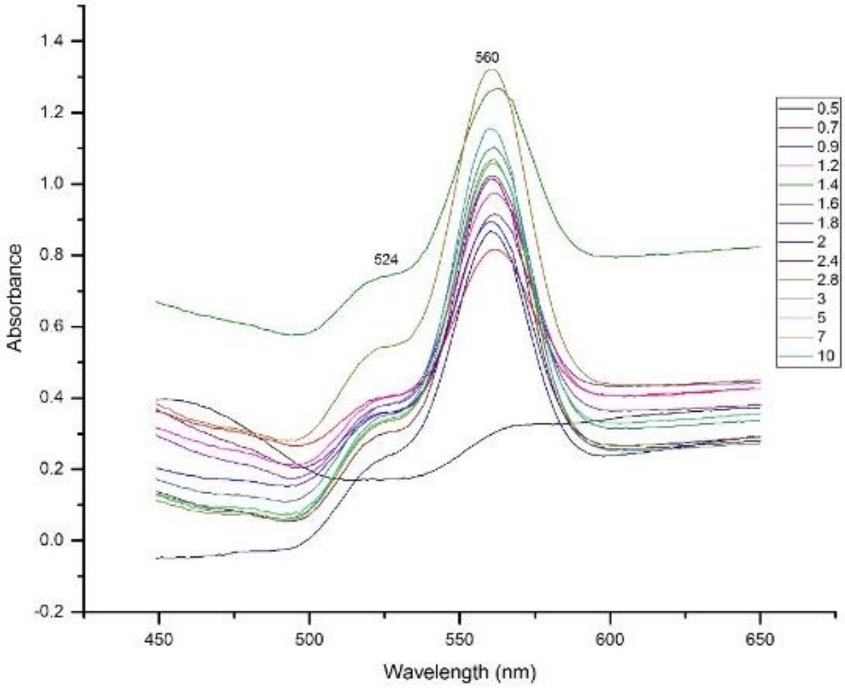

Figure 3-18: The absorption of each concentration of the surfactant SDS from 0.5 – 10 mM within 0.7 M SHG phase using the MC540 spectrophotometric method.

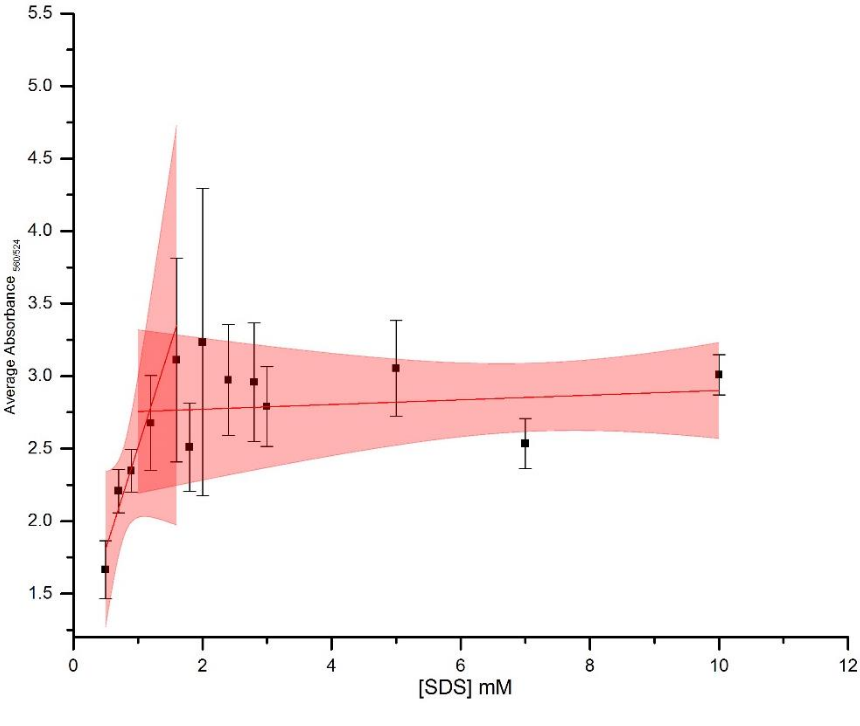

Figure 3-19: Graph of SDS concentration (mM) and absorbance ratio between monomeric and dimeric merocyanine 540 in 0.7 M silica hydrogel phase. The inflection point indicates the CMC point of the surfactant in SHG.

3.3.2 Pinacyanol Chloride as reporter dye

Whilst the decolourisation of merocyanine in our higher concentration silicate hydrogel systems will be discussed later (Chapter 4), we decided to explore a different reporter dye in the anticipation that such colour changes would not occur. PC was selected as a new reporter dye. As outlined in section 3.2.4.2, PC has self-assembly behaviour that allows us to monitor dimer vs monomer formation on the basis of their differential visible absorption behaviour. Thus, PC has been used as a reporter dye to measure CMCs on the basis that monomer formation and concomitant absorption near 608 nm is favoured when pinacyanol becomes incorporated within a micellar structure.

3.3.2.1 At 0.5 M SHG

A concentration series of the surfactant SDS was prepared directly in disposable cuvettes with the final concentration of SDS shown in Table 3-10. To each cuvette was also added a mixture of 0.5 M of sodium silicate solution, acid solution (i.e: Barge method of production of SHG) and an ethanolic solution of blue dye PC to afford a final concentration of PC of 1 x 10^{-5} M. The systems were allowed to gel for 24 hrs prior to any analysis being performed so that we could ensure we were operating under the SHG environment.

Results from Table 3-10 shows an absorption values above one absorption unit which indicated as a high PC concentration, to solve this issue, the concentration of PC was decreased from 1 x 10^{-5} M to 5 x 10^{-6} M (Table 3-11).

Table 3-10: The absorption values of a series of different concentrations of surfactant SDS solutions at 608 in 0.5 M silica hydrogel phase with 1x10^{-5} M PC.

[SDS] mM	1st 608nm	2nd 608nm	3rd 608nm	Average	St.Div
0.5	0.155385	0.366891	0.336397	0.286224	0.093351
0.8	0.381156	0.492453	0.517931	0.463846	0.059389
1	0.642463	0.828256	0.820785	0.763835	0.085877
1.5	0.808543	1.046614	0.96275	0.939303	0.098596
2	0.762091	1.067113	1.034832	0.954678	0.136816
2.5	0.893455	1.035747	1.114704	1.014635	0.09155
3	0.777867	1.07359	1.143368	0.998275	0.158434

5	0.72482	1.011192	0.958364	0.898125	0.124429
8	0.670271	1.11692	1.086958	0.958049	0.203858
12	0.704511	1.432726	1.280639	1.139292	0.313644
15	0.798569	1.11014	1.203836	1.037515	0.173236
18	0.729607	1.487926	1.216276	1.144603	0.313703

Table 3-11: The absorption values of a series of different concentrations of surfactant SDS solutions at 608 in 0.5 M silica hydrogel phase with 5x10^{-6} M PC.

[SDS] mM	1st 608nm	2nd 608nm	3rd 608nm	Average	St.Div
0.5	0.254059	0.19549	0.259404	0.236317	0.035459
0.8	0.331069	0.491465	0.420377	0.414304	0.08037
1	0.598571	0.628803	0.674203	0.633859	0.038069
1.5	0.747151	0.802123	0.717368	0.755547	0.042997
2	0.809138	0.816909	0.808896	0.811647	0.004558
3	0.928428	0.880902	0.855889	0.888406	0.036847
4	0.869745	0.827258	0.839076	0.84536	0.02193
5	0.821839	0.850902	0.84614	0.839627	0.015588
6	0.932139	0.879259	0.968829	0.926742	0.045028
7	0.937482	0.978935	0.96519	0.960536	0.021115
8	1.01833	0.973491	0.975634	0.989152	0.025292
10	0.910873	1.020088	1.063559	0.998173	0.078667
13	0.898319	1.028298	1.007781	0.978133	0.069878
17	0.916971	1.06484	1.050973	1.010928	0.081664

The samples show a similar overall peaks shape as compared with the one in aqueous environment with slightly change from the aqueous phase of the interested peak from 605 nm to 608 nm see Figure 3-20 for one representative run of the absorption of each concentration of the surfactant SDS from 0.5 – 17 mM in SHG phase using PC spectrophotometric method. Figure 3-20 is the raw data acquired from the instrument and one can see the required to re-plot after applying background correction to ascertain the results as shown in Figure 3-21.

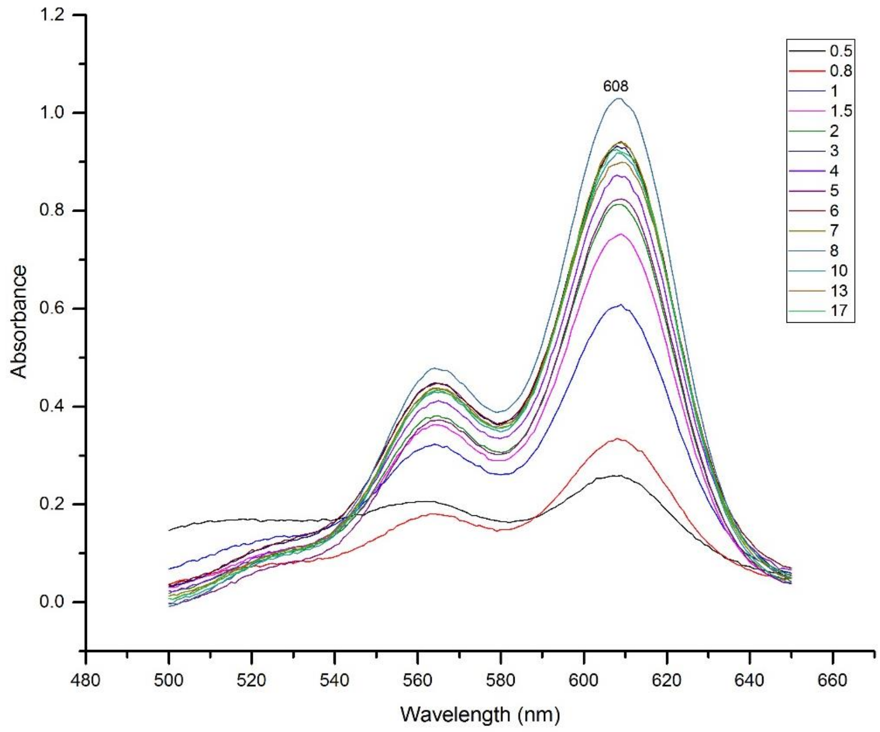

Figure 3-20: The absorption of each concentration of the surfactant SDS from 0.5 – 17 mM within SHG phase using 5x10^{-6} of PC spectrophotometric method for the first measurements.

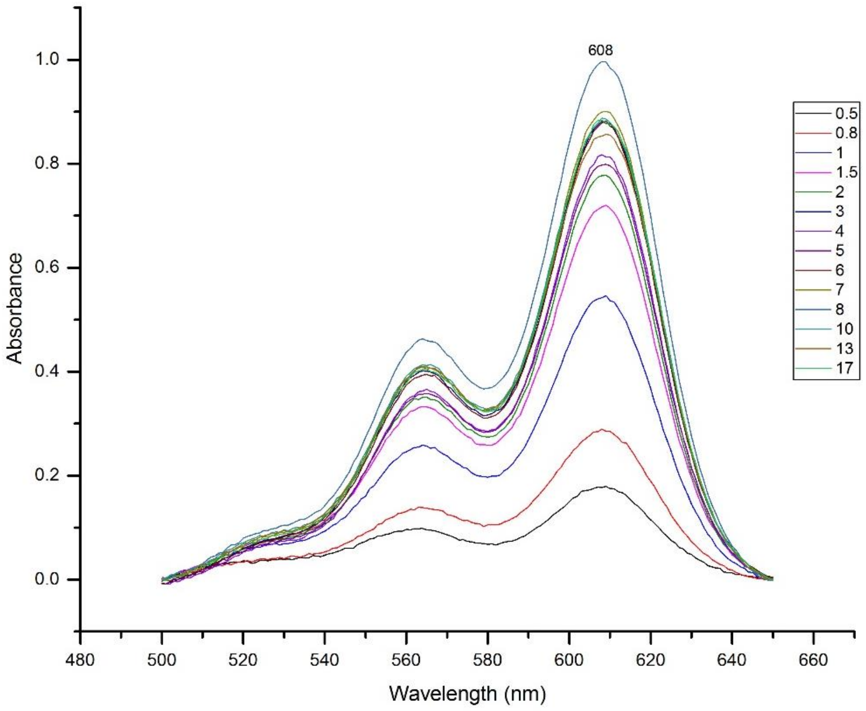

Figure 3-21: The absorption data plot from Figure 3-20 after applying background correction by OriginPro software. Note the start point and the end point of each scan.

To estimate the CMC value of the surfactant SDS, a method have been suggested by T. Namani and P. Walde[122] in which a series of different concentrations of SDS were prepared in disposable cuvettes and mixed with an ethanolic solution of a blue dye PC, resulting the dye concentration in each cuvette is equal to 5x10^{-6} M. Figure 3-23 shows the absorption in the visible region of a series of SDS concentration of three repeats, CMC value estimated as 1.4 ± 0.4 mM

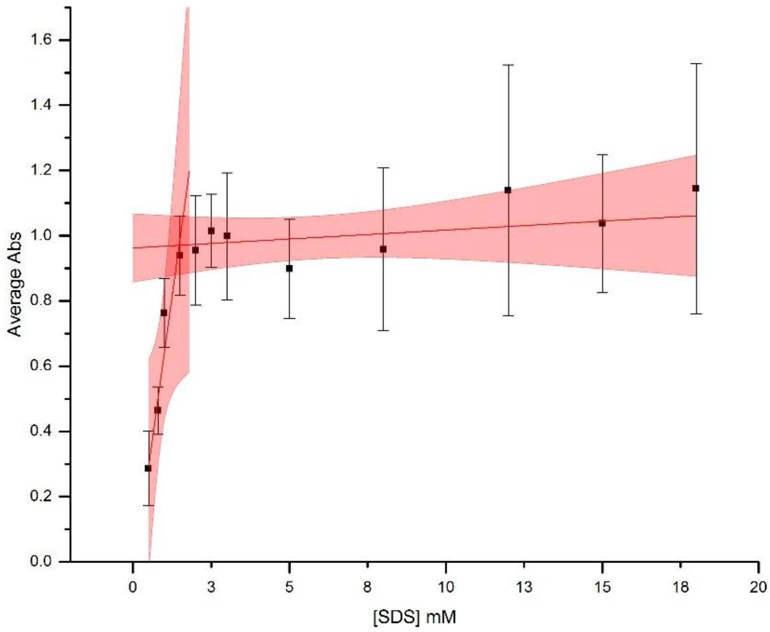

Figure 3-22: Plotted graphs between the SDS concentration (mM) and the absorbance at 608 nm values in 0.5 M silica hydrogel phase using 1x10^{-5} M PC dye indicator. The inflection point refers to the CMC point of the surfactant in SHG.

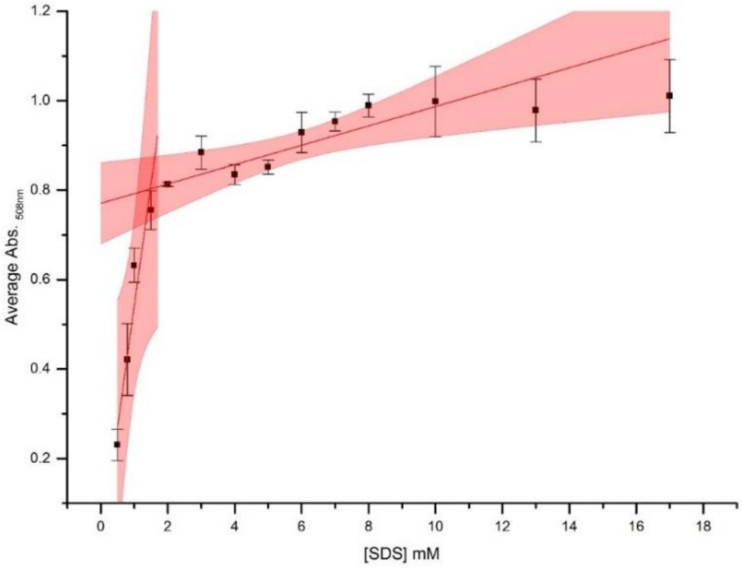

Figure 3-23: Plotted graphs between the SDS concentration (mM) and the absorbance at 608 nm values in 0.5 M silica hydrogel phase using 5x10^{-6} M PC dye indicator. The inflection point refers to the CMC point of the surfactant in SHG.

As noted above, the position of the maxima wavelength shifted from 605 ± 2 nm within aqueous phase to 608 ±2 nm within the SHG phase and as the original method used the wavelength at 605 ± 2 nm, a decision made to plot the data from absorption sheet for absorption at 605 nm to make sure that the CMC was not affected.

Table 3-12 shows the data collected of Figure 3-20 in which the absorption at 506 nm used to plot Figure 3-24 of the CMC estimation point.

From Figure 3-24 one can estimate the CMC at the upper inflection point at 1.4 ± 0.5 mM which is similar to what we find earlier and that’s why we used the absorption at 608 ± 2 nm in the coming data.

Table 3-12: The absorption values of a series of different concentrations of surfactant SDS solutions at 605 in 0.5 M silica hydrogel phase with 5x10^{-6} M PC.

[SDS] mM	1st	2nd	3rd	Average	St.Div
0.5	0.254683	0.196272	0.259702	0.236886	0.035262
0.8	0.32236	0.482384	0.412486	0.405743	0.080225
1	0.590636	0.614077	0.660004	0.621572	0.035286
1.5	0.727564	0.781391	0.695669	0.734875	0.043326
2	0.790088	0.793553	0.78301	0.788884	0.005373

3	0.905509	0.855389	0.829145	0.863348	0.038799
4	0.846114	0.801538	0.814149	0.8206	0.022977
5	0.79957	0.822952	0.821177	0.814566	0.013018
6	0.905707	0.851094	0.938072	0.898291	0.04396
7	0.911303	0.947305	0.934032	0.93088	0.018207
8	1.000481	0.939852	0.942758	0.96103	0.034196
10	0.887416	0.988447	1.031103	0.968989	0.073793
13	0.870658	0.99147	0.977899	0.946676	0.066182
17	0.893984	1.032275	1.017275	0.981178	0.075884

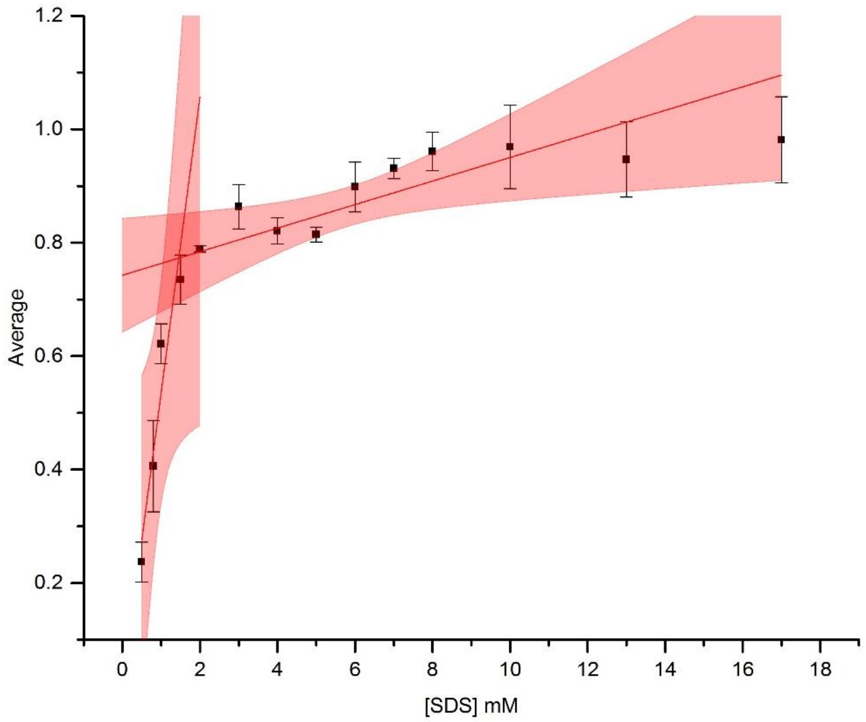

Figure 3-24: Plotted graphs between the SDS concentration (mM) and the absorbance at 605 nm values in 0.5 M silica hydrogel phase by using PC dye indicator. The inflection point refers to the CMC point of the surfactant in SHG.

Subsequently, we elected to operate at a PC concentration of 5 x 10^{-5} M and to examine the self-assembly of SDS in SHG's containing greater quantities of silicate. Thus, we have used the same experimental method as that described above in 3.3.2.1 with SHG's at 0.6 – 1.0 M silica. With SDS, the same method have been used as follows: a concentration's series of the surfactant SDS was prepared directly in disposable cuvettes with the final concentration of SDS shown in Table 3-13; Table 3-14; Table 3-15; Table 3-16 and Table 3-17 for concentrations of 0.6; 0.7; 0.8; 0.9 and 1.0 M respectively. To each cuvette was also added a mixture of sodium silicate solution, acid solution (i.e: Barge method of production of SHG) and an ethanolic solution of blue dye PC to afford a final concentration of PC of 5x10^{-6} M for 0.6 and 0.7 M SHG while using 1x10^{-5} M for the other SHG concentrations. The systems were allowed to gel for 24 hrs prior to any analyses being performed so that we could ensure we were operating under the SHG environment.

The overall shape of the absorption peaks of PC within SHG environment remain the same as comparing with aqueous environment with only peak's maxima has shifted from 605nm(±2) to 608nm(±2) as shown in Figure 3-25; Figure 3-27; Figure 3-29; Figure 3-31 and Figure 3-33 for concentrations of 0.6; 0.7; 0.8; 0.9 and 1.0 M respectively of SHG.

3.3.2.2 At 0.6 M SHG

To estimate the CMC value of the surfactant SDS in more the concentrated SHG's, the T. Namani and P. Walde[122] method was again used although care needed to be taken this time over both the rapidity of component addition in that the more silicate-rich gels gelled faster and over precipitation and associated lack of optical clarity in the resultant gels. Data were collected in the same manner, in triplicate, as those described above for the 0.5 M gels (section 3.3.2.1). For these studies, the dye PC was used in cases of SHG's concentration (0.6 and 0.7) M at a concentration of 5x10^{-6} M, and the reaming measurements at a concentration of 5x10^{-5} M due to low absorption values and optical clarity issue. The acquired data are reproduced in Table 3-13, Table 3-14, Table 3-15, Table 3-16 and Table 3-17 and the plotted graphs of absorbance vs [SDS] are found in Figure 3-26, Figure 3-28, Figure 3-30, Figure 3-32 and Figure 3-34.

Table 3-13: The absorption values of a series of different concentrations of surfactant SDS solutions at λ_{max} 608 in 0.6 M silica hydrogel phase with 5x10^{-6} M PC.

[SDS] mM	1st 608nm	2nd 608nm	3rd 608nm	Average	St.Div
0.5	0.567156	0.398585	0.478456	0.481399	0.084324
0.7	0.606217	0.67918	0.722572	0.669323	0.0588
0.9	0.535743	0.800298	0.74631	0.694117	0.139787
1.3	0.817356	0.860506	0.888911	0.855591	0.036029

1.7	0.93498	0.902961	0.860112	0.899351	0.037564
2	0.911556	0.942909	0.898956	0.917807	0.022633
2.5	0.818297	0.956759	0.954482	0.909846	0.079292
3	0.877668	0.934305	1.050518	0.954164	0.088119
5	0.975795	1.002952	0.970912	0.98322	0.017262
7	0.989758	1.04382	1.061894	1.031824	0.037534
9	0.970418	0.982087	1.027082	0.993196	0.029921
11	1.006605	0.870455	1.013925	0.963662	0.080802
14	1.053535	1.084062	1.032792	1.056796	0.02579
17	1.017195	1.028714	1.012656	1.019522	0.008278

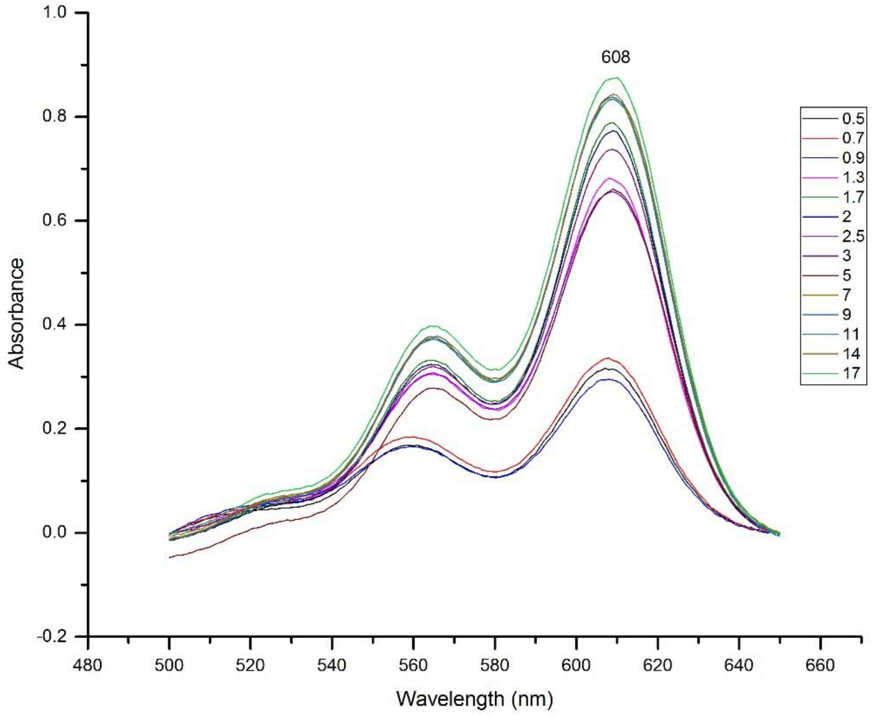

Figure 3-25: The absorption of each concentration of the surfactant SDS from 0.5 – 17 mM within 0.6 M SHG phase using 5x10^{-6} of PC spectrophotometric method after applying background correction.

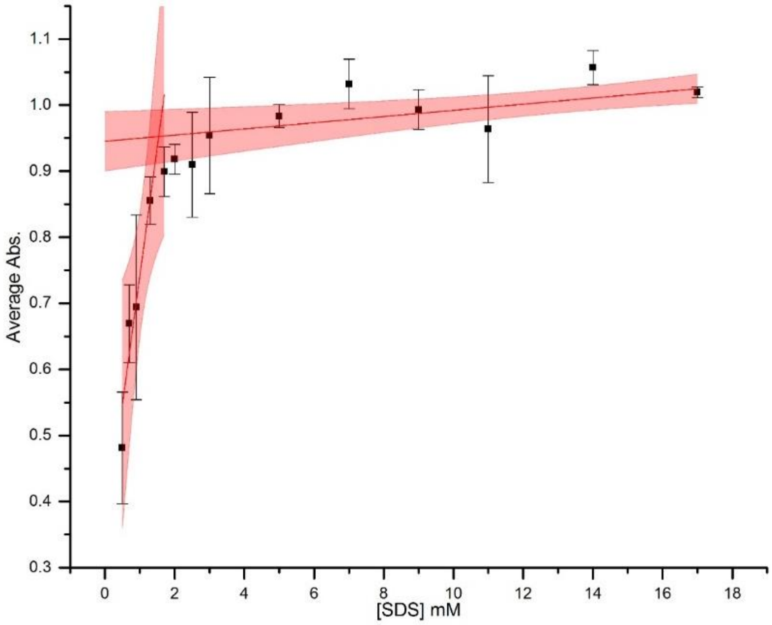

Figure 3-26: Plotted graphs between the SDS concentration (mM) and the absorbance at 608 nm values in 0.6 M silica hydrogel phase by using PC dye indicator. The inflection point refers to the CMC point of the surfactant in SHG.

3.3.2.3 At 0.7 M SHG

Table 3-14: The absorption values of a series of different concentrations of surfactant SDS solutions at λ_{max} 608 in 0.7 M silica hydrogel phase with $5x10^{-6}$ M PC.

[SDS] mM	1st 608nm	2nd 608nm	3rd 608nm	Average	St.Div
0.3	0.270694	0.319218	0.440723	0.343545	0.087586
0.5	0.226138	0.534706	0.629129	0.463324	0.210765
0.7	0.582861	0.879747	0.957831	0.806813	0.197838
0.9	0.870827	0.951881	0.898596	0.907101	0.041191
1.2	0.905993	1.024122	0.978981	0.969699	0.059609
1.5	0.941658	0.976992	0.957395	0.958681	0.017702
1.8	0.923578	0.999131	1.074846	0.999185	0.075634
2.2	0.44002	1.032464	1.143363	0.871949	0.378149
2.5	0.818368	1.083444	1.170328	1.024047	0.183344

3	1.00213	1.053384	1.093458	1.049657	0.045778
3.5	1.062823	0.964451	0.990123	1.005799	0.051025
4	1.14922	0.938557	1.062945	1.050241	0.105904
6	1.21972	1.129988	1.142384	1.16403	0.048625
10	1.251293	1.004189	1.049477	1.101653	0.131556

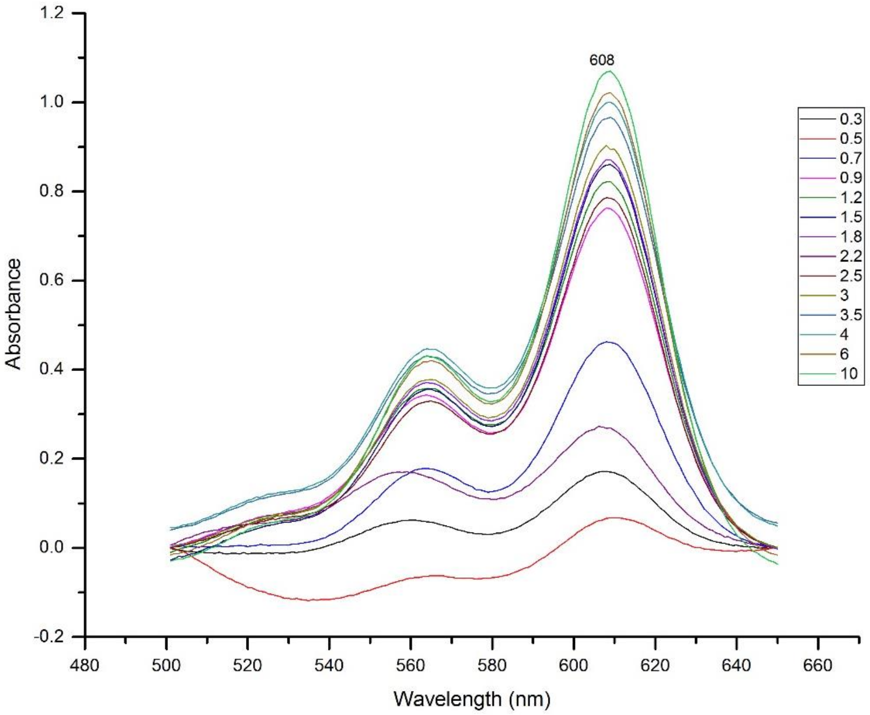

Figure 3-27: The absorption of each concentration of the surfactant SDS from 0.3 – 10 mM within 0.7 M SHG phase using 5x10^{-6} M of PC spectrophotometric method after applying background correction.

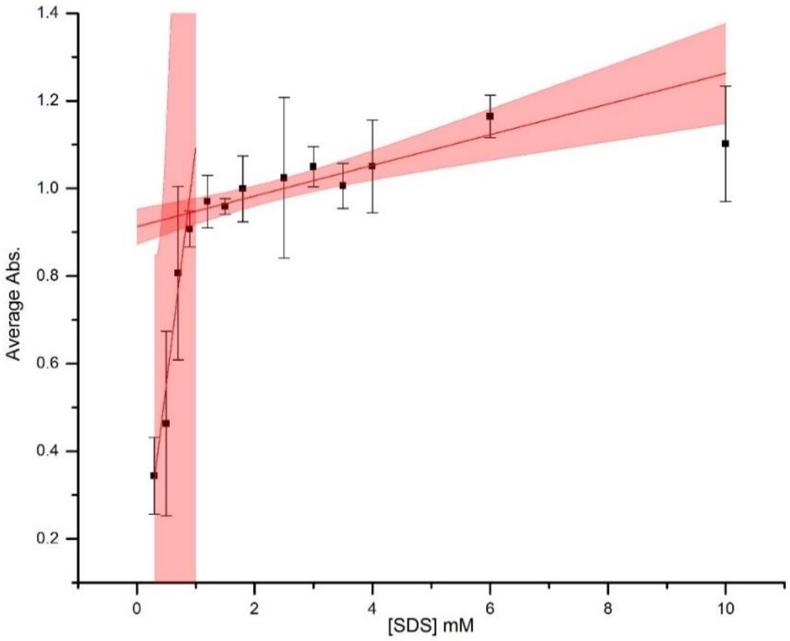

Figure 3-28: Plotted graphs between the SDS concentration (mM) and the absorbance at 608 nm values in 0.7 M silica hydrogel phase by using PC dye indicator. The inflection point refers to the CMC point of the surfactant in SHG.

3.3.2.4 At 0.8 M SHG

Table 3-15: The absorption values of a series of different concentrations of surfactant SDS solutions at λ_{max} 608 in 0.8 M silica hydrogel phase with $1x10^{-5}$ M PC.

[SDS] mM	1st 608nm	2nd 608nm	3rd 608nm	Average	St.Div
0.2	0.230064	0.344914	0.252043	0.275674	0.060963
0.4	0.238768	0.273937	0.21698	0.243228	0.028739
0.6	0.513058	0.539539	0.460597	0.504398	0.040177
0.8	0.629495	0.571276	0.486246	0.562339	0.072042
1	0.501993	0.603038	0.593161	0.566064	0.055707
1.3	0.691382	0.611253	0.632965	0.6452	0.041442
1.6	0.556492	0.596901	0.639181	0.597525	0.041348
1.9	0.594131	0.615934	0.626285	0.612117	0.016413
2.2	0.603777	0.595565	0.63199	0.610444	0.019106

2.5	0.62051	0.659309	0.597368	0.625729	0.031299
3	0.560226	0.5764	0.543985	0.560203	0.016207
5	0.564167	0.620825	0.604427	0.596473	0.029155
7	0.624768	0.736736	0.730187	0.69723	0.06284
10	0.782552	0.722577	0.721867	0.742332	0.034833

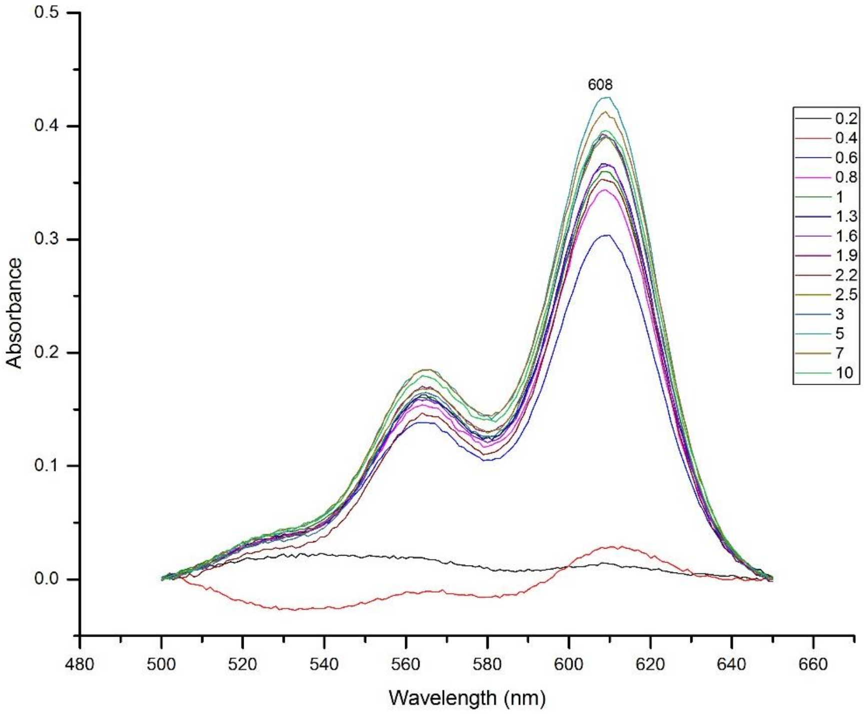

Figure 3-29: The absorption of each concentration of the surfactant SDS from 0.3 – 10 mM within 0.8 M SHG phase using 1x10^{-5} M of PC spectrophotometric method after applying background correction.

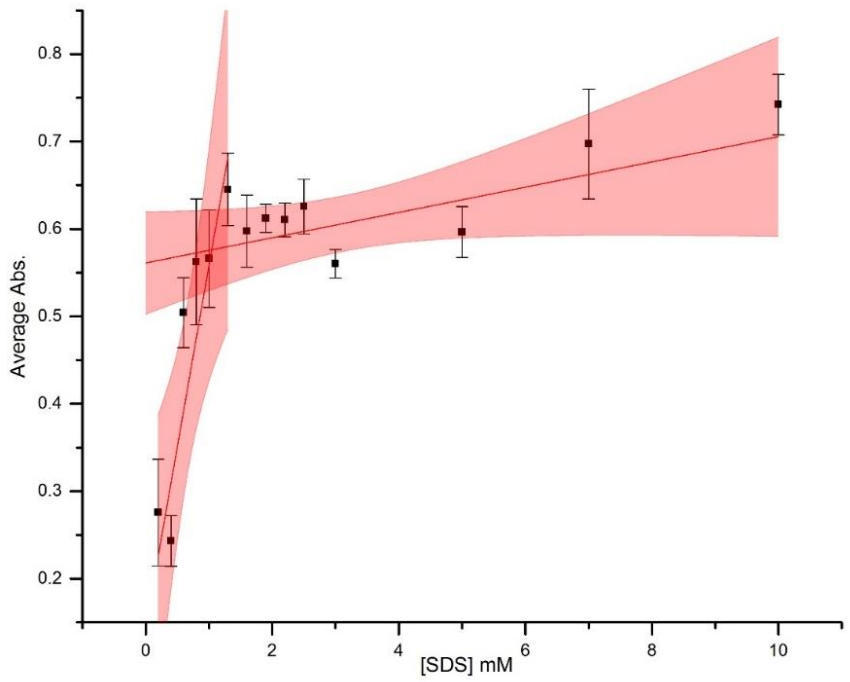

Figure 3-30: Plotted graphs between the SDS concentration (mM) and the absorbance at 608 nm values in 0.8 M silica hydrogel phase by using PC dye indicator. The inflection point refers to the CMC point of the surfactant in SHG.

3.3.2.5 At 0.9 M SHG

Table 3-16: The absorption values of a series of different concentrations of surfactant SDS solutions at λ_{max} 608 in 0.9 M silica hydrogel phase with $1x10^{-5}$ M PC.

[SDS] mM	1st 608nm	2nd 608nm	3rd 608nm	Average	St.Div
0.2	0.070802	0.090308	0.067863	0.076324	0.012199
0.4	0.094512	0.072349	0.114643	0.093835	0.021155
0.6	0.356659	0.360851	0.344042	0.353851	0.008749
0.8	0.371272	0.347939	0.355339	0.358183	0.011923
1	0.486799	0.362868	0.392865	0.414177	0.064656
1.3	0.393243	0.42678	0.401845	0.407289	0.017419
1.6	0.460567	0.382669	0.411032	0.41809	0.039426
1.9	0.409313	0.394357	0.396328	0.399999	0.008126
2.4	0.422361	0.494421	0.444988	0.453923	0.036852
3	0.363247	0.369409	0.284842	0.339166	0.047147

4	0.362838	0.57562	0.385352	0.44127	0.116894
6	0.427179	0.507094	0.44182	0.458698	0.042547
8	0.496066	0.475774	0.457224	0.476355	0.019428
11	0.471958	0.507601	0.478293	0.48595	0.019015

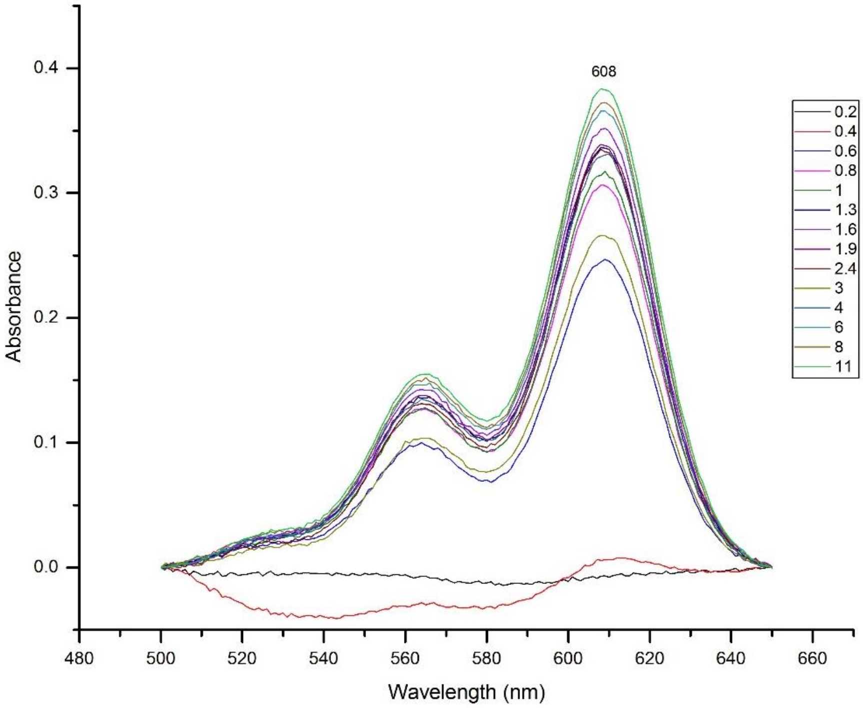

Figure 3-31: The absorption of each concentration of the surfactant SDS from 0.2 – 11 mM within 0.9 M SHG phase using 1x10^{-5} M of PC spectrophotometric method applying background correction.

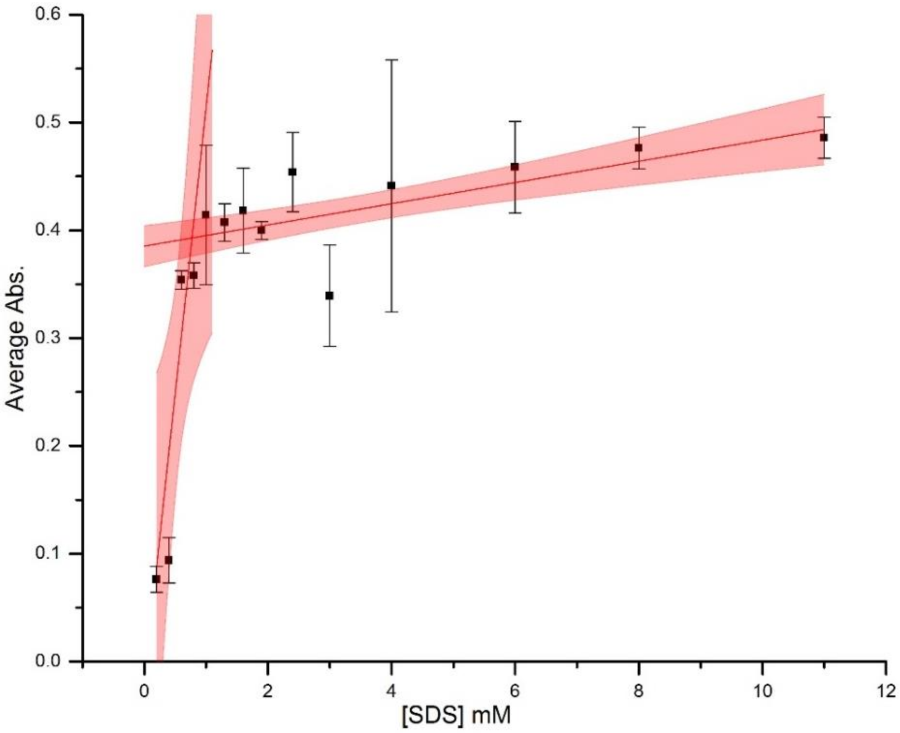

Figure 3-32: Plotted graphs between the SDS concentration (mM) and the absorbance at 608 nm values in 0.9 M silica hydrogel phase by using PC dye indicator. The inflection point refers to the CMC point of the surfactant in SHG.

3.3.2.6 At 1.0 M SHG

Table 3-17: The absorption values of a series of different concentrations of surfactant SDS solutions at λ_{max} 608 in 1.0 M silica hydrogel phase with $1x10^{-5}$ M PC.

[SDS] mM	1st 608nm	2nd 608nm	3rd 608nm	Average	St.Div
0.2	0.158719	0.187734	0.08705	0.144501	0.051826
0.4	0.34473	0.165838	0.161991	0.224186	0.104412
0.6	0.437375	0.348036	0.317999	0.367803	0.062095
0.8	0.441242	0.333276	0.328644	0.367721	0.063714
1	0.401928	0.363316	0.467488	0.410911	0.052664
1.2	0.494026	0.365352	0.355907	0.405095	0.077161
1.5	0.384447	0.366294	0.526786	0.425842	0.087889
1.8	0.502322	0.397757	0.436835	0.445638	0.052835
2.2	0.45989	0.403463	0.561982	0.475112	0.080348

2.7	0.485578	0.375196	0.372157	0.410977	0.064624
3.5	0.484689	0.344717	0.365824	0.39841	0.075461
5	0.615555	0.478945	0.458616	0.517705	0.085348
7	0.559874	0.449755	0.483229	0.497619	0.056452
10	0.584621	0.605653	0.617711	0.602661	0.016746

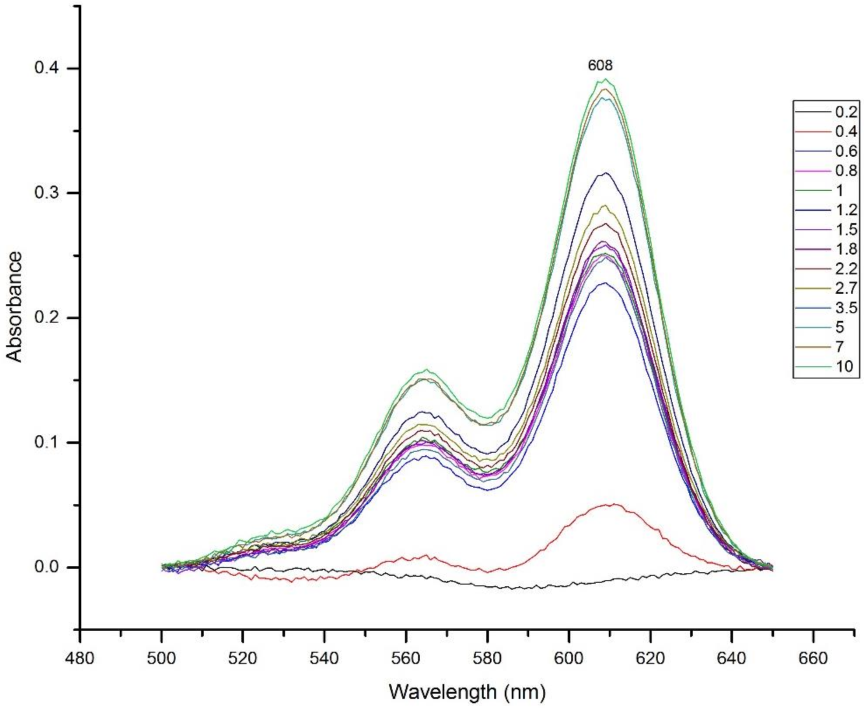

Figure 3-33: The absorption of each concentration of the surfactant SDS after applying background correction from 0.2 – 10 mM within 1.0 M SHG phase using 1x10^{-5} M of PC spectrophotometric method.

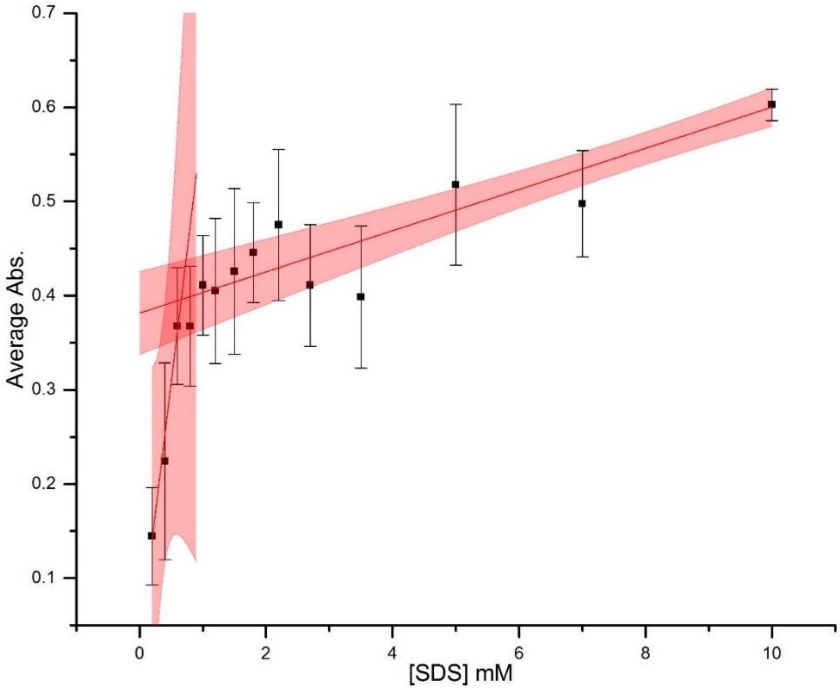

Figure 3-34: Plotted graphs between the SDS concentration (mM) and the absorbance at 608 nm values in 1.0 M silica hydrogel phase by using PC dye indicator. The inflection point refers to the CMC point of the surfactant in SHG.

To summarize the above results, CMC values of SDS with the help of PC dye estimated according to the same method used in aqueous phase by plotting average absorbance of three repeats against the SDS concentration. The shape of the plotted graph shows a steadily increase in the absorbance at 608nm with increases in the concentration of SDS, after a certain concentration, no more absorption peak maxima increase and goes almost flat which indicate passing the critical point (CMC). By plotting two selective line between the first pattern below CMC which is steadily absorbance increase and the second pattern which indicates the flat pattern above the CMC point and the intersection between these two lines used to estimate the CMC point as shown in Figure 3-26; Figure 3-28; Figure 3-30; Figure 3-32 and Figure 3-34.

Plotted results shows decreases with increases in the SHG concentration as follow: (1.4 ± 0.4 mM); (1.5 ± 0.2); (0.8 ± 0.3); (1.0 ± 0.2); (0.7 ± 0.4) and (0.6 ± 0.2) millimolar for the 0.5; 0.6; 0.7; 0.8; 0.9 and 1.0 molar of SHG

3.4 Discussion and Analysis of Results

3.4.1 Merocyanine vs Pinacyanol Chloride

It is clear from the results outlined above that both MC 540 and PC return CMC values for SDS in the 0.5 M silica hydrogel sample that are comparable: 1.3 ± 0.7 mM (merocyanine) and 1.4 ± 0.4 mM (pinacyanol chloride). Given the far more rapid decolourisation of merocyanine (order of hours to days) over PC (where indeed we also see some decolourisation on the timescale of weeks), we have elected to proceed with measurements using the latter reporter dye. An initial investigation of the decolourisation phenomenon of MC540 is described in Chapter 4.

3.4.2 CMC Values as function of Silicate Concentration

For quick comparison of the CMC values for 0.5, 0.6, 0.7, 0.8, 0.9, 1.0 M SHGs, Table 3-18 shows decreasing of the CMC values with increasing SHG concentrations.

Table 3-18: CMC values of SDS according to SHG's concentration increasing

SHG concentration / M	CMC value	Error margin
0.5	1.4	0.4
0.6	1.5	0.2
0.7	0.8	0.3
0.8	1.0	0.2
0.9	0.7	0.4
1.0	0.6	0.2

Whilst the CMC values do not appear to change significantly across the series of SHG's, there is perhaps a slight trend towards decreasing CMC with values of 1.4 ± 0.4 mM (0.5 M SHG) descending to 0.6 ± 0.2 mM (1.0 M SHG). The differential between these two is not especially large but may be statistically significant.

When one begins to consider the factors which may be influencing the decrease in CMC between aqueous and SHG phase itself, there are several questions which logically arise:

1. What is the role (if any) of the gel phase itself?
2. What is the role (if any) of the silica matrix within the gel?
3. What is the role (if any) of the presence of salts within the hydrogel phase?
4. What is the role (if any) of the ionic strength within the hydrogel phase?

Examining this collection of questions, it may be difficult to ascertain definitively if the gel phase itself is having an effect, but independent studies by another member of our research group has confirmed that there does indeed appear to be a strong salt and possibly also ionic strength effect on CMC values in aqueous solution, as has been found by others[123].

For example, the data outlined in Figure 3-35 below have been collected by a PhD research colleague in our laboratory, Mrs Seham Alanazi, who is examining this salt effect in more details[123]. This image shows how the CMC of SDS decreases with increasing concentrations of added salts, all sodium salts. It is clear that increasing salt concentration, up to a certain level, between 0.2-0.3 M leads to significant reduction of the CMC, essentially bringing it into the region that we are observing in the SHG phase as outlined in this chapter. Beyond this threshold salt concentration, the CMC appears to show little further change. We can make an approximate calculation of what the salt concentration is likely to be in our 0.5-1.0 M SHG formulations as follows:

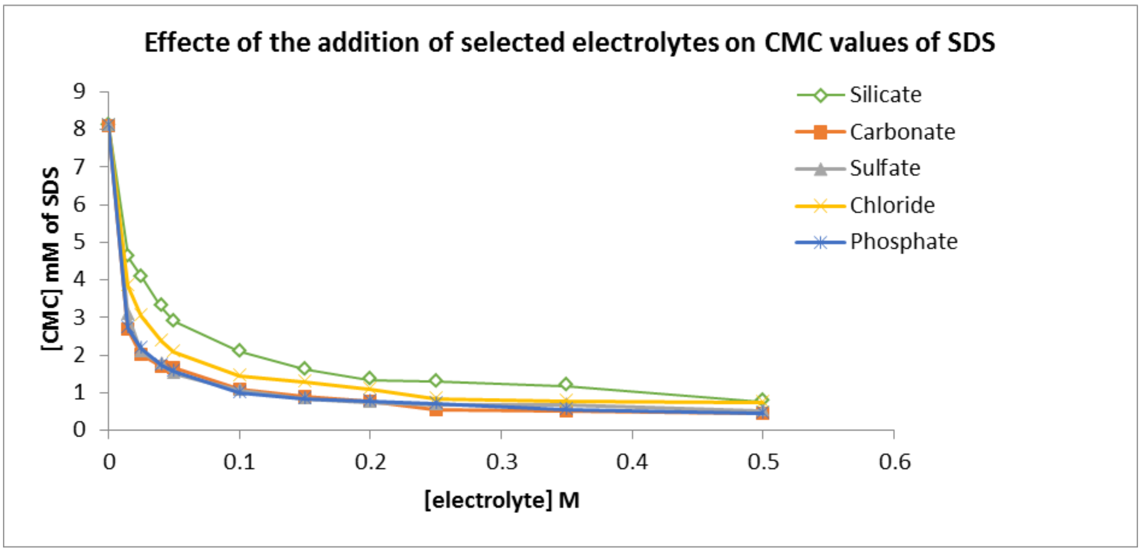

Figure 3-35: CMC values of SDS as a function of electrolytes concentration[123]

One further issue which arose in comparing the experimental measurements of CMC in aqueous and the SHG phases was that the shape of the absorbance vs [SDS] curves was different (Figure 3-36).

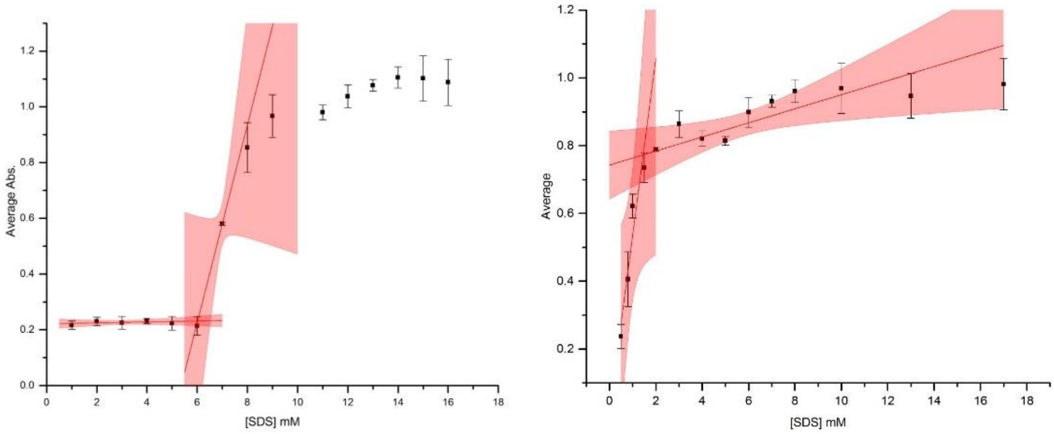

Figure 3-36: Plotted graphs between the SDS concentration (mM) and the absorbance at 605 nm in aqueous phase (*left*) and 0.5 M SHG (*right*) by using PC as reporter dye.

As can be clearly seen from the left hand side image of Figure 3-36, which is the aqueous phase CMC measurement, there are two clear transition points in the behaviour of the PC reporter dye. The first at *ca.* 6 mM show the point at which a significant intensity of signal is observed at 608 nm, this being associated with absorbance of PC in the monomeric phase. This in turn is what would be expected as the dye molecule beings to penetrate an amphiphilic micelle. Thus, this point represents the on-set of micellation. The second transition occurs in the aqueous phase at *ca*. 9 mM [SDS] and represents the point at which monomer formation and hence co-assembly of amphiphile and pinacyanol dye has reached an equilibrium point.

What can clearly be seen from comparison of the two images in Figure 3-36 is that in the SHG phase, the lower, onset, transition is not clearly defined. This may indeed be a result of such a transition being shifted to increasingly smaller concentrations. Therefore, in the absence of more detailed studies designed to probe this in more detail, we are not in a position to compare on-set micellation points between aqueous and gel phases. However, we are able to make that comparison for the second transition point, the equilibrium point and this is what has been done here. Interestingly, this same effect, of a clear diminution of the first onset transition point is also found in CMC measurements that we have made on SDS in the aqueous phase in the presence of salts (see Figure 3-37 for an example[123]).

To what extent such effects translate to the silica hydrogel phase, we do not as yet know and are beyond the scope of this thesis. However, it is certainly the case that the silica hydrogels produced here are commensurate with both reducing the CMC of a representative amphiphile whilst also providing a barrier to material loss through the physical nature of the gel phase itself.

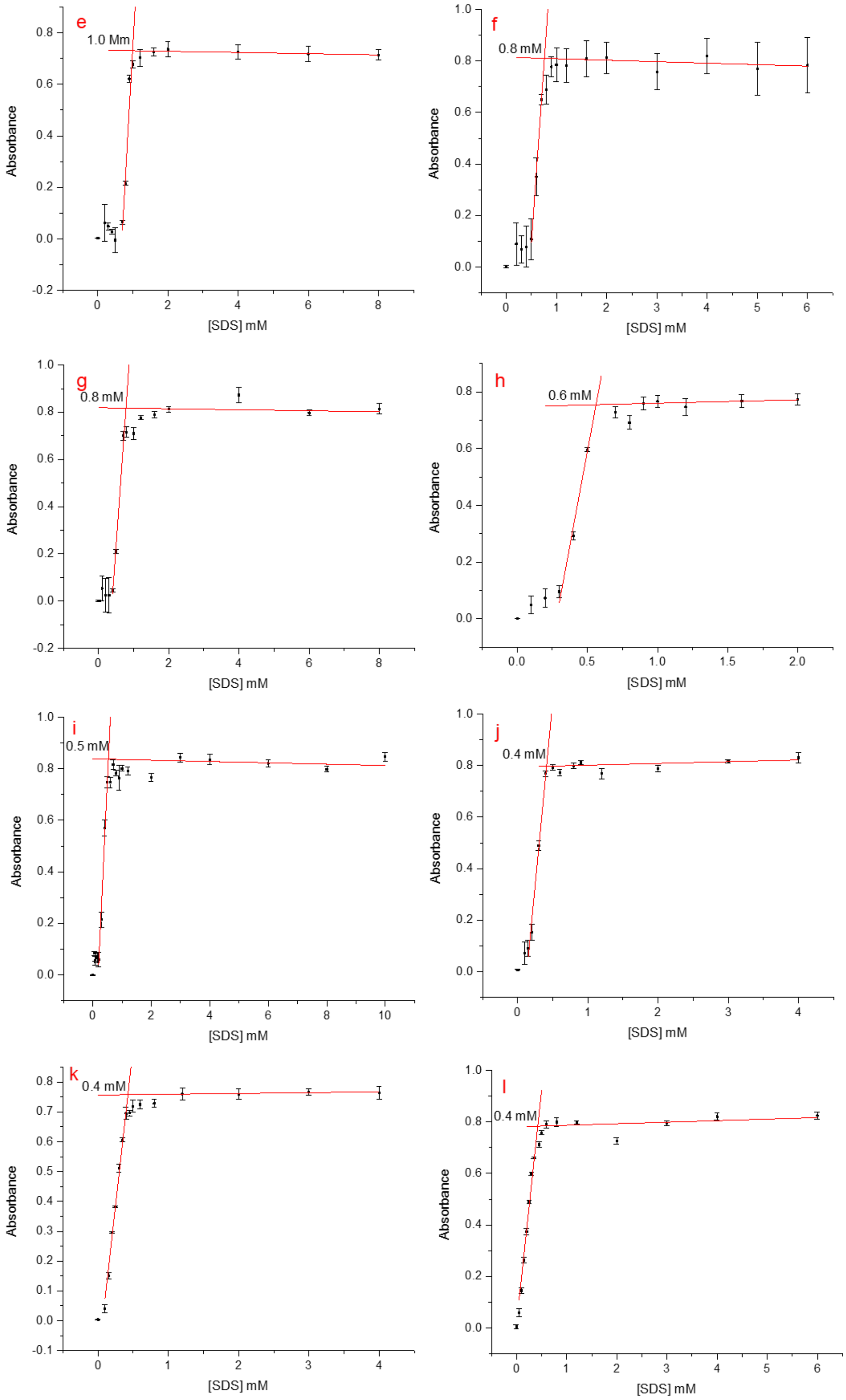

Figure 3-37: Estimation of the CMC values by plotting specific absorbance of SDS versus concentration at the wavelength of 608 nm in carbonate solution: a) 0.015 M , b) 0.025 M , c) 0.04 M , d) 0.05 M , e) 0.1 M, f) 0.15 M , g) 0.2 M , h) 0.25 M , i) 0.35 M , j) 0.5 M , k) 0.7 M and l) 0.9 M[123].

3.5 Conclusion

Overall, the content and main conclusions from this chapter may be summarised as follows:

1. The critical micelle concentrations (CMC) of the surfactant SDS have been measured using UV-VIS spectrophotometry in the silica hydrogel phase (SHG) and compared to the aqueous phase
2. Overall, the CMC of SDS is noted to be lower in the SHG phase than in water. There is evidence that this may be due to the salt components within the gel
3. One of the colourimetry dyes that we were using in these studies, MC540, was observed to undergo decolourization in the more concentrated SHG's; this effect has been studies more in Chapter 4

Chapter 4 Effects of the Hydrogel Phase on Molecular Aggregation of Amphiphilic Dyes

4.1 Merocyanine 540 Decolourisation. Introduction

During experiments to measure the CMC of SDS in SHG media (described in Chapter 3) using spectrophotometric measurements with the red dye merocyanine 540 (MC 540) shown in Figure 4-1, an observation was made that, in certain SHG preparations, the initial red colour of the dye would of disappeared, becoming yellow and then subsequently colourless after a certain time. Amphiphiles have complementary hydrophilic and hydrophobic regions. In polar solvents for instance, water, spontaneous self-assembly occurs to generate micelles[124]. This is due to head hydrophilicity and tail hydrophobicity and their preferred orientation with respect to water. A micelle structure contains outward-facing hydrophilic heads (towards water) and inward-facing hydrophobic tails (away from water). In studies described in Chapter 3, a description of how the critical micelle concentration of the model amphiphile sodium dodecylsulfate (SDS) was influenced by self-assembly within the hydrogel phase. In order to make such measurements spectrophotometrically, we exploited the difference in self-assembly behaviour of MC 540 when the latter partitions between aqueous and micellar phases[73]. However, the dye decolourisation behaviour made it challenging to get effective, reproducible results which necessitated switching to another dye reporter, pinacyanol chloride (Chapter 3). In this Chapter, a description in a little more details some of the work that been performed to try to probe this decolourisation behaviour.

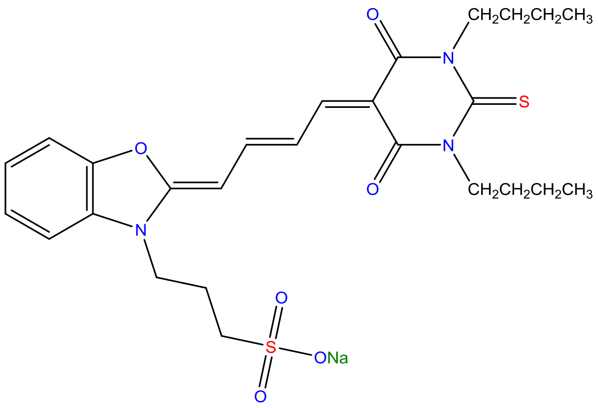

Figure 4-1: Molecular structure of merocyanine 540

4.2 Aims & Objectives

In examining the decolourisation behaviour of MC 540, we wanted to try to probe the following questions:

(i) What might be the mechanism(s) of decolourisation & what environmental factors might be implicated?
(ii) Is decolourisation linked in any fundamental way to the hydrogel phase itself?
(iii) Does the presence of an amphiphile such as SDS have any effect upon the decolourisation?

4.3 Experiments to Probe the Mechanism of Decolourisation

4.3.1 The Role of Singlet Molecular Oxygen

First instincts when looking at the structure of MC 540 (Figure 4-1) is that the colour loss is related to the loss of conjugation of the molecule. The extended conjugation of double bonds (Figure 4-2) and electron rich atoms results in a delocalised system, which results in lower excitation energies (in the visible spectral region) to promote electrons to higher energy orbitals such as the π* orbital. Disruption of this conjugation will result in higher excitation energies and no absorption in the visible region[125].

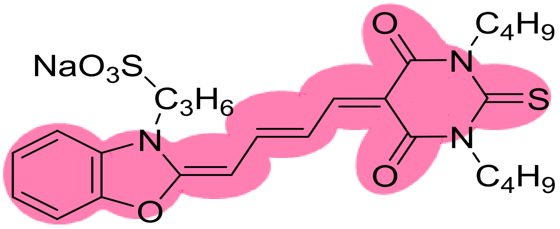

Figure 4-2: MC 540 highlighted to show extended conjugation

Initial investigations into the mechanism for decolourisation lead to a well-established, documented and patented photo-oxidation reaction. This reaction involved a photooxidation process of MC 540 (MC^{s*}) by a mechanism such as the one shown in Scheme 4-1. In this case, the singlet oxygen is generated by the triplet excited state of the dye itself interacting with the triplet oxygen[126, 127].

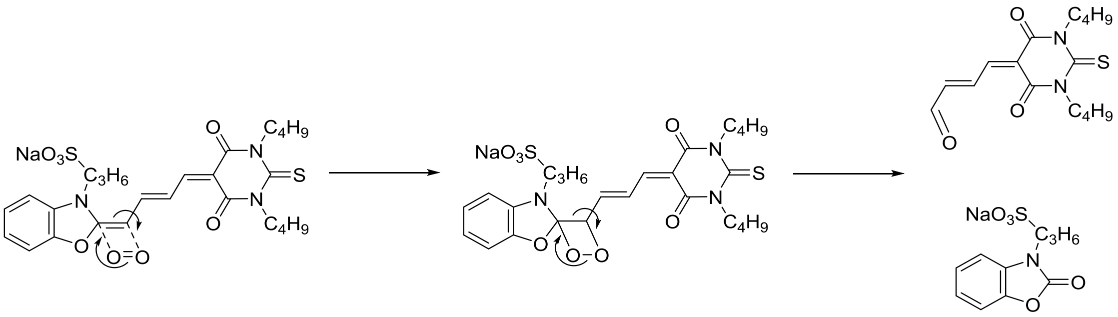

Scheme 4-1: Reaction of MC^{s*} with SMO to produce photo-oxidation products

The dye would become excited by the absorption of either visible or UV spectrum light to its singlet state. The singlet oxygen, that is oxygen also in its singlet excited state, would then have the ability to interact with the dye molecule, and this interaction would quench the excitation of both molecules. The attack is most likely to occur at the Spiro-carbon as shown in Scheme 4-1, as this is the most δ+ point of attack, but attack at the other end of the butane chain is also likely due to the stabilisation of anions from the diketone at this position. This was confirmed by Toutchkine *et al* who demonstrated the improved photo-stability and retardation of photo-bleaching of similar merocyanine dyes by substitution at this point [128]. This reaction would theoretically be facilitated in the hydrogel environment due to the reduced dissociation ability of the singlet oxygen in gel media. This is both due to increased likelihood of adsorption and the increased viscosity.

Viscosity provides a physical barrier to the transport of the molecule through its environment. It is also likely that the ‘product’ molecules would be isolatable intermediates to more stable products shown in Scheme 4-2 as detailed and patented by Franck and Schneider [129, 130].

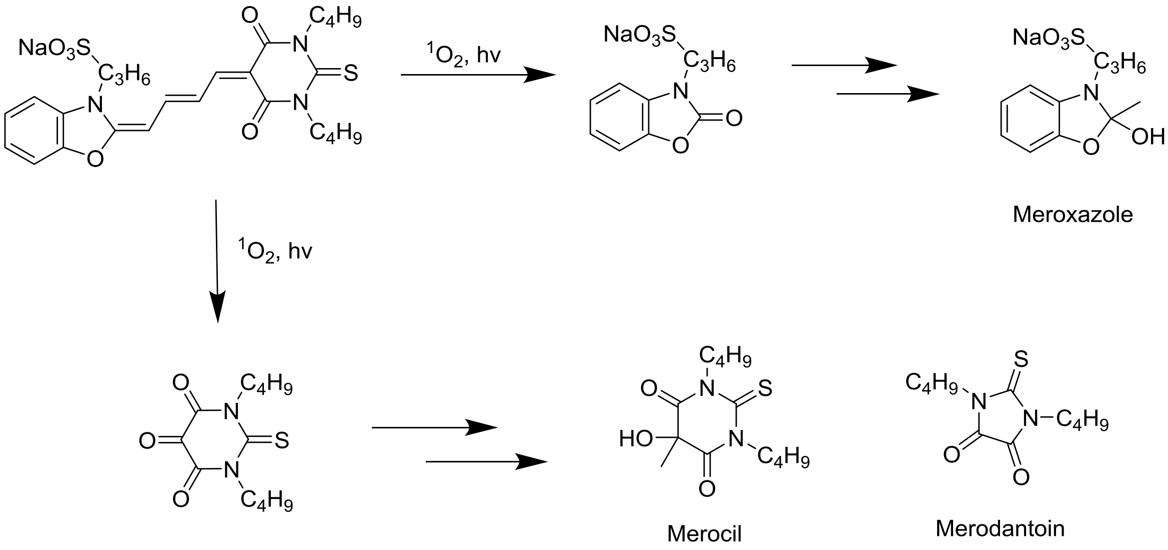

Scheme 4-2: Breakdown of MCN through photo-oxidation to produce key identified intermediates and products, namely; Meroxazole, Merocil, and Merodantoin [129, 130]

An investigation has begun with no SDS system to determine the effects of atmospheric oxygen (or there lack of) on the rate of decolourisation of MC540. Additionally, Argon and septum's were chosen over nitrogen and a glove bag / para-film combination as argon is a heavier gas and would more easily displace the oxygen, as well as being purer than the mains nitrogen. Septum's and needles provided a better seal from the atmosphere than the use or para-film and a glove bag as well as being considerably easier for the operator to handle.

Contrary to expectations, samples freed from atmospheric oxygen still decoloured over time in all cases. It was thought at first that this was due to samples not being fully evacuated of oxygen, hence the development of the degassing methodology, however it was decided this was not the case due to two key observations:

1. In many but not all cases, samples decolourise from the bottom of the cuvette first, then the decolourisation continues upwards (Figure 4-3).
2. During the degassing of a solution of water, acetic acid and dye decolourisation started to occur without gel formation (Figure 4-4).

If decolourisation was directly related to atmospheric oxygen it would be logical for samples to decolour fastest where the concentration of oxygen would be highest, i.e. at the surface of the sample, in contact with the air as one can see in Figure 4-3. However, what is observed shows the opposite, implying the occurrence of a different effect.

Figure 4-3: Photograph of a 1.0 M silica gel sample decolourising primarily from the bottom of the disposable cuvette to the top.

The decolourisation of the dye in aqueous solution was unexpected phenomenon which noticed as well, as decolourisation has previously only been observed in the gel media. The stock solution of MC 540 in ethanol is very stable and retained its full colour throughout this investigation. The only difference between normal dye solution and this aqueous decolourised sample was the bubbling of argon. It was possible that this could be directly related to an interaction with the gas, although Argon is an inert. Three gas types; argon, nitrogen and compressed air, were bubbled through three samples of the same solution for 30 minutes to determine if this effect was exclusive to argon.

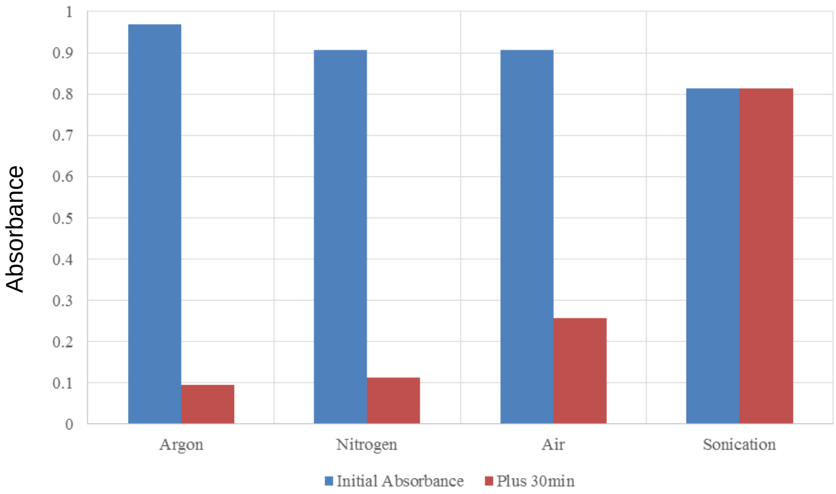

Figure 4-4: Absorbance at 510 nm of four un-gelled samples i) as soon as they were prepared and (blue columns) ii) after bubbling of the respective gas or sonication for 30 minutes (red columns)

It is clearly shown by Figure 4-4 that this effect is universal to bubbling of all gas types tested. The hypothesis was that the agitation of the mixture by the bubbles and subsequent influx of kinetic energy may be causing the phenomenon. Logically, sonicating the solutions in a water bath would have a similar effect[131]. However, no decolourisation was observed after 2 hours of sonication, the main effective reason for using sonication is to remove entrapped gases but, the decolourization issue is not related to presence or absence of oxygen gas.

4.3.2 The Effect of pH on MC 540 decolourization

After reaching a somewhat inconclusive scenario with respect to the effects of oxidation, it was decided to probe whether or not pH might have an effect. Increasing the pH of the solution promotes the formation of aggregates as the repulsive forces between similarly negatively charged moieties in the dye molecules are decreased by the presence of salt cations.

Firstly, conduct an examination of the visible absorption characteristics of MC 540 at buffered pH values of 4 and 7 which revealed (Figure 4-5) a negligible differential in terms of absorption. Subsequently, a time-logged pH measurement of the natural, un-buffered, pH of MC 540 in water at 10 µM concentration at 20°C returns a stable pH window of between 5.9-6.0 pH units after *ca* 3000 secs (Figure 4-6).

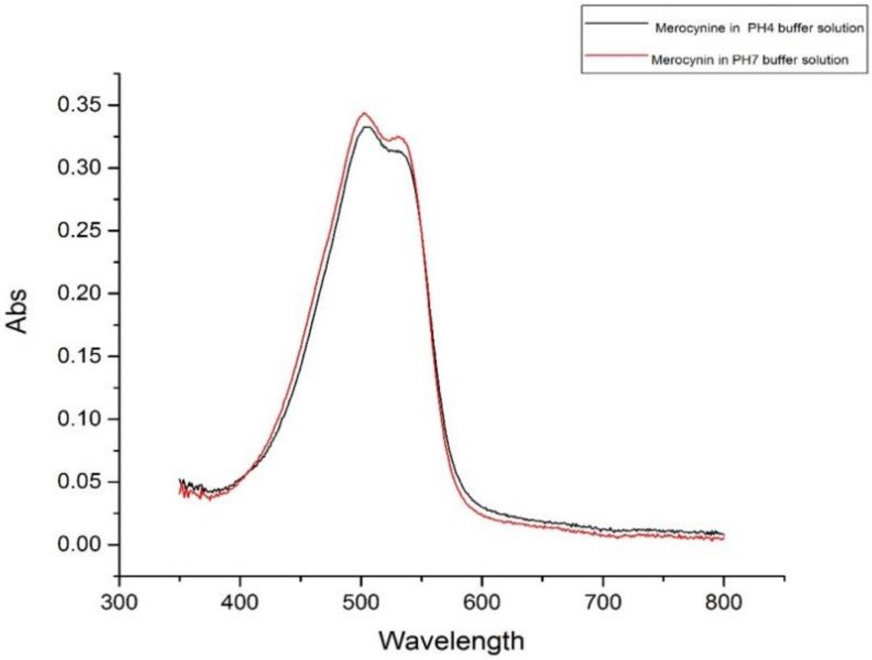

Figure 4-5 UV-Vis spectra of MC 540 (10 μM) in two buffered solutions (pH 4 and 7).

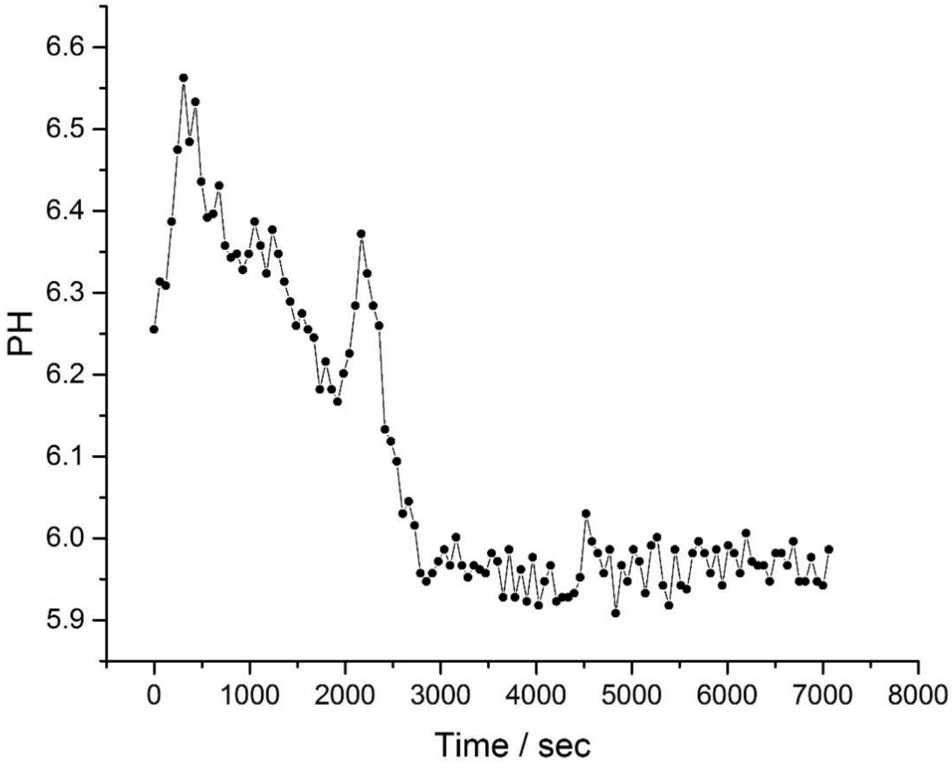

Figure 4-6: Time-logged pH values of MC 540 (10 μM) in the aqueous phase

However, the decolourisation behaviour that we are observing is not strictly an aqueous environment but one based upon a hydrogel. Therefore, it is necessary to consider the pH of MC 540 in the SHG environment both as a function of silicate concentration and of added SDS. The pH value of SHG (1.0 M silicate) stabilised at pH 9.8 after 45 mins (Figure 4-7) at ambient temperature. When the same measurement is made of a SHG (1.0 M silicate) containing MC 540 (1 x 10^{-5} M) the pH reading (see Figure 4-8) stabilises at 10.28 after 30 min; the sample had completely decolourized after 17 mins under these conditions. Comparing these observations to those made on aqueous solutions of MC 540 (1 x 10^{-5} M), we note that at a pH of 12.4, the colour changes to a light yellow after several minutes but that at a pH of 10.3 there is no effective change of colour over a period of at least one hour.

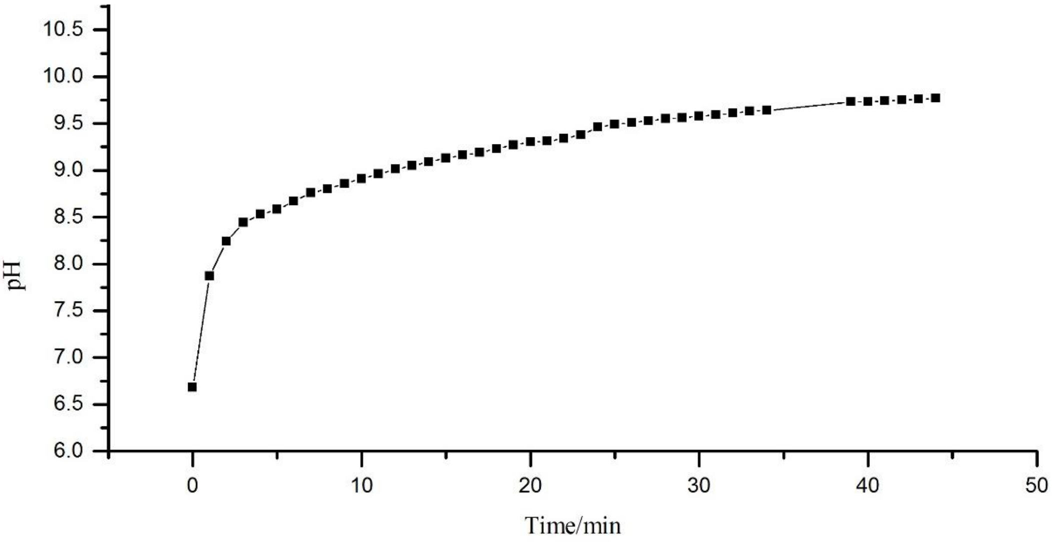

Figure 4-7: Time-logged pH values of 1.0 M SHG.

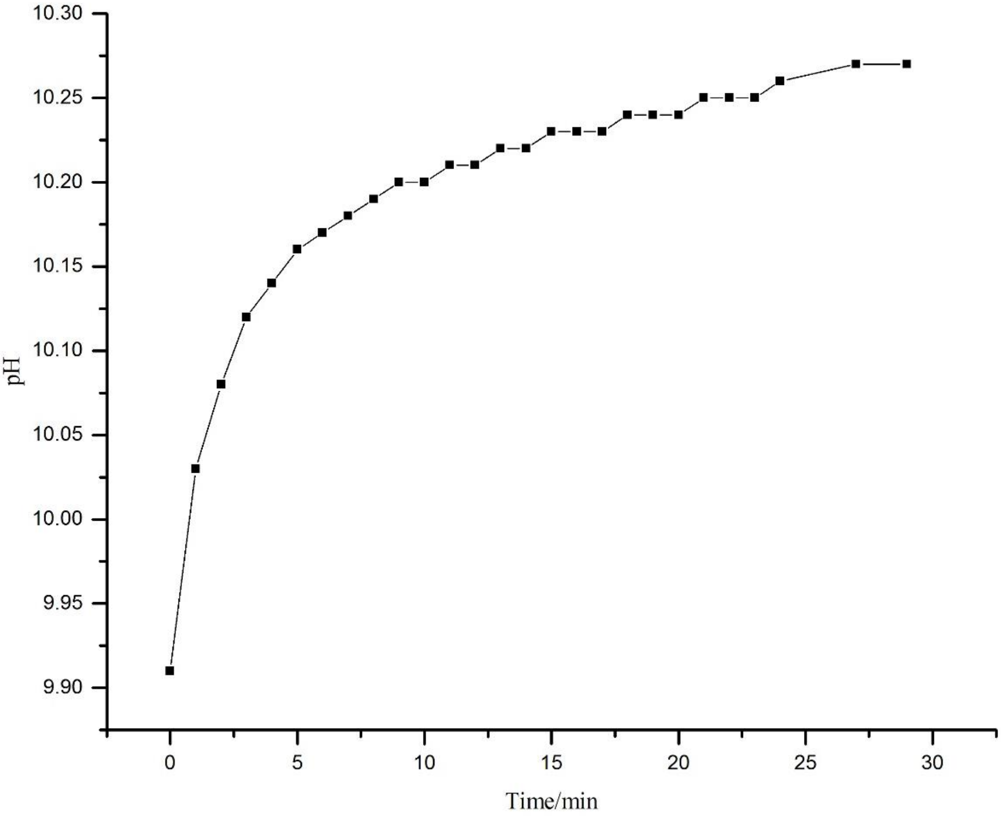

Figure 4-8: Time-logged pH values of 1.0 M SHG with 1x10^{-5} M of the dye MC 540

Therefore, as MC 540 is definitively decolourized when encapsulated within a silica hydrogel (SHG) environment at a pH regime which, in aqueous conditions, does not lead to decolourisation, we cannot make any claim for a strong pH effect on the bleaching.

4.3.3 Experiments to Probe Effects of the Presence of Amphiphiles and Gel Phase on the Decolourisation of Merocyanine

Building on the discussions above on MC 540 aggregation behaviour. Just as pH is found to influence the self-assembly behaviour of the dye, so too might the presence of a second amphiphile, above the critical micelle concentration, be capable of influencing of MC 540 self-assembly. This encouraged us asking the question: is the rate of this decolourisation process dependent upon the concertation of surfactant SDS and the concentration of silicate used in the hydrogel preparation? As can be seen in Figure 4-9, the decolourisation of MC happens far more rapidly in SHG formulations that have higher quantities of silicate. The series of images on the left-hand side show MC 540 photographed after 3 h in SHG formulations containing 1.0 M silicate whereas the right-hand column has parallel samples in 0.5 M silicate formulations photographed after 28 h. It can clearly be seen that decolourisation is more advanced in the 1.0 M formulation of SHG. Moreover, the images reveal also an effect of the presence of the amphiphile SDS on MC 540 decolourisation. The cuvette containing SHG at 1.0 M silicate level of preparation but without any SDS in it, decolorized after about 1 hour. Subsequent additions of SDS at 3, 10 and 18 mM levels, result in longer decolourisation times at 1.0 M silicate level SHG; for example with the SDS concentration at 18 mM (1.0 M silicate) decolourisation required about 9.5 hours for complete loss of colour.

Figure 4-9: Decolourisation of MC 540 in SHG formulations in the presence of SDS at 3, 10 & 18 mM. The left-hand column contains 1.0 M formulation SHG and have been photographed after 3 h. The right-hand column has 0.5 M formulation SHG and is photographed after 28 h. The concentration of merocyanine is 0.01 mM in all cases.

The effect of the presence of amphiphile SDS on MC 540 decolourisation has also been probed spectrophometrically In Figure 4-10 are displayed the time evolution of the decolourisation of MC 540, measured spectrophotometrically at 559 nm. As one can see clearly from the data, decolourisation is rapid in the absence of added amphiphile SDS, essentially reaching a plateau within 1h at ambient temperature. The subsequent introduction of SDS at modest levels (3 & 5 mM) but levels above the CMC in the SHG media (see Chapter 3)results in a marked attenuation of the decolourisation such that the absorbance at 559 nm has been reduced to half its initial value by *ca*. 2.5 h. Interestingly the rates of decolourisation appear to be attenuated even more at concentrations at and above the CMC for SDS in water (see above for 10 and 18 mM entries). We note also that even though the MC 540 was deployed at the same concentration (10 µM) in each experiment in Figure 4-10, the initial absorbance values of each run are somewhat different. This could be due to random time fluctuations in introducing the samples into the spectrometer post-preparation.

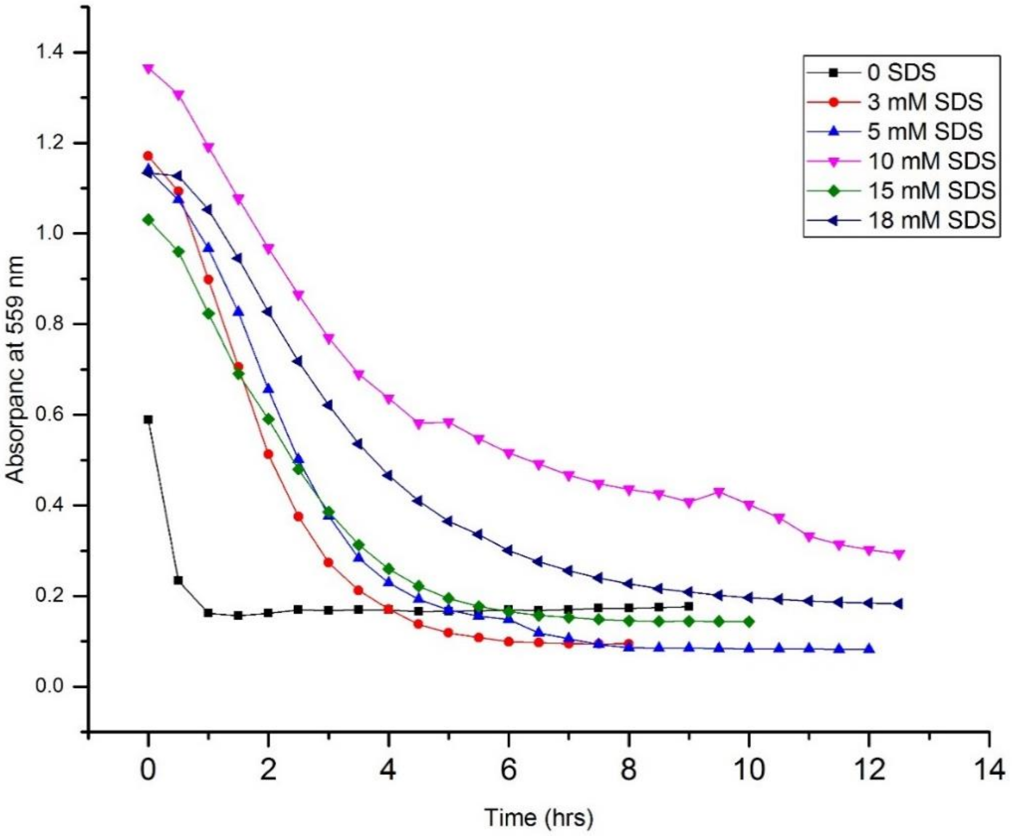

Figure 4-10: Different concretions of surfactant SDS in 1.0 M silica hydrogel environment plotted graph between the absorbance values at 525 nm against time. For data see Figure 7-11 **to** Figure 7-16

4.4 Mathematical expression of the decolourization plot

However, in the absence of these modified experiments, it is perhaps of value to re-express the data in Figure 4-10 in terms of a mathematical equation and see which will fit better to the proposed equation. Here will express two kinetic equations which are first-order kinetic equation and Gaussian equation:

4.4.1 first-order kinetic equation

If one attempts to model the decolourisation of MC 540 in terms of first order-kinetics, one may express this as follows:

$$\frac{-\,d[MC^c]}{dt} = K.\,[MC^c]$$ **Equation 4-1**

$$\ln[MC^c] = K.\ t + \ln[MC^c]^0$$ **Equation 4-2**

Where [*MC* ^{c}] represents the concentration of colourized merocyanine at a given time t, [*MC* ^{c}]^0 is that concentration at the specific point time point *t* = 0 and *k* represent the observed first-order rate constant for this model. Standard integration of Equation 4-1 affords Equation 4-2 which is what may be plotted to confirm first order behaviour[132]. Making the connection through the Beer-Lambert equation that spectrophotometric absorbance is directly proportional to solution concentration; we have re-plotted parts of the data in Figure 4-11 according to Equation 4-2. The data show far-from-ideal first order-kinetics. If one takes the data range over the first 3 h however (Figure 4-12), one could almost make a case for linearity in this window, but it is tenuous at best.

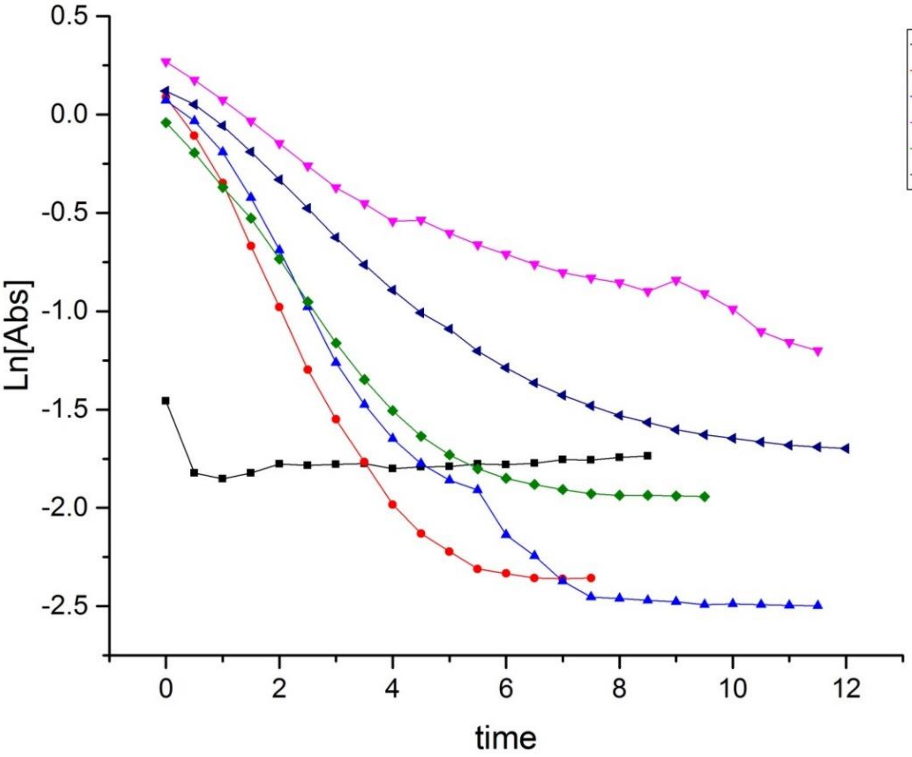

Figure 4-11: Data from Figure 4-10 plotted to first order behaviour according to Equation 4-2

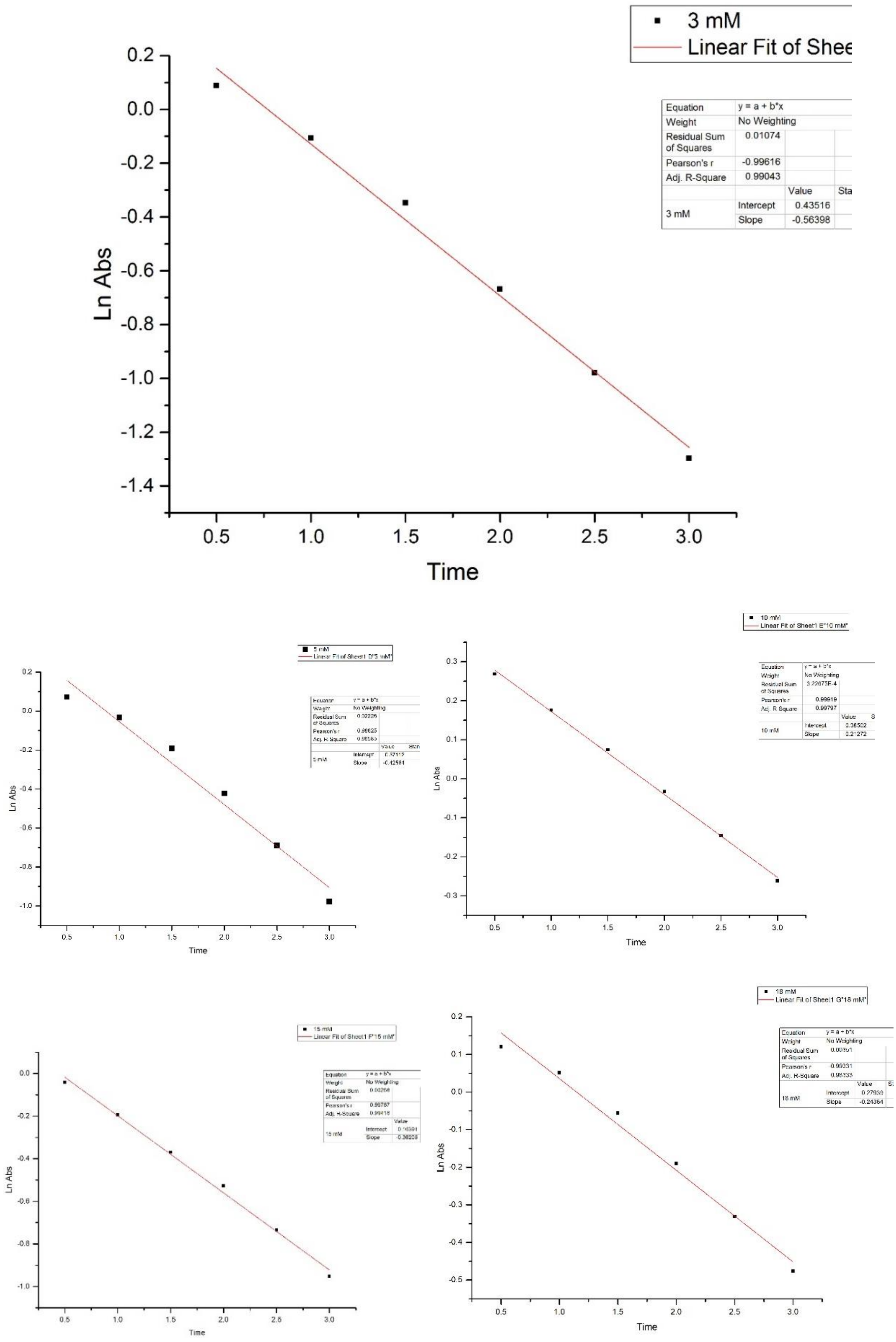

Equation	y = a + b*x		Sta
Weight	No Weighting		
Residual Sum of Squares	0.01074		
Pearson's r	-0.99616		
Adj. R-Square	0.99043		
		Value	Sta
3 mM	Intercept	0.43516	
	Slope	-0.56398	

Equation	y = a + b*x		
Weight	No Weighting		
Residual Sum of Squares	0.02226		
Pearson's r	0.98625		
Adj. R-Square	0.98563		
		Value	Stan
5 mM	Intercept	0.37112	
	Slope	-0.42584	

Equation	y = a + b*x		
Weight	No Weighting		
Residual Sum of Squares	3.22675E-4		
Pearson's r	0.99919		
Adj. R Square	0.99797		
		Value	S
10 mM	Intercept	0.38502	
	Slope	0.21272	

Equation	y = a + b*x	
Weight	No Weighting	
Residual Sum of Squares	0.00268	
Pearson's r	0.99787	
Adj. R-Square	0.99418	
		Value
15 mM	Intercept	0.16391
	Slope	-0.36206

Equation	y = a + b*x		
Weight	No Weighting		
Residual Sum of Squares	0.00351		
Pearson's r	-0.99031		
Adj. R-Square	0.98333		
		Value	S
18 mM	Intercept	0.27939	
	Slope	-0.24364	

Figure 4-12: **Selected data from Figure 4-10 plotted to first order behaviour according to Equation 4-2 (top) 3 mM SDS, (middle right) 5 mM SDS, (middle left) 10 mM SDS, (bottom right) 15 mM SDS, (bottom left) 18 mM SDS**

4.4.2 Gaussian Fit

Whilst a linear kinetic relationship for the MC 540 decolourisation is not supported by the data over the length of the decolourisation process, mathematical fitting of the data in Figure 4-11 demonstrates that a Gaussian distribution is a better fit, according to Equation 4-2 (Figure 4-13).

$$\ln[MC^c] = \ln[MC]^0 + \left[\frac{A}{w.\left(\frac{\pi}{2}\right)^{\frac{1}{2}}}\right]^{-2\left(\frac{X-X_c}{W}\right)^2} \qquad \textbf{Equation 4-3}$$

Where the following terms are:

$[MC^c]^o$ = Concentration of coloured form of MC 540 at the asymptote point

A is a constant

W = is the Gaussian width at half-height

X_c = the maximum height point of the x value

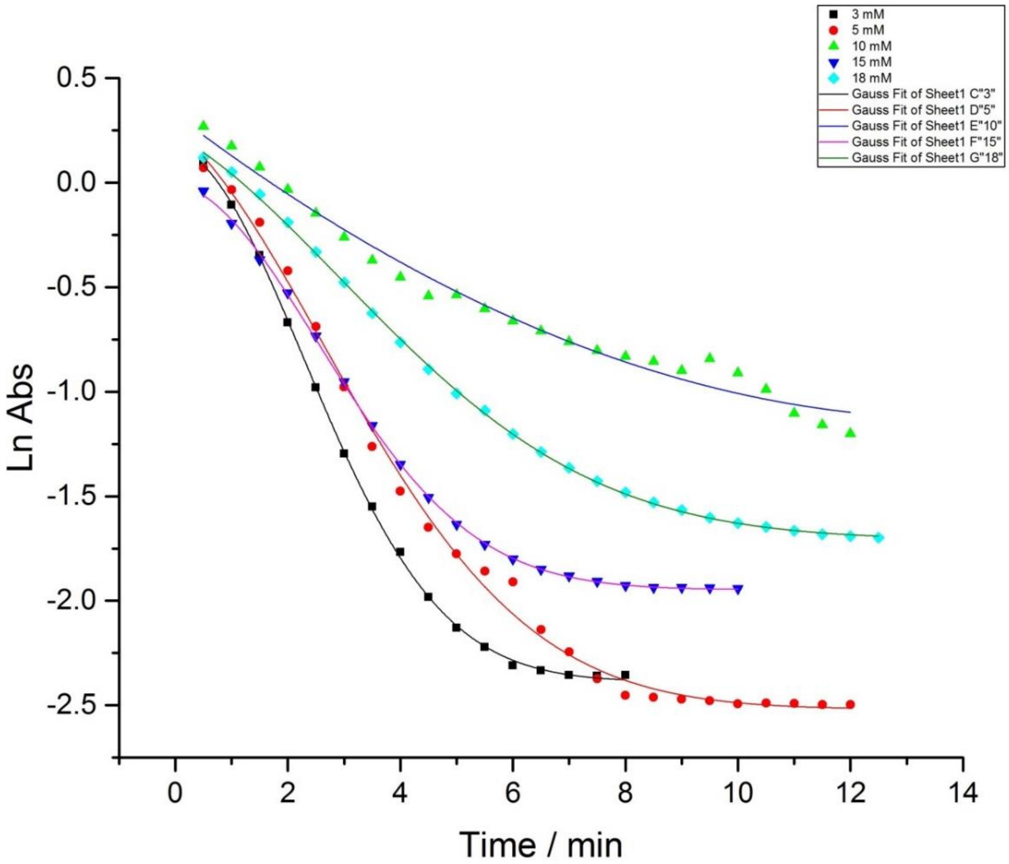

Figure 4-13: Data from Figure 4-11 showing an analytical fit to a Gaussian function in Equation 4-2

The data in Figure 4-13 have, at present, only a single series of repetitions at each SDS concentration so if any firm conclusions are to be drawn from a mathematical analysis it is envisaged that each will need to be repeated in triplicate to afford some level of error field.

Table 4-1: Absorbance at 559 nm MC 540 (10 µM) of SHG's prepared from 0.5 M (black squares), 0.75 M (red circles) and 1.0 M (blue triangles) silicate solutions in the presence of SDS (18 mM).

Time/ hrs	0.5 M silicate SHG	0.75 M silicate SHG	1 M silicate SHG
0	1.113841	1.304666	1.1336
0.5	1.149	1.335	1.128
1	1.164	1.340	1.053
1.5	1.166	1.345	0.946
2	1.163	1.339	0.827
2.5	1.154	1.335	0.718
3	1.131	1.335	0.621
3.5	1.109	1.329	0.536
4	1.098	1.334	0.466
4.5	1.098	1.336	0.499
5	1.093	1.330	0.365
5.5	1.093	1.326	0.336
6	1.092	1.322	0.301
6.5	1.091	1.319	0.276
7	1.089	1.313	0.256
7.5	1.087	1.310	0.240
8	1.088	1.309	0.227
8.5	1.085	1.300	0.217
9	1.062	1.298	0.209
9.5	1.056	1.292	0.201
10	1.052	1.290	0.196
10.5	1.052	1.286	0.193
11	1.051	1.277	0.189
11.5	1.049	1.273	0.186
12	1.048	1.270	0.184
12.5	1.048	1.265	0.183
13	1.047	1.264	
13.5	1.045	1.269	

14	1.049	1.261	
14.5	1.045	1.252	
15	1.045	1.230	
15.5	1.044	1.221	
16	1.046	1.228	
16.5	1.050	1.218	
17	1.049	1.217	
17.5	1.054	1.207	
18	1.056	1.202	
18.5	1.058	1.194	
19	1.058	1.188	
19.5	1.058	1.183	
20	1.062	1.180	

The data used to plot Figure 4-14 are collected in Table 4-1. It can be seen from Figure 4-14 (a) that the process of decolourisation in the SHG environment prepared from 0.5 M silicate was slower overall than those performed in 0.75 M and 1.0 M silicate SHG’s. Despite the differences in starting absorbance in each case, it is clear that the most shallow curve, representing the slowest decolourisation, can be attributed to the 0.5 M silicate SHG. As shown in Figure 4-14 (b), the same data in Figure 4-13 can be fitted to the same Gaussian expression as in Figure 4-13, demonstrating that the underlying principles of the phenomenon on probably connected in both cases.

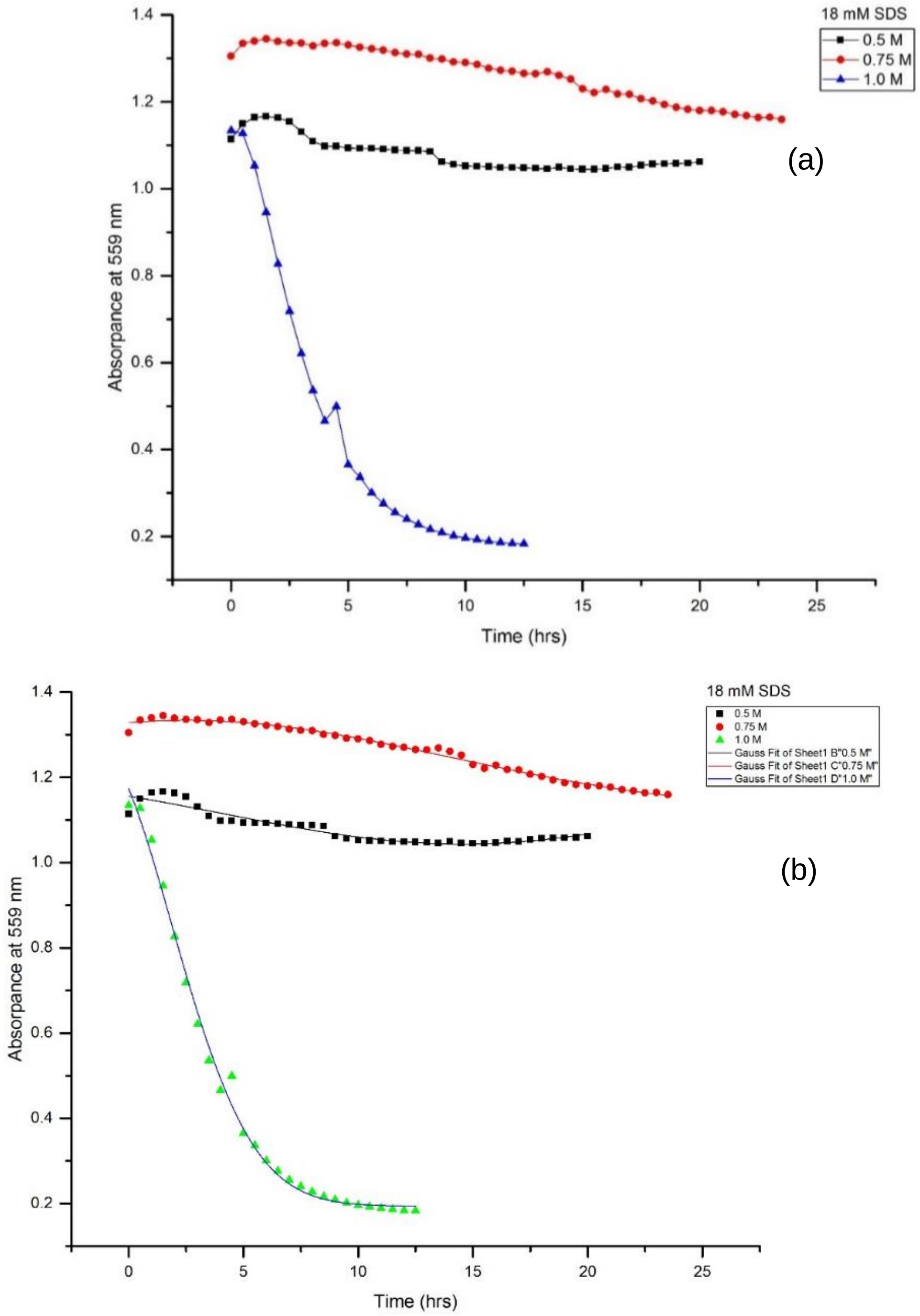

Figure 4-14: (a) Time evolution of the SHG-SDS MC 540 system involving 18 mM of surfactant SDS in different concentrations of silica hydrogel environment (0.5, 0.75, 1.0M silicate). (b) Gaussian fit to data in (a).

4.5 Conclusion

Overall, the content and main conclusions from this chapter may be summarised as follows:

1. A number of potential factors have been explored as possible factors in the decolourization of MC 540 including the photooxidation, pH effects, and the presence of amphiphilic surfactants
2. Whilst overall, a definitive mechanism for the decolourisation proved elusive, neither singlet oxygen nor pH are major factors
3. It appeared also that the presence of increasing concentrations of amphiphile SDS resulted in a diminution of decolourization
4. As part of this study, a simple spectrophotometric method for following gelation times on the basis of light scattering emerged. This method is currently being explored in more detail within the group as a broad-based approach to examining gelation times.

Chapter 5 Diffusional characteristic of small and large molecules in the SHG

In order to give a more detailed description of a typical diffusion ordered spectroscopy (DOSY) experiment, it is important to first understand all of the parameters which must be controlled in order to attain the diffusion coefficient of a molecule in an NMR sample. To understand how the diffusion coefficient has been calculated, need at the beginning to explain it in more details about the mathematical expression and the theory behind it.

5.1 Molecular Diffusivity in Water and the Gel Phase. The Stokes-Einstein Model

The underlying core scientific theory for the DOSY concept is centred on the relationships developed by Stokes and Einstein, in which expression for the diffusion constant for a molecule in solution is expressed by the following equation:

$$\boldsymbol{D = \frac{RT}{N}.\frac{1}{6\pi.Z.r}}$$

Equation 5-1

In which: D represents the diffusion constant of the molecule under investigation, R the gas constant, T the absolute temperature, Z the viscosity of the diffusion medium, N Avogadro's number and r the hydrodynamic radius of the molecule. Equation 5-1 represents the Stokes-Einstein equation[133].

5.1.1 Derivation of the Stokes-Einstein Equation[133]

The relationship between molecular movement and diffusion in a liquid medium was first expressed by Einstein, under the condition that the particles move independently from each other:

$$\boldsymbol{D = \frac{\bar{\Delta}^2}{2t}}$$

Equation 5-2

The relation contains within it an expression of the diffusion constant D in terms of $\overline{\Delta}^2$ which represents the mean square of the deviation of the molecule in a given direction over time t. If the assumption is made that the molecules possess the same kinetic energy as they would as gas molecules at the same temperature, then the following equation is satisfied:

$$\overline{\boldsymbol{\Delta}}^{\boldsymbol{2}} = \frac{\boldsymbol{2.T.R}}{\boldsymbol{N}} . \frac{\boldsymbol{t}}{\boldsymbol{C}}$$ **Equation 5-3**

Where assumptions are centred on the ideal gas law, with *R* representing the gas constant, *N* Avogadro's number, *T* the absolute temperature and finally, *C*, which is a constant representing the frictional resistance of the molecule, which defines the liquid phase (as molecules of an ideal gas have no intermolecular interactions). Substitution of Equation 5-2 into Equation 5-3 yields:

$$\boldsymbol{D} = \frac{\boldsymbol{R.T}}{\boldsymbol{N}} . \frac{\boldsymbol{1}}{\boldsymbol{C}}$$ **Equation 5-4**

Stokes' relation involves the demonstration that a hydrodynamic relation holds for particles of a spherical nature, which move in a medium consisting of small molecules relative to the diffusing molecule:

$$\boldsymbol{C} = \boldsymbol{6\pi} . \boldsymbol{Z} . \boldsymbol{r}$$ **Equation 5-5**

Where *r* is equal to the hydrodynamic radius of the particle and Z represents the viscosity of the medium of diffusion. Finally, by substituting Equation 5-5 in Equation 5-4, we get Equation 5-1

5.1.2 The Validity of the Stokes-Einstein Equation

Before any further investigation is made on the basis of this theory, it would be sensible to ascertain the validity of the results of the equation in comparison to experimental data. Studies conducted by Thovert into the diffusion constants of 130 organic substances concluded that the diffusion constant tends to vary inversely as the viscosity of the solvent, which is in coherence with the Stokes-Einstein equation[133].

Further investigations conducted by Cheng *et al.* using polystyrene latex particles (which are similar in size to virus particles) demonstrated values for intrinsic viscosity which were in agreement to the Einstein theory, furthermore, it was confirmed that the diameter of the latex particles showed conformity to the Stokes-Einstein law[134]. Based on the evidence from this literature, it is clear that the Stokes-Einstein equation forms a good theoretical basis for the foundations of this chapter.

It is clear that molecular diffusion behaviour will not be consistent when transferring between aqueous solution and gel phase media. The reason for the difference between the two is the viscosity of each phase, which we have seen has an inverse effect on the diffusion constant for a given molecule. It is obvious that the gel phase will have a higher viscosity than the aqueous phase due to the presence of the particulate aggregate polymer network that makes up the gel phase, and this will be one of the main contributing factors in the difference between the diffusion constants of the same molecule in each phase.

5.2 The Use of Diffusion Ordered Spectroscopy (DOSY) to Measure Molecular Diffusion

Standard nuclear magnetic resonance (NMR) experiments utilise NMR active nuclei and place them in the presence of an external magnetic field, which causes alignment of the nuclear magnetic moment with the external field. When the external magnetic field is constant and homogeneous, the populations of the energy levels of the nuclei at thermal equilibrium have specific values. When an oscillating magnetic radio frequency (RF) field is applied in the transverse plane to the external magnetic field, this causes a change in the population of the energy levels of the nuclei exposed to the transverse field, and the generation of a new magnetic moment along the plane of the RF field, whose amplitude is proportional to the number of nuclear spins present in the sample, which is dependent on the type of nuclei present[98]. As soon as the RF field is removed, the system (nuclear spins) realigns with the external magnetic field and the rate at which this realignment occurs is characterised by the longitudinal (T_1) and transverse (T_2) relaxation times. The relaxation times represent a loss of coherence in the plane which the RF field was applied. The decaying signal (realignment) of nuclear spins is used in the production of conventional one dimensional NMR spectra, by applying a Fourier-transform operation to the acquired free induction decay time signal, a frequency domain spectrum is acquired[100].

One dimension that is constant for all nuclei in a molecule is the diffusion constant[100], and its connection to the molecular structure is based on the ideas developed by the Stokes-Einstein relation (*vide supra*) in the way that the diffusion constant depends inversely on the frictional resistance of the molecule[100].

The implementation of diffusion ordered NMR spectroscopy (DOSY) is possible as pulse magnetic field gradient NMR experiments can provide information about translational motion[100, 101]. The principle of obtaining the DOSY spectrum is similar to that of conventional two dimensional NMR, in that a variable is selected which modulates the signal which is detected, and then this variable is incremented to produce a spectrum related to the translation (diffusion) of the investigated molecule. The variable selected in the case of DOSY experiments is the areas of magnetic field gradient pulses[100].

In order to give a more detailed description of a typical DOSY experiment, it is important to first understand all of the parameters which must be controlled in order to attain the diffusion coefficient of a molecule in an NMR sample. Using pulsed field gradients, molecules in a sample can be spatially labelled based on their position in the tube. The Stimulated echo (STE) sequence allows for the calculation of the diffusion coefficient of a molecule in an NMR sample. The STE sequence begins with a 90º radiofrequency pulse. After a delay of time τ, the first gradient pulse δ is applied, the purpose of which is to encode the positions of the molecules. After the first gradient pulse, the molecules in the sample are allowed to diffuse for time Δ before a second gradient pulse δ is applied and the diffusion coefficient can be calculated.

The best way to imagine a PFG NMR experiment which uses a stimulated echo (STE) sequence with pulse field gradients (PFG's) is to imagine layers of the sample scattered along, and lying perpendicular to the z axis[135]. These layers experience a uniform magnetic field B_0 (Figure 5-1) creating a magnetisation ribbon in the co-ordinate frame as shown in the bottom left of Figure 4[135]. The pulse field gradient has the effect of twisting this ribbon into a helix[135]. The layers also contain a large number of nuclear spins and have an associated magnetisation vector which is assigned to the positions of the layers on the z-axis [135]. The STE experiment starts with a 90˚ radio frequency pulse in respect to the z-axis, which rotates all the magnetisation vectors to the y-direction, and the signal detected along the y-axis decays in amplitude over time due to NMR dephasing which results from magnetic inhomogeneity's which are amplified by the PFG[135]. In order to detect a signal, the magnetisation vectors must be refocused, which requires a sequence with two gradient pulses of equal magnitude δ[135] (The STE sequence). The first pulse utilises position dependent phase angles to encode nuclear positions and sensitizes the sample to diffusion[135]. The second pulse reverses the encoding of the first pulse and brings the magnetisation vectors back into the yz plane, forming an echo, and the amplitude of the echo is used to calculate the diffusion constant[135].

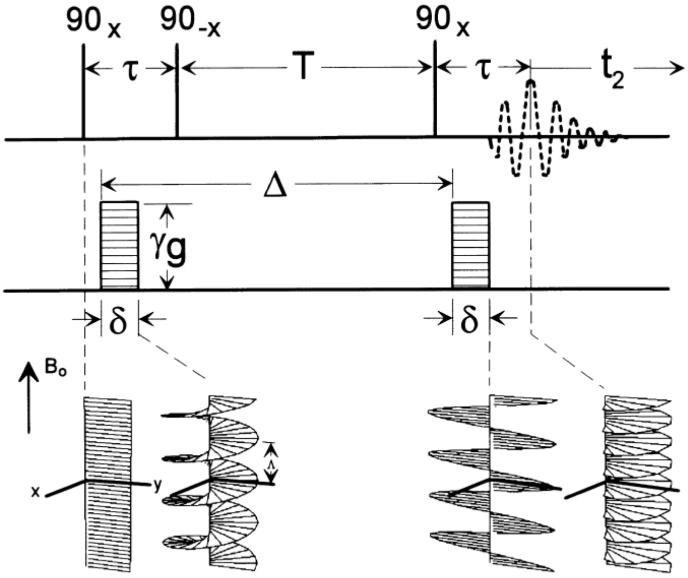

Figure 5-1: The Stimulated Echo Sequence (STE). Top: shows the sequence of pulses and the time differences *τ* and T between the first and second, and second and third pulses respectively. Middle: image demonstrating the refocusing of the magnetisation after the particles are allowed to diffuse for time Δ. Bottom: depiction of the magnetisation helix as a result of the gradient pulse.

The software used to interpret the data acquired from the DOSY experiments in this chapter will be the GNAT software. This software is freely available and is capable of comparing data from 3 different major manufacturers (Bruker, JEOL and Varian). It must be noted that DOSY is actually the name for a processing method for pulse-field-gradient NMR data but the technique has adopted the name DOSY and so this paper will refer to the technique as DOSY to follow suit[136]

DOSY spectroscopy is able to separate the NMR signals from the different components within an NMR sample, based on the hydrodynamic radius of the species resulting from its diffusion coefficient. The typical DOSY experiment consists of recording a series of spectra, with incremented pulsed field gradient (PFG) amplitude in a stimulated echo (STE) experiment. The one dimensional NMR spectrum is then transformed into a two dimensional spectrum by performing an exponential fit on the decaying NMR signal amplitude as a function of increasing PFG amplitude and extracting the diffusion constant from the equation used to produce the fit. In an ideal PFG-STE experiment, the decay of the signal amplitude with respect to increasing PFG amplitude is described by the Stejskal-Tanner equation[102].

$$\boldsymbol{S} = \boldsymbol{S}_{\circ}\boldsymbol{e}^{-\mathbf{D}\boldsymbol{\gamma}^{2}\boldsymbol{\delta}^{2}\boldsymbol{g}^{2}\bar{\Delta}} \qquad \textbf{Equation 5-6}$$

Where S = signal amplitude, S_0 = echo amplitude in absence of diffusion, D = diffusion coefficient, δ = gradient pulse width, γ = magnetogyric ratio and $\bar{\Delta}$ is the diffusion time corrected for the effects of finite gradient pulse width[102].

In practice, there may be significant deviations from an exponential decay profile and these deviations arise from the variation of the magnitude of the applied PFG over the entire area of the NMR sample. In other words, if all of the diffusing components in the NMR sample do not feel the same strength of gradient pulse, they will have different diffusional attenuation with respect to increasing gradient strength[102].

The standard DOSY Processing tool built into the GNAT software is high resolution (HR) DOSY. In this method, the experimental data for the NMR signal amplitude decay is fitted to the Stejskal-Tanner equation. This processing method should only be used when there are only one diffusing species in the sample, as the fitting assumes that all NMR signals arise from a single component i.e. one exponential decay profile. This technique, if used appropriately results in standard errors (arising from the fitting process) in the diffusion coefficient of 0.2 %. The best use of HR DOSY is when experimental NMR signals are well resolved throughout the series of spectra. However this is rarely the case, and there is usually some signal overlap which results in inaccurate values for the diffusion coefficient of the overlapping signals[102].

When there is more than one component under investigation, standard HR DOSY should be replaced with multi-exponential fitting to the experimental data. The multi-exponential approach to the fitting of the experimental data accounts for overlapping signals by separating signals which differ greatly in their diffusion coefficient. If the two overlapping signals are assumed to be the sum of two exponentials i.e [102]:

$$\boldsymbol{S} = \boldsymbol{S}_{\circ}\boldsymbol{A}\boldsymbol{e}^{-\mathrm{D}\gamma^2\delta^2 g^2 \bar{\Delta}} + \quad \boldsymbol{S} = \boldsymbol{S}_{\circ}\boldsymbol{B}\boldsymbol{e}^{-\mathrm{D}\gamma^2\delta^2 g^2 \bar{\Delta}} \qquad \textbf{Equation 5-7}$$

Where components A and B add together to form the overall signal. The differing diffusion coefficients of each component allows the signals to be separated. This approach works well for signals which have significantly different diffusion coefficients.

Fundamentally, the quality of the experimental data is key to a successful DOSY experiment. The GNAT software allows for careful editing of the raw data to optimise it for DOSY processing, and these methods will be explored herein.

5.3 Optimisation of DOSY Data Using the GNAT Software

Once the files have been converted using JEOL Delta software, it is possible to import the files into the GNAT software. An introductory manual[137] to the GNAT software has recently been produced and details the processing tools available on the software. This section is dedicated to describing the procedure for optimising the imported data to produce the most accurate and clean DOSY spectra using the GNAT software. All the data used in this report is processed in a manner which produces the best DOSY spectrum for that dataset (see the experimental section for full processing details), below is a detailed example using the AMP.2Na sample within SHG media.

5.3.1 Fourier Transformation using Lorentzian Window Function Multiplication

The first step in the process is the Fourier Transformation of the imported FID. Figure 11 A) shows the imported raw FID with no processing performed on it. The first step is converting this time domain FID spectrum into a frequency domain spectrum and this is done through the mathematical operation known as Fourier Transform, the intricacies of which can be found elsewhere[138]. Without utilising the window function tool, the raw FID can be Fourier Transformed to give a frequency domain spectrum. It would be unwise to continue with this spectrum in the case of DOSY processing as there are some issues with truncation artefacts such as sinc-wiggles which arise from acquisition times which are too short, and truncation of the FID which occurs during data collection. It is important to remove these errors as DOSY processing methods rely heavily on clean, well resolved peaks. To resolve these issues using the GNAT, a window function can be applied to the FID. The window function multiplies the FID using Lorentzian (*lw*) and Gaussian *(Gw)* parameters by the function below (where t is time)[137]

$$e^{-t\,\pi\,lw-\left(\frac{\pi\,gw\,t}{2\sqrt{\ln(2)}}\right)^2} \qquad \textbf{Equation 5-8}$$

The user can enter values for *lw* and *gw* and doing so alters the linewidth of the resulting spectrum. In the case of this example, values of *lw* = 1 and *gw* = 0 were used so that the signal decays in an exponential fashion (see green decay curve in Figure 5-2). Doing so removes sinc-wiggles which can be seen in the resultant spectrum.

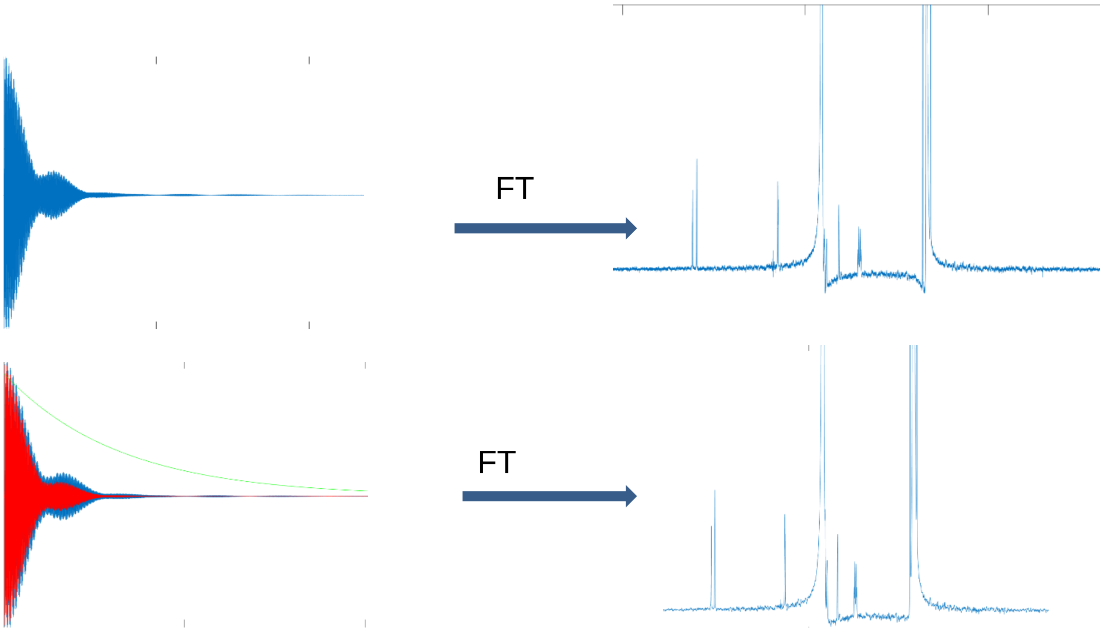

Figure 5-2: Fourier transformation of FID for AMP.2Na sample data. Showing the frequency domain spectrum before and after a window function is applied.

5.3.2 Phase Correction

The next step in appropriately processing DOSY Data is correcting for phase errors in the resulting frequency domain spectrum. The phase of a signal in an

NMR spectrum is the degree to which NMR resonances are above or below the baseline (the amount of absorption/dispersion character in the specific signal). The sign of the phase (positive/negative or real/complex) is determined in the FID (periodic time domain function) by the value of the function at time = 0 [139] and which axis the magnetisation vector lies on after the refocusing pulse, relative to the receiver[139]. The phase of an NMR spectrum should be corrected so that the peak in the real spectrum is in entirely absorption mode as this allows for the exclusion of complex data points in the resulting DOSY spectrum which, if not removed, give rise to positive and negative signals which ultimately cancel each other out.

The GNAT Software offers both manual and automatic phase correction, the latter utilises a Hilbert Transformation to correct the phase of the frequency spectrum, details of this transformation can be found elsewhere[140]. In the case of this example, automatic phase correction was applied. Figure 5-3 depicts pre- and post- automatic phase correction of the frequency domain spectra for the AMP.2Na data set.

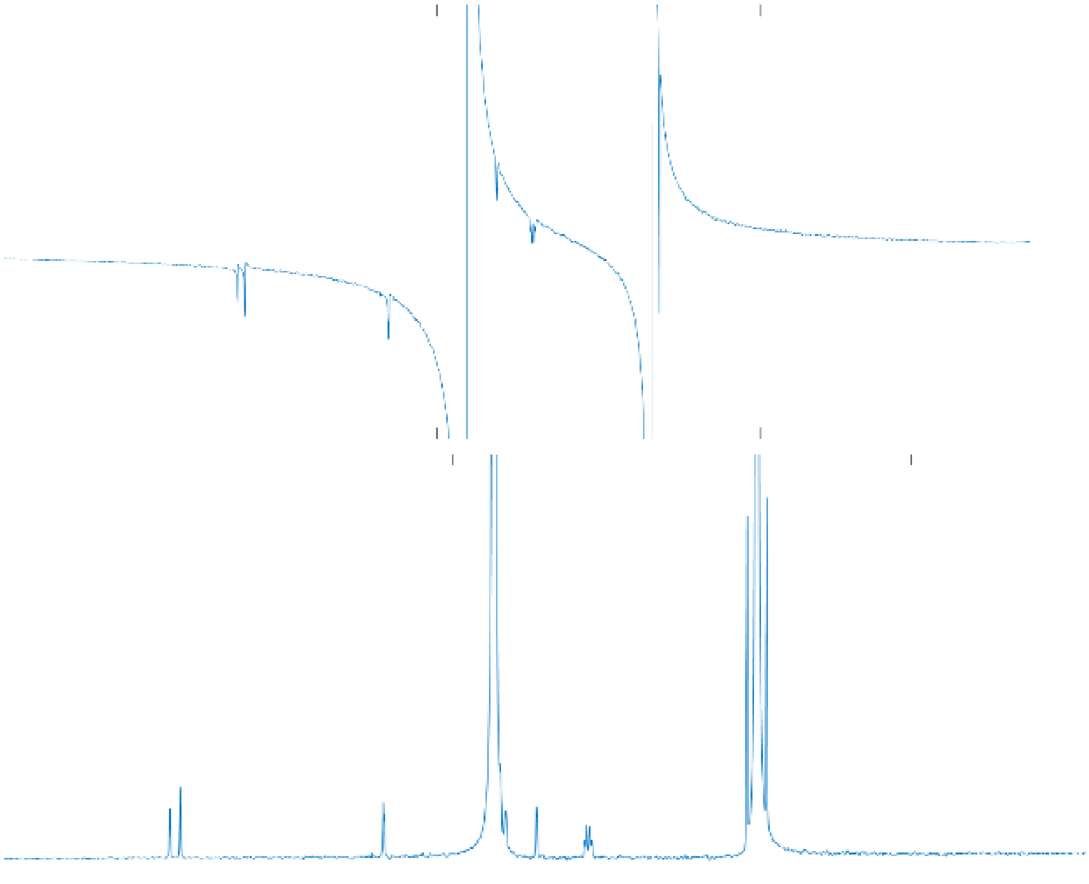

Figure 5-3: Top: Frequency domain spectrum before phase correction, note the dispersion peaks are most pronounced for the broad water and acetic acid signals. The bottom: frequency domain spectrum after automatic phase correction, all peaks are in absorption mode.

5.3.3 Baseline Correction

After phase correction, the next important step in the processing of the raw DOSY data is to correct the baseline of the frequency domain spectrum. Distorted baselines are a result of the corruption of the first few data points in the FID. The errors in these data points lead to low frequency modulations in the Fourier-transformed frequency domain spectrum which create a distorted baseline. It is necessary to correct such errors before DOSY processing as they offset intensity values which lead to inaccuracy when assigning peaks[141]. The GNAT software offers both manual and automatic baseline correction and the latter will be used in this example. In automatic baseline correction, the regions of the spectrum that contains signal are selected automatically, after all signal regions have been selected the remaining baseline region is fitted to a user selected polynomial order and this is then subtracted from the spectrum. In the case of this example the polynomial order was chosen to be 5 so that the fitted curve would fit 5 constraints, and have a higher maximum number of inflection points included into the fitting, to account for regions of the spectrum where some dispersion line-shape peaks still remain after phase correction.

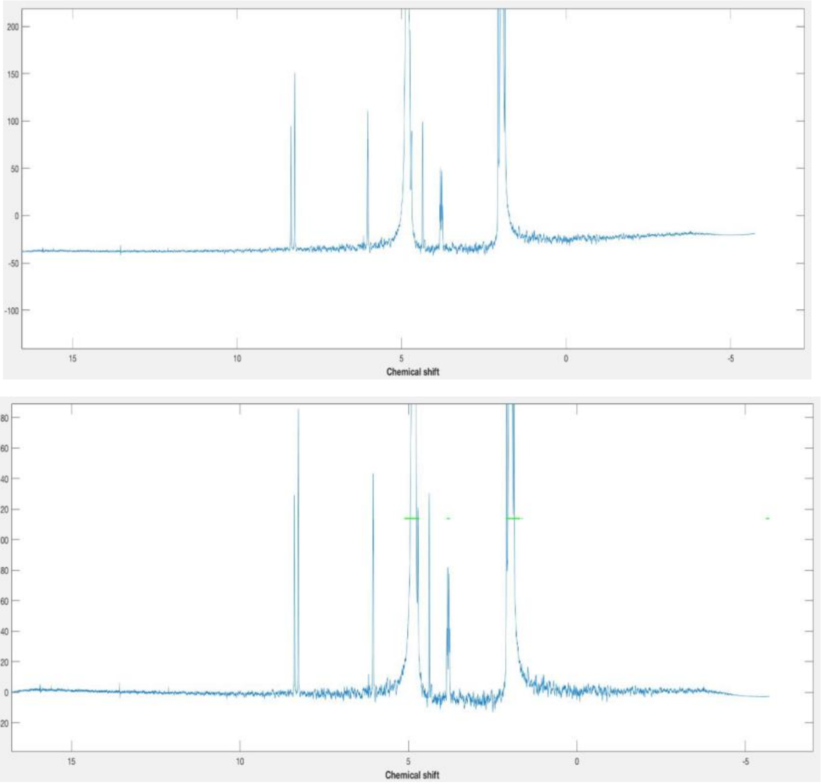

Figure 5-4: Images of the frequency domain spectrum for the AMP.2Na SHG data set. Automatic baseline correction was used and the polynomial order was set to 5. Top image before baseline correction and the baseline on -40 x-axis and after applying base line correction brought to 0.

5.3.4 Reference Deconvolution

Reference deconvolution has been proven to correct systematic errors in NMR spectra[142]. Errors such as line shape distortions, phase errors and frequency shifts can be corrected by correcting a resolved experimental reference signal against an ideal reference signal[137]. Reference deconvolution is particularly important in DOSY analysis because the processing methods rely heavily on the linearity of the data i.e. the shapes of the signals of individual resonances should remain the same throughout the array of spectra[137]. Figure 5-5 showed the frequency domain spectrum before reference deconvolution. Top right showing overlapping signals from water and AMP.2Na molecule. Middle left and right highlighting the left (red) right (green) and centre (black) lines for the selected reference signal (signal 2) this peak was selected as there was poor shimming which could be corrected by adding some Gaussian fitting parameters to the peak. The bottom right show the resulting spectrum after reference deconvolution of peak 2.

With lw=-0.1 and gw=10 line shape parameters to broaden the peaks to account for errors throughout the array of spectra.

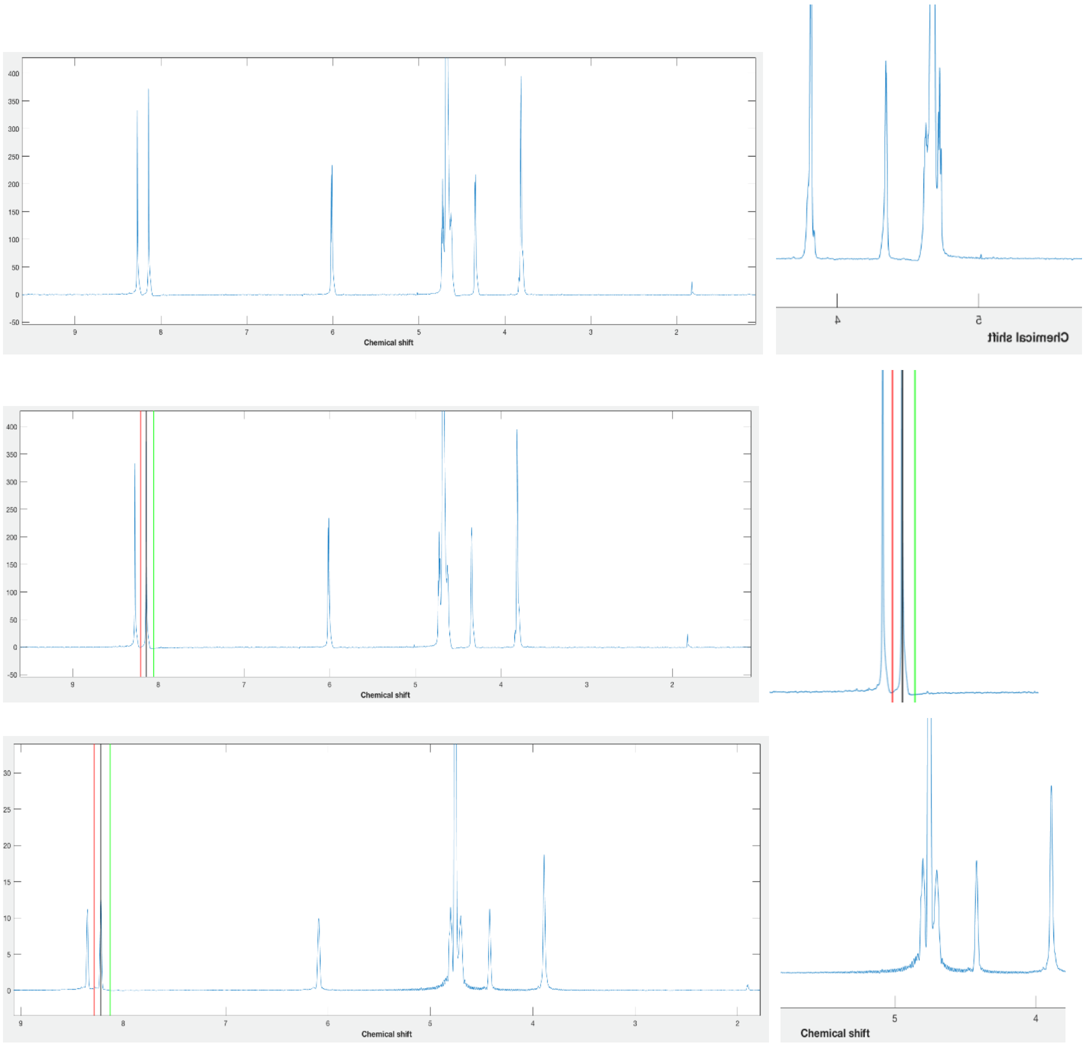

Figure 5-5: Reference deconvolution of AMP.2Na aqueous data.

5.4 Selection of Molecular Systems for DOSY Investigation

Our original plan was to investigate the difference in the diffusional behaviour of four molecules between an SHG phase and an aqueous phase:

(i) Adenosine phosphates (AMP, ADP and ATP) as exemplars of charged species
(ii) Ribose as an exemplar of a small prebiotically relevant molecule

Most of our work has focused on (i) and (ii) as there were several technical problems with SDS which we are yet to fully overcome. Nevertheless, each system will be described in turn.

5.4.1 Adenosine Phosphate Systems

Adenosine monophosphate disodium salt (AMP.2Na), adenosine diphosphate disodium salt (ADP.2Na), and adenosine triphosphate disodium salt (ATP.2Na). The latter two compounds are commercially available and were purchased from Sigma. The former was synthesised from 0.1 g, 2.88 x10^{-4} mol adenosine 3' monophosphate (from Sigma-Aldrich) *via* dissolution into a minimum amount of D_2O (*ca.* 3mL), and then addition of 0.0230g, 5.75x10^{-4} mol $NaOH_{(s)}$ (ground from pellets) and evaporating this mixture to yield a white solid powder, which was dried in an oven at 60°C for 24 hrs to yield the disodium salt of adenosine monophosphate, AMP.2Na (0.0943 g, 85%). The disodium salts of each molecule were selected for use as they are suitably soluble in the media used in these investigations and have the same ionic strength.

5.4.2 1D NMR analysis

Initial 1D NMR experiments were conducted on the samples were to be subjected to DOSY investigations, so that reference chemical shift values could be determined for later use in DOSY analysis to assess the diffusional behaviour of the molecule. The NMR solvent used throughout all experiments is D_2O, the significance of this is that all ^1H NMR signals originate from the adenosine unit of each molecule (AMP,ADP and ATP) see Figure 5-6 below.

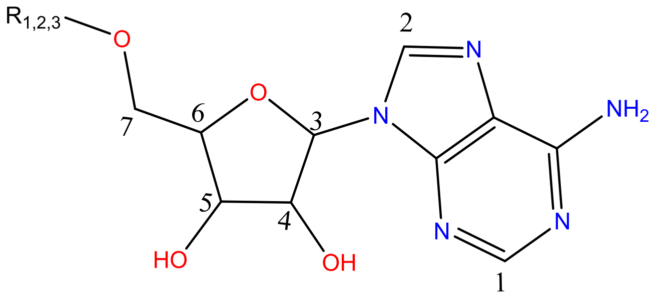

Figure 5-6: Diagram of adenosine subunit that detectable by ^{1}H NMR signals for the compounds AMP, ADP, and ATP under DOSY investigation. numbers indicate ^{1}H environments which will be generated NMR signal and can be identified in the DOSY analysis.

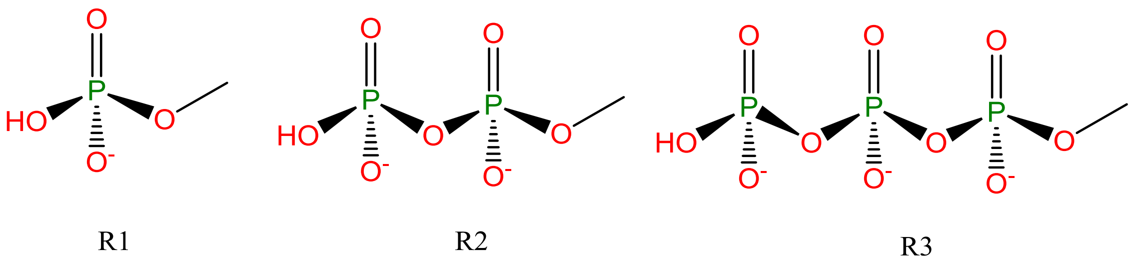

Figure 5-7: Schematic of the three compounds under investigation. Adenosine core unit is common amongst all three molecules under investigation. R1 = Monophosphate subunit (AMP), R2 =Diphosphate subunit (ADP), R3 = Triphosphate subunit (ATP).

The ^{1}H NMR Spectra for AMP, ADP and ATP are summarised in Table 5-1 (See appendix for full ^{1}H NMR spectra). The first set of data analysed are for samples at neutral pH, and the molecules under investigation in this first instance are in their respective disodium salt forms. In the second set of data, the pH of the hydrogel solution was adjusted to pH 12 via NaOH addition, as a result, all of the hydroxyl groups on the phosphate side-chains are deprotonated (high charge state). The reason for testing at a high pH regime is to see whether or not the charge state of the molecule affects the diffusional behaviour, be it through interactions with the silica hydrogel particulate polymer network or through variations to molecular size due to the presence of counter-ions which may alter the hydrodynamic radius of the diffusing molecule. For each data set the NMR signals are referenced in relation to

Figure 5-6 and Figure 5-7

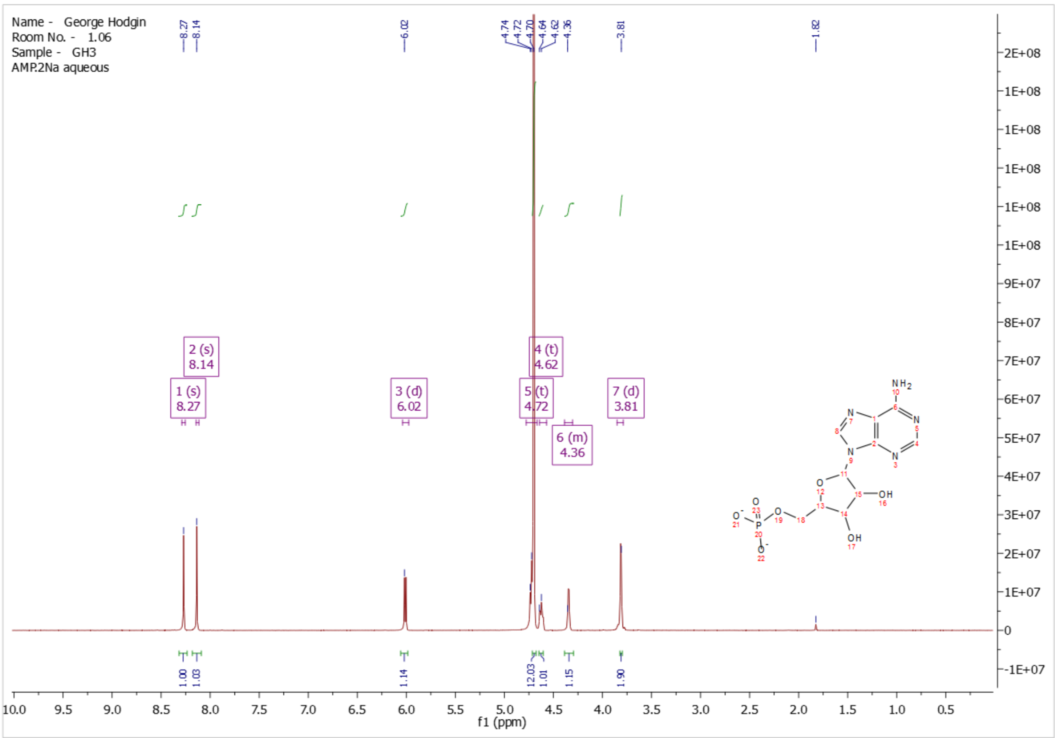

Figure 5-8: 1H NMR spectra AMP.2Na aq D_2O, 1H NMR (400 MHz, D2O) δ 8.27 (s, 1H), 8.14 (s, 1H), 6.02 (d, 1H), 4.72 (t, 1H), 4.62 (t, 1H), 4.39 – 4.31 (m, 1H), 3.81 (d, 1H).

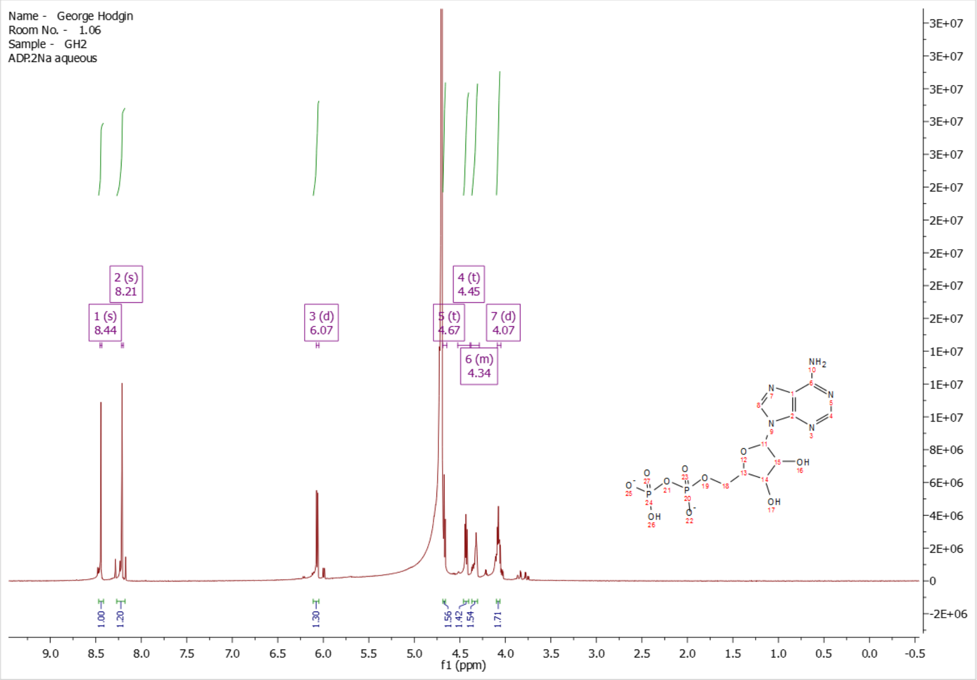

Figure 5-9: ADP.2Na aq D_2O 1H NMR (400 MHz, D_2O) δ 8.44 (s, 1H), 8.21 (s, 1H), 6.07 (d, J = 5.6 Hz, 1H), 4.67 (t, J = 5.4 Hz, 1H), 4.45 (t, 1H), 4.38 – 4.29 (m, 2H), 4.07 (d, 1H).

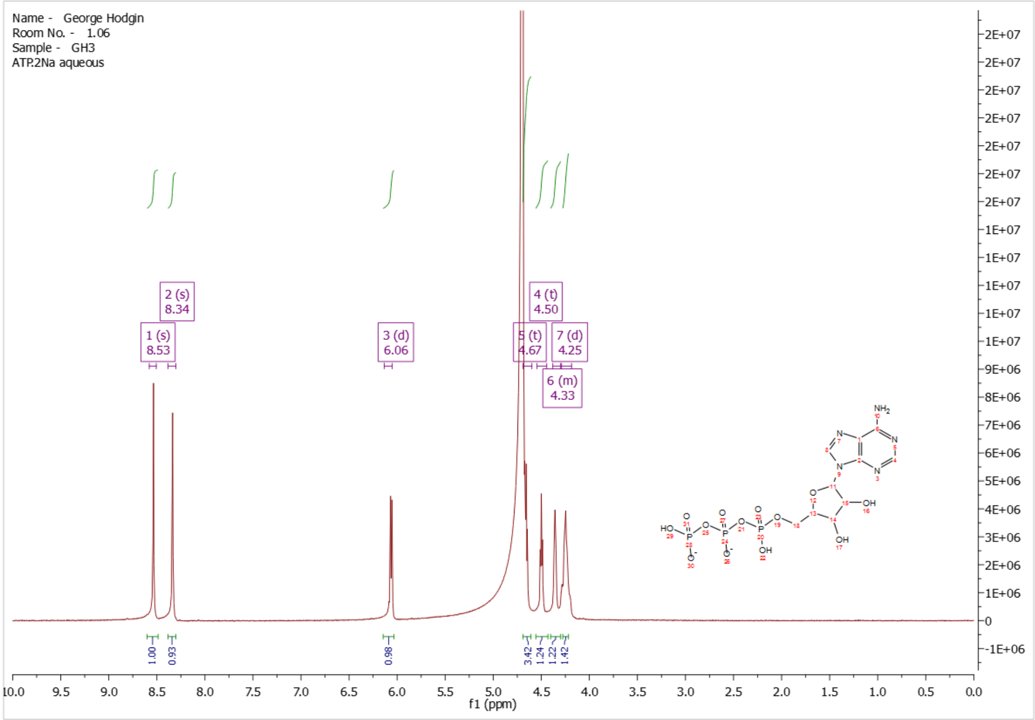

Figure 5-10: ATP.2Na aq D_2O ^1H NMR (400 MHz, D_2O) δ 8.53 (s, 1H), 8.34 (s, 1H), 6.06 (d, J = 5.4 Hz, 1H), 4.67 (t, 3H), 4.50 (t, J = 4.4 Hz, 1H), 4.38 – 4.30 (m, 1H), 4.25 (d, J = 3.7 Hz, 2H).

Table 5-1: Summarised NMR data collected for each molecule in both aqueous and SHG media. ^1H NMR Environment chemical shift (δ) / ppm

Medium	Molecule	1	2	3	4	5	6	7
D_2O	AMP.2Na	8.27	8.14	6.02	4.62	4.72	4.39-4.31	3.81
D_2O	ADP.2Na	8.44	8.21	6.07	4.45	4.67	4.38-4.29	4.07
D_2O	ATP.2Na	8.53	8.34	6.06	4.50	4.67	4.38-4.30	4.25
SHG	AMP.2Na	8.35	8.12	5.99	4.24	-	4.39-4.32	4.00
SHG	ADP.2Na	8.35	8.10	5.98	4.23	-	4.42-4.32	4.01
SHG	ATP.2Na	8.40	8.13	5.97	4.29	-	4.51-4.42	4.14
pH 12 SHG	AMP	8.35	8.23	6.01	4.68	-	4.34	3.80
pH 12 SHG	ADP	8.37	8.12	6.02	4.39	-	4.28	4.03
pH 12 SHG	ATP	8.36	8.10	5.98	4.41	-	4.25	4.10
pH 12 D_2O	AMP	8.30	8.16	6.06	4.45	4.72	3.89	3.85

pH 12 D_2O	ATP	8.44	8.17	6.06	4.33	4.50	4.19	4.16
pH 12 D_2O	ADP	8.34	8.03	5.95	4.33	-	4.20	3.91
pH 12 D_2O	ATP	8.44	8.17	6.06	4.33	4.50	4.19	4.16

From this initial investigation, it is clear that the ^{1}H spectrum for each molecule is similar, and that the peaks selected will be easily comparable through DOSY analysis. It should be noted that the SHG ^{1}H NMR spectra have two solvent signals, one occurring at ~4.68 ppm from water (present in the sodium silicate solution) and one at ~1.86 ppm from acetic acid (necessary to form SHG phase). The signal from the acetic acid methyl group does not impede the peaks for the molecules under investigation and will not affect the DOSY analysis. However, the water peak can overlap with reference peaks 4 and 5, this is problematic when carrying out DOSY analysis as the diffusion peaks may merge together and the average diffusion coefficient of the two peaks will be presented on the DOSY spectrum. Where this is the case and the results for each signal differs greatly, the data from these reference peaks will be ignored, and only the well resolved peaks which remain unaffected by overlapping chemical shift will be used.

5.4.3 Analysis of DOSY Spectra produced by JEOL Software

The data for DOSY processing using the GNAT software was collected on a JEOL spectrometer. JEOL has its own DOSY processing software and using this it is possible to obtain a DOSY Spectrum which demonstrates the reference peaks which will be identified using the GNAT program, without going into details of the processing methods. The JEOL software automatically applies some processing to the raw data (Fourier Transform, phase and baseline correction), this processing can be altered in the JEOL Delta program. This modification is necessary for processing DOSY data with GNAT.

If imported without removal of all processing steps, the data imports as a processed spectrum rather than a raw FID. The problem with this is that the processing methods which are so useful on the GNAT program cannot process an already processed spectrum. The data should be saved in JEOL Generic format. Once the file conversion (using the JEOL Delta program) has successfully completed the data saves as 2 files, one file containing the FID

(.Bin) and one containing the processing methods (.hdr). Both files should be present in the same directory for the file import into the GNAT to be successful.

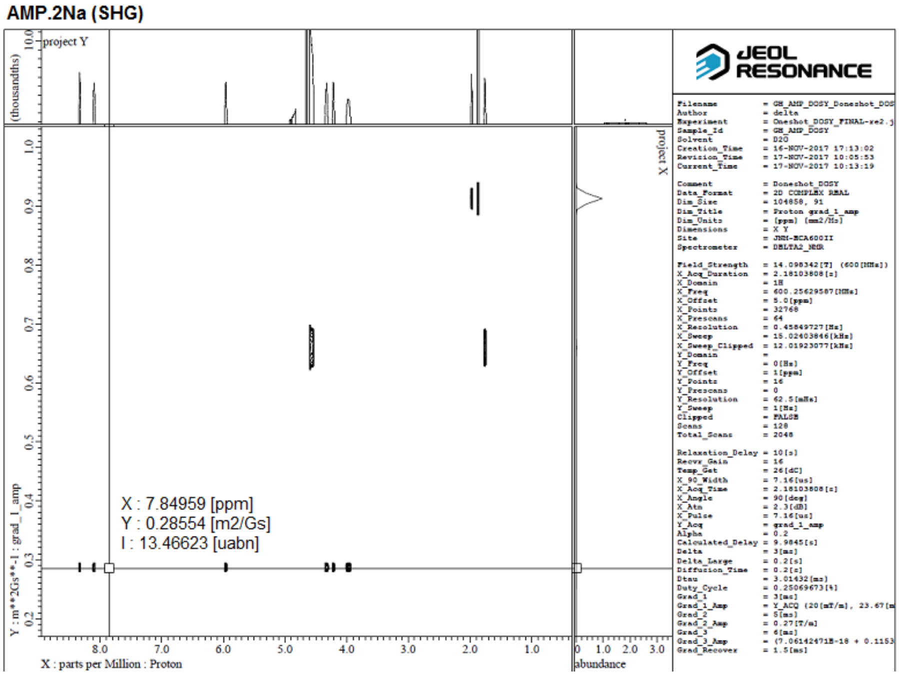

```
Filename           = GH_AMP_DOSY_Doneshot_DOS
Author             = delta
Experiment         = Oneshot_DOSY_FINAL-re2.j
Sample_Id          = GH_AMP_DOSY
Solvent            = D2O
Creation_Time      = 16-NOV-2017 17:13:02
Revision_Time      = 17-NOV-2017 10:05:53
Current_Time       = 17-NOV-2017 10:13:19

Comment            = Doneshot_DOSY
Data_Format        = 2D COMPLEX REAL
Dim_Size           = 104858, 91
Dim_Title          = Proton grad_1_amp
Dim_Units          = [ppm] [mm2/Ms]
Dimensions         = X Y
Site               = JNM-ECA600II
Spectrometer       = DELTA2_NMR

Field_Strength     = 14.098342[T] (600[MHz])
X_Acq_Duration     = 2.18103808[s]
X_Domain           = 1H
X_Freq             = 600.25629587[MHz]
X_Offset           = 5.0[ppm]
X_Points           = 32768
X_Prescans         = 64
X_Resolution       = 0.45849727[Hz]
X_Sweep            = 15.02403846[kHz]
X_Sweep_Clipped    = 12.01923077[kHz]
Y_Domain           =
Y_Freq             = 0[Hz]
Y_Offset           = 1[ppm]
Y_Points           = 16
Y_Prescans         = 0
Y_Resolution       = 62.5[mHz]
Y_Sweep            = 1[Hz]
Clipped            = FALSE
Scans              = 128
Total_Scans        = 2048

Relaxation_Delay   = 10[s]
Recvr_Gain         = 16
Temp_Get           = 26[dC]
X_90_Width         = 7.16[us]
X_Acq_Time         = 2.18103808[s]
X_Angle            = 90[deg]
X_Atn              = 2.3[dB]
X_Pulse            = 7.16[us]
Y_Acq              = grad_1_amp
Alpha              = 0.2
Calculated_Delay   = 9.9845[s]
Delta              = 3[ms]
Delta_Large        = 0.2[s]
Diffusion_Time     = 0.2[s]
Dtau               = 3.01432[ms]
Duty_Cycle         = 0.25069673[%]
Grad_1             = 3[ms]
Grad_1_Amp         = Y_ACQ (20[mT/m], 23.67[m
Grad_2             = 5[ms]
Grad_2_Amp         = 0.27[T/m]
Grad_3             = 6[ms]
Grad_3_Amp         = (7.06142471E-18 + 0.1153
Grad_Recover       = 1.5[ms]
```

Figure 5-11: DOSY Spectrum produced through the JEOL software, showing the reference peaks for the AMP disodium salt molecule in the SHG diffusion medium (highlighted with a horizontal line).

5.5 Analysis of the Plot Residuals for each Dataset

The quality of the experimental data is assessed through the quality of the fitting to the residual plot of the signal amplitude vs the squared gradient amplitude. This plot shows the effect of increasing the squared gradient amplitude on the amplitude of each individual ^{1}H NMR signal. In an ideal case, the signal amplitude should decay in an exponential manner with respect to increasing squared gradient amplitude, any deviations from this ideal case lead to inaccuracies in the resulting diffusion constant for that NMR signal. This is a good way of assessing the quality of the data and the choice of processing methods. As the outcome of the data is unexpected by the rules of the Stokes-Einstein equation, it is necessary to analyse the quality of the data so that confidence in the conclusions of the results can be made.

5.5.1 DOSY Processing

After all adjustments are made to the frequency domain spectrum, DOSY processing can be performed on the data. HR-DOSY is the default processing method in the GNAT. This method assumes that each peak originates from one single species and uses a mono-exponential fit of the Stejskal-Tanner equation to produce the DOSY spectrum, this fitting will be used for the aqueous samples. In the case of the SHG phase samples there are multiple components in the sample, namely: water, acetic acid, sodium silicate, D_2O and the molecule under investigation (AMP/ADP/ATP). As a result a multi-exponential fit of the Stejskal-Tanner equation must be performed. Using this method, the number of components is reduced until statistically significant results have been obtained. The number of peaks to be fitted in the DOSY spectrum is determined by the number of integrated peaks in the frequency domain spectrum.
Figure 5-12 shows the DOSY spectrum attained for the AMP.2Na SHG sample.

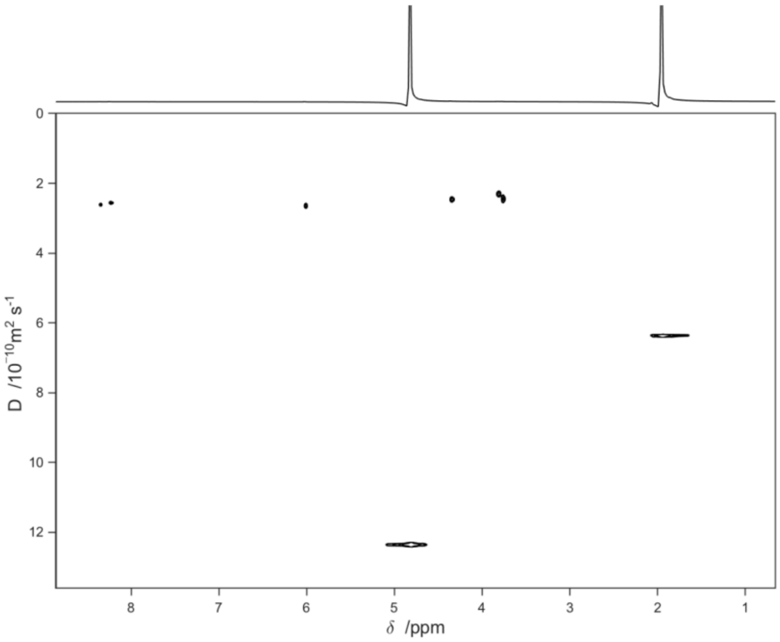

Figure 5-12: The DOSY Spectrum for the AMP.2Na SHG sample data. Here the difference between the diffusion constants of the 3 components which can be detected by 1H NMR in the sample can be seen clearly.

The diffusion coefficients for each individual signal are stored in a data folder automatically. The diffusion coefficient of the molecule is given in units of $D/10^{-10}$ m^2 s^{-1} The error associated with the approximations of the exponential fit is also saved. Table 5-2 shows the diffusion coefficient for each signal for the AMP.2Na SHG sample, relative to the signals in Figure 5-7.

Table 5-2: DOSY results for chemical shift signals relative to Figure 5-12

NMR Signal	Chemical Shift / ppm	Diffusion coefficient / 10^{-10} m^2 s^{-1}	Error / 10^{-10} m^2 s^{-1}
Acetic Acid	1.96	6.36	0.008
7	4.00	2.30	0.066
6	4.36	2.46	0.053
Water	4.83	12.35	0.019
Water	5.13	12.13	0.190
3	5.99	2.64	0.044
2	8.12	2.55	0.02
1	8.35	2.61	0.031

The accuracy of the results for DOSY processing can be assessed through the plot residuals. For each peak, it is possible to assess how the increase in the gradient increment affects the decay of the amplitude of the signal. In a perfect DOSY experiment, the amplitude of the signal should decay exponentially with respect to increasing gradient amplitude, following the Stejskal-Tanner line equation. The DOSY processing routine fits a line to the experimental data and using the GNAT it is possible to check the accuracy of this fitting, and thus the accuracy of the diffusion coefficient for that signal. Figure 5-13 shows the plot residuals for each peak in the resulting DOSY Spectrum.

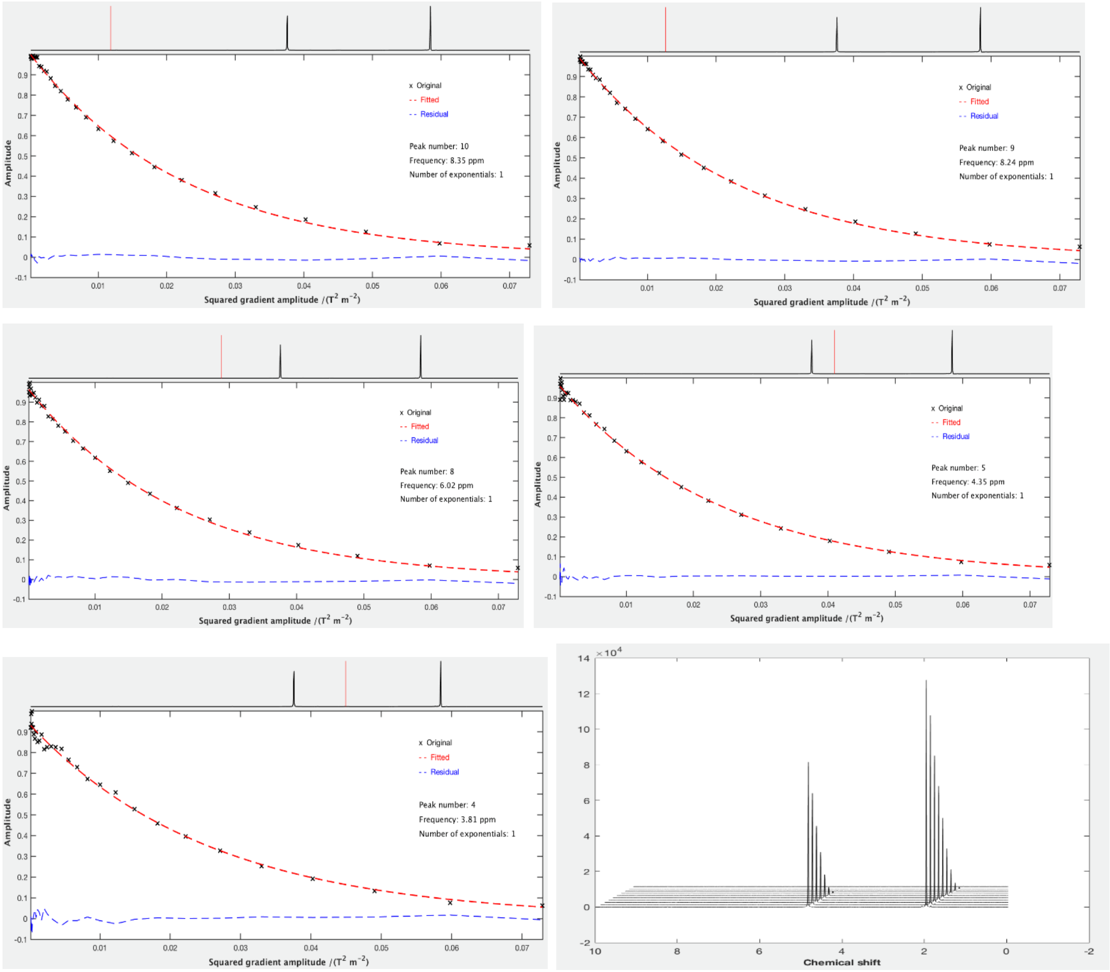

Figure 5-13: Plot of signal amplitude vs squared gradient amplitude for the observed signals in the frequency domain spectrum. The red fitted curve matches well with the experimental data points. The bottom right image shows the decay in signal amplitude over the array of spectra.

The data in this case, fits well with the exponential approximation of the DOSY processing routine and we can be confident in the results for the diffusion coefficients of each signal, however it is necessary to look at how the plots for each signal compare with one another in order to accurately predict the diffusion coefficient of the whole molecule. Should there be any deviation from the exponential fitting, the GNAT software can be used to remove any anomalous data using the ‘Prune’ tool, where any data point in an array of spectra can be selected and missed out when it comes to the final DOSY processing. The ‘Prune’ tool allows the user to make the data better fit to the approximations of the processing routine, and by doing so, it also allows them to reduce the error in the final diffusion coefficient.

5.5.2 DOSY Processing results

The most appropriate manner in which to process DOSY data using the GNAT software has now been demonstrated and can be applied to all the experimental data collected for this research. Hydrogel samples containing ATP, ADP and AMP at both neutral pH (where the molecules under investigation are in their disodium salt forms), and at high pH regime (pH 12) (where all hydroxyl groups are deprotonated) were made for comparison with the same molecules but with only D_2O as the NMR solvent (the aqueous environment). The tables 12 -15 below show the summarised diffusion coefficients of each NMR signal referenced to Figure 5-6 for each sample.

5.5.3 AMP DOSY Results

Summarised below are the results obtained for the DOSY analysis of AMP in the various media (D_2O, pH 12 D_2O, SHG and pH 12 SHG). For details of the NMR processing see Figure 5-8.

Table 5-3: AMP SHG DOSY Results

NMR Signal	Chemical Shift / ppm	Diffusion coefficient / 10^{-10} m^2 s^{-1}	Error/ 10^{-10} m^2 s^{-1}
Acetic Acid	1.96	6.36	0.008
7	4.00	2.30	0.067
6	4.36	2.46	0.053
Water	4.43	12.35	0.019
Water	5.13	12.13	0.190
3	5.99	2.64	0.044
2	8.12	2.55	0.021
1	8.35	2.61	0.032

Table 5-4: AMP pH 12 D_2O Results

NMR Signal	Chemical Shift / ppm	Diffusion coefficient / 10^{-10} m^2 s^{-1}	Error/ 10^{-10} m^2 s^{-1}
7	3.85	3.54	0.031
6	3.89	3.56	0.038
4	4.72	3.67	0.056
5	4.45	3.02	0.217
Water	4.83	15.57	0.158
3	6.06	3.31	0.042
2	8.16	3.39	0.018
1	8.3	3.45	0.031

The tables above detail the diffusion constants for each NMR reference signal (Figure 5-12). At first glance it is clear that in the case of the SHG samples, the water signal interferes with signals 4 and 5. For example, signal 4 in the SHG pH 12 sample has a diffusion coefficient of 4.02 $\times 10^{-10} m^2 S^{-1}$ which is significantly higher than the rest of the reference signals. The higher diffusion constant in this case is due to the overlap between the water signal and the reference signal, this results in an averaged diffusion constant of the two signals. Where this is the case, such peaks should be ignored. In the case of the D_2O samples, the water peak is much less broad, and therefore there is little to no overlap between the water peak and peaks 4 and 5. This means that the value of the diffusion constant for these signals is that of the reference signal only. A more clear comparison of the effect of changing the diffusing media can be seen in Figure 5-5 below.

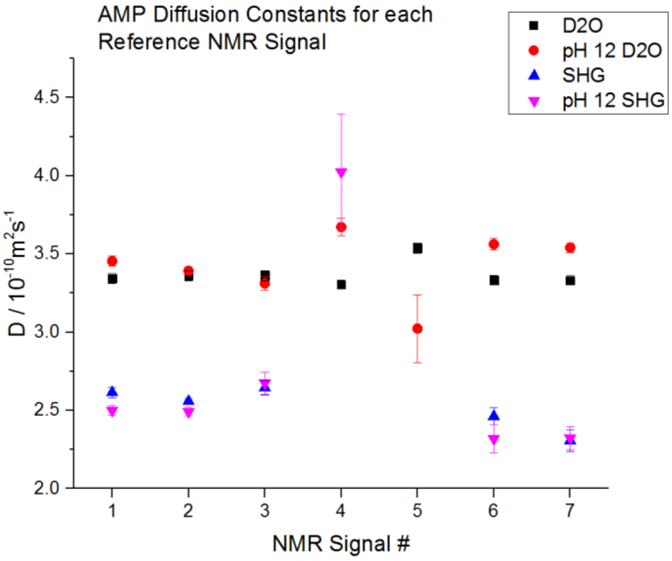

Figure 5-14: A graph to show the diffusion constants of each reference NMR signal for AMP, in each of the 4 different media.

From Figure 5-5 we can see that there is a clear difference in the diffusion constants of the reference NMR Signals of AMP when moving from an aqueous (D_2O) media to an SHG media. This phenomenon is to be expected, as the Stokes-Einstein equation predicts that diffusional behaviour varies inversely with viscosity. If reference signal 4 is removed from the pH 12 SHG dataset (due to water interference) a linear fit can be performed on the data so as to achieve a value for the diffusion constant of the AMP molecule in the various media. Figure 5-15 shows the data with linear fitting and the diffusion constants for the AMP molecule represented by the y-intercept of the linear fit.

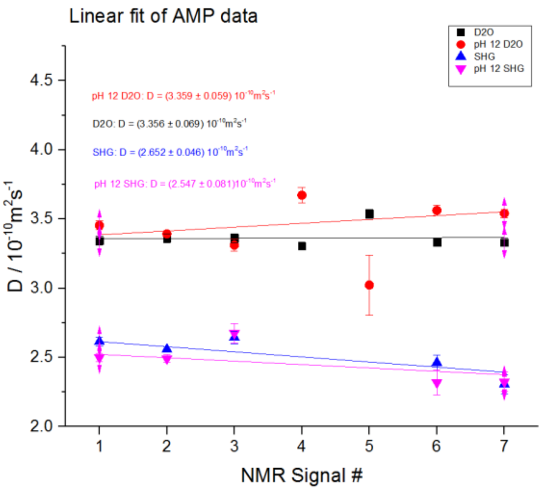

Figure 5-15: Linear fit of the AMP dataset, pH 12 SHG signal 4 is excluded from the linear fit due to inaccurate diffusion constant due to overlap with water signal.

5.5.4 AMP Plot Residuals Analysis

Starting with the AMP dataset, which showed abnormally low diffusion constants for every diffusion medium. Figure 5-16 shows the residual plots for each diffusing medium. Note that the GNAT software only permits the viewing of the residual plots of 5 signals at a time, so the signals selected show the most deviation from the ideal (e.g. signal 4 in the AMP SHG sample) as these signals give the most information about the quality of the experiment.

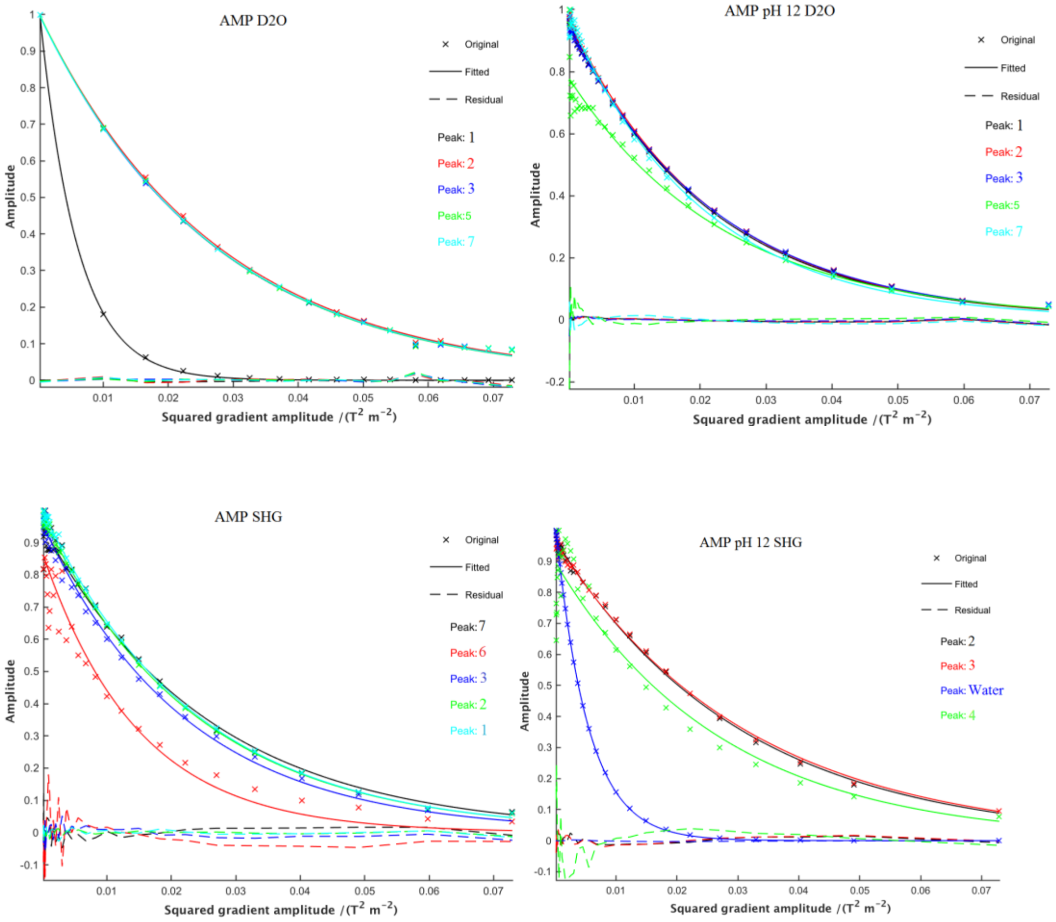

Figure 5-16: The Residual plots of signal amplitude vs squared gradient amplitude for each diffusion medium of AMP (relative to Figure 5-6).

At first glance the fitting seems to correlate well with the data suggesting that the results are valid. The number of gradient steps in each case is 32, except from the D$_2$O medium where the number of steps is 16. The significance of this is that with more gradient steps, the truer the fitting is to the experimental data. This is important in cases such as the SHG diffusion medium where there are frequent irregularities in the data points, as the decay in the signal is much smoother. The abnormal peak 4 (referenced to

Figure 5-6) in the pH 12 SHG sample clearly has a much poorer fitting for this signal than for the rest, this is due to the signal overlap with the water signal. The water signal, in general, has a much sharper decay than any of the other signals. The blue signal represents the decay in amplitude of the water ^{1}H NMR signal with respect to increasing gradient amplitude, note how peak 4 in pH 12 SHG plot seems to be the average of a signal from the diffusing molecule and the water signal (the decay for signal 4 is much sharper due to overlap with the water peak). This merging of signals is the cause of anomalous diffusion coefficients. The same effect can be seen for signal 6 in the SHG plot, in this case the overall quality of the fittings of each peak is poorer than for the pH 12 SHG sample (see residual line in the SHG plot of Figure 5-16), this can be seen by the larger range of diffusion constants for each signal in Table 5-3 (AMP SHG sample), compared to Table 5-4 (AMP pH 12 SHG sample). The best place to look for deviations from the fitted curve is the residual line at the bottom of each plot, for the red and green signals in the SHG and pH 12 SHG plots respectively, it is clear that the majority of the deviation from the fitted curve occurs at the start of the data acquisition, this is why it is especially important in the case of SHG samples to have a high number of gradient steps, so that any anomalous data can be removed through the ‘Prune tool’ in the GNAT software see 5.3.3.

It appears that, although there are some abnormalities resulting from overlapping signals, the dataset for the AMP molecule is accurate based on analysis of the plot residuals. To further validate the results, repeat readings should be taken and then cross referenced to ensure that the data is consistent.

5.5.5 ADP DOSY Results

Summarised below are the results obtained for the DOSY analysis of ADP in the various media (D_2O, pH 12 D_2O, SHG and pH 12 SHG). For details of the exact processing regime see appendix. Also see appendix for individual DOSY spectra produced using the GNAT software.

Table 5-5: ADP SHG Results

NMR Signal	Chemical Shift / ppm	Diffusion coefficient / 10^{-10} m^2 s^{-1}	Error/ 10^{-10} m^2 s^{-1}
AcOH	1.87	6.56	0.081
7	4.01	7.36	2.309
6	4.39	9.85	3.338
4	4.23	11.31	3.983
Water	4.68	14.32	0.249
3	5.98	1.68	0.607
2	8.10	3.31	0.319
1	8.35	3.37	0.317

Table 5-6: ADP SHG pH12 Results

NMR Signal	Chemical Shift / ppm	Diffusion coefficient / 10^{-10} m^2 s^{-1}	Error /10^{-10} m^2 s^{-1}
AcOH	1.87	6.46	0.027
7	4.03	2.14	0.232
6	4.28	2.36	0.243
4	4.39	2.65	0.538
Water	4.68	14.17	0.027
3	6.02	3.02	0.379
2	8.12	2.57	0.097
1	8.37	2.52	0.119

Table 5-7: ADP D_2O results

NMR Signal	Chemical Shift / ppm	Diffusion coefficient / 10^{-10} m^2 s^{-1}	Error / 10^{-10} m^2 s^{-1}
7	4.07	3.51	0.023
6	4.29	3.61	0.031
4	4.45	3.55	0.020
5	4.67	3.68	0.062
Water	4.72	15.51	0.105
3	6.07	3.61	0.028
2	8.21	3.56	0.019
1	8.44	3.53	0.029

Table 5-8: ADP pH12 D_2O

NMR Signal	Chemical Shift / ppm	Diffusion coefficient / 10^{-10} m^2 s^{-1}	Error / 10^{-10} m^2 s^{-1}
7	3.91	3.41	0.024
6	4.20	3.55	0.056
4	4.33	3.74	0.090
Water	4.59	15.41	0.074
3	5.95	3.34	0.032
2	8.03	3.33	0.020
1	8.34	3.35	0.017

This dataset shows similar trends to the AMP dataset. However the data obtained for the SHG sample is abnormal and does not behave in the same manner as the AMP SHG sample. Figure 5-17 shows the dataset without linear fitting so that the reference peaks can be considered individually

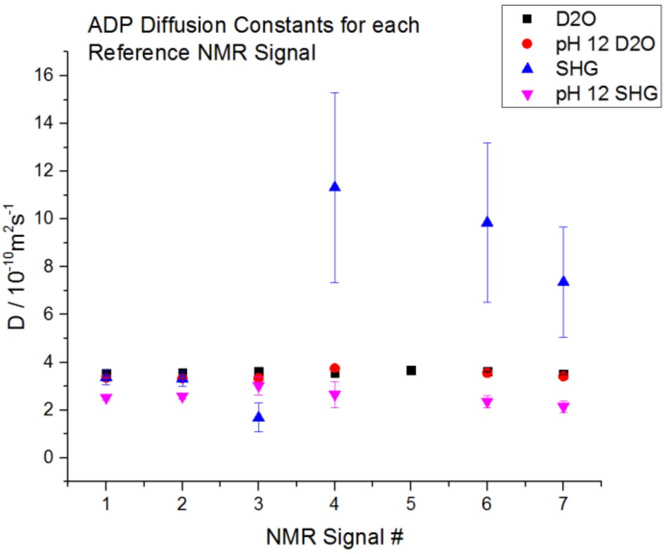

Figure 5-17: A graph to show the diffusion constants of each reference NMR signal for ADP, in each of the 4 different media.

The abnormality of the results for the SHG sample can be seen clearly here. The value for the diffusion constant of reference signal number 4 can be easily believed due to overlapping with the water signal. However, the reasons for the abnormally high values for reference signals 3, 6 and 7 are less obvious. The rest of the results appear to follow the same trend as the AMP dataset. To see the trend more clearly, reference signals 3, 4, 6 and 7 are removed in

Figure 5-18.

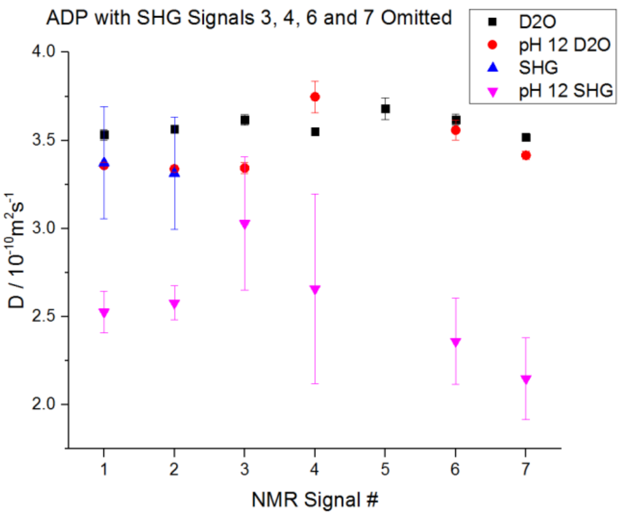

Figure 5-18: graph to show the diffusion constants of each reference NMR signal for ADP, in each of the 4 different media. Anomalous signals 3, 4, 6 and 7 from the SHG sample are removed.

To make a comparison between this dataset and the AMP dataset, the linear fit of each set of sample data was taken in the same manner as for the AMP dataset. See Figure 5-19

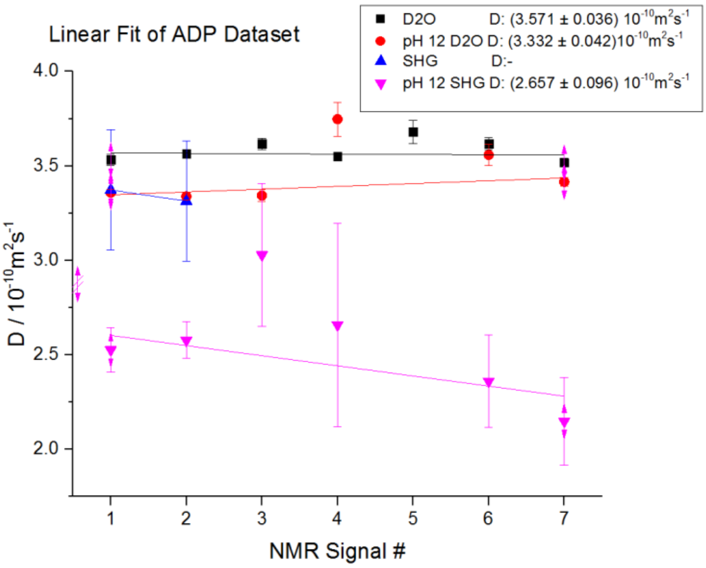

Figure 5-19: Linear fit of the ADP dataset, showing the diffusion constant of AMP in each media. The anomalous results for the SHG sample mean that a linear fit cannot be performed as there are only 2 data points.

In the case of the AMP dataset, the average diffusion coefficient was highest in the pH 12 D_2O sample, closely followed by the D_2O sample. Here, in the case of the ADP dataset, the opposite is true and there is a significant difference between the molecular diffusion constant of the molecule in D_2O and in pH 12 D_2O (error bars do not overlap). It is difficult to suggest reasons which concern experimental technique for this difference as repeat readings were not conducted, however it is possible to assess the quality of the residual fitting as discussed in section 5.3.4. Analysis of the fitting will provide an insight into the quality of the data and will give scope for improvements to future measurements.

5.5.6 ADP Plot Residuals Analysis

The next question in proving the validity of the results is analysing the plot residuals for the ADP dataset. This is the most important dataset to analyse, as it is this data that is in disagreement with the Stokes-Einstein equation. Figure 5-20 shows the residual plots for each diffusing medium. Note that the GNAT software only permits the viewing of the residual plots of 5 signals at a time, so the signals selected show the most deviation from the ideal.

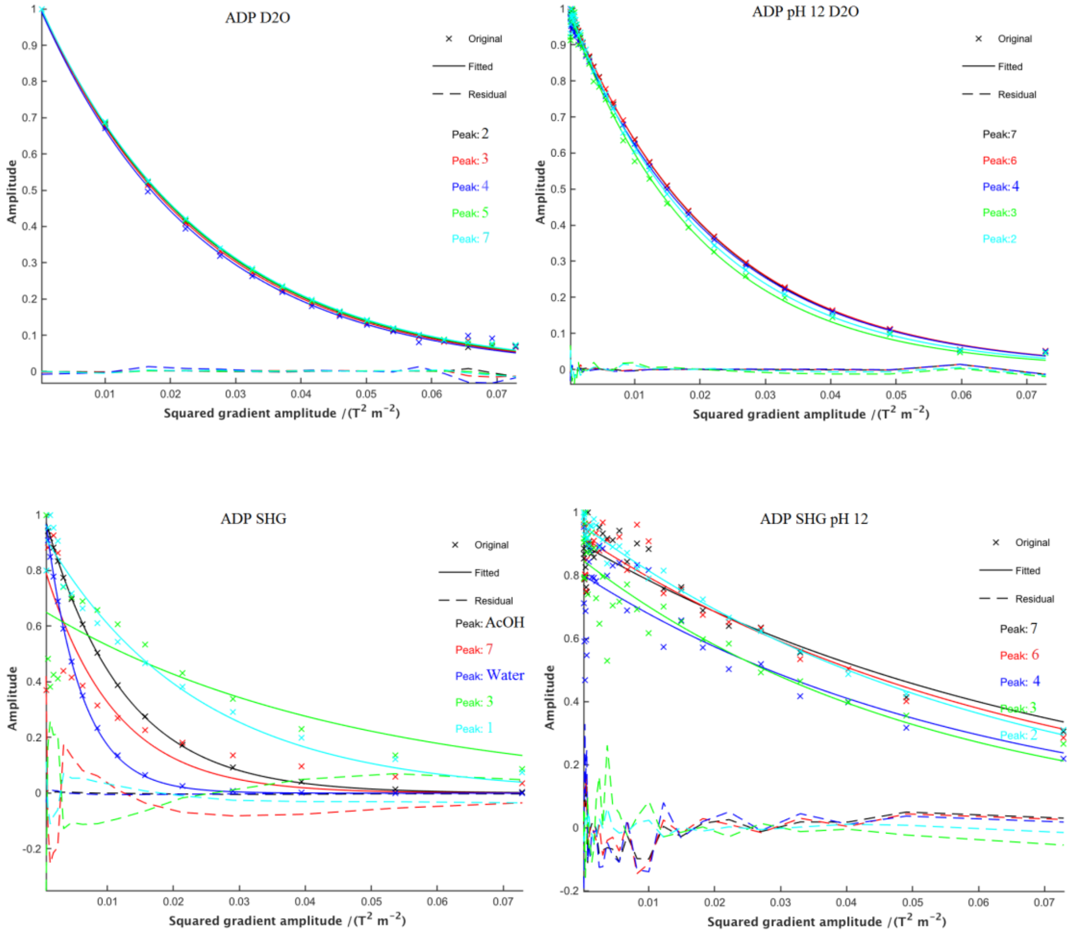

Figure 5-20: The Residual plots of signal amplitude vs squared gradient amplitude for each diffusion medium of ADP. The legend on the right of each plot shows the original experimental data points (represented by crosses), the fitted curve (filled line) and the residual (dotted line).

From the data, it’s clear that the data does not fit well with the fitted curve in the cases of the SHG and pH 12 SHG samples, although both D_2O based sample data fit very well with their fitted curves. The highly anomalous results for the diffusion coefficient of the SHG sample which were discovered in section 5.5.4 can be explained here. The data consists of 16 gradient steps in the case of the SHG sample, this means that there is less of a buffer to anomalous results. If we compare the SHG data to the pH 12 data we can see that in the pH 12 SHG data, there are many anomalies, much like those in the SHG dataset, however in the case of the pH 12 SHG data, there are 32 gradient steps, i.e. more room for error with respect to decaying signal amplitude. This is why the pH 12 SHG data has a much better fitting than the SHG data and thus gives more accurate results for the diffusion constant of each NMR signal. It can be clearly seen that in the SHG sample, the fitting to the water and acetic acid peaks are near perfect, the reason for this is that the signals for both water and acetic acid are much more intense than for the signals for the ADP molecule. The significance of this is that the decrease in the amplitude of the signal due to increasing gradient steps is much less pronounced for the water and therefore there is more room for error per gradient step. In the case of the ADP NMR signals, the decrease in the signal amplitude is much more pronounced and the signals decay more rapidly than the water or acetic acid signals.

The large discrepancies in the individual signal diffusion constants for the SHG can be seen in Figure 5-20. For the diffusion constant of each individual signal to be equal, the fitted curves should lie on top of one another. In the case of the SHG data, the curves are spread out, which results in a large range of diffusion constants for the individual NMR signals. It is possible to visualise the magnitude of the difference by referring to Figure 5-21. The same effect can be seen in the pH 12 SHG data, where signals 3 and 4 are separate from the rest of the plotted curves, the effect of this can be seen in Table 5-6. The fitting of curves 3 and 4 is not particularly brilliant and this results in diffusion coefficients which are larger than the rest of the signals for the ADP molecule.

The data for the ADP SHG sample showed no clear correlation and the range of diffusion coefficients for each NMR signal was too large to be able to confidently state the diffusion coefficient of the molecule. For future research, more gradient steps should be used in the data acquisition to ensure a smoother decay profile of the signal amplitude with respect to increasing squared gradient amplitude.

5.5.7 ATP DOSY Results

Summarised below are the results obtained for the DOSY analysis of ATP in the various media (D_2O, pH 12 D_2O, SHG and pH 12 SHG). For details of the NMR processing regime see Figure 5-10. Also see appendix for individual DOSY spectra produced using the GNAT software.

Table 5-9: ATP SHG results

NMR Signal	Chemical Shift / ppm	Diffusion coefficient / 10^{-10} m^2 s^{-1}	Error /10^{-10} m^2 s^{-1}
AcOH	1.86	7.36	0.222
7	4.14	2.54	0.205
4	4.29	3.17	0.312
6	4.46	3.06	0.699
Water	4.67	15.43	0.322
3	5.97	2.56	0.245
2	8.13	2.39	0.065
1	8.40	2.47	0.090

Table 5-10: ATP SHG pH12 results

NMR Signal	Chemical Shift / ppm	Diffusion coefficient / 10^{-10} m^2 s^{-1}	Error /10^{-10} m^2 s^{-1}
AcOH	1.82	6.51	0.013
7	4.10	2.37	0.232
6	4.25	2.73	0.272
4	4.42	4.16	0.383
Water	4.63	9.58	0.927
3	5.98	2.33	0.132
2	8.10	2.21	0.040
1	8.36	2.21	0.051

Table 5-11: ATP D_2O results

NMR Signal	**Chemical Shift / ppm**	**Diffusion coefficient / 10^{-10} m^2 s^{-1}**	**Error /10^{-10} m^2 s^{-1}**
7	4.25	2.69	0.022
6	4.34	2.70	0.019
4	4.50	2.68	0.035
5	4.67	2.90	0.117
Water	4.61	15.72	0.059
3	6.06	2.76	0.015
2	8.34	2.75	0.015
1	8.53	2.68	0.014

Table 5-12: ATP pH12 D_2O

NMR Signal	**Chemical Shift / ppm**	**Diffusion coefficient / 10^{-10} m^2 s^{-1}**	**Error /10^{-10} m^2 s^{-1}**
7	4.16	3.06	0.052
6	4.19	2.87	0.040
4	4.33	2.97	0.044
5	4.50	3.12	0.051
Water	4.68	15.16	0.088
3	6.06	2.92	0.033
2	8.17	2.92	0.031
1	8.44	2.92	0.031

The data in Table 5-9 Table 5-10 Table 5-11 Table 5-12 are summarised in Figure 5-21, again here it is visible that there is overlap between peak 4 and the water peak, with peak 5 being totally consumed by the water peak and thus does not show up on the DOSY spectrum.

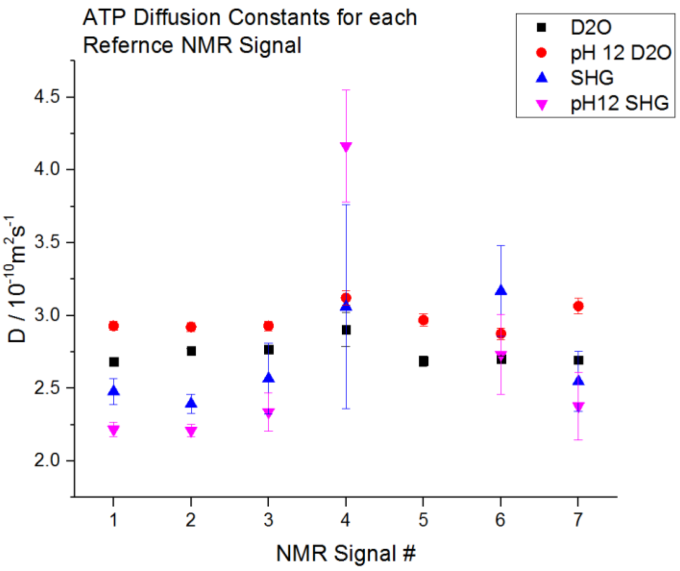

Figure 5-21: A graph to show the diffusion constants of each reference NMR signal for ATP, in each of the 4 different media.

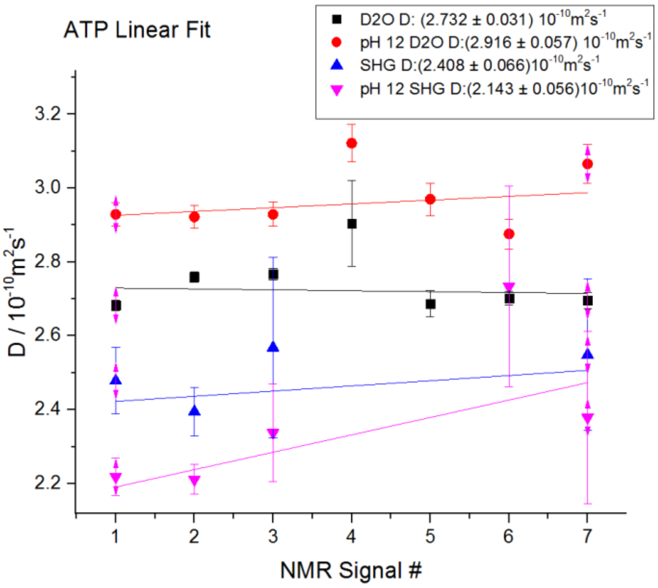

Figure 5-22: Linear fitting of each sample data for ATP in the various media. Anomalous signals 4 and 6 from the SHG, and signal 4 from the pH 12 SHG samples are removed.

5.5.8 ATP Plot Residuals Analysis

Finally, the plot residuals of signal amplitude vs squared gradient amplitude for the ^{1}H NMR signals of the ATP molecule in the various diffusion media will be analysed. The diffusion data obtained for ATP seemed to be the most accurate in terms of its agreement with the Stokes-Einstein equation. With the largest hydrodynamic radius, the ATP molecule should have the lowest diffusion constant from a purely theoretical perspective. This results obtained through DOSY spectroscopy are in agreement with this theoretical estimation. For further confirmation of the validity of the results, let us analyse the quality of the fitting of the plot of signal amplitude vs squared gradient amplitude, in order to reduce the quality of the experimental data points which are used in the calculation of the diffusion constant of a specific NMR signal (see Figure 5-6). Figure 5-23 shows the plot residuals for each diffusion media.

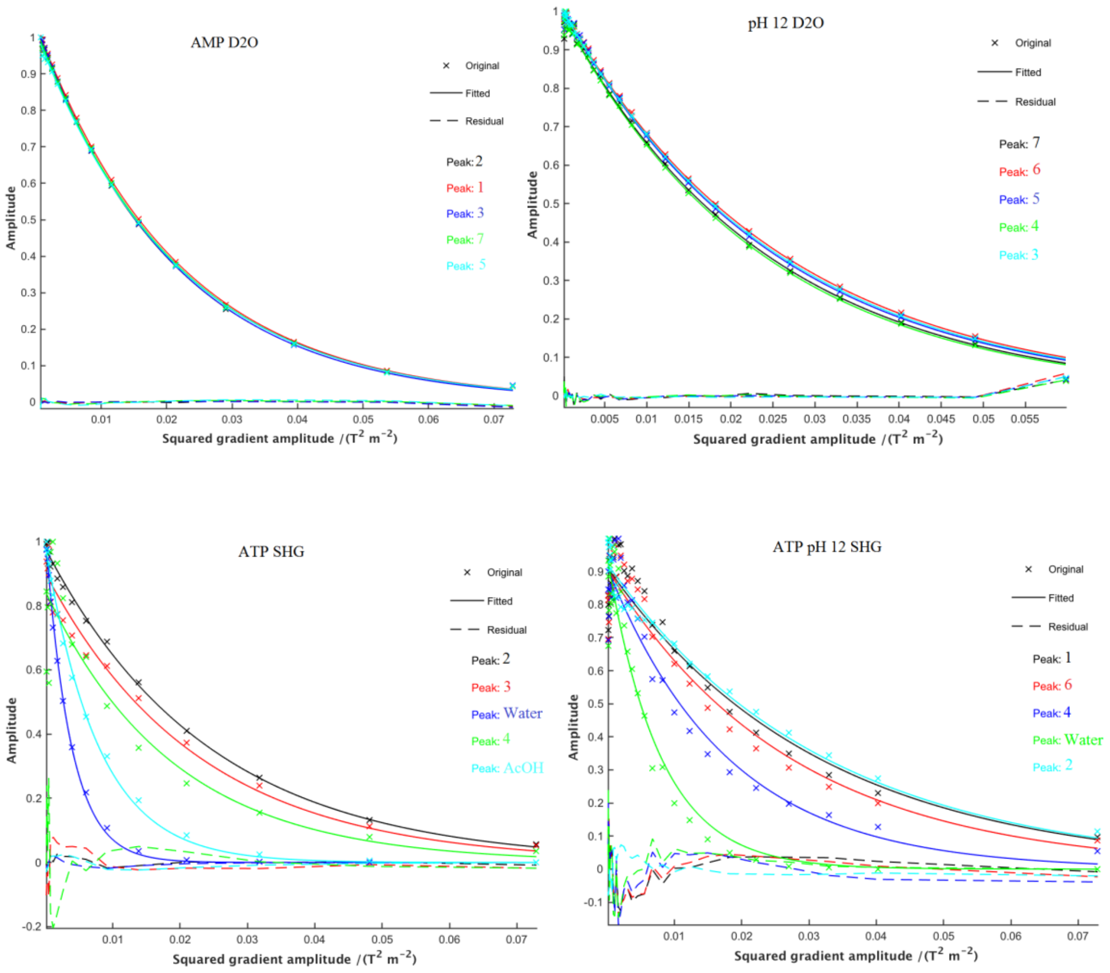

Figure 5-23: the plot residuals of signal amplitude vs squared gradient amplitude for the ATP molecule in each diffusion medium.

Again, the data for the D_2O and pH 12 D_2O samples shows a good agreement with the fitted curve and this allows for confidence in the final result for the diffusion constant of the molecule in these diffusion media. As for the SHG samples, the fitted curves do not lie on top of each other as they do in the D_2O samples, this difference is noticeable by the differing values for the diffusion coefficients of each signal in Table 5-9 (SHG sample) and Table 5-10 (pH 12 SHG sample). The signals with the most deviation (signal 4 from the pH 12 SHG sample, and signals 4 and 6 in the SHG sample (signal 6 is absent from this residual plot)) are excluded from the linear fit which produced the value for the diffusion constant of the ATP molecule. Excluding these signals gives data which has, on the whole, much better fittings and therefore we can be confident in the final value for the diffusion constant of the ATP molecule in these media.

5.6 Ribose Systems

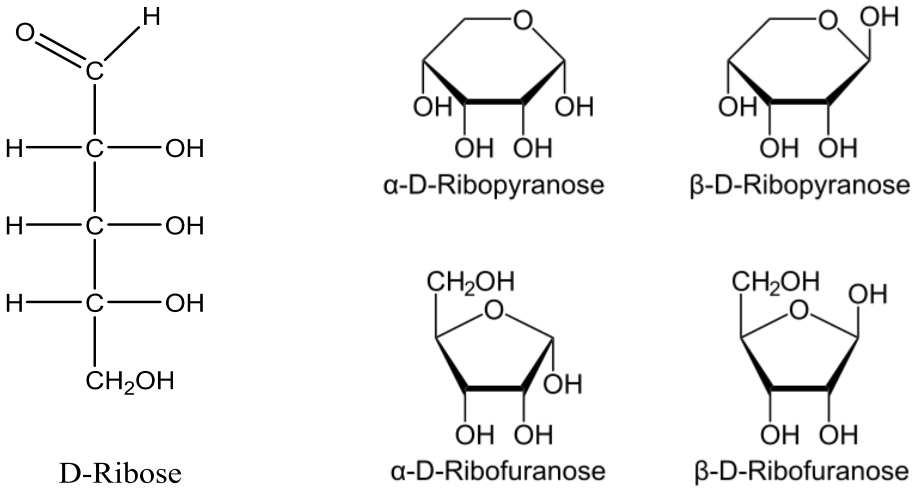

D-Ribose

α-D-Ribopyranose

β-D-Ribopyranose

α-D-Ribofuranose

β-D-Ribofuranose

Figure 5-24: Left: open chain D-Ribose structure. Right: four cyclic versions of ribose[143].

Ribose has been examined with the help of BRUKER instrument, most manufacture instruments has their own built-in processing method but, will not be able to change the parameters of calculating the diffusion coefficient and found to be 6.4 / 10^{-10} m^2 s^{-1}. The DOSY processing software (GNAT) will provide some freedom of changing the parameters and eventually for better results.

5.6.1.1 GNAT results of Ribose in deuterium water

After applying the suitable parameters for GNAT software, the diffusion coefficient has been calculated as 5.72 ± 0.689 / 10^{-10} m^2 s-1. The plot shown in Figure 5-25 shows three integrals peaks has been chosen in the GNAT software and the residuals plot in Figure 5-26 shows the fitting of squared gradient amplitude.

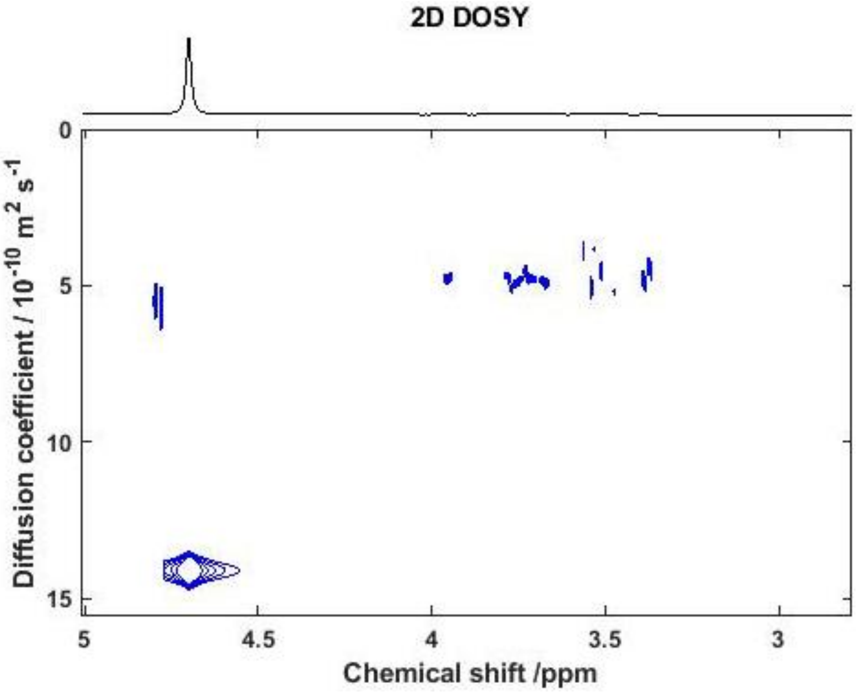

Figure 5-25: 2D DOSY results of ribose in deuterium water produced through the GNAT software, showing the reference peaks for the diffusion medium. The diffusion constant of the molecule is given by the Y coordinate value.

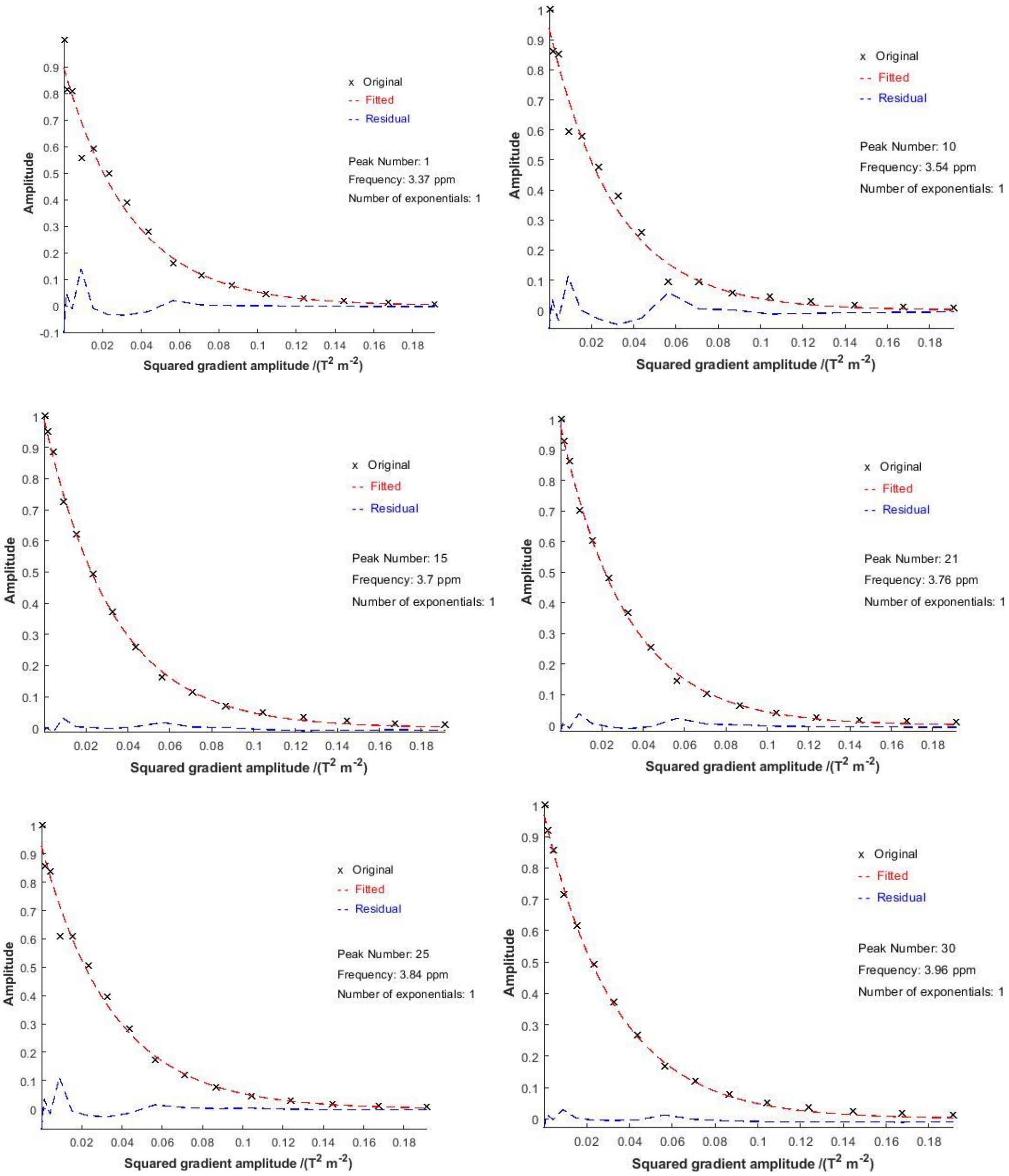

Figure 5-26: The Residual plots of signal amplitude vs squared gradient amplitude for each diffusion medium of ribose (relative to Figure 5-25) of peaks numbers 1, 10, 15, 21, 25 and 30.

5.6.2 GNAT results of Ribose in Hadean water

The diffusion coefficient have been collected from Bruker instrument as

5.6 / 10^{-10} m^2 s^{-1} while calculated with the help of GNAT processing software by applying the appropriate parameters and found to be

5.46 ± 0.142 / 10^{-10} m^2 s^{-1}

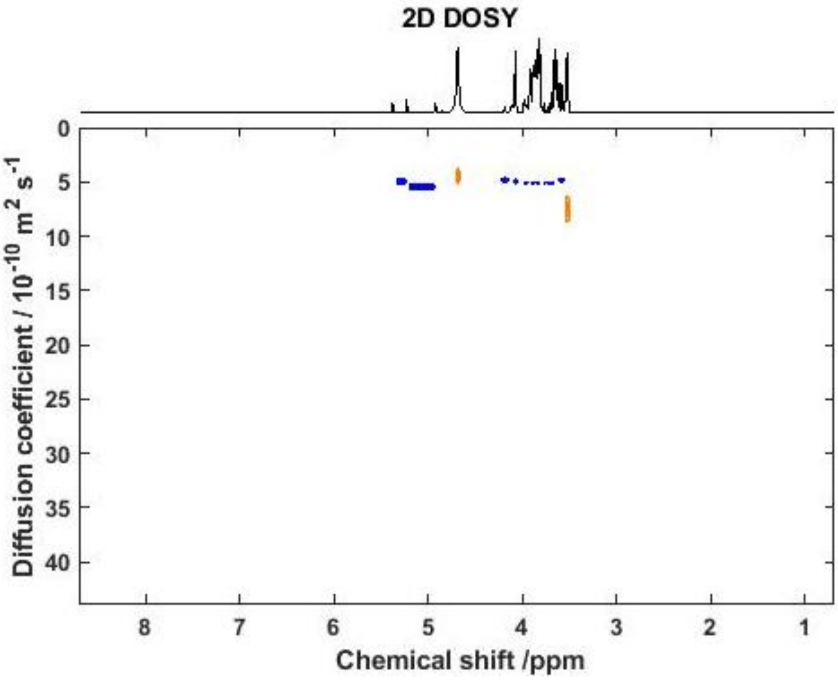

Figure 5-27: Ribose in Hadean water solution as calculated from GNAT processing software.

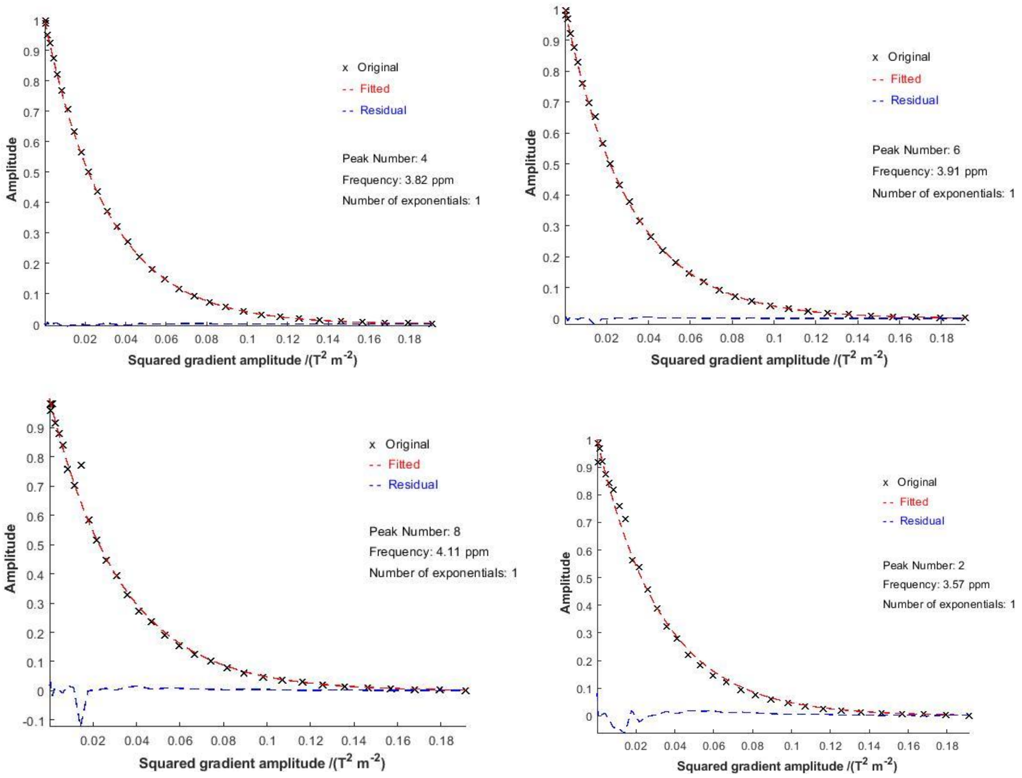

Figure 5-28: The Residual plots of signal amplitude vs squared gradient amplitude for each diffusion medium of ribose (relative to Figure 5-27) of peaks numbers 2, 4, 6 and 8.

5.7 Discussion of DOSY Results

After all processing methods have been performed the final results for the diffusion coefficients of the AMP, ADP and ATP molecules (represented by the y-intercept of a linear fit of the diffusion coefficient for each reference NMR signal) are shown in Table 5-13, Table 5-14 and Table 5-15 below. The error arises from the errors in the exponential decay fit to the signal amplitude vs squared gradient amplitude residual plot, and the error in the linear fit performed using the Origin software.

Table 5-13: AMP Diffusion Constants in the Various Media

Diffusion Media	**Diffusion constant /10^{-10} m^2 s^{-1}**
D_2O	3.35 ± 0.069
pH 12 D_2O	3.35 ± 0.059
SHG	2.65 ± 0.046
pH 12 SHG	2.54 ± 0.081

Table 5-14: ADP Diffusion Constants in the Various Media

Diffusion Media	**Diffusion constant/10^{-10} m^2 s^{-1}**
D_2O	3.57 ± 0.036
pH 12 D_2O	3.33 ± 0.042
SHG	-
pH 12 SHG	2.65 ± 0.096

Table 5-15: ATP Diffusion Constants in the Various Media

Diffusion Media	**Diffusion constant/10^{-10} m^2 s^{-1}**
D_2O	2.73 ± 0.031
pH 12 D_2O	2.91 ± 0.057
SHG	2.40 ± 0.066
pH 12 SHG	2.14 ± 0.056

To see if there is a clear trend in the data, the diffusion coefficients in the various diffusion media for each molecule are plotted in Figure 5-29.

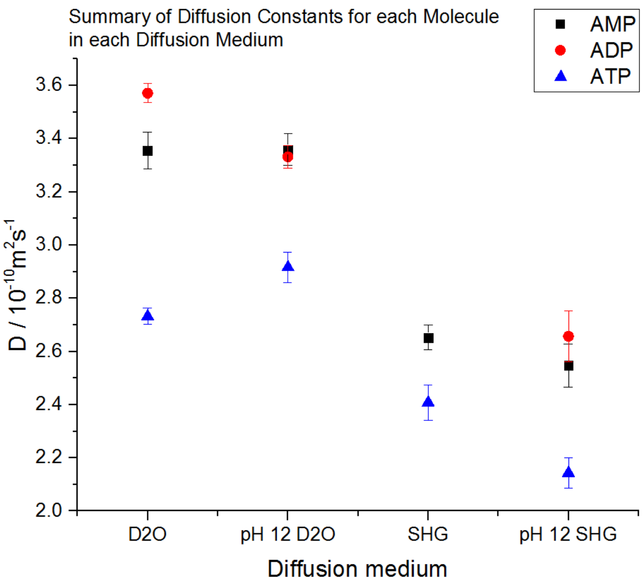

Figure 5-29: The diffusion coefficients of each molecule in each diffusion medium with associated errors.

The data shows an unexpected result in the fact that the larger ADP molecule has a larger diffusion constant than the smaller AMP molecule in the D_2O and pH 12 SHG media (pH 12 D_2O values for AMP and ADP have a negligible difference). The order of the magnitude of the molecular diffusion coefficients (ADP > AMP > ATP) is in contradiction to the Stokes-Einstein equation as ADP has a larger hydrodynamic radius r than AMP, and therefore the expected diffusion constant for AMP should be higher than for ADP. ATP has the lowest diffusion coefficient in each case and this result is in agreement with the Stokes-Einstein equation. This brings into question the validity of the results. To assess the quality of the data, the next section will be dedicated to analysing the residual plot of the signal amplitude vs the squared gradient amplitude. By doing so it is possible to check whether the fitted curve represents the data well, and thus validates the processing regime. Analysis of residual plots also gives an insight into the quality of the experimental data, if the data points do not show a general trend, then it is likely that the experiment should be repeated in order to achieve better results.

5.8 Comparison of results from GNAT to results produced from JEOL software.

In order to further assess the quality of the data, a comparison can be made between a leading DOSY processing software, produced by JEOL. The details of the processing regime for the production of the DOSY spectrum using the JEOL software will not be outlined here. Table 5-16 and shows a comparison between the values of the diffusion coefficients obtained through each processing software.

Table 5-16: GNAT data results compared with JEOL data results

		GNAT	JEOL
Sample	**Diffusion medium**	**Diffusion constant / 10^{-10} m^2 s^{-1}**	**Diffusion constant / 10^{-10} m^2 s^{-1}**
AMP	D_2O	3.35 ± 0.069	3.42
	pH 12 D_2O	3.35 ± 0.059	3.41
	SHG	2.65 ± 0.046	2.85
ADP	D_2O	3.57 ± 0.036	3.70
	pH 12 D_2O	3.33 ± 0.042	3.61
	SHG	-	3.04
	pH 12 SHG	2.65 ± 0.096	3.61
ATP	D_2O	2.73 ± 0.031	2.96
	pH 12 D_2O	2.91 ± 0.057	3.68
	SHG	2.40 ± 0.066	4.34
	pH 12 SHG	2.14 ± 0.056	3.68

This comparison shows that there is a clear difference in the manner in which the data is processed on the JEOL and GNAT software, and this clearly leads to different values for the diffusion constant of the molecule. The data produced by the GNAT software produces a clear trend that can be seen in each of the 3 molecules, in that the values for the diffusion constant of the D_2O and pH 12 D_2O samples are similar, there is then a clear decrease in the diffusion constant in each case as the medium changes from an aqueous to a hydrogel environment (as predicted by the Stokes-Einstein equation) and the SHG and pH 12 SHG samples have similar values for their respective diffusion constants. The same cannot be said for the JEOL processing results. The AMP dataset most closely follows the trend set by the results of the GNAT, with both the D_2O and pH 12 D_2O samples having diffusion constants that are within the error range of the value for the GNAT software. The most surprising dataset for the JEOL software is that of ATP, there is no trend to the data at all and the results do not adhere to the rules of the Stokes-Einstein equation. This comparison shows how powerful the GNAT software is, utilising all of the available processing tools allows for a much more accurate result for the diffusion constant of a molecule.

5.9 Conclusion

Overall, the content and main conclusions from this chapter may be summarised as follows:

1. Molecular diffusion coefficients have been measured for a range of molecule types with a prebiotic provenance (AMP, ADP, ATP, ribose and an amphiphile, SDS) in the silica hydrogel (SHG) phase and compared to the aqueous phase.
2. Molecular diffusion was found to be retarded in the SHG phase compared to the aqueous

Chapter 6 Experimental

6.1 General considerations

In this section are collected a description of the laboratory materials, chemicals and methods that have been used in this research

The water used in all experimental preparations was ultra-pure deionized water prepared using the Purite Select Analyst deionization system. Sodium silicate solution was commercial (from Sigma-Aldrich) and contains (≤ 27% SiO_2 and ≤ 10% NaOH). Hydrochloric acid, glacial acetic acid, sodium dodecylsulphate, merocyanine 540, pyrene and pinacaynol chloride were purchased from Sigma-Aldrich and were used as received. All experiments were conducted under ambient temperature conditions unless otherwise stated. All data, graphs and images within this report were prepared using MS Excel, ChemDraw Prime and OriginPro software as appropriate.

6.2 Analytical preparations and calculations

This section contains a description on all the different pieces of analytical equipment that used to accomplish this work: including CPD, SEM, DLS, solution conductivity, surface tension, UV-Vis spectrophotometry and fluorimetry.

6.2.1 Standard Operating Protocol (SOP) for Preparation of silica hydrogels (SHG’s)

SHGs were prepared by combining two solutions: (A) a solution of 360 µL glacial acetic acid diluted by addition of 7600 µL of ultra-pure deionized water, and (B) 1250, 2500 and 3750 µL respectively of a sodium silicate solution (≤ 27% SiO2 and ≤ 10% NaOH), diluted to 8000 µL with ultra-pure deionized water to prepare 0.5, 0.75 and 1.0 M formulation respectively. The sodium silicate solution was poured into the acid solution in a test tube. The tube was sealed and then inverted slowly (shaking the tube must be avoided) several (*ca* 3-5) times to mix the components thoroughly and allowed to stand overnight or until gelation had been observed to take place. The gelation process that took place in the tube and confirmed by two methods (i) visual cloudy appearance took place instead of clear solution before gelation and (ii) the viscosity of the hydrogel seems to be higher than the reactants solution. This method was one that was modified slightly (order of mixing of solutions and nature of silicate solution used) from that reported by Barge et al [104]. We have herein used the named Barge Method to refer to this SOP.

6.2.2 Critical Point Drying (CPD), BET surface area & Scanning Electron Microscopy (SEM)

Initial sodium silicate solution concentrations of 0.5 M prepared as detailed in (SOP) section above. Whilst still remaining liquid, each samples (1 mL) was poured carefully into a plastic cuvette tube within which each of the caps had been earlier perforated by a narrow-gauge exit needle to allow water egress and acetone ingress during the CPD process. Each sample was inverted and left to gel over a period of 24 hrs before being subsequently submitted for CPD preparation.

A Polaron E3100 system was used to perform the CPD, under the guidance of Mr Martin Fuller within the Faculty of Biological Sciences, University of Leeds (Figure 6-1). The resulted samples (*ca* 11 – 12 mg) as dry samples were then used in SEM and porosity measurements.

Figure 6-1: Critical Point Drying instrumentation; Faculty of Biological Science, University of Leeds

Sample imaging was conducted using two different SEM instruments. The first one was a model of Carl Zeiss EVO MA15: variable pressure W SEM with Oxford Instruments AZtecEnergy EDX system with 80mm X-Max SDD detector- secondary and backscattered imaging, EDX elemental mapping and linescans plus CZ STEM detector [144]. All pictures was taken with magnification between 200 X to 2.0 KX and at 20.00 KV. Images were observed in secondary electron or backscattered mode. The sample imaging was conducted either in the Leeds Electron Microscopy and Spectroscopy Centre (LEMAS) by Mr Stuart Micklethwaite, School of Chemical and Process Engineering, University of Leeds. The second SEM instrument used was a model of FEI Nova NanoSEM 450 operating at 3 kV or 18 kV for EDX; samples were Ir coated, prior to viewing. Element analysis (EDX) - EDAX from AMETEK software TEME V 3.4 within the School of Chemistry in collaboration with Dr’s Alex Kulak and Angela Bejarano-Villafuerte from Meldrum group. BET instrument used of model ASAP2020 form Micromeritics, samples was degassing 3 hrs at 120 ºC before measurements. All BET measurements were performed by Dr Alex Kulak (School of Chemistry, University of Leeds)

The samples collected from the CPD lab were dry and contained silica from the 0.5, 1.0 and 1.5 M silicate hydrogel preparations along with samples that had been aged and those which also contained additives including SDS and merocyanine. They were inserted into the sample chamber under high vacuum (6.3×10^{-6} Torr). The image magnification varied from 100 – 1 µm with high resolution and the resulting secondary electron mode images are reproduced in the appropriate sections of this report.

6.2.3 Sample preparation for Average Particle Size Measurements (DLS)

Samples of SHG’s (4 mL) were prepared directly in a disposable cuvette as stated earlier by using the Barge method and sealed directly after being prepared and inserted in a Malvern Zetasizer Nano ZSP model used for average particle size measurements using the technique of dynamic light scattering. The setup of the instrument was made to collect the result and calibrated for 120 seconds with water refractive index and the measurement angle equals to 173^{o} back scatter at ambient temperature and set to collect readings every 600 seconds.

For those SHG samples which were analysed in the presence of SDS, freshly prepared stock solutions of SDS (2.5×10^{-2} M) were prepared and introduced into the acid phase of the Barge Method preparation (solution B) in an appropriate degree of dilution to achieve the necessary overall amphiphile concentration.

6.3 Critical Micelle Concentration Measurements in aqueous

6.3.1 Surface Tension Method in Water

An aqueous solution (250 mL) of SDS (0.02 M) was prepared as a stock solution in a volumetric flask. By dilution of this stock solution, a set of 6 further solutions were prepared of concentrations 0.00125, 0.0025, 0.005, 0.0075, 0.01 and 0.015 M each in 100 mL volumetric flasks.

Starting with pure water, the capillary rise was measured within capillaries of diameter 1.2 mm. The capillary tube was banded with a metal scale by a plastic rubber and both ends were connected fit together. Aliquots (15 mL) of each of the above prepared solutions was poured into 25 mL beakers and the capillary was inserted (with scale attached) and held horizontally with the end of the capillary immersed in the solution. The sample rise (cm) within the capillary was measured and used to calculate the surface tension through the mathematical equation. Both capillary and the 25 mL beakers were subsequently cleaned thoroughly and used to repeated the same procedure for the next sample. The value of surface tension of each SDS concentration are calculated and plotted to indicate the CMC point.

6.3.2 Solution Conductivity Method in Water

An aqueous solution of sodium dodcecylsulphate (0.1 M) was prepared in a 250 mL volumetric flask. Using a calibrated pipette, 200 mL of freshly deionized water was added into a beaker of total volume 400 mL. A magnetic stirrer was inserted and was maintained stirring throughout the experiment. A fixed burette (50 mL) and conductance cell (JENWAY 4520 conductivity meter; Porter laboratory, SoC). were then introduced to the system. The burette was charged with the SDS solution and aliquots (1 mL) were introduced into the flask to a total of 50 mL. After each aliquot addition, a reading of solution conductance was taken under ambient temperature conditions. The same procedure repeated three time to calculate the average readings and estimate the error percent and construct error bars.

6.3.3 Fluorescence Method in Water

To perform this experiment, the following stock solutions were freshly prepared:

(i) Pyrene (25.2 mg) dissolved in ethanol (25 mL) was sonicated for 10 minutes to dissolve the suspension to a final concentration of 5 mM. The final concentration of pyrene in each cuvette is 0.01 mM.

(ii) A stock solution of SDS (0.721 g) in 100 mL of ultra-pure deionized water was compiled to achieve a concentration of 25 mM. During the dissolution process, bubble formation must be avoided by ensuring slow addition of water to the volumetric flask. In Table 6-1 are collected the volumes each stock solution used in each cuvette and the concentration of SDS in each cuvette.

Table 6-1: The content of each cuvette in the fluorescence experiment in aqueous phase

[SDS] mM	SDS µL	pyrene µL	water µL
1	160	8	3832
2	320	8	3672
3	480	8	3512
4	640	8	3352
5	800	8	3192
6	960	8	3032
7	1120	8	2872
8	1280	8	2712
9	1440	8	2552
10	1600	8	2392
11	1760	8	2232
12	1920	8	2072
13	2080	8	1912
14	2240	8	1752
15	2400	8	1592

Data were collected using a HORIBA Fluorolog Triax 320 fluorimeter (School of Chemistry, University of Leeds) calibration (run with air and deionised water) process was conducted prior to any data collection.

6.3.4 Spectrophotometric Method in Water

To perform this experiment, the following stock solutions were freshly prepared:

Merocyanine 540 (0.0138 g) was dissolved in ethanol (25 mL) with sonication (10 mins) to afford a solution with concentration of 1 mM. The final concentration of merocyanine 540 in each cuvette is 0.01 mM. The cuvette path-length was 1 cm. In a similar fashion, SDS (0.72 g) was dissolved in ultra-pure deionized water (100 mL) to obtain a solution concentration of 25 mM. It was observed that during dissolution, air bubbles had a tendency to form. This proved to be somewhat problematic in the subsequent optical analysis so, in order to prevent bubble formation, water was added to the volumetric flask in as slow a manner as possible. The subsequent spectrophotometric analyses were performed using a Cary 100 UV-Vis spectrophotometer from Agilent Technology (School of Chemistry, University of Leeds), using Scan Software Version: 4.20(468), Double Beam Mode and scan range of 200.00 – 800.00 nm at ambient temperature. The instrument needs an internal reference cell for base-line correction so a reference cuvette containing water is used in all aqueous experiments and SHG in the gel-phase experiments.

Table 6-2: The content of each 4mL cuvette in the UV-Vis spectroscopy experiment in aqueous phase

[SDS] mM	SDS µL	Merocyanine µL	water µL
1	160	40	3800
2	320	40	3640
3	480	40	3480
4	640	40	3320
5	800	40	3160
6	960	40	3000
7	1120	40	2840
8	1280	40	2680
9	1440	40	2520
10	1600	40	2360
11	1760	40	2200
12	1920	40	2040
13	2080	40	1880
14	2240	40	1720

15	2400	40	1560
16	2560	40	1400
17	2720	40	1240
Ref.	0	40	3960

6.3.5 Fluorescence Method in Hydrogel Phase

To calculate the CMC point in the gel phase, the same stock solutions of pyrene and SDS were prepared as used under aqueous conditions (section 6.3.3 above). In addition, the sodium silicate solution was prepared by diluting an aliquot of the stock silicate solution described above (16 mL) to 25 mL using ultra-pure deionized water, the final concentration of silicate used in the SHG was then 0.5 M. Again, the gels were prepared using the Barge method[104].

Table 6-3: The content of each cuvette in the fluoresce experiment in silica hydrogel phase

[SDS] mM	SDS µL	Sodium Silicate diluted solution µL	Glacial acetic acid µL	pyrene µL	water µL
1	160	375	60	8	2397
2	320	375	60	8	2237
3	480	375	60	8	2077
4	640	375	60	8	1917
5	800	375	60	8	1757
6	960	375	60	8	1597
7	1120	375	60	8	1437
8	1280	375	60	8	1277
9	1440	375	60	8	1117
10	1600	375	60	8	957
11	1760	375	60	8	797
12	1920	375	60	8	637
13	2080	375	60	8	477
14	2240	375	60	8	317
15	2400	375	60	8	157

6.4 Critical Micelle Concentration Measurements in SHG

6.4.1 Spectrophotometric Method in Hydrogel Phase

To calculate the CMC point in the gel phase, the same set of stock solutions for both merocyanine and SDS were prepared. In addition, more dilute sodium silicate solutions were prepared by diluting silicate solution (16 mL of sodium silicate solution) to 25 mL in ultra-pure deionized water, the final concentration of SHG were 0.5, 0.75 and 1.0 M – each of these solution concentrations could only have come from different volumes of the original stock solution. The calculations of sodium silicate solution and the preparation process based on Barge method as described previously. Table 6-4 indicates the preparation solutions for a representative experiment in a 0.5 M SGH environment. However, to prepare appropriate solutions in order to achieve SHG silicate concentrations of 0.75 and 1.0M respectively, sodium silicate solutions were diluted from 375 µL to 500 µL (to achieve 0.75 M silicate) and 750 µL (to achieve 1.0 M silicate) respectively.

Table 6-4: The content of each 3mL cuvette in the UV-Vis spectroscopy experiment in 0.5 M silica hydrogel phase

[SDS] mM	SDS µL	Sodium Silicate diluted solution µL	Glacial acetic acid µL	Merocyanine µL	water µL
0.5	60	375	60	30	2475
0.75	90	375	60	30	2445
1	120	375	60	30	2415
1.5	180	375	60	30	2355
2	240	375	60	30	2295
3	360	375	60	30	2175
5	600	375	60	30	1935
7	840	375	60	30	1695
8	960	375	60	30	1575
8.5	1020	375	60	30	1515
9	1080	375	60	30	1455
10	1200	375	60	30	1335
12	1440	375	60	30	1095

15	1800	375	60	30	735
18	2160	375	60	30	375
21	2520	375	60	30	15
Ref.	0	375	60	30	2535

Table 6-5: The content of each 3mL cuvette in the UV-Vis spectroscopy experiment in 0.75 M silica hydrogel phase

[SDS] mM	SDS µL	Sodium Silicate diluted solution µL	Glacial acetic acid µL	Merocyanine µL	water µL
0.2	24	565	60	30	2321
0.4	48	565	60	30	2297
0.6	72	565	60	30	2273
0.8	96	565	60	30	2249
1	120	565	60	30	2225
1.5	180	565	60	30	2165
2	240	565	60	30	2105
3	360	565	60	30	1985
5	600	565	60	30	1745
7	840	565	60	30	1505
8	960	565	60	30	1385
9	1080	565	60	30	1265
11	1320	565	60	30	1025
14	1680	565	60	30	665
16	1920	565	60	30	425
18	2160	565	60	30	185
Ref.	0	565	60	30	2345

Table 6-6: The content of each 3mL cuvette in the UV-Vis spectroscopy experiment in 1.0 M silica hydrogel phase

[SDS] mM	SDS µL	Sodium Silicate diluted solution µL	Glacial acetic acid µL	Merocyanine µL	water µL
0.5	60	750	60	30	2100
0.75	90	750	60	30	2070
1	120	750	60	30	2040
1.5	180	750	60	30	1980
2	240	750	60	30	1920
3	360	750	60	30	1800
5	600	750	60	30	1560
7	840	750	60	30	1320
8	960	750	60	30	1200
8.5	1020	750	60	30	1140
9	1080	750	60	30	1080
10	1200	750	60	30	960
12	1440	750	60	30	720
15	1800	750	60	30	360
18	2160	750	60	30	0
Ref.	0	750	60	30	2160

6.5 Merocyanine 540 decolourisation experiments

The stock solutions prepared previously are used considering the following concentration. In a similar fashion, SDS (0.7209 g) was dissolved in ultra-pure deionized water (100 mL) to obtain a solution concentration of 25 mM. merocyanine 540 (0.01 g) was dissolved in ethanol (25 mL) with sonication (10 mins) to afford a solution with concentration 1mM.The final concentration of merocyanine 540 in each cuvette is 0.01 mM. SHG prepared directly in the cuvette as described using Barge method. Table 6-7 indicates the preparation solutions for a representative experiment in a 1.0 M SGH environment. However, to prepare appropriate solutions in order to achieve SHG silicate concentrations of 0.75 and 0.5 M respectively, sodium silicate solutions were diluted from 750 µL to 500 µL (to achieve 0.75 M silicate) and 375 µL (to achieve 0.5 M silicate) respectively.

Table 6-7: The content of each 3mL cuvette in the merocyanine 540 decolourisation experiment in 1.0M silica hydrogel phase

[SDS] mM	SDS µL	Sodium Silicate diluted solution µL	Glacial acetic acid µL	Merocyanine 540 µL	water µL
0	0	750	60	30	2160
3	360	750	60	30	1800
5	600	750	60	30	1560
10	1200	750	60	30	960
15	1800	750	60	30	360
18	2160	750	60	30	0
Ref.	0	750	60	30	2160

The experiments were conducted in the Porter Laboratory, School of Chemistry, University of Leeds using a Cary 100 UV-Vis spectrophotometer from Agilent technologies. Calibration and baseline correction was conducted after 15 min of initiating the instrument (to allow to stabilize the lamp). The instrument set to collect readings each 10 minutes continuously for 18 hrs with a full scan wavelength range between 200 – 800 nm using: Scan Software Version: 4.20(468), Double Beam Mode and at ambient temperature

6.5.1 pH Studies on Merocyanine 540

For the pH measurements, two pH-meter instruments were used. The first meter, a SCHOCHEM SN 2024 pH-meter, was connected to a PC upon which pH-logging software had previously been installed, allowing automated pH measurements to be made every 60 seconds. The second instrument was a JENWAY 350 pH meter unit and was connected to a microprobe from SIGMA-ALDRICH. Calibration of the pH-meters was carried out using buffer solutions of pH 7 & pH 4 before experiments were run. Gel solutions (10 mL) for analysis were prepared according to the Barge method described earlier to prepare SHG samples. The colour disappearance was monitored visually and the microprobe used to maintain the physical structure of SHG sample.

6.6 Sample preparation for SEM-EDX analysis of SHG-pyrophosphate binding nature

The binding nature of phosphorous containing compounds (namely sodium pyrophosphate) to the silica hydrogel polymer matrix was determined through SEM-EDX analysis.

SHG samples were prepared with differing sodium silicate concentrations, and for the purpose of this investigation, solution A was saturated with sodium pyrophosphate (solubility = 170 mg/mL in water –SCBT).

Table 6-8: Solution A

Hydrogel sample	[SSS] / M	Vol Glacial acetic acid / µL	Vol. Distilled water / µL	Mass of pyrophosphate / g
1	0.5	226	4765	0.4515
2	0.6	226	4765	0.4550
3	0.7	226	4765	0.4560
4	0.8	226	4765	0.4512
5	0.9	226	4765	0.4534
6	1.0	226	4765	0.4515

Table 6-9: Solution B

Hydrogel Sample	[SSS] / M	Vol. Distilled Water / uL	Vol. SSS / uL
1	0.5	4232	784
2	0.6	3919	1097
3	0.7	3605	1411
4	0.8	3292	1724
5	0.9	2978	2038
6	1.0	2665	2351

The samples were left for 2 days so that gelation could occur. Freeze drying was performed after gelation was successful in all samples to remove all water from the samples, leaving a white uniform powder after 2 days for freeze drying under reduced pressure. After freeze drying, dialysis was performed on each sample. In each case, the sample was placed into dialysis tubing (washing into the tubing from the container with distilled water) and the sealed tubing was placed into a water bath which was replenished daily. The dialysis was carried out for 4 days and after this time the remaining solid in the dialysis tubing was subjected to freeze drying. The resulting white uniform powder was then analysed using an SEM-EDX instrument. After initial investigations discovered the presence of phosphorous on the surface of the remaining silica, acid dialysis was carried out on the same samples, in order to determine if the silica – phosphorus binding is chemical or physical in nature. In the case of acid dialysis, the procedure was identical to that of the first dialysis experiment, but in this case, the water bath was adjusted to pH 2 *via* addition of 37% of concentrated HCl solution in water

6.7 Diffusion coefficient experiments

6.7.1 Materials

Sodium silicate solution was commercial (from Merck KGaA, Damstadt, Germany) and contained (≤27% SiO_2 and ≤10% NaOH), Density = 1.296-1.396 g / mL. Adenosine 5’ triphosphate disodium salt hydrate: Sigma Aldrich. Adenosine 5’ Diphosphate disodium salt: Alfa Aesar. Adenosine 5’ monophosphate from yeast: Sigma Aldrich. D_2O: 99.9% atom D, MW = 20.03 g / mol, Boiling point 101.4 °C, Sigma Aldrich. Glacial Acetic Acid: Sigma Aldrich. Sodium Pyrophosphate: Sigma Aldrich. D-(--)-Ribose; M.W. = 150.13 Assay = 98% from FisherBiotech

6.7.2 Analytical Methods and Settings

A two-channel Jeol ECA600ii NMR Spectrometer operating with a 14.1 T magnetic field, equipped with a 5 mm ROYAL probe with z-axis field gradients and Bruker Avance Neo 500 MHz spectrometer with a 5 mm BBO smartprobe equipped with a z-gradient coil with a maximum nominal gradient strength of 53 G cm^{-1} for DOSY measurements. A two-channel Bruker AV3 300 NMR spectrometer operating with a 7.05 T magnetic field, equipped with a 5 mm BBF-H-D probe with z-axis field gradients for (^{1}H analysis). Analysis of resulting spectra was achieved through use of MestreNova Research lab software. Abbreviations used in NMR analysis: s= singlet, d= doublet, t= triplet, q= quartet, m= multiplet.

Table 6-10 describes the processing parameters used for each sample in the GNAT software, for an explanation of each parameter consult chapter 5.

Table 6-10: DOSY processing parameters for each sample. fn = Fourier number, the number of data points used in the Fourier transform. Lw & Gw = Lorentzian and Gaussian linewidth parameters. No. of gradient steps = the number of data points used in the calculation of the diffusion coefficient. Baseline correct polynomial order. Reference Deconvolution. No. of exponentials and Prune Regions.

		FT	**Window function**						
Diffusion Medium	**Sample**	**fn**	**Lw**	**Gw**	**No. of gradient steps**	**Baseline correct polynomial order**	**Reference Deconvolution**	**No of exponentials**	**Prune Regions**
SHG	AMP	32768	1	0	32	5	no	5	-
SHG	ADP	8192	3	3	16	5	no	5	1-7
SHG	ATP	8192	1	0	16	5	no	mono	-
D_2O	AMP	16384	1	0	16	5	no	mono	-
D_2O	ADP	32768	1	0	16	5	yes	mono	-
D_2O	ATP	32768	1	0	16	5	no	mono	-
SHG	AMP pH 12	8192	2	1	32	2	no	5	31
SHG	ADP pH 12	8192	2	1	32	2	no	5	31
SHG	ATP pH 12	8192	2	1	32	2	no	5	31, 32
D_2O	AMP pH 12	32768	1	0	32	4	no	mono	1-10
D_2O	ADP pH 12	32786	1	0	32	2	no	mono	-
D_2O	ATP pH 12	32768	1	0	32	2	no	mono	31

6.7.3 Sample Preparation for DOSY Experiments

6.7.3.1 Protocol for the preparation of Silica Hydrogels:

Initial investigations into the preparation of SHG utilised the recipe used from Barge Method[104] . A range of different hydrogels were prepared in test tubes, which varied in sodium silicate solution concentration ([SSS]).

Table 6-11: Solution A

Hydrogel	Vol. glacial acetic acid / µL	Vol. Distilled water / µL
1	360	7600
2	360	7600
3	360	7600
4	360	7600
5	360	7600
6	360	7600

Table 6-12: Solution B

Hydrogel	Molarity [SSS] / M	Vol. SSS / µL	Vol. Dist. water / µL
1	0.5	1250	6750
2	0.6	1750	6250
3	0.7	2250	5750
4	0.8	2750	5250
5	0.9	3250	4750
6	1.0	3750	4250

Solution A was added to solution B and the combined solution was left overnight to gel. All hydrogels formed successfully, this initial test yielded a foundation recipe on which further preparations could be centred.

6.7.4 Preparation of the Molecules under DOSY Investigation:

Adenosine monophosphate disodium salt, adenosine diphosphate disodium salt, and adenosine triphosphate disodium salt were used in this study of which the latter two compounds are commercially available and were purchased from Sigma. The former was synthesised from 0.1 g, 2.88 x10^{-4} mol adenosine 3' monophosphate (from Sigma-Aldrich) *via* dissolution into a minimum amount of D_2O (*ca* 3 mL) followed by the addition of 0.0230 g, 5.75 x 10^{-4} mol NaOH(s) (ground from pellets) and evaporating this mixture to yield a white solid powder, which was dried in an oven at 60°C for 24 hrs to yield the disodium salt of Adenosine monophosphate, AMP.2Na (0.0943 g, 85%). The disodium salts of each molecule were selected for use as they are suitably soluble in the media used in these investigations and can be used for comparison with the same species but in a high charge state

6.7.5 Preparation of Silica Hydrogels in NMR Tubes:

For all future investigations regarding DOSY experiments, the sodium silicate concentration of the hydrogel environment is chosen to be 0.5 M, as at this concentration hydrogels are optically pure and the uniformity of the hydrogel can be easily seen.

To achieve a precise concentration in each sample, the protocol used by Barge method is scaled down from a volume of 15960 µL to 3000 µL (scale factor of 5.32). A 3000 µL total volume was chosen as this was the lowest volume in which it is feasible to form a hydrogel using the method above (sufficient acetic acid is required for gelation to occur). Solution A (containing the solid sample under investigation) and solution B are mixed with slow inversion of the container, and from the mixed solution 500 µL is pipetted into an NMR tube. Note that in the case of NMR samples, D_2O is used in place of distilled water.

Table 6-13: Solution A

Vol. glacial acetic acid / µL	Vol. D_2O / µL	Mass ATP-2Na/ADP-2Na/AMP-2Na / mg
68	1429	30

Table 6-14: Solution B

Vol. SSS / μL	Vol. D_2O / μL
235	1269

After 24hrs, gelation had occurred. The hydrogels that formed were optically pure, uniform and of equal volume as a result of the precision of the protocol used. As a result, measurements of the diffusional behaviour of molecules can be conducted with confidence in the validity of the results.

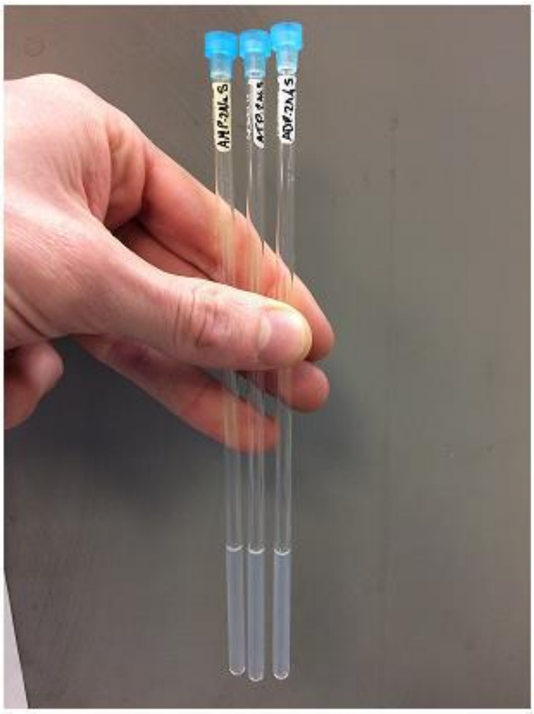

Figure 6-2: Image demonstrating the successful preparation of SHG's at 0.5 M [SSS] using the protocol described in 6.7.5.

6.7.6 Preparation of SHG's at High pH Regime:

To assess how the charge state affects the diffusional behaviour of molecules in both an SHG phase and an aqueous phase, it was first necessary to prepare a stock D_2O solution with a pH of ~12. To do this, sodium hydroxide pellets were crushed into a fine powder and this was added to a beaker of D_2O until the pH was adjusted to pH 12. The pH was of the stock solution was measured via electronic pH meter, to be 12.40 and this value was confirmed through pH paper tests.

Using the pH 12 D_2O stock solution, SHG's were prepared in much the same manner as in6.7.5, however the D_2O is replaced with the high pH stock solution. Initial attempts using this method failed, the issue was resolved by addition of 75 µL Glacial acetic acid rather than the 68 µL used previously. It is thought that there is a neutralisation effect from the high pH stock solution which prevents the acid catalysis of the gelation reaction.

Table 6-15: Solution A

Vol. glacial acetic acid / µL	Vol. High pH stock solution / µL	Mass ATP-2Na/ADP-2Na/AMP-2Na / mg
75	1429	30

Table 6-16: Solution B

Vol. SSS / µL	Vol. High pH stock solution / µL
235	1269

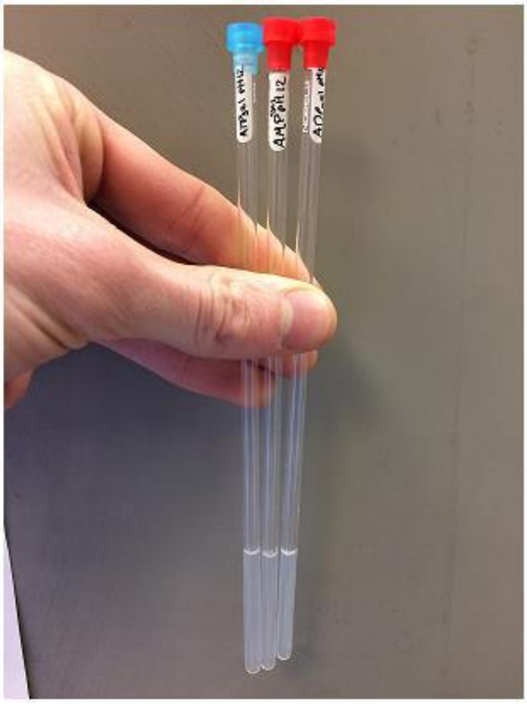

Figure 6-3: Image demonstrating the successful preparation of SHG's at 0.5 M [SSS] in high pH regime, using the protocol described in6.7.5

Chapter 7 Summary, Conclusion and Future Work

Below is a chapter-by-chapter summary of the key findings from the work presented here. To summarize the work which has been done during my study as following ordered according to the relevant chapters:

7.1 Chapter 2:

To prepare SHG in a practical method, there are two different acidic reagent can be used with the same procedure. First acidic reagent used was a strong mineral acid hydrochloric acid, the standard 0.5 M SHG prepared successfully but with higher concentrations of SHG the issue of the precipitation arises. The second acidific reagent used was the weak acid glacial acetic acid. Formulations made using the latter are named Barge method[104]. Barge method appears to be the most suitable and most durable method of preparing SHG (SOP) used in the lab without any chemical issues even with up to 1.5 M SHG. Silica hydrogels produced by the Barge method appears optically clear and homogeneously formed without any precipitate formation.

Critical point drying has been used prior to surface examinations to maintain the integrity of the structure, visualize the cross-linked network and the dendritic growth of silica matrix structure. This method is also used for preparing delicate biological samples for electron microscopy

The dried SHG samples have been examined by scanning electron microscopy to visualize the surface morphologies of the samples along with surface porosity. Energy dispersive X-ray studies identify salts present in the matrix structure which can be removed with the help of dialysis which involves immersing a SHG sample contained within a dialysis tube (semipermeable membrane) in water, dialysis tube to allow removal of water-soluble salts. After four days of dialysis, the sample is dried using lyophilisation (freeze-drying). After freeze drying, the sample is visualised again with SEM and the results showed increased porosity in the silica matrix which is supported by BET studies where surface area is almost triple the pre-dialysed values and all water soluble molecules have been removed as determined by EDX.

Dynamic light scattering experiments showed that the best cuvette environment to be used in the DLS instrument is a closed SHG system to prevent water evaporation. The particle size distribution (Z-average) provides an approximation of gelation; this process took *ca* 120 min in an open system and *ca* 200 min in the closed system. The presence of amphiphile SDS surfactant in the gelling SHG leads to an increase in the average particle size distribution. Thermogravimetric analysis, on five different concentrations of SHG within 0.5-1.0 M have been examined, which resulted in the following water-volatile content measurements: 0.5 M (94.6%), 0.6 M (93.6%), 0.7 M (92.2%, 0.8 M (91.6 M), 0.9 M (90.5%) and 1.0 M (89.3%).

The first derivative graphs which are known also as differential thermogravimetry (DTG) give information about different thermal events in the mass loss which, in the case of the SHG's studies here, appear as shoulders on the graphs. These may indicate different degrees of bound vs free water.

As a conclusion of this chapter:

- Optically clear SHG's form well using the Barge method even with a higher concentration of SHG.
- CPD followed by dialysis is a good mechanism to prepare salt-free silica matrices.
- Different forms of silica have been detected by SEM.
- The presence of amphiphiles in the gel systems appears to increase the average particle size.
- Thermogravimetric analysis and the first derivative of thermal analysis of gel samples used to examine water content within SHG's.

7.2 Chapter 3

This chapter focuses on measurements of the critical micelle concentration of a representative surfactant within an aqueous and silica hydrogel (SHG) media, the first such study of its kind to the best of our knowledge

The surfactant, sodium dodecyl sulphate (SDS) has been examined and the CMC measured in the aqueous phase with the help of four different techniques and the results appear to illustrate slightly different values depending on the method used.

Surface tensiometry using the capillary rise concept gives a CMC value of 6.1 mM, solution conductivity experiments using NaOH titration gives a CMC value of 7.9 mM. Fluorescence spectroscopy has also been used in which the fluorescence of pyrene probe provides a, CMC of 6.0 mM. In addition to these, UV-Vis spectrophotometry based on the absorption of dye molecules (merocyanine 540 and pinacynol chloride) which partition within micelles. Using merocyanine 540 the CMC of SDS was found to be 7.3 mM which is slightly lower than its value when estimated with pinacynol chloride dye which is 7.8 mM

Changing from an aqueous environment to SHG environment provides some experimental problems: both tensiometry and conductivity methods involves dynamic and continuous solution movements neither of which are suitable for a gel-phase medium. Moreover, fluorescence spectroscopy proves of little effective use in the SHG medium as broad featureless signals were obtained.

The most applicable method found to provide reasonable CMC results within SHG phases was the UV-Vis spectroscopic technique. The overall shape of the Abs vs [SDS] plot in the SHG phase was slightly different to those observed in the aqueous phase, in that the onset-transition point was barely if at all visible. However, the second, equilibrium, transition was and it was this set of values that were compared between both phases.

Using merocyanine 540 , starting with 0.5 M SHG, the CMC values for SDS were found to be 1.3 ± 0.7 mM, at 0.6 M SHG the CMC changed slightly to 1.1 ± 0.2 mM. When increasing the concentration of SHG to a higher concentration of 0.7 M, two observations noted: 1) the system gelled quicker and 2) the red merocyanine colour vanished and the CMC recorded at ca. 1.0 ± 0.5 mM.

With the second probe pinacynol chloride, decolourisation over the measurement period was not a problem and CMC values could be measured at higher silicate SHGs. For 0.5 M SHG the CMC measured was 1.4 ± 0.4 mM; 0.6 M SHG the CMC = 1.5 ± 0.2 mM, with 0.7 M SHG CMC = 0.8 ± 0.3 mM; 0.8 M of SHG = 1.0 ± 0.2 mM; with the help of 0.9 M of SHG the CMC points estimation = 0.7 ± 0.4 mM and the highest concentration used was 1.0 M of SHG and the CMC point estimated at 0.6 ± 0.2 mM. These values are all very close but the difference between 0.5 M and 1.0 M SHGs suggests that CMC values fall slightly.

As a conclusion of this chapter:

- Colorimetric indicator and UV-VIS spectrophotometry allow measurements of CMC on amphiphiles within the SHG phase.
- Generally speaking, as the salt content of the SHG increases so the CMC values decrease.

7.3 Chapter 4:

During experiments to measure the CMC of SDS in SHG media (described in Chapter 3) using spectrophotometric measurements with the red dye merocyanine 540, an observation was made that, in higher silicate concentrations of SHG preparations, the initial red colour of the dye would of disappear, turning to pale yellow and then subsequently colourless after a certain time. The rate of this decolourisation process appeared to depend upon the concentration of the surfactant SDS and the concentration of silicate used in the hydrogel preparation method.

The study extended to examine the effect of surfactant on the decolourisation in which three different concentrations of SHG (0.5, 0.75 and 1.0) M. The results demonstrated that decolourisation was accelerated at the higher silicate formulations. Experiments were then performed on 0.5 M SHG's containing various concentrations of SDS, which demonstrated that the amphiphile protected the dye molecule from decolourisation to some degree.

Further investigations into the behaviour within SHGs media showed that all spectra of gelling SHG formulations suffered from baseline shifting in which the absorbance across a range of wavelengths increases with time. The base line shift is presumably due to scattering effects of the particulates that arise as the gelation process continues. This effect has been explored briefely as a possible simple method for determining gelation times in SHG's.

In order to probe this decolourisation phenomenon, a few scenarios have been proposed and studied, the first proposal was the effect of pH of the SHG.

The pH value of SHG (1.0 M silicate) stabilised at pH 9.8 after 45 mins at ambient temperature. While the same measurement is made of a SHG (1.0 M silicate) containing merocyanine at a concentration of 1 x 10^{-5} M, the pH stabilises at 10.3 after 30 min. from aqueous solutions of merocyanine readings, we note that at a pH of 12.4, the colour changes to a light yellow after several minutes but that at a pH of 10.3 there is no effective change of colour over a period of at least one hour. Therefore, the fact that decolourisation is observed in SHG formulations at pH 10.3 suggests that the reason behind the decolourisation is neither likely to be pH solely nor the singlet oxygen effect.

Another reason was proposed that decolourisation is primarily the shift of equilibrium between different dye states to two key colourless states; the H-aggregate and water adducts. Similar observations have been made by many groups [145, 146]. As of yet, no viable alternative mechanism has been suggested, however, more evidence is required before this can be stated as the ‘definitive’ explanation.

As a conclusion of this chapter:

- Decolourisation appears to be more facile in SHG’s with higher salt concentrations
- Decolourisation appears to be retarded in the presence of added amphiphile
- The definitive cause for the decolourisation is not yet known but neither singlet oxygen nor pH appear to be involved.
- Results suggest that incorporation of merocyanine within micellar structures leads to stabilisation of the dye towards decolourisation
- Our studies indicated that a base-line drift effect was occurring as the gel phase was forming. This is most probably due to light scattering and could potentially offer a simple mechanism for quantifying gelation times

7.4 Chapter 5

The molecular diffusivity of small neutral and charged molecules of potential importance to prebiotic chemistry which have been studied in this chapter, comparing their behaviours in the aqueous and SHG phases. Data has been collected on two different instrument manufacturers (Jeol and Bruker) from three different research groups (SoC, Mathias Nilsson group from University of Manchester and Georgelin group in Paris, France).

Each instrument has its own processing built-in software in which all parameters are fixed, therefore we elected to use the unified processing software called General NMR Analysis Toolkit (GNAT) in which the processing parameters can be entered and manipulated manually on datasets that had been collected on any instrument

Charged molecules adenosine monophosphate, adenosine diphosphate and adenosine triphosphate have been examined using on a Jeol instrument within SoC.

Diffusion constants differ with media used as follow: adenosine monophosphate AMP in deuterium water 3.4 ± 0.069, within basic environment of pH 12 3.4 ±

0.059, within 0.5 M SHG 2.7 ± 0.046 and within modified pH 12 of SHG environment 2.5 ± 0.081.

For adenosine diphosphate ADP: within deuterium water environment; 3.5 ± 0.036, within modified pH 12 deuterium water; 3.3 ± 0.042 and within 0.5 M SHG and pH 12 media; 2.7 ± 0.096.

Adenosine triphosphate ATP: within deuterium water; 2.7 ± 0.031, within pH 12 modified deuterium water; 2.9 ± 0.057 ,when shift to 0.5 M of SHG; 2.4 ± 0.066 , and within pH 12 modified SHG environment; 2.1 ± 0.056. The unit of the diffusion constants in all cases is 10^{-10} m^2 s^{-1}.

The quality of the above experimental data was assessed through the quality of the fitting to the residual plot of the signal amplitude vs the squared gradient amplitude.

The diffusion constant of ribose has been studied as well using Bruker instrumentation (Paris, France) and GNAT software as follows: with the help of Bruker manufacturer software the diffusion constant with deuterium water environment were found to be 6.4 10^{-10} m^2 s^{-1} while with the help of the GANT software was found to be 5.7 ± 0.68 x 10^{-10} m^2 s^{-1}.

In stimulated Hedean water, the Bruker result was 5.6 10^{-10} m^2 s^{-1} while the GNAT reading at 5.5 ± 0.14 x10^{-10} m^2 s^{-1}. The validity and reliability of the results have been subjected the residual plots.

As a conclusion of this chapter:

- Diffusion appears to be slowed in the SHG phase compared to the water environment.
- The quality of some of the data is called into question as a result of the residual analysis

7.5 Future plans and recommendations

As stated in the Aims and Objectives section, the overarching aim of my project is to study how molecular interactions, of potential relevance to abiogenesis, could be influenced by geologically plausible hydrogel environments. The work reported in this thesis set the groundwork for this and has established, at this stage, that differences are to be expected and could turn out to be significant in the context of an origin. There are several lines of enquiry that have been opened up in this thesis which could logically be pursued in greater detail or initiated as a “next-phase” project. Some of these are collected below:

(i) How do the CMC’s of long chain carboxylic acids and simple orthophosphate esters (putative prebiotic amphiphiles) change when measured in a silica hydrogel phase?

We have used sodium dodecylsulfate in this thesis but of course, this does not have an especially strong prebiotic provenance. More reasonable materials could include long-chain carboxylate and phosphate species, both of which have been demonstrated to be components of meteoritic inventories[147] or to have been potentially available to be prepared under plausible prebiotic conditions[148]. One could specifically examine here both micelle formation within the SHG phase and also the potential for vesicle formation when the above mentioned amphiphiles are combined with co-aggregating molecular such as long-chain alcohols[60]

(ii) Is it possible to visualize vesicle formation within the SHG environment?

In addition to fluorescent microscopy, an examination of vesicle formation, SHG formation and ultimately vesicle formation within SHG environments using the technique of small angle X-ray scattering (SAXS) would be most valuable

(iii) Explore the merocyanine decolourization phenomenon in more detail

We have uncovered an unusual process which could be examined more closely. Certainly, there is a need to perform a more statistically relevant mathematic analysis of the observations collected here along with analytical studies as the mechanism of the process.

(iv) Expand the scope of using DOSY to measure molecular diffusion in the gel phase

There is considerable scope to do this from the preliminary studies described in Chapter 5. There are some considerable instrumentation limitations perhaps the most significant of these being the use of a suitable NMR probe that is capable of collecting good data in aqueous electrolyte gels. However, there are some very interesting questions to ask, such as how molecular diffusion in the gel phase changes as one creates self-assembled aggregate

7.6 Appendix

Chapter 3 appendix

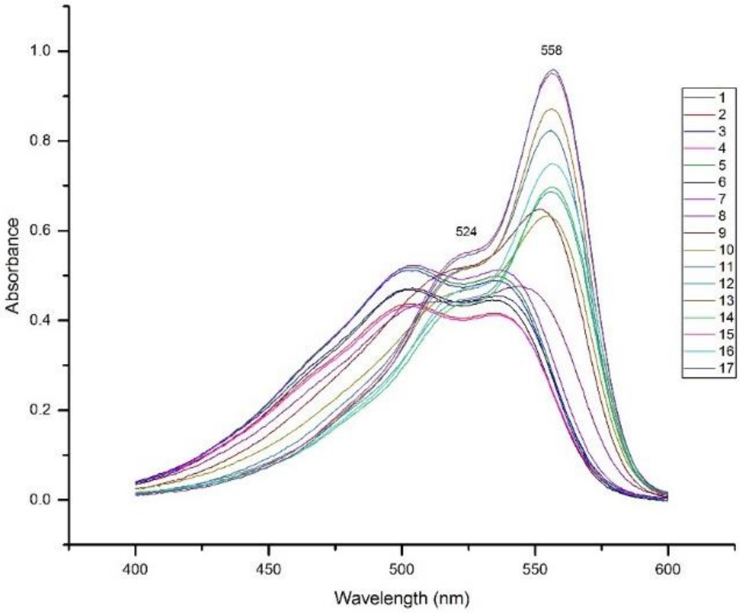

Figure 7-1: The absorption of each concentration of the surfactant SDS from 1 – 17 mM in aqueous phase using the MC540 spectrophotometric method for the second measurements.

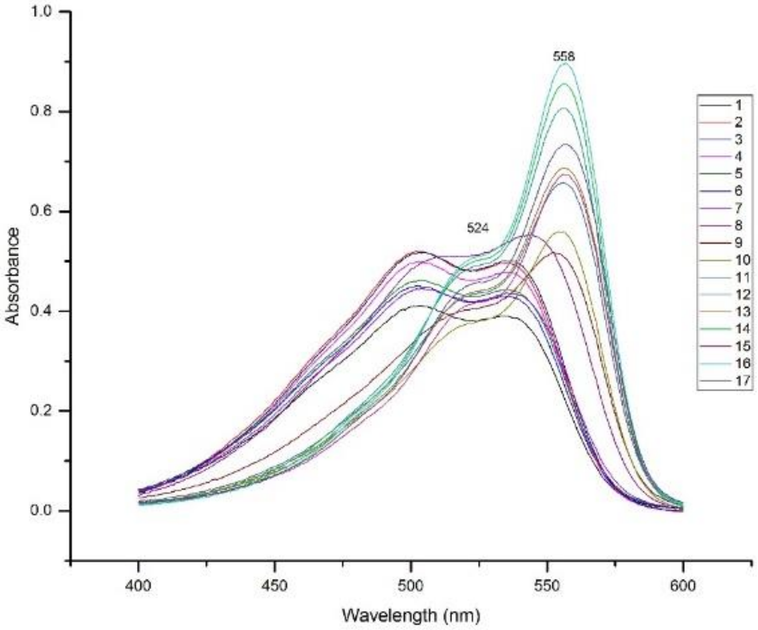

Figure 7-2: The absorption of each concentration of the surfactant SDS from 1 – 17 mM in aqueous phase using the MC540 spectrophotometric method for the third measurements.

Table 7-1: Linear fitting equation of the first maxima of absorption-concentration curve of MC 540

Equation	y = a + b*x		
Weight	No Weighting		
Residual Sum of Squares	0.00352		
Pearson's r	0.99971		
Adj. R-Square	0.99937		
		Value	Standard Error
1st maxima	Intercept	-0.02183	0.00978
1st maxima	Slope	22.8201	0.17237

Table 7-2: Linear fitting equation of the second maxima of absorption-concentration curve of MC 540

Equation	y = a + b*x		
Weight	No Weighting		
Residual Sum of Squares	0.01013		
Pearson's r	0.99922		
Adj. R-Square	0.99828		
		Value	Standard Error
2nd maxima	Intercept	-0.05247	0.01659
2nd maxima	Slope	23.35603	0.29227

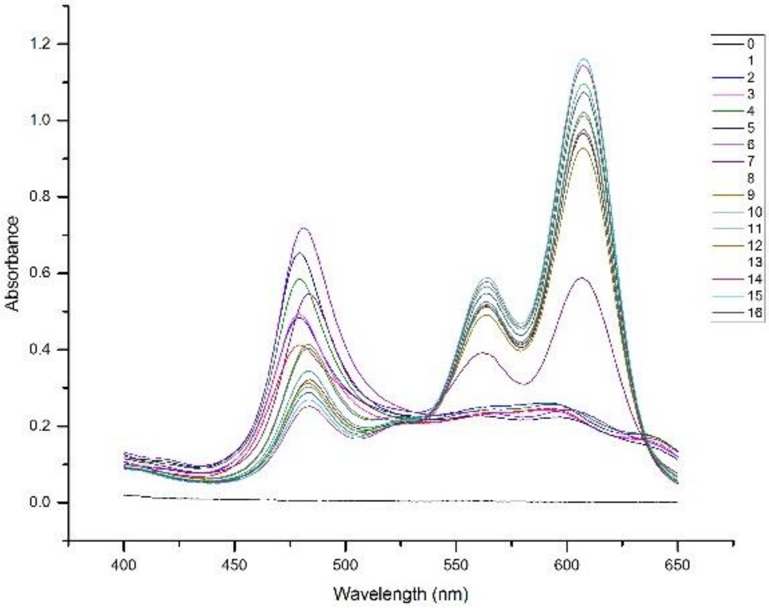

Figure 7-3: The absorption of each concentration of the surfactant SDS from 1 – 16 mM in aqueous phase using the PC spectrophotometric method for the second measurements.

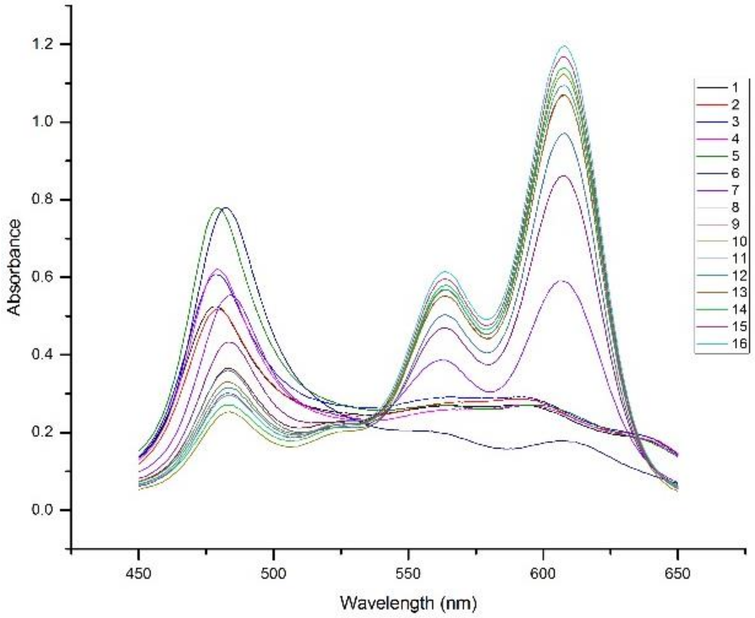

Figure 7-4: The absorption of each concentration of the surfactant SDS from 1 – 16 mM in aqueous phase using the PC spectrophotometric method for the third measurements.

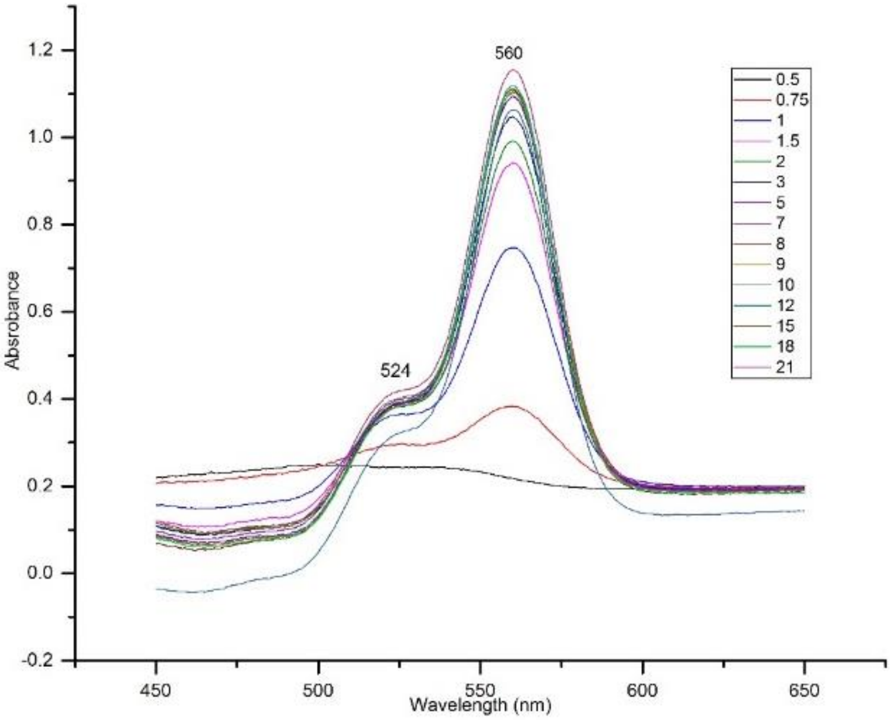

Figure 7-5: The absorption of each concentration of the surfactant SDS from 0.5 – 21 mM within 0.5M SHG phase using the MC540 spectrophotometric method for second measurements.

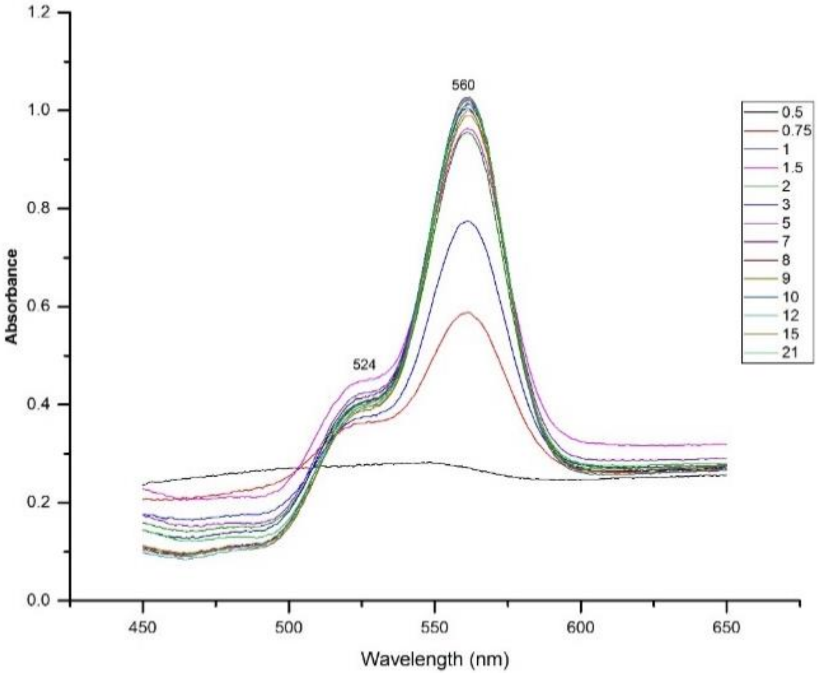

Figure 7-6: The absorption of each concentration of the surfactant SDS from 0.5 – 21 mM within 0.5M SHG phase using the MC540 spectrophotometric method for the third measurements.

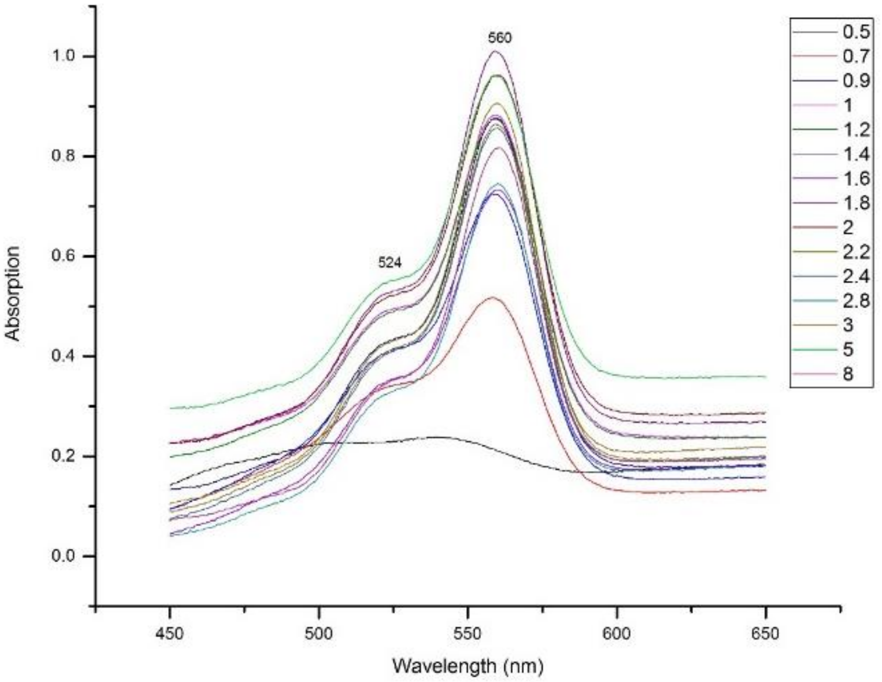

Figure 7-7: The absorption of each concentration of the surfactant SDS from 0.5 – 10 mM within 0.6M SHG phase using the MC540 spectrophotometric method for the second measurements

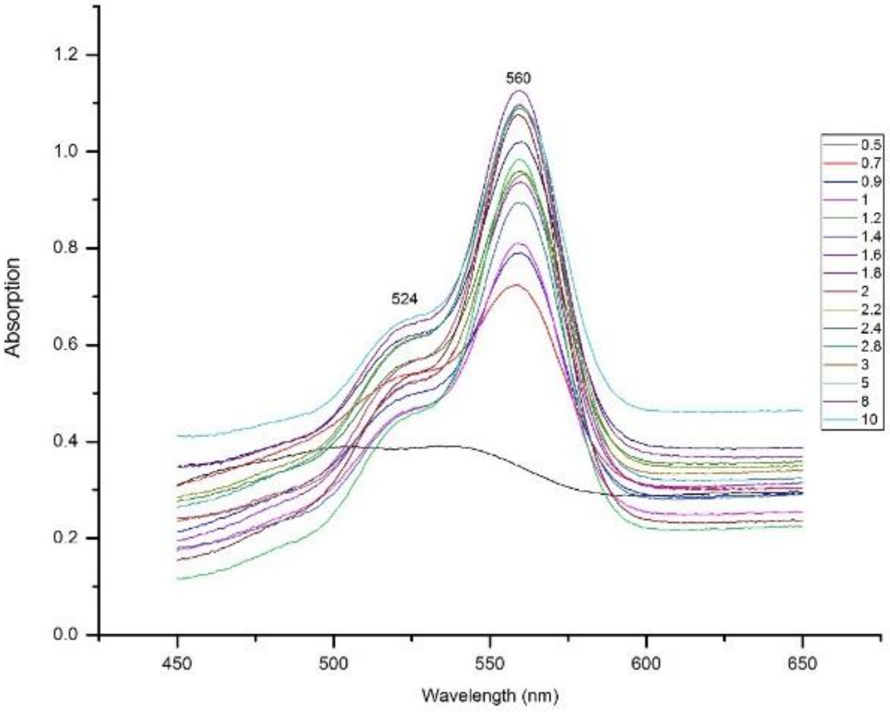

Figure 7-8: The absorption of each concentration of the surfactant SDS from 0.5 – 10 mM within 0.6M SHG phase using the MC540 spectrophotometric method for the third measurements

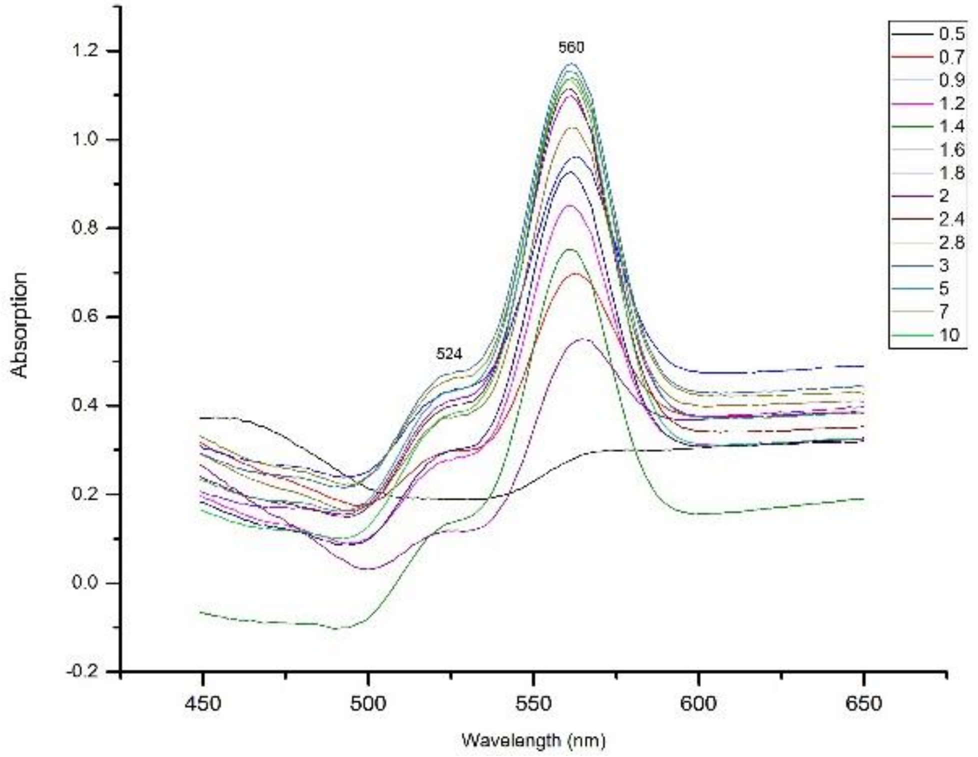

Figure 7-9: The absorption of each concentration of the surfactant SDS from 0.5 – 10 mM within 0.7 M SHG phase using the MC540 spectrophotometric method for the second measurement.

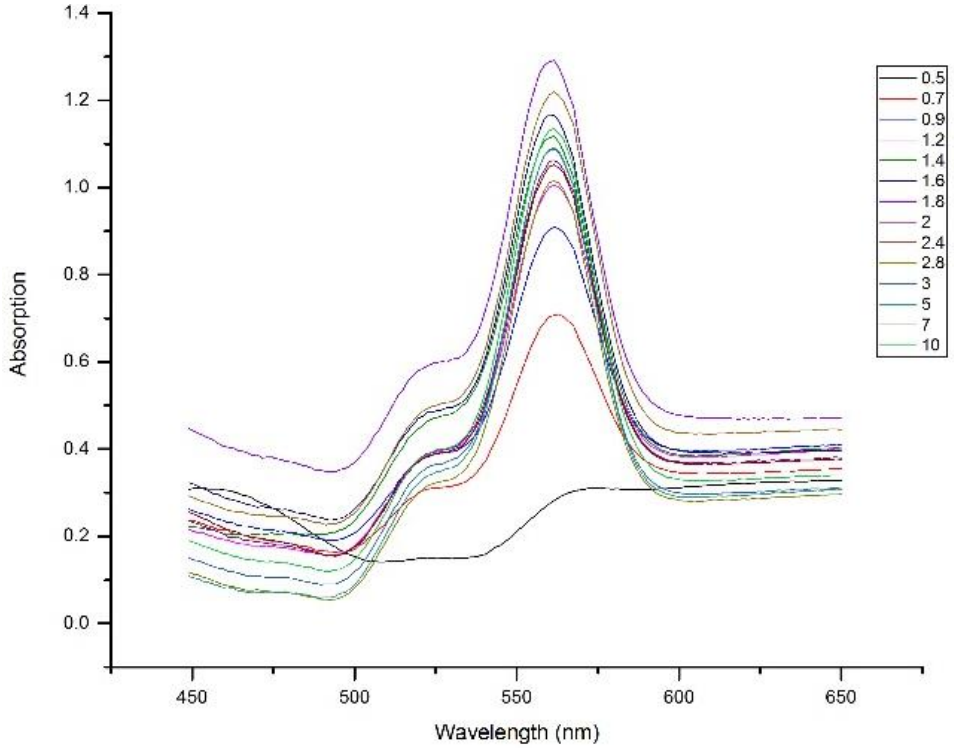

Figure 7-10: The absorption of each concentration of the surfactant SDS from 0.5 – 10 mM within 0.7 M SHG phase using the MC540 spectrophotometric method for the third measurement .

Table 7-3: Vertical fitting of CMC measurements of pyrene in aqueous phase

Equation	y = a + b*x		
Weight	No Weighting		
Residual Sum of Squares	6.58E+09		
Pearson's r	-0.99931		
Adj. R-Square	0.99725		
		Value	Standard Error
B	Intercept	1.14E+07	347383
B	Slope	-1.55E+06	57368.41

Table 7-4: Horizontal fitting of CMC measurements of MC540 in aqueous phase

Equation	y = a + b*x		
Weight	No Weighting		
Residual Sum of Squares	2.43E+10		
Pearson's r	0.57899		
Adj. R-Square	0.20228		
		Value	Standard Error
B	Intercept	484956.4	132596.3
B	Slope	17615.8	11093.8

Table 7-5: Vertical fitting of CMC measurements of MC540 in aqueous phase

Equation	y = a + b*x
Weight	Instrumental
Residual Sum of Squares	85.58126
Pearson's r	0.94621
Adj. R-Square	0.87438

		Value	Standard Error	
B	Intercept	0.93436	0.00578	
B	Slope	0.00636	9.72E-04	

Table 7-6: Horizontal fitting of CMC measurements of MC540 in aqueous phase

Equation	y = a + b*x		
Weight	Instrumental		
Residual Sum of Squares	0.31382		
Pearson's r	0.99853		
Adj. R-Square	0.99558		
		Value	Standard Error
B	Intercept	-0.17359	0.04866
B	Slope	0.1566	0.00602

Table 7-7: Vertical fitting of CMC measurements of PC in aqueous phase

Weight	Instrumental		
Residual Sum of Squares	0.94117		
Pearson's r	0.99635		
Adj. R-Square	0.98541		
		Value	Standard Error
B	Intercept	-1.90154	0.21192
B	Slope	0.3545	0.03039

Table 7-8: Horizontal fitting of CMC measurements of PC in aqueous phase

Equation	y = a + b*x
Weight	Instrumental
Residual Sum of Squares	0.73712

Pearson's r	0.39747		
Adj. R-Square	-0.05252		
		Value	Standard Error
B	Intercept	0.22154	0.00678
B	Slope	0.0017	0.00196

Table 7-9: Vertical fitting of CMC measurements of MC in 0.5 M SHG phase

Equation	y = a + b*x		
Weight	Instrumental		
Residual Sum of Squares	0.0055		
Pearson's r	0.99995		
Adj. R-Square	0.99978		
		Value	Standard Error
B	Intercept	-0.25219	0.0139
B	Slope	0.16639	0.00173

Table 7-10: Horizontal fitting of CMC measurements of MC in 0.5 M SHG phase

Equation	y = a + b*x		
Weight	Instrumental		
Residual Sum of Squares	0.87667		
Pearson's r	0.87604		
Adj. R-Square	0.72093		
		Value	Standard Error
B	Intercept	1.29989	0.07836
B	Slope	0.02343	0.00577

Table 7-11: Vertical fitting of CMC measurements of MC in 0.6 M SHG phase

Equation	y = a + b*x		
Weight	Instrumental		
Residual Sum of Squares	3.81062		
Pearson's r	0.99204		
Adj. R-Square	0.97623		
		Value	Standard Error
B	Intercept	0.15437	0.12337
B	Slope	1.62162	0.14551

Table 7-12: Horizontal fitting of CMC measurements of MC in 0.6 M SHG phase

Equation	y = a + b*x		
Weight	Instrumental		
Residual Sum of Squares	1.32971		
Pearson's r	0.09765		
Adj. R-Square	-0.11427		
		Value	Standard Error
B	Intercept	1.95846	0.03454
B	Slope	0.00264	0.00952

Table 7-13: Vertical fitting of CMC measurements of MC in 0.7 M SHG phase

Equation	y = a + b*x			
Weight	Instrumental			
Residual Sum of Squares	1.28662			
Pearson's r	0.93507			
Adj. R-Square	0.81153			
		Value	Standard Error	
Ave	Intercept	1.10412	0.29857	Ave

Ave	Slope	1.40334	0.37617	Ave

Table 7-14: Horizontal fitting of CMC measurements of MC in 0.7 M SHG phase

Equation	y = a + b*x		
Weight	Instrumental		
Residual Sum of Squares	5.10142		
Pearson's r	0.21871		
Adj. R-Square	-0.1426		
		Value	Standard Error
Ave	Intercept	2.73964	0.24898
Ave	Slope	0.01613	0.03217

Table 7-15: Horizontal fitting of CMC measurements of SDS with 1 x 10^{-5} M of PC in 0.5 M SHG phase

Equation	y = a + b*x		
Weight	Instrumental		
Residual Sum of Squares	0.6594		
Pearson's r	0.40615		
Adj. R-Square	-0.00205		
		Value	Standard Error
Average Abs	Intercept	0.96248	0.04085
Average Abs	Slope	0.00549	0.00552

Table 7-16: Vertical fitting of CMC measurements of SDS with 1 x 10^{-5} M of PC in 0.5 M SHG phase

Equation	y = a + b*x
Weight	Instrumental
Residual Sum of Squares	1.8091
Pearson's r	0.95604

Adj. R-Square	0.87101		
		Value	Standard Error
Average Abs	Intercept	-0.05477	0.14368
Average Abs	Slope	0.69575	0.1509

Table 7-17: Horizontal fitting of CMC measurements of SDS with 1 x 10^{-6} M of PC in 0.5 M SHG phase

Equation	y = a + b*x		
Weight	Instrumental		
Residual Sum of Squares	8.72242		
Pearson's r	0.95798		
Adj. R-Square	0.87659		
		Value	Standard Error
B	Intercept	-0.00319	0.1158
B	Slope	0.54399	0.11517

Table 7-18: Vertical fitting of CMC measurements of SDS with 1 x 10^{-6} M of PC in 0.5 M SHG phase

Equation	y = a + b*x		
Weight	Instrumental		
Residual Sum of Squares	15.17783		
Pearson's r	0.80137		
Adj. R-Square	0.59108		
		Value	Standard Error
B	Intercept	0.77064	0.0384
B	Slope	0.02164	0.00611

Table 7-19: Vertical fitting of CMC measurements of PC in 0.5 M SHG phase with 605 nm

Equation	*y = a + b*x*
Weight	*Instrumental*

Residual Sum of Squares	*9.20864*		
Pearson's r	*0.95201*		
Adj. R-Square	*0.8595*		
		Value	*Standard Error*
Average	*Intercept*	*0.0154*	*0.1186*
Average	*Slope*	*0.52094*	*0.11842*

Table 7-20: Horizontal fitting of CMC measurements of PC in 0.5 M SHG phase with 605 nm

Equation	y = a + b*x		
Weight	Instrumental		
Residual Sum of Squares	20.03558		
Pearson's r	0.75191		
Adj. R-Square	0.50327		
		Value	Standard Error
Average	Intercept	0.74265	0.04247
Average	Slope	0.02076	0.00688

Table 7-21: Vertical fitting of CMC measurements of SDS with PC in 0.6 M SHG phase

Equation	y = a + b*x		
Weight	Instrumental		
Residual Sum of Squares	1.1862		
Pearson's r	0.97069		
Adj. R-Square	0.91336		
		Value	Standard Error
Average Abs.	Intercept	0.35244	0.07525

Average Abs.	Slope	0.38997	0.06827

Table 7-22 Horizontal fitting of CMC measurements of SDS with PC in 0.6 M SHG phase

Equation	y = a + b*x		
Weight	Instrumental		
Residual Sum of Squares	9.56684		
Pearson's r	0.79696		
Adj. R-Square	0.58302		
		Value	Standard Error
Average Abs.	Intercept	0.94528	0.01899
Average Abs.	Slope	0.00468	0.00134

Table 7-23: Vertical fitting of CMC measurements of SDS with PC in 0.7 M SHG phase

Equation	y = a + b*x		
Weight	Instrumental		
Residual Sum of Squares	0.22292		
Pearson's r	0.97559		
Adj. R-Square	0.90355		
		Value	Standard Error
B	Intercept	0.01197	0.09946
B	Slope	1.07977	0.24305

Table 7-24: Horizontal fitting of CMC measurements of SDS with PC in 0.7 M SHG phase

Equation	y = a + b*x
Weight	Instrumental
Residual Sum of Squares	3.35319
Pearson's r	0.9069

Adj. R-Square	0.7971		
		Value	Standard Error
B	Intercept	0.91275	0.01714
B	Slope	0.03499	0.00614

Table 7-25: Vertical fitting of CMC measurements of SDS with PC in 0.8 M SHG phase

Equation	y = a + b*x		
Weight	Instrumental		
Residual Sum of Squares	16.02827		
Pearson's r	0.90453		
Adj. R-Square	0.77272		
		Value	Standard Error
B	Intercept	0.1438	0.07443
B	Slope	0.4143	0.09765

Table 7-26: Horizontal fitting of CMC measurements of SDS with PC in 0.8 M SHG phase

Equation	y = a + b*x		
Weight	Instrumental		
Residual Sum of Squares	14.31255		
Pearson's r	0.6728		
Adj. R-Square	0.36144		
		Value	Standard Error
B	Intercept	0.56105	0.024
B	Slope	0.01446	0.00649

Table 7-27: Vertical fitting of CMC measurements of SDS with PC in 0.9 M SHG phase

Equation	y = a + b*x
Weight	Instrumental

Residual Sum of Squares	79.52808			
Pearson's r	0.91203			
Adj. R-Square	0.77573			
		Value	Standard Error	
B	Intercept	-0.0173	0.08088	
B	Slope	0.53131	0.13794	

Table 7-28: Horizontal fitting of CMC measurements of SDS with PC in 0.9 M SHG phase

Equation	y = a + b*x		
Weight	Instrumental		
Residual Sum of Squares	5.47061		
Pearson's r	0.90958		
Adj. R-Square	0.80267		
		Value	Standard Error
B	Intercept	0.38533	0.00808
B	Slope	0.00984	0.0017

Table 7-29: Vertical fitting of CMC measurements of SDS with PC in 0.1 M SHG phase

Equation	y = a + b*x		
Weight	Instrumental		
Residual Sum of Squares	0.0815		
Pearson's r	0.99465		
Adj. R-Square	0.97865		
		Value	Standard Error
B	Intercept	0.03017	0.02375
B	Slope	0.55453	0.05761

Table 7-30: Horizontal fitting of CMC measurements of SDS with PC in 0.1 M SHG phase

Equation	y = a + b*x		
Weight	Instrumental		
Residual Sum of Squares	1.9423		
Pearson's r	0.96685		
Adj. R-Square	0.92549		
		Value	Standard Error
B	Intercept	0.38152	0.01863
B	Slope	0.02187	0.00218

Chapter 4 appendix

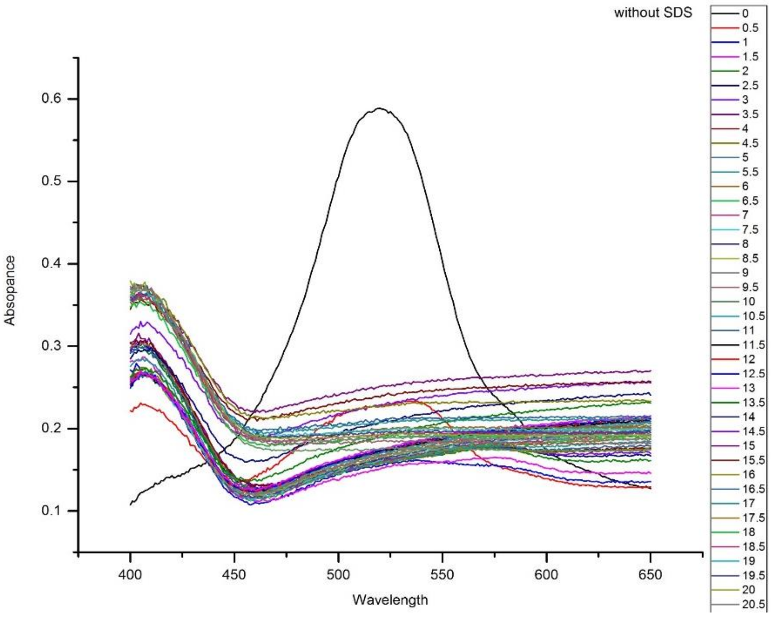

Figure 7-11: The actual absorption spectra for MC 540 under 1.0 M SHG conditions (without any SDS).

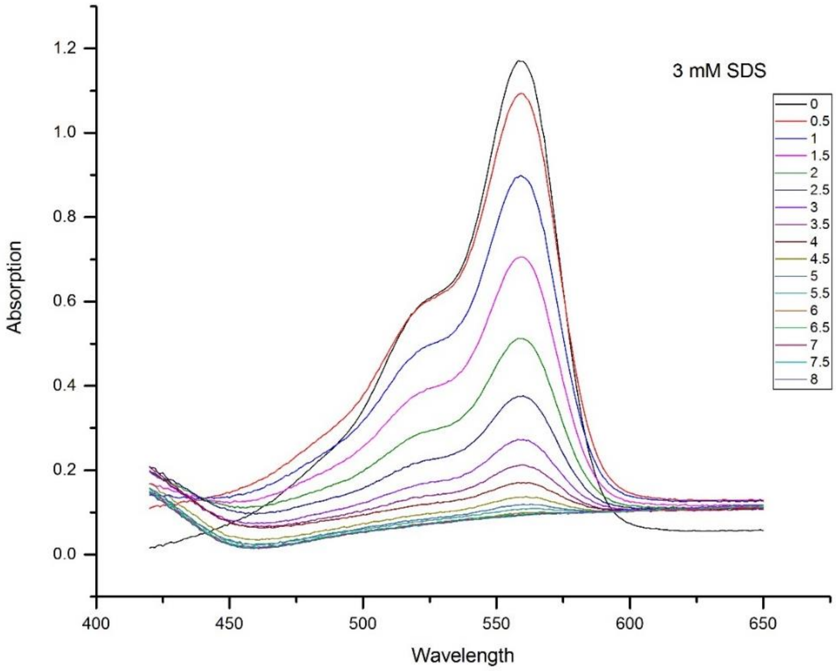

Figure 7-12: The actual absorption spectra for MC 540 under 1.0 M SHG conditions (3 mM SDS)

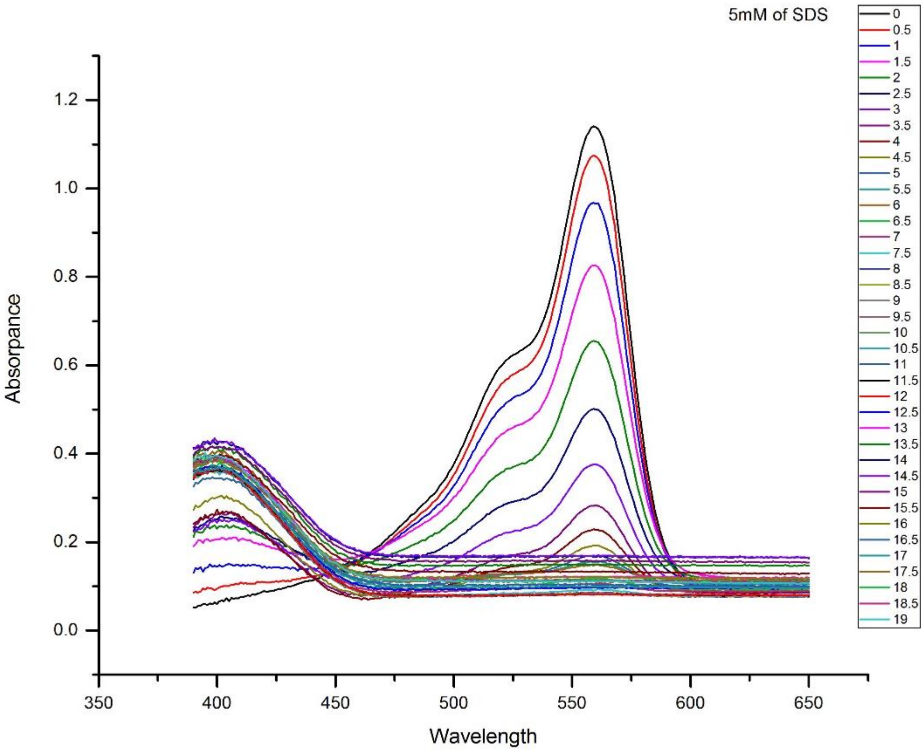

Figure 7-13: The actual absorption spectra for MC 540 under 1.0 M SHG conditions (5 mM SDS)

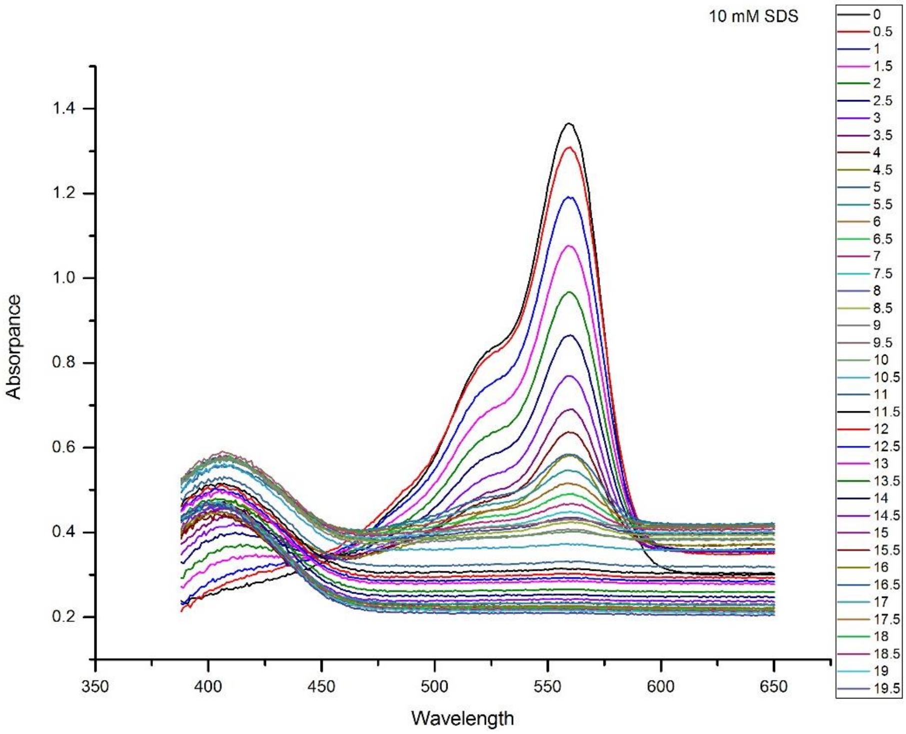

Figure 7-14: The actual absorption spectra for MC 540 under 1.0 M SHG conditions (10 mM SDS)

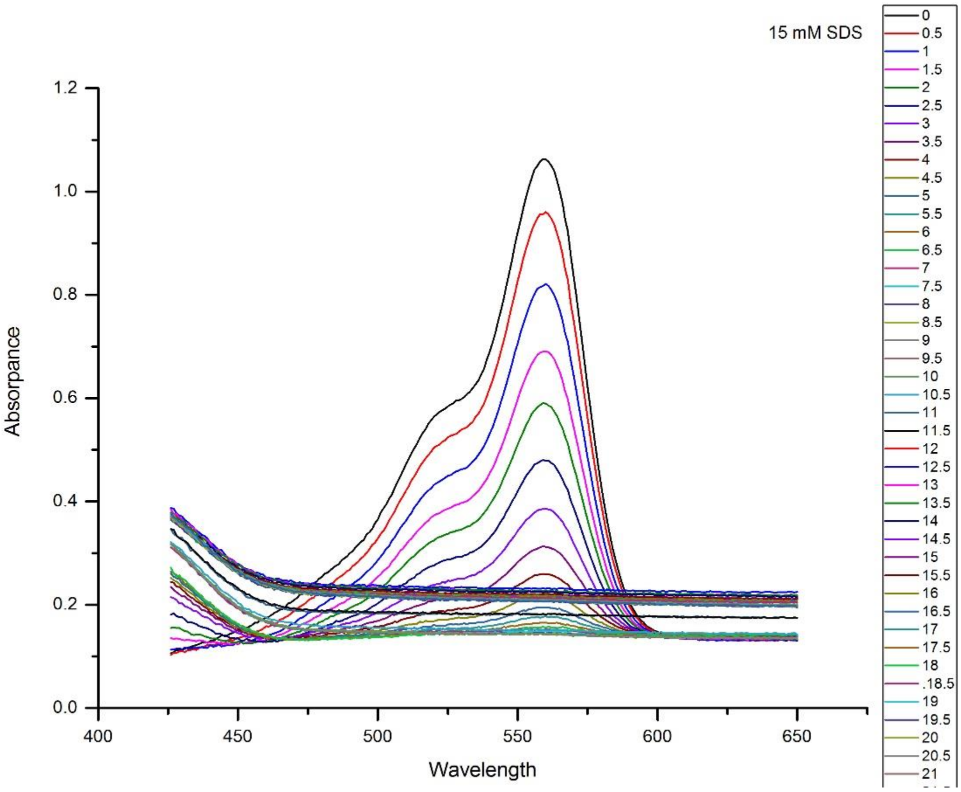

Figure 7-15: The actual absorption spectra for MC 540 under 1.0 M SHG conditions (15 mM SDS)

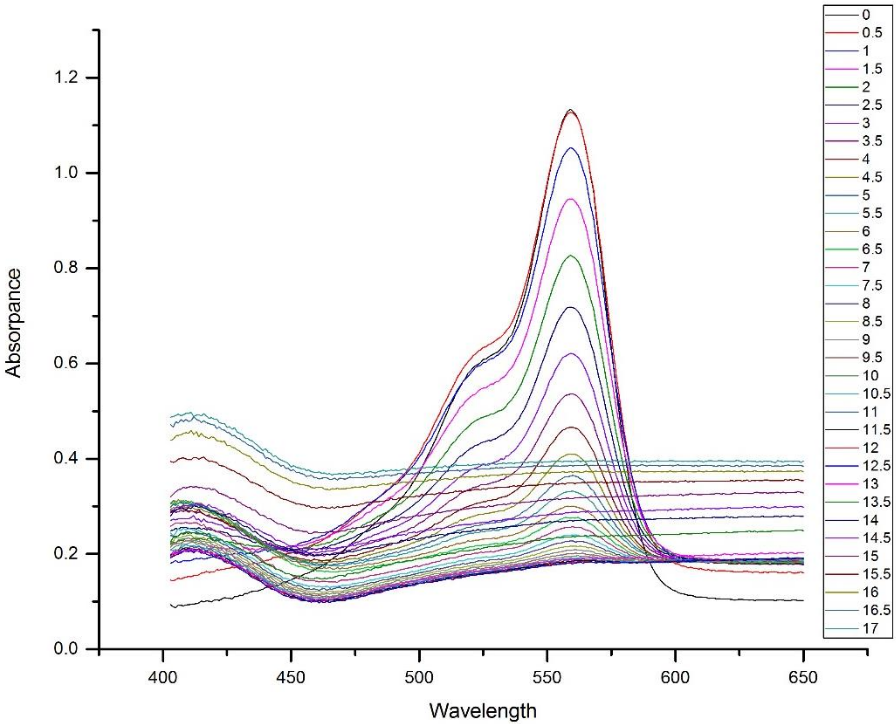

Figure 7-16: The actual absorption spectra for MC 540 under 1.0 M SHG conditions (18 mM SDS)

Chapter 5 appendix

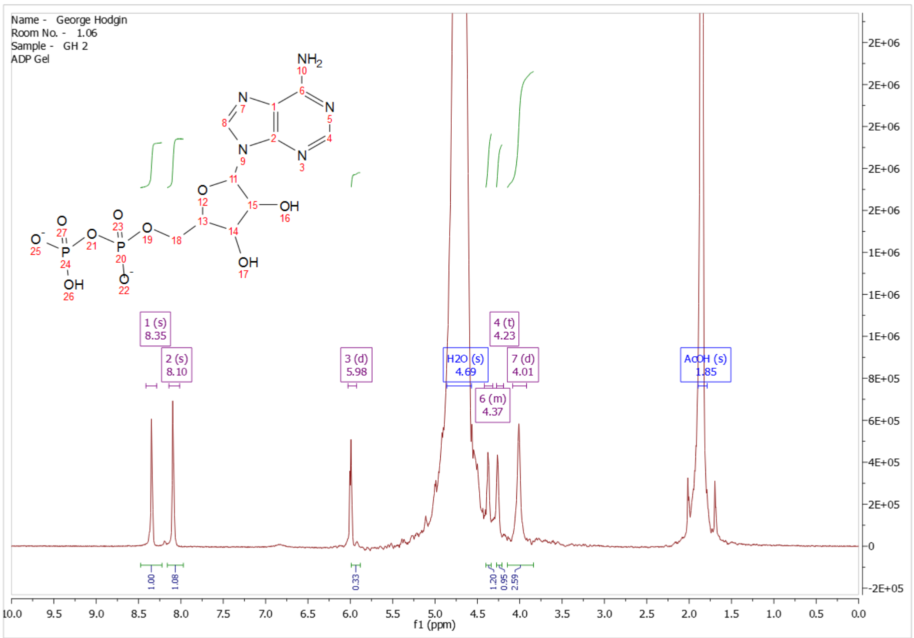

Figure 7-17: AMP SHG 1H NMR (400 MHz, D_2O) δ 8.35 (s, 1H), 8.10 (s, 1H), 5.98 (d, J = 15.3 Hz, 1H), 4.69 (s, 222H), 4.42 – 4.32 (m, J = 17.3 Hz, 1H), 4.23 (t, J = 28.6 Hz, 1H), 4.01 (d, 1H), 1.85 (s, 26H).

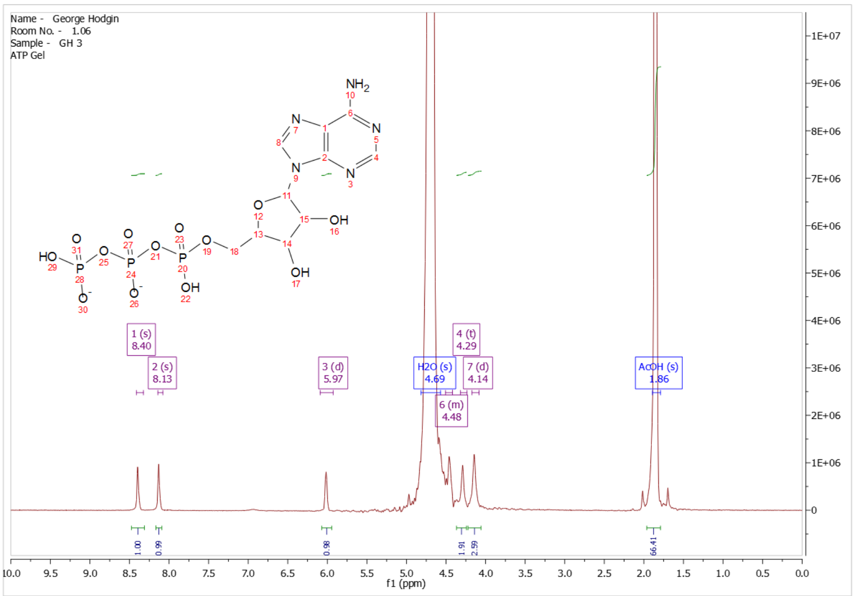

Figure 7-18: ATP SHG 1H NMR (400 MHz, D_2O) δ 8.40 (s, 1H), 8.13 (s, 1H), 5.97 (d, 1H), 4.69 (s, 266H), 4.51 – 4.42 (m, J = 13.2 Hz, 1H), 4.29 (d, 1H), 4.14 (t, 1H), 1.86 (s, 32H).

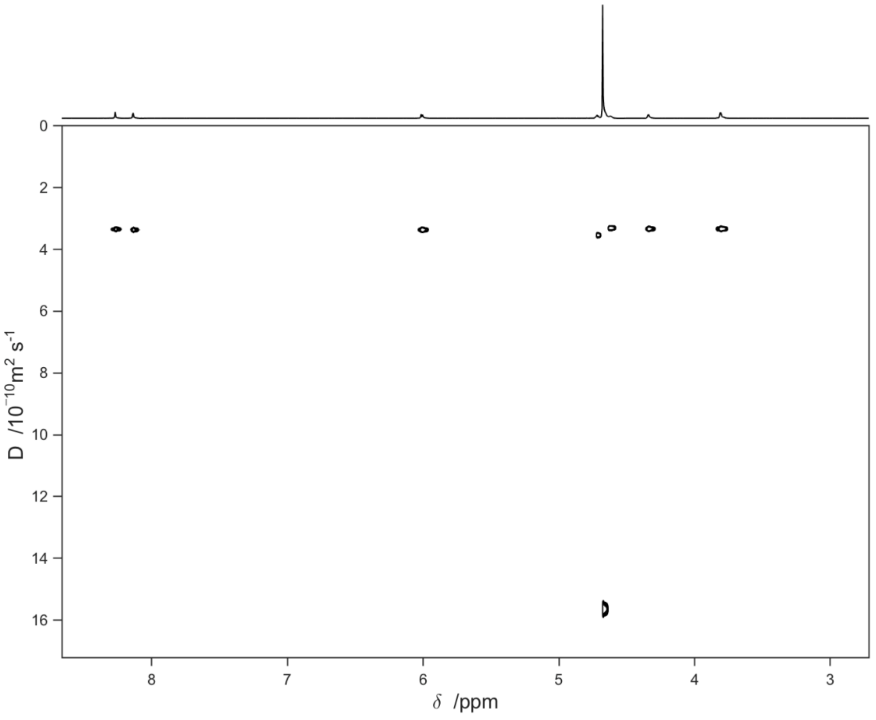

Figure 7-19: AMP in D_2O

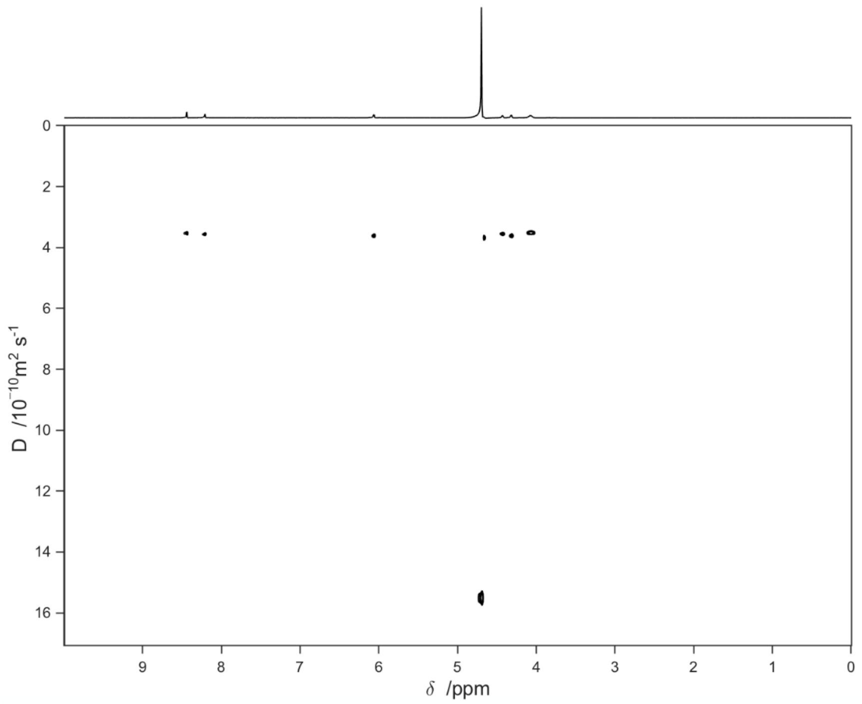

Figure 7-20: ADP in D_2O medium

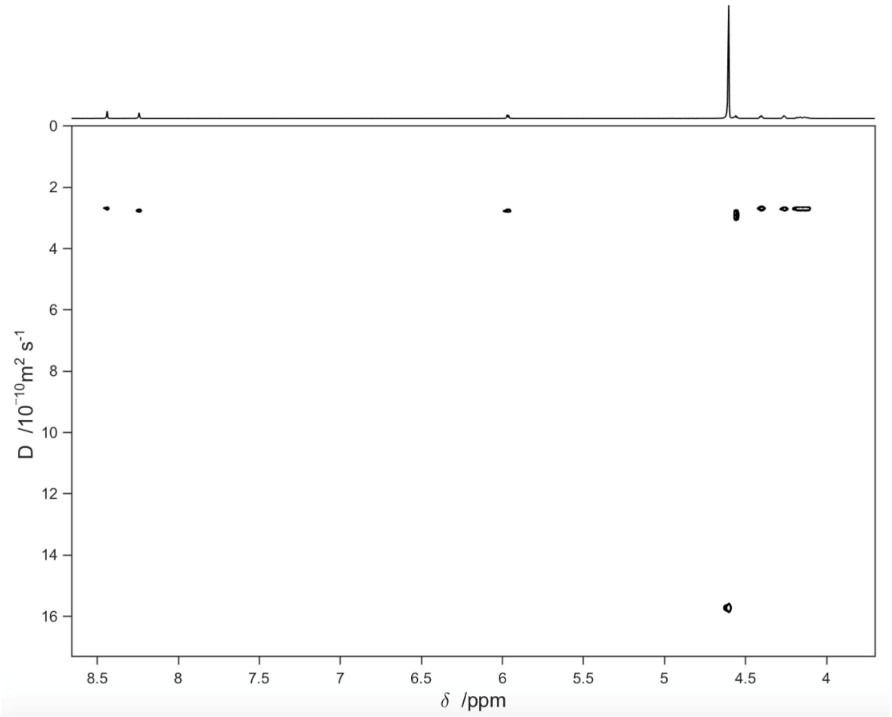

Figure 7-21: ATP in D_2O medium

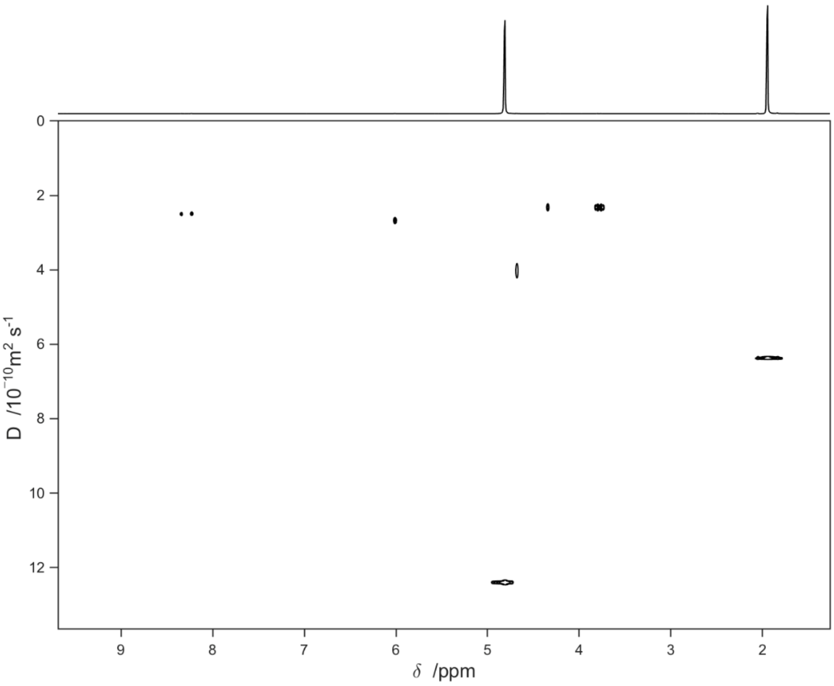

Figure 7-22: AMP in SHG environment

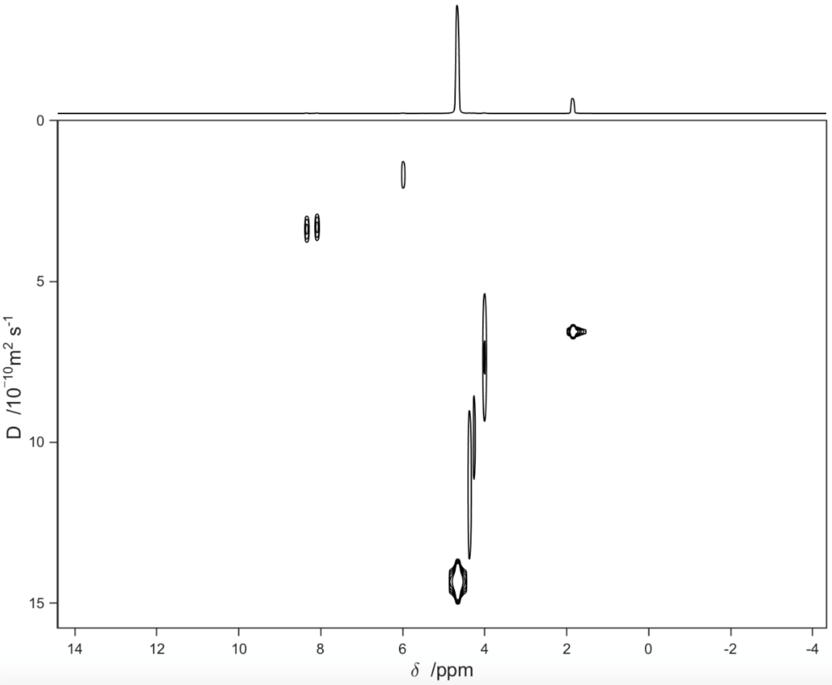

Figure 7-23: ADP in SHG environment

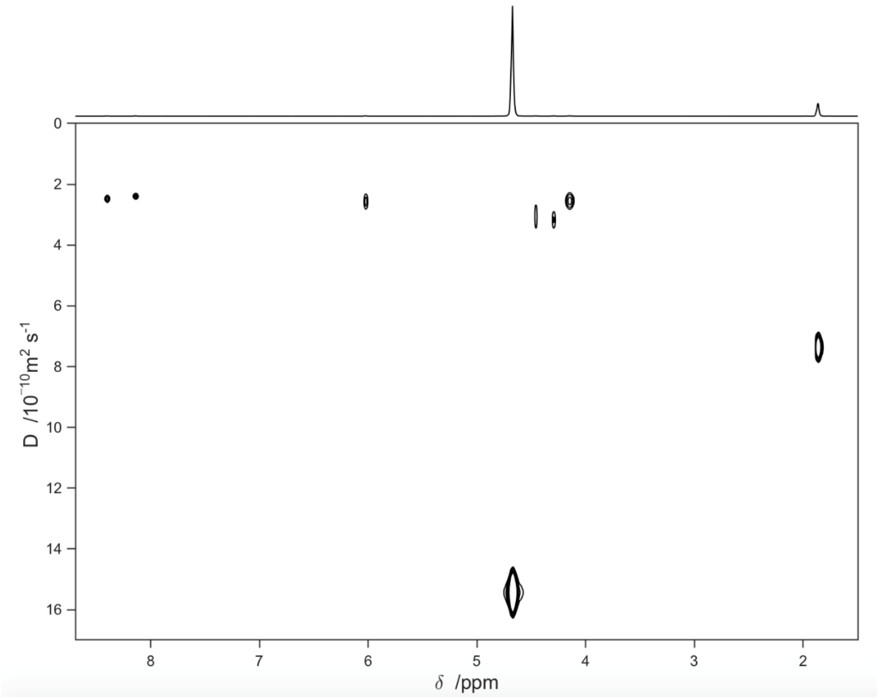

Figure 7-24: ATP in SHG environment

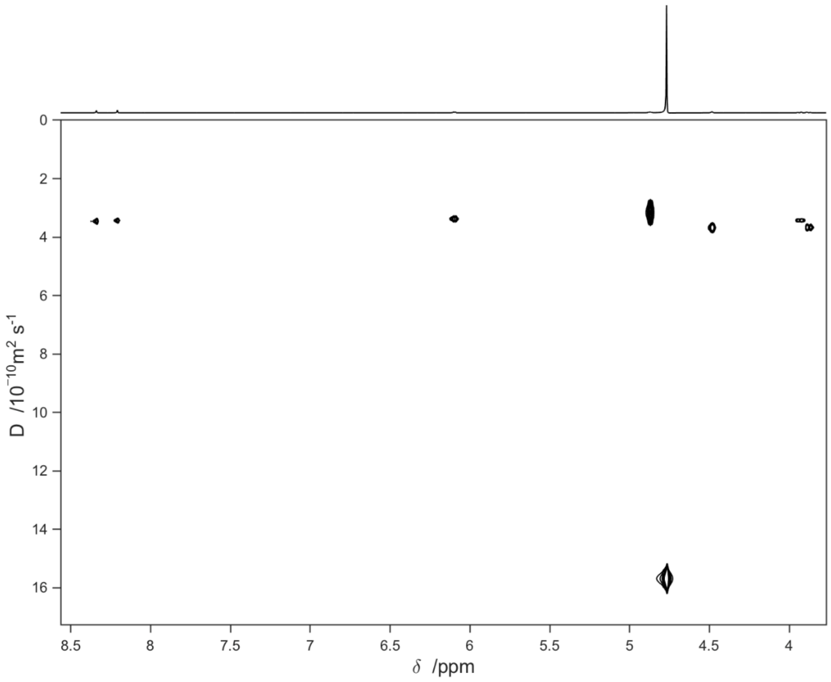

Figure 7-25: AMP pH12 in D_2O medium

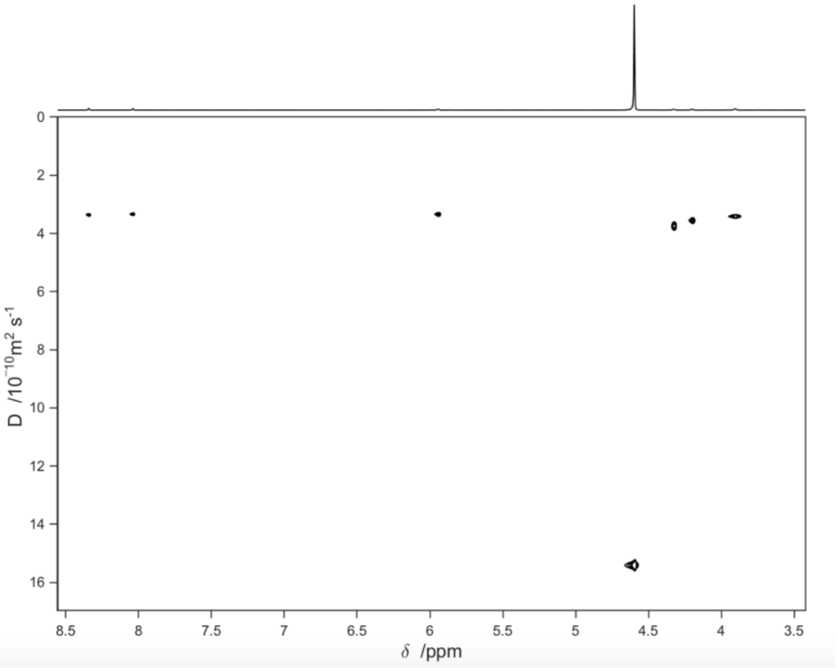

Figure 7-26: ADP pH12 in D_2O medium

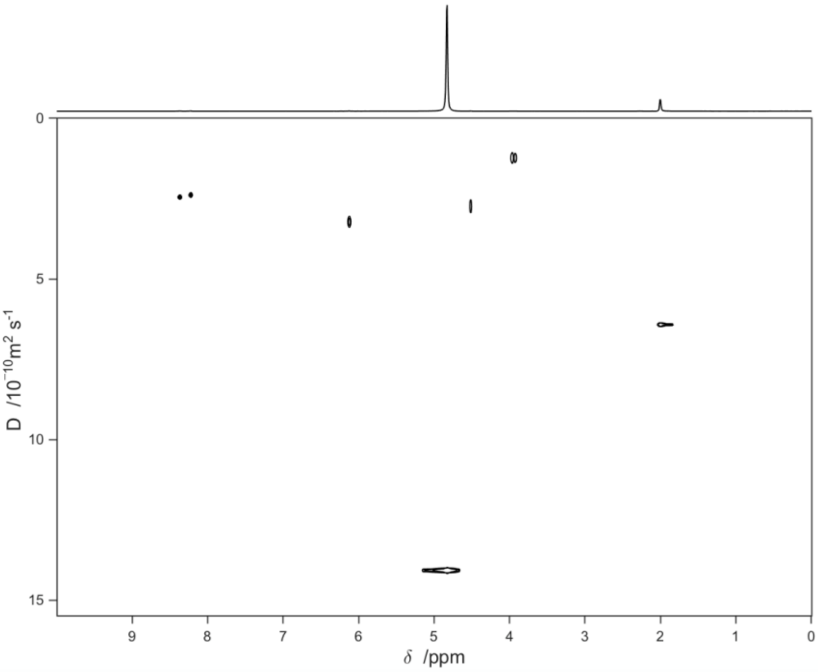

Figure 7-27: ATP pH12 in D_2O medium

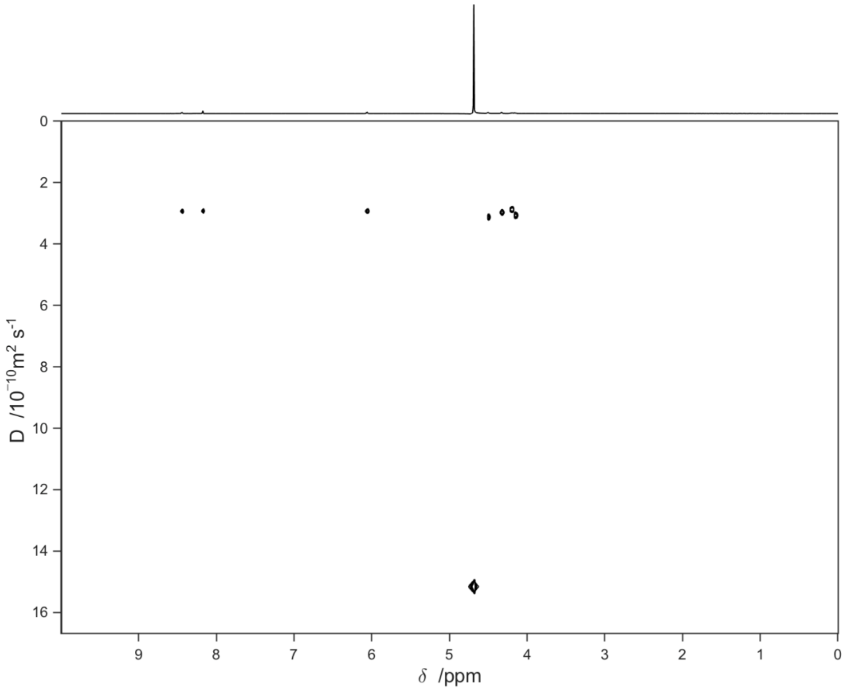

Figure 7-28: AMP at pH12 within SHG environment

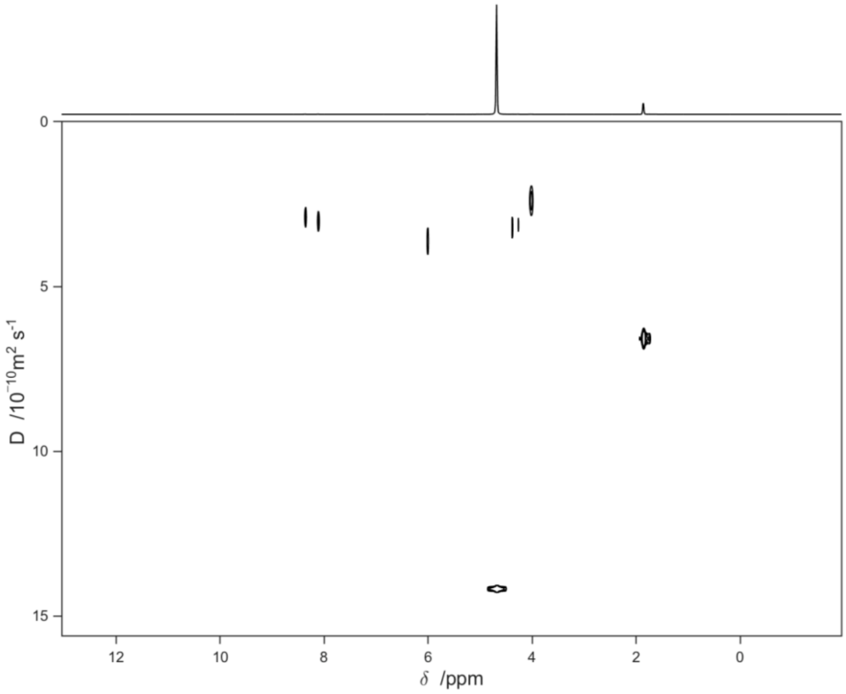

Figure 7-29: ADP at pH12 within SHG environment

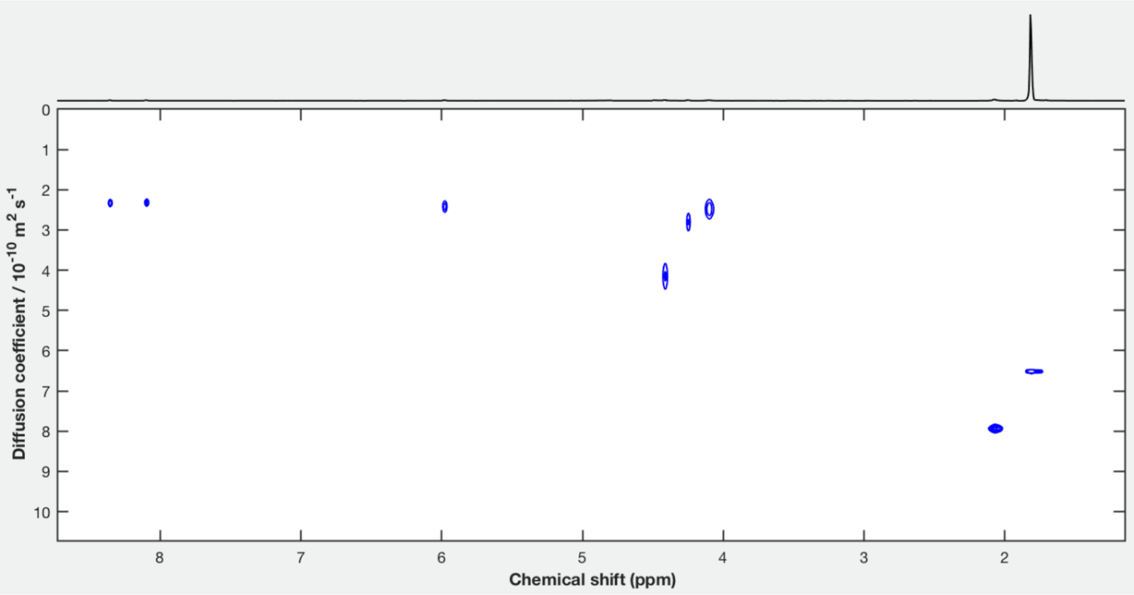

Figure 7-30: ATP at pH12 within SHG environment

7.7 References

1. Ahmed, E.M., Hydrogel: Preparation, characterization, and applications: A review. Journal of Advanced Research 2015, 6(2), 105-121.

2. Atkins, P.W., De Paula, J., Atkins' Physical chemistry. Oxford University Press. Oxford, 2014.

3. Almdal, K., Dyre, J., Hvidt, S., Kramer, O., Towards a phenomenological definition of the term 'gel'. Polymer Gels and Networks 1993, 1(1), 5-17.

4. Singh, A., Sharma, P.K., Garg, V.K., Garg, G., Hydrogels: A review. International Journal of Pharmaceutical Sciences Review and Research 2010, 4(2), 97-105.

5. Hamidi, M., Azadi, A., Rafiei, P., Hydrogel nanoparticles in drug delivery. Advanced Drug Delivery Reviews 2008, 60(15), 1638-1649.

6. Lu, C., Zahedi, P., Forman, A., Allen, C., Multi-arm PEG/Silica Hydrogel for Sustained Ocular Drug Delivery. Journal of Pharmaceutical Sciences 2014, 103(1), 216-226.

7. Yang, Z.-X., Chen, B.-A., Wang, H., Xia, G.-H., Cheng, J., Pei, X.-P., Wang, F., Bao, W., Handy, rapid and multiplex detection of tumor markers based on encoded silica–hydrogel hybrid beads array chip. Biosensors and Bioelectronics 2013, 48, 153-157.

8. Siow, K.S., Kumar, S., Griesser, H.J., Low-Pressure Plasma Methods for Generating Non-Reactive Hydrophilic and Hydrogel-Like Bio-Interface Coatings – A Review. Plasma Processes and Polymers 2015, 12(1), 8-24.

9. Saxena, A.K., Synthetic biodegradable hydrogel (PleuraSeal) sealant for sealing of lung tissue after thoracoscopic resection. The Journal of Thoracic and Cardiovascular Surgery 2010, 139(2), 496-497.

10. Chen, X., Martin, B.D., Neubauer, T.K., Linhardt, R.J., Dordick, J.S., Rethwisch, D.G., Enzymatic and chemoenzymatic approaches to synthesis of sugar-based polymer and hydrogels. Carbohydrate Polymers 1995, 28(1), 15-21.

11. Zhang, L., Zhang, X., Li, K., Xiao, W., Xiao, Y., Zheng, L., Fan, H., Preparation of collagen–chondroitin sulfate–hyaluronic acid hybrid hydrogel scaffolds and cell compatibility in vitro. Carbohydrate Polymers 2011, 84(1), 118-125.

12. Wang, F., Li, Z., Khan, M., Tamama, K., Kuppusamy, P., Wagner, W.R., Sen, C.K., Guan, J., Injectable, rapid gelling and highly flexible hydrogel composites as growth factor and cell carriers. Acta Biomaterialia 2010, 6(6), 1978-1991.

13. Krsko, P., McCann, T.E., Thach, T.-T., Laabs, T.L., Geller, H.M., Libera, M.R., Length-scale mediated adhesion and directed growth of neural cells by surface-patterned poly(ethylene glycol) hydrogels. Biomaterials 2009, 30(5), 721-729.

14. Trevors, J.T., Pollack, G.H., Hypothesis: the origin of life in a hydrogel environment. Progress in Biophysics and Molecular Biology 2005, 89(1), 1-8.

15. Beebe, D.J., Moore, J.S., Bauer, J.M., Yu, Q., Liu, R.H., Devadoss, C., Jo, B.-H., Functional hydrogel structures for autonomous flow control inside microfluidic channels. Nature 2000, 404(6778), 588-590.

16. Wilson, S.L., Ahearne, M., El Haj, A.J., Yang, Y., Chapter 8 Mechanical Characterization of Hydrogels and its Implications for Cellular Activities. Hydrogels in Cell-Based Therapies, The Royal Society of Chemistry: 2014; pp 171-190.

17. Abul-Haija, Y.M., Ulijn, R.V., Chapter 6 Enzyme-Responsive Hydrogels for Biomedical Applications. Hydrogels in Cell-Based Therapies, The Royal Society of Chemistry: 2014; pp 112-134.

18. Jena, K.K., Rout, T.K., Narayan, R., Raju, K.V.S.N., Novel organic–inorganic hybrid coatings prepared by the sol–gel process: corrosion and mechanical properties. Polymer International 2012, 61(7), 1101-1106.

19. Cairns-Smith, A., The origin of life: clays. Frontiers of Life 2001, 1, 169-192.

20. Trevors, J.T., Abel, D.L., Chance and necessity do not explain the origin of life. Cell Biology International 2004, 28(11), 729-739.

21. Bashkin, V.N., Howarth, R.W., Modern biogeochemistry. Springer Science & Business Media. 2002.

22. Bebié, J., Schoonen, M.A.A., Pyrite and phosphate in anoxia and an origin-of-life hypothesis. Earth and Planetary Science Letters 1999, 171(1), 1-5.

23. Segré, D., Ben-Eli, D., Deamer, D.W., Lancet, D., The lipid world. Origins of Life and Evolution of the Biosphere 2001, 31(1-2), 119-145.

24. Ingber, D.E., The origin of cellular life. BioEssays 2000, 22(12), 1160-1170.

25. Trevors, J., The subsurface origin of microbial life on the Earth. Research in microbiology 2002, 153(8), 487-491.

26. Pollack, G.H., Cells, gels and the engines of life: a new, unifying approach to cell function. Ebner & Sons. Seattle, WA, 2001.

27. Yang, D.Y., Peng, S.M., Hartman, M.R., Gupton-Campolongo, T., Rice, E.J., Chang, A.K., Gu, Z., Lu, G.Q., Luo, D., Enhanced transcription and translation in clay hydrogel and implications for early life evolution. Scientific Reprts 2013, 3(Journal Article), 3165.

28. Trevors, J.T., Hypothesized origin of microbial life in a prebiotic gel and the transition to a living biofilm and microbial mats. Comptes rendus - Biologies 2011, 334(4), 269-272.
29. Williamson, B., Stanley, C., Wilkinson, J., Implications from inclusions in topaz for greisenisation and mineralisation in the Hensbarrow topaz granite, Cornwall, England. Contributions to Mineralogy and Petrology 1997, 127(1-2), 119-128.
30. Štemprok, M., Greisenization (a review). Geologische Rundschau 1987, 76, 169-175.
31. Cammarata, M., Levantino, M., Cupane, A., Longo, A., Martorana, A., Bruni, F., Structure and dynamics of water confined in silica hydrogels: X-ray scattering and dielectric spectroscopy studies. The European Physical Journal E 2003, 12(S1), 63-66.
32. Ferri, F., Frisken, B.J., Cannell, D.S., Structure of silica gels. Physical Review Letters 1991, 67(25), 3626-3629.
33. Bale, H.D., Schmidt, P.W., Small-angle X-ray-scattering investigation of submicroscopic porosity with fractal properties. Physical Review Letters 1984, 53(6), 596.
34. Peri, J., Hensley Jr, A., The surface structure of silica gel. The Journal of Physical Chemistry 1968, 72(8), 2926-2933.
35. Sukhyy, K.M., Belyanovskaya, E.A., Kozlov, Y.N., Kolomiyets, E.V., Sukhyy, M.P., Structure and adsorption properties of the composites ‘silica gel–sodium sulphate’, obtained by sol–gel method. Applied Thermal Engineering 2014, 64(1–2), 408-412.
36. Bray, D., Critical point drying of biological specimens for scanning electron microscopy. Supercritical Fluid Methods and Protocols 2000, 235-243.
37. Catlouge, Criticel Point Drying. 2015.
38. Ruwin Pandithage, D., Brief Introduction to Critical Point Drying. Leica Microsystems: December 11, 2012; Vol. 2011.
39. Technologies, Q., Critical Point Drying Procedure. TECHNICAL BRIEF Critical Point Drying, 2009.
40. Reimer, L., Scanning electron microscopy: physics of image formation and microanalysis. Springer. Berlin, 1998.
41. Reimer, L., Scanning Electron Microscopy: Physics of Image Formation and Microanalysis, Second Edition. Measurement Science and Technology 2000, 11(12), 1826.
42. Schatten, H., Scanning Electron Microscopy for the Life Sciences. Cambridge University Press. 2012.
43. Rangel-Yagui, C.d.O., Pessoa Jr, A., Tavares, L.C., Micellar solubilization of drugs. Journal of Pharmacy and Pharmaceutical Sciences 2005, 8(2), 147-163.

44. Ritacco, H., Kovensky, J., Fernández-Cirelli, A., Castro, M.J., A simplified method for the determination of critical micelle concentration. Journal of Chemical Education 2001, 78(3), 347.
45. Nagarajan, R., Amphiphilic surfactants and amphiphilic polymers: principles of molecular assembly. Amphiphiles: molecular assembly and applications, ACS symposium series. American Chemical Society, Washington, DC, 2011; pp 1-22.
46. Tanford, C., The hydrophobic effect: formation of micelles and biological membranes. Wiley. New York, 1973.
47. Tanford, C., Theory of micelle formation in aqueous solutions. The Journal of Physical Chemistry 1974, 78(24), 2469-2479.
48. Hine, R., Martin, E., ed.^eds., **A Dictionary of Biology**. 7 edn., Oxford University Press, 2015.
49. Yu, D., Huang, F., Xu, H., Determination of critical concentrations by synchronous fluorescence spectrometry. Analytical Methods 2012, 4(1), 47-49.
50. Guida, V., Thermodynamics and kinetics of vesicles formation processes. Advances in colloid and interface science 2010, 161(1), 77-88.
51. Smith, J.A., Ng, K.S., Mead, B.E., Dopson, S., Reeve, B., Edwards, J., Wood, M.J., Carr, A.J., Bure, K., Karp, J.M., Extracellular vesicles commercial potential as byproducts of cell manufacturing for research and therapeutic use. Bioprocess Int 2015, 13, 20-28.
52. Wagner, A., Vorauer-Uhl, K., Liposome Technology for Industrial Purposes. Journal of Drug Delivery 2011, 2011.
53. Philippot, J.R., Schuber, F., Liposomes as tools in basic research and industry. CRC press. 1994.
54. Palivan, C.G., Goers, R., Najer, A., Zhang, X., Car, A., Meier, W., Bioinspired polymer vesicles and membranes for biological and medical applications. Chemical Society Reviews 2016, 45(2), 377-411.
55. Cheung, K.-H., Keerthikumar, S., Roncaglia, P., Subramanian, S.L., Roth, M.E., Samuel, M., Anand, S., Gangoda, L., Gould, S., Alexander, R., Extending gene ontology in the context of extracellular RNA and vesicle communication. Journal of biomedical semantics 2016, 7(1), 19.
56. Adams, R., DOSY – Practicalities and Pitfalls. 2015.
57. Iraci, N., Leonardi, T., Gessler, F., Vega, B., Pluchino, S., Focus on extracellular vesicles: Physiological role and signalling properties of extracellular membrane vesicles. International journal of molecular sciences 2016, 17(2), 171.
58. Kavanagh, K., Fungi: biology and applications. John Wiley & Sons. 2011.

59. Goodson, H.V., Molecular evolution of the myosin superfamily: application of phylogenetic techniques to cell biological questions. Soc. Gen. Physiol. Ser 1994, 49, 141-157.
60. Albertsen, A.N., Duffy, C., Sutherland, J.D., Monnard, P.-A., Self-assembly of phosphate amphiphiles in mixtures of prebiotically plausible surfactants. Astrobiology 2014, 14(6), 462-472.
61. Apel, C.L., Deamer, D.W., Mautner, M.N., Self-assembled vesicles of monocarboxylic acids and alcohols: conditions for stability and for the encapsulation of biopolymers. Biochimica et Biophysica Acta (BBA)-Biomembranes 2002, 1559(1), 1-9.
62. Monnard, P.A., Deamer, D.W., Membrane self ‐ assembly processes: Steps toward the first cellular life. The Anatomical Record 2002, 268(3), 196-207.
63. Mansy, S.S., Szostak, J.W., Thermostability of model protocell membranes. Proceedings of the National Academy of Sciences 2008, 105(36), 13351-13355.
64. Burlatsky, S.F., Atrazhev, V.V., Dmitriev, D.V., Sultanov, V.I., Timokhina, E.N., Ugolkova, E.A., Tulyani, S., Vincitore, A., Surface tension model for surfactant solutions at the critical micelle concentration. Journal of Colloid and Interface Science 2013, 393(1), 151-160.
65. Gruen, D., The hydrophobic effect: Formation of micelles and biological membranes By , Wiley, New York, 1979, 2nd ed., $18.50. Journal of Colloid and Interface Science 1980, 77(2), 588.
66. Tanford, C., The hydrophobic effect: formation of micelles and biological membranes 2d ed. J. Wiley. Newyork Chichester, 1980.
67. Dominguez, A., Fernandez, A., Gonzalez, N., Iglesias, E., Montenegro, L., Determination of Critical Micelle Concentration of Some Surfactants by Three Techniques. Journal of Chemical Education 1997, 74(10), 1227.
68. Parfitt, G., Smith, A., Conductivity of sodium dodecyl sulfate solutions below the critical micelle concentration. The Journal of Physical Chemistry 1962, 66(5), 942-943.
69. Wong, J.E., Duchscherer, T.M., Pietraru, G., Cramb, D.T., Novel fluorescence spectral deconvolution method for determination of critical micelle concentrations using the fluorescence probe PRODAN. Langmuir 1999, 15(19), 6181-6186.
70. Ramamurthy, V., Photochemistry in organized and constrained media. VCH Publishers. 1991.
71. Ananthapadmanabhan, K.P., Goddard, E.D., Turro, N.J., Kuo, P.L., Fluorescence probes for critical micelle concentration determination

Langmuir 1985, 1(3), 352-355.

72. Rager, T., Meyer, W.H., Wegner, G., Winnik, M.A., Influence of chain length and salt concentration on block copolymer micellization. Macromolecules 1997, 30(17), 4911-4919.
73. Wicken, A., Evans, J., Knox, K., Critical micelle concentrations of lipoteichoic acids. Journal of Bacteriology 1986, 166(1), 72-77.
74. Fisher, L., Oakenfull, D., Environment of solubilized molecules in bile salt micelles. Australian Journal of Chemistry 1979, 32(1), 31-39.
75. Mukerjee, P., The nature of the association equilibria and hydrophobic bonding in aqueous solutions of association colloids. Advances in Colloid and Interface Science 1967, 1(3), 242-275.
76. Mukerjee, P., Mysels, K.J., Critical micelle concentrations of aqueous surfactant systems. DTIC Document: 1971.
77. Donchi, K.F., Robert, G.P., Ternai, B., Derrick, P.J., A surface-active merocyanine dye as a probe of micellar environments. Australian Journal of Chemistry 1980, 33(10), 2199-2206.
78. Weeks, E.R., Understanding Dynamic Light Scattering. Wyatt Technology: Emory University, 2008.
79. Goldburg, W., Dynamic light scattering. American Journal of Physics 1999, 67(12), 1152-1160.
80. Pecora, R., Doppler Shifts in Light Scattering from Pure Liquids and Polymer Solutions. The Journal of Chemical Physics 1964, 40(6), 1604.
81. Sartor, M., Dynamic light scattering. University of California, San Diego 2003, 2-21.
82. Berne, B.J., Pecora, R., Dynamic Light Scattering: With Applications to Chemistry, Biology, and Physics. Dover Publications. 2013.
83. McNeil, S.E., Nanotechnology for the biologist. Journal of Leukocyte Biology 2005, 78(3), 585-594.
84. Guenet, J.-M., Thermoreversible gelation of polymers and biopolymers. Academic Press. London, 1992.
85. Krevelen, D.W.v., Nijenhuis, K.t., Properties of polymers: their correlation with chemical structure ; their numerical estimation and prediction from additive group contributions. Elsevier. Amsterdam;Boston;, 2009.
86. Chambon, F., Winter, H.H., Stopping of crosslinking reaction in a PDMS polymer at the gel point. Polymer Bulletin 1985, 13(6), 499-503.
87. Winter, H.H., Chambon, F., Analysis of linear viscoelasticity of a crosslinking polymer at the gel point. Journal of Rheology (1978-present) 1986, 30(2), 367-382.

88. Tanaka, T., Experimental methods in polymer science: modern methods in polymer research and technology. Academic. London;San Diego, Calif;, 1999.
89. Shibayama, M., Norisuye, T., Gel Formation Analyses by Dynamic Light Scattering. Bulletin of the Chemical Society of Japan 2002, 75(4), 641-659.
90. Hill, J.O., For better thermal analysis and calorimetry. International Confederation for Thermal Analysis. 1991.
91. Gallagher, P.K., Brown, M.E., Kemp, R., Handbook of thermal analysis and calorimetry. Elsevier. 1998.
92. Brown, M., Introduction to thermal analysis: Techniques and applications (hot topics in thermal analysis and calorimetry). Kluwer Academic Publishers, Dordrecht: 2002.
93. Raju, P.M., Infiltration Growth processing of YBCO nano-composites: shape forming, microstructural and magnetic studies. PhD dissertation Shodhganga : a reservoir of Indian theses. Hayderabad University, 2013.
94. Chandran, K., Kamruddin, M., Anthonysamy, S., Ganesan, V., Thermal Decomposition Behavior of Sodium Alkoxides of Relevance to Fast Reactor Technology. Reactions and Mechanisms in Thermal Analysis of Advanced Materials, John Wiley & Sons, Inc.: 2015; pp 333-392.
95. Benes, E., Improved quartz crystal microbalance technique. Journal of Applied Physics 1984, 56(3), 608-626.
96. Thomas, J.M., Williams, B.R., Theory and applications of vacuum microbalance techniques. Quarterly Reviews, Chemical Society 1965, 19(3), 231-253.
97. Peschel, A., Langhoff, A., Uhl, E., Dathathreyan, A., Haindl, S., Johannsmann, D., Reviakine, I., Lipid phase behavior studied with a quartz crystal microbalance: A technique for biophysical studies with applications in screening. The Journal of chemical physics 2016, 145(20), 204904.
98. Chartoff, R., Turi, E., Thermal characterization of polymeric materials. Academic Press: New York 1997, 1, 513.
99. Freire, E., Differential scanning calorimetry. Protein stability and folding, Springer: 1995; pp 191-218.
100. Sørland, G.H., Pulsed Field Gradient—NMR Sequences. Dynamic Pulsed-Field-Gradient NMR, Springer: Springer Series in Chemical Physics, 2014; Vol. 110, pp 1-35.
101. Stejskal, E.O., Tanner, J.E., Spin diffusion measurements: spin echoes in the presence of a time ‐ dependent field gradient. The journal of chemical physics 1965, 42(1), 288-292.

102. Nilsson, M., Connell, M.A., Davis, A.L., Morris, G.A., Biexponential fitting of diffusion-ordered NMR data: practicalities and limitations. Analytical chemistry 2006, 78(9), 3040-3045.

103. Zhao, X., Jin, F., Zhou, L., Wang, Q., Pu, X., Chapter 5 - Reconstruction of Sag-Wide Reservoir Characteristics. In Zhao, X., Jin, F., Zhou, L., Wang, Q., Pu, X., eds.Re-exploration Programs for Petroleum-Rich Sags in Rift Basins, Gulf Professional Publishing: 2018; pp 185-269.

104. Barge, L., Hammond, D., Chan, M., Potter, S., Petruska, J., Nealson, K., Precipitation patterns formed by self - organizing processes in porous media. Geofluids 2011, 11(2), 124-133.

105. Li, Z., Li, X., Xia, Q., Xi, H., Effects of pore sizes of porous silica gels on desorption activation energy of water vapour. Applied Thermal Engineering 2007, 27(5), 869-876.

106. Hu, X., Wang, X., Liu, J., Zhang, S., Jiang, C., He, X., Fabrication of mesoporous dendritic silica nanofibers by using dendritic polyaniline templates. Materials Chemistry and Physics 2012, 137(1), 17-21.

107. Gorrell, I.B., Henderson, T.W., Albdeery, K., Savage, P.M., Kee, T.P., Chemical Transformations in Proto-Cytoplasmic Media. Phosphorus Coupling in the Silica Hydrogel Phase. Life 2017, 7(4), 45.

108. Christy, A.A., Quantitative determination of surface area of silica gel particles by near infrared spectroscopy and chemometrics. Colloids and Surfaces A: Physicochemical and Engineering Aspects 2008, 322(1), 248-252.

109. Gull, M.J.C., Prebiotic phosphorylation reactions on the early Earth. 2014, 5(2), 193-212.

110. Danaei, M., Dehghankhold, M., Ataei, S., Hasanzadeh Davarani, F., Javanmard, R., Dokhani, A., Khorasani, S., Mozafari, M.J.P., Impact of particle size and polydispersity index on the clinical applications of lipidic nanocarrier systems. 2018, 10(2), 57.

111. Panalytical, M., Dynamic Light Scattering (DLS) - Understanding the Basics. Azo Nano 2013.

112. Mamane, H., Ducoste, J.J., Linden, K.G.J.A.o., Effect of particles on ultraviolet light penetration in natural and engineered systems. 2006, 45(8), 1844-1856.

113. Calcabrini, M., Onna, D.J.J.o.C.E., Exploring the Gel State: Optical Determination of Gelation Times and Transport Properties of Gels with an Inexpensive 3D-Printed Spectrophotometer. 2018, 96(1), 116-123.

114. Whitesides, G.M., Grzybowski, B., Self-assembly at all scales. Science 2002, 295(5564), 2418-2421.

115. Philp, D., Stoddart, J.F., Self‐assembly in natural and unnatural systems. Angewandte Chemie International Edition in English 1996, 35(11), 1154-1196.
116. Ball, P., Borley, N.R., The self-made tapestry: pattern formation in nature. Oxford University Press Oxford. 1999.
117. Jakab, K., Norotte, C., Damon, B., Marga, F., Neagu, A., Besch-Williford, C.L., Kachurin, A., Church, K.H., Park, H., Mironov, V., Tissue engineering by self-assembly of cells printed into topologically defined structures. Tissue Engineering Part A 2008, 14(3), 413-421.
118. Kalyanasundaram, K., Thomas, J., Environmental effects on vibronic band intensities in pyrene monomer fluorescence and their application in studies of micellar systems. Journal of the American Chemical Society 1977, 99(7), 2039-2044.
119. Wong, J., Duchscherer, T., Pietraru, G., Cramb, D., Novel fluorescence spectral deconvolution method for determination of critical micelle concentrations using the fluorescence probe PRODAN. Langmuir 1999, 15(19), 6181-6186.
120. Albertsen, A.N., Duffy, C.D., Sutherland, J.D., Monnard, P.A., Self-Assembly of Phosphate Amphiphiles in Mixtures of Prebiotically Plausible Surfactants. Astrobiology 2014, 14(6), 462-472.
121. Ganguly, B., Nath, R., Spectral studies of pinacyanol chloride in sodium alkyl sulfate. Chemcal and Maters Resreach 2012, 2, 13-23.
122. Namani, T., Walde, P.J.L., From decanoate micelles to decanoic acid/dodecylbenzenesulfonate vesicles. Langmuir 2005, 21(14), 6210-6219.
123. Alanzi, S., A multi-analytical investigation of the hydrogel phase. Unpublished Results 2019.
124. Lombardo, D., Kiselev, M.A., Magaz, #xf9, , S., Calandra, P., Amphiphiles Self-Assembly: Basic Concepts and Future Perspectives of Supramolecular Approaches %J Advances in Condensed Matter Physics. 2015, 2015, 22.
125. Clark, J., UV-visible Absorption Spectra. Chemguide: Helping You To Understand Chemistry 2011, 30.
126. Baillet, G., Campredon, M., Guglielmetti, R., Giusti, G., Aubert, C., Dealkylation of N-substituted indolinospironaphthoxazine photochromic compounds under UV irradiation. Journal of Photochemistry and Photobiology A: Chemistry 1994, 83(2), 147-151.
127. Baillet, G., Giusti, G., Guglielmetti, R., Comparative photodegradation study between spiro[indoline—oxazine] and spiro[indoline—pyran] derivatives in solution. Journal of

Photochemistry and Photobiology A: Chemistry 1993, 70(2), 157-161.
128. Toutchkine, A., Nguyen, D.V., Hahn, K.M., Merocyanine Dyes with Improved Photostability. 2007, 9(15).
129. Gulliya, K.S., Franck, B., Matthews, J.L., Schneider, U., Photooxidation products and derivatives thereof of merocyanine-540, their preparation and uses. Google Patents: 1994.
130. Franck, B., and Schneider, U., Photooxidation Products of Merocyanine 540 formed under Preactivation Conditions for Tumour Therapy. Photochemistry and Photobiology 1992, 56(2), 271-276.
131. Ge, J., Qu, J., Degradation of azo dye acid red B on manganese dioxide in the absence and presence of ultrasonic irradiation. Journal of Hazardous Materials 2003, 100(1–3), 197-207.
132. Scholz, G., Scholz, F.J.C., First-order differential equations in chemistry. 2014, 1(1), 1.
133. Miller, C.C., The Stokes-Einstein law for diffusion in solution. Proceedings of the Royal Society of London. Series A, Containing Papers of a Mathematical and Physical Character 1924, 106(740), 724-749.
134. Cheng, P., Schachman, H., Studies on the validity of the Einstein viscosity law and Stokes' law of sedimentation. Journal of polymer science 1955, 16(81), 19-30.
135. Johnson Jr, C.S.J.P.i.n.m.r.s., Diffusion ordered nuclear magnetic resonance spectroscopy: principles and applications. 1999, 34(3-4), 203-256.
136. Nilsson, M.J.J.o.M.R., The DOSY Toolbox: A new tool for processing PFG NMR diffusion data. 2009, 200(2), 296-302.
137. Castañar, L., Poggetto, G.D., Colbourne, A.A., Morris, G.A., Nilsson, M.J.M.R.i.C., The GNAT: A new tool for processing NMR data. 2018, 56(6), 546-558.
138. Keeler, J., Chapter 4: Fourier Transformation and Data Processing. 2004. web 2004.
139. Facey, G., The Phase of an NMR Spectrum. online 2010.
140. Ernst, R.R.J.J.o.M.R., Numerical Hilbert transform and automatic phase correction in magnetic resonance spectroscopy. 1969, 1(1), 7-26.
141. Xi, Y., Rocke, D.M.J.B.b., Baseline correction for NMR spectroscopic metabolomics data analysis. 2008, 9(1), 324.
142. Morris, G.A., Barjat, H., Home, T.J.J.P.i.n.m.r.s., Reference deconvolution methods. 1997, 31(2-3), 197-257.
143. Ashenhurst, J., The Haworth Projection. Online 2019.
144. Harrington, J., Leeds Electron Microscopy and Spectroscopy Centre. LEMAS facilities, University of Leeds.

145. Bayraktutan, T., Onganer, Y., Meral, K., Polyelectrolyte-induced H-aggregation of Merocyanine 540 and its application in metal ions detection as a colorimetric sensor. Sensors and Actuators B: Chemical 2016, 226, 52-61.
146. Liu, C., Lu, Y., He, S., Wang, Q., Zhao, L., Zeng, X.J.J.o.M.C.C., The nature of the styrylindolium dye: transformations among its monomer, aggregates and water adducts. 2013, 1(31), 4770-4778.
147. Lai, J.C.-Y., Pearce, B.K., Pudritz, R.E., Lee, D.J.I., Meteoritic abundances of fatty acids and potential reaction pathways in planetesimals. 2019, 319, 685-700.
148. Deamer, D.J.L., The role of lipid membranes in life’s origin. 2017, 7(1), 5.